Alla mia famiglia,

colonna portante della mia vita.

A Toto,

rifugio sicuro della mia anima.

UNIVERSITÀ CAMPUS BIO-MEDICO DI ROMA

Corso di Dottorato di Ricerca in

SCIENZE E INGEGNERIA PER L'UOMO E L'AMBIENTE/

SCIENCE AND ENGINEERING FOR HUMANS AND ENVIRONMENT

Curriculum *Bioingegneria/ Bioengineering*

XXXV ciclo a.a. 2019-2020

Flexible Wearable Systems Based on Fiber Bragg Grating Technology for Monitoring Respiratory Parameters and Body Postures in Clinical and Occupational Settings

Martina Zaltieri

Coordinatore
Prof. Giulio Iannello

Tutor
Prof. Emiliano Schena

Co-Tutor
Eng. Carlo Massaroni

Abstract

The 21st century has been an era marked by profound technological innovation that has led to the digitization of every aspect of our daily lives. Among the sectors that have been most involved in the process, the 4.0 paradigm has had a particular impact on industry and healthcare, placing the well-being of workers and patients in the spotlight. In fact, the digital breakthrough has brought substantial changes in the way of working, putting the occupational health and safety of the workers at the foreground. On the other hand, digitalization has enabled the transition from a hospital-centered to a patient-centered approach to healthcare.

In this context, the use of wearable technologies has been given wide resonance, as wearables can be valuable allies in the care of individuals, helping to make an assessment of their general health status by monitoring some significant parameters related to physical (e.g., respiratory rate, posture, or body movement) and psychological conditions (e.g., respiratory rate) of the user. This is of great utility in both the occupational field, to assess the health status of ever more stressed and sedentary workers, and the clinical setting, to monitor the well-being of patients and the correct execution of rehabilitation tasks.

This thesis work aims at presenting novel flexible wearable systems based on fiber Bragg grating (FBG) sensing technology to take advantage of their excellent features (i.e., small dimensions, flexibility, high sensitivity to strain and immunity to electromagnetic radiations). The preliminary study, the design and the fabrication steps that led to the realization of the devices, as well as their validation process have been accurately described. Such wearable systems aim to monitor the state of health of workers in their occupational setting and patients during rehabilitation processes through the detection of parameters related to the respiratory activity, movements and body postures.

Summary

List of Abbreviations

A%: Accuracy Percentage

AH: Absolute Humidity

AI: Artificial Intelligence

AL: Left Abdomen

AR: Right Abdomen

ARm: Axial Rotation Movements

BBS: Broadband Source

BDA: Big Data Analytics

BH: BioHarness

BMs: Body Movements

CC: Cloud Computing

CM: Circular Movement

CO_2: Carbon Dioxide

CT: Computed Tomography

CTMs: Compensatory Trunk Movements

d: Distance

DAQ: Data Acquisition

fb: Fast Breathing

FBG: Fiber Bragg Grating

F/E: Flexion/Extension

FEV1: Forced Expiratory Volume in the first second

FLOW: Flowmeter

FM: Forward Movement

FNR: False Negative Rate

FS: Flexible Sensor

FVC: Forced Vital Capacity

FWHM: Full-Width Half-Maximum

GUI: Graphic User Interface

$\mathbf{h_{err}}$: Hysteresis Error

HR: Hearth Rate

I 4.0: Industry 4.0

IoT: Internet of Things

IQR: Interquartile Range

IT: Information Technology

LA: Left Acromion

LE: Left Elbow

LM: Lateral Movement

LOAs: Limits of Agreement

LW: Left Wrist

M: marker

MAE: Mean Absolute Error

MAPE: Mean Absolute Percentage Error

MIMU: Miniature Inertial Measurement Unit

MoCap: Motion Capture

MOD: Mean of Difference

MPE: Mean Percentage Error

MRI: Magnetic Resonance Imaging

nb: Normal Breathing

$\mathbf{O_2}$: Oxygen

OBJ: Object

OEP: Optoelectronic Plethysmography

PD: Photodiode

PDMS: polydimethylsiloxane

PE: Polyethylene

PEF: Peak Expiratory Flow

PI: Polyimide

PLA: Polylactic Acid

PSD: Power Spectral Density

PVC: Polyvinyl Chloride

R: Relative Displacement

R^2: Root Mean Square

$\mathbf{R}(\boldsymbol{\lambda})$: Reflectivity

RA: Right Acromion

RE: Right Elbow

RH: Relative Humidity

RR: Respiratory Rate

RW: Right Wrist

$\mathbf{S}_{\boldsymbol{\varepsilon}}$: Strain Sensitivity

$\mathbf{S}_{\mathbf{RH}}$: Relative Humidity Sensitivity

$\mathbf{S}_{\mathbf{T}}$: Temperature Sensitivity

sb: Slow Breathing

SD: Standard Deviation

SEE: Soft Sensing Element

SH: Smart Healthcare

SPs: Sitting Postures

t: Time

T: Temperature

T_R: Respiratory Period

TEC: Thermo-Electric Controller

TIA: Transimpedance Amplifier

TL: Left Thorax

TP: True Prediction

TPR: True Positive Rate

TR: Right Thorax

V: volume

WD: Wearable Device

WDM: Wavelength-Division Multiplexing

$\boldsymbol{\alpha_{FE}}$: Flexion/Extension Angle

β: Linear Regression Slope

Δε: Strain Variation

$\boldsymbol{\delta\eta_{eff}}$: Effective Refractive Index Modulation Amplitude

$\boldsymbol{\Delta\lambda_B}$: Bragg Wavelength Shift

ΔT: Temperature Variation

ε: Strain

$\boldsymbol{\eta_{eff}}$: Effective Refractive Index

θ: Lumbar Angle

$\boldsymbol{\theta_{AR}}$**:** Axial Rotation Angle

Λ: Spatial Periodicity

$\boldsymbol{\lambda_B}$: Bragg Wavelength

τ: Response Time

Φ: Phase Angle

%E and %**e**: Percentage Error

$\boldsymbol{\%E_{abs}}$: Absolute Percentage Error

List of Figures

List of Tables

List of Equations

Chapter 1 – Introduction

1. Rationale and aims of the thesis work

The 21st century technological revolution has been a source of change and opportunities for industry and healthcare. The ever-increasing amount of scientific knowledge has led to a constant technological advancement which has accompanied the evolution of human society in multiple ways and continues to do so. The modern electricity generation systems, the power transmission and distribution facilities, together with the capillary transport interconnection, highly advanced education and modern medicine are just several of the countless scientific innovations which have been achieved during the succession of the industrial revolutions and that impacted and improved our everyday lives [1]. Among the sectors that have been most involved in the process, the technological innovation has had a particular impact on industry and healthcare fields.

Indeed, in the 21st century, the growing global demand for fast and massive production of consumer goods, which nevertheless collided with the urgency to adopt a more environmentally sustainable and resource-saving manufacturing, has carried industrial progression to its fourth and latest phase so far, also known as “Industry 4.0” (I 4.0) [2], [3]. The information technology (IT) approach led the industry to a new digitally evolved era which laid its basis on novel methodologies such as Internet of Things (IoT), Big Data Analytics (BDA), Cloud Computing (CC) and Artificial Intelligence (AI) and advanced scientific technologies [4]–[6] This digital breakthrough has brought substantial changes in the way of working, resulting in modification in how to conceive occupational health and safety. Moreover, the wave of this scientific progress has also swept over the healthcare ground, profoundly changing it [7]. IoT, BDA, CC and AI have contributed to a deep digitization of the health system, in an epoch in which the increasing demand for healthcare services that could only be provided in hospitals was leading the system to collapse. Therefore, the IT approach together with the use of innovative technology, has enabled the transition towards the 4.0 paradigm by shifting from a hospital-centric to a patient-centric smart healthcare (SH) approach.

Within this framework, the usage of wearable devices (WDs) has become extremely diffused and popular. Indeed, their use allows a careful analysis of the user's psycho-physical state through the detection of physiological and motor-related variables. This is of major importance both in the occupational sphere, where workers are increasingly sedentary and stressed, and in the medical sphere, as it promotes home monitoring of the patient by means of telemedicine, thus avoiding overloading the hospital system.

Among the wide range of physiological variables that can be detected for assessing an individual's state of health through the usage of WDs, respiratory rate (RR) has been recognized as one of the most informative, because an alteration in its physiological values easily correlates with states of psychophysical stress. In addition, the estimation of the body motion (BM), intended as the control of movements performed by specific body districts, can be highly useful both in clinic and in occupational context to check the correct execution of a movement or verify the subject's behavior in maintaining a sitting or standing posture.

Starting from these premises, this work thesis wants to find its space in the context of the scientific research which arose on new wearable technologies at the service of the care of the subjects in both occupational settings and SH.

More precisely, this work aims at presenting the study, design, fabrication and validation of flexible wearable systems based on FBG technology, specifically focusing on the following applications: RR and BMs monitoring in SH and occupational contexts.

To do so, the following course of research objectives was followed:

1. Study of the literature background to identify the clinical and occupational need to be addressed;
2. Project and design and of the WD following the principle of wearability to meet the need;
3. Identification of the features that would make the system innovative compared to what is found in the literature;
4. Fabrication of the WD and preliminary test to verify the WD’s acceptability by the user;
5. Assessment of the WD on a population on volunteers to verify the WD’s usability in the desired context and the impact of the results on the current literature.

This thesis work is organized as follows:

In this first chapter, an analysis of the socio-economic and technological changes brought by the advent of I 4.0 and SH has been presented. Then, an insight on the roles played by the WDs in the occupational and healthcare context has been reported, together with an analysis of the main informative physiological variables to be detected. Then, a brief description of the technical features that a WD must fulfil, and an analysis of the main technologies used in the realization of these systems are given.

Chapter 2 will be dedicated to deepening of the knowledge of FBG technology. A focus will be placed on the theoretical background and the measurement principles which enable the detection of respiratory and motion movements.

In Chapter 3, a deepen study of the literature will be reported showing the solutions based on FBGs proposed to date for RR and BMs monitoring.

In Chapter 4, the design and development of soft flexible systems based on FBG technology for RR and BMs monitoring will be presented, following the evolutionary process that led from the manufacture of a single sensor to more complex multisensory systems. In addition, their assessments performed on healthy volunteers and patients against a benchmark, with particular attention to the results obtained will be described.

In Chapter 5, the contributions that this thesis has made to the current state of research within the WDs will be discussed. Also, the limit of this thesis work will be pointed out, together with some hints for future developments.

2. Social context and technological advancements leading industry and healthcare to a 4.0 approach

This paragraph will take an in-depth look at the historical and social context, as well as the main technological factors that led to a reorganization and modernization of the industrial and clinical systems.

2.1. From the first industrial revolution to Industry 4.0

The term "industrial revolution" indicates a process of deep technological innovation which entailed a profound and irreversible transformation in the productive system of the human society, leading to changes in its economic and social background [8]. It is common to refer to four different industrial revolutions (i.e., first, second, third and fourth industrial revolutions) as these took place in as many distinct periods, ranging from the 1760s to the present days. Below, the main features of the four industrial revolutions are reported:

1) *First Industrial Revolution*: from the 1760s until the late 1840s, an epoch of rapid technological development took place mainly in England and the United States, that lead to the transformation of many rural societies into urbanized metropolises [9]. The first industrial revolution has been depicted as the initial essential step toward the transition from the ancient to the modern age industry. In fact, for the first time, more efficient methodologies and innovative scientific breakthroughs drove manufacturing, production, and transportation processes to a more advanced level. Indeed, before the advent of the first industrial revolution, the society was predominantly agricultural, but the mechanization promoted by this phenomenon implemented the economy based on industrial production. Relevant innovations worth mentioning are textile machines, steam power, telegraphs and railways, all discoveries that have profoundly contributed to changing the social economy of the time.

2) *Second Industrial Revolution*: almost a century later, between 1870 and 1914, a novel wave of technological improvement has rapidly raised, which led to the discovery and exploitation of new sources of energy such as electricity, oil and gases [10]. The massive availability of such resources profoundly revolutionized the world of transports as it provided the suitable substrate for the invention and perfection of faster transports such as automobiles and airplanes. Also, telegraphs and telephones drastically changed the telecommunications sphere. This period has been defined as second industrial revolution.

3) *Third Industrial Revolution*: the third industrial revolution occurred in 1969, thus starting the so called "digital revolution"[11]. In this context, novel technologies such as personal computers and modern electronic components supported by efficient telecommunications, paved the way to a scientific improvement which found its climax in the space research and biotechnology. Also, a great focus was placed in the employment of nuclear power as innovative and enduring source of energy. Moreover, these discoveries were promoted by the high level of automation reached by means of programmable machineries.

4) *Fourth Industrial Revolution*: the fourth industrial revolution, or more commonly called "Industry 4.0" (I4.0), promotes the evolution of industrial manufacturing via digitization of modern technologies. I 4.0 emerged in Germany in the first years of the 2010s as part of a government program promoting the computerization of industrial production. It spread first across Europe and then across the entire globe [1], [12]. I 4.0 based its revolution on the inclusion of the so-called "intelligent machines" in the production chain. This was boosted by the introduction of novel and breakthrough technological methods such as IoT, BDA, CC and AI [4]–[6], that promoted the development of an industry based on the IT approach (i.e., IT industry) [13]. Even nowadays, the 4.0 paradigm continues to profoundly influence and modify the way the modern industry is conceived.

In Figure 1.1, a schematization of the four industrial revolutions is reported, showing their period of occurrence and their main characteristics.

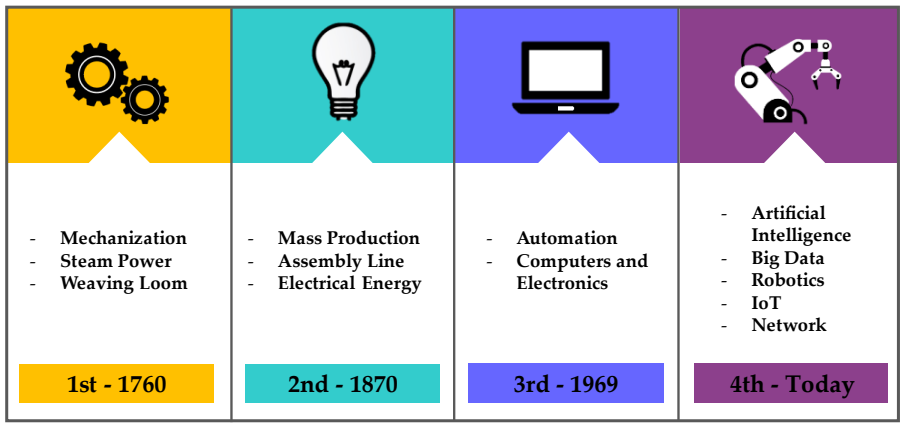

Figure1.1. The four industrial revolutions, their period of occurrence and main features.

In the following subparagraphs, the architecture of I 4.0 is first presented, followed by an analysis of how the adoption of the 4.0 paradigm has changed work roles and, consequently, led to an evolution of the concept of occupational health and safety.

2.1.1. Architecture of Industry 4.0

I 4.0 is founded on an architecture based on the four design principles identified by Hermann et al. in [14] and discussed as follows:

1) *Interconnection*: capability of technological devices, components (such as machines, sensors, WDs, etc.) and personnel to connect and share data via IoT.

2) *Information Transparency:* context-aware information on the treatment of the acquired data;

3) *Technical Assistance:* ability of the system to offer technical support to operators through the provision of clear and comprehensible information to help them make autonomous and informed decisions. Also, we talk about technical assistance in the case of cooperation with robots performing unpleasant tasks instead of the operator;

4) *Decentralized Decisions:* ability of the system to autonomously make decisions and perform task with no operator control. Operators are called to take action only in cases of conflict or interferences.

In Figure 1.2, a schematic of the I 4.0 architecture is shown. To summarize, these complex design principles enable the establishment of factories 4.0 by integrating at

different hierarchical levels. Machineries and devices communicate between them and with human being, so improving the production through the semi-automatic control of each execution step. Also, this approach enables increasingly fast and high-performance manufacturing through decentralized and automated complexity management.

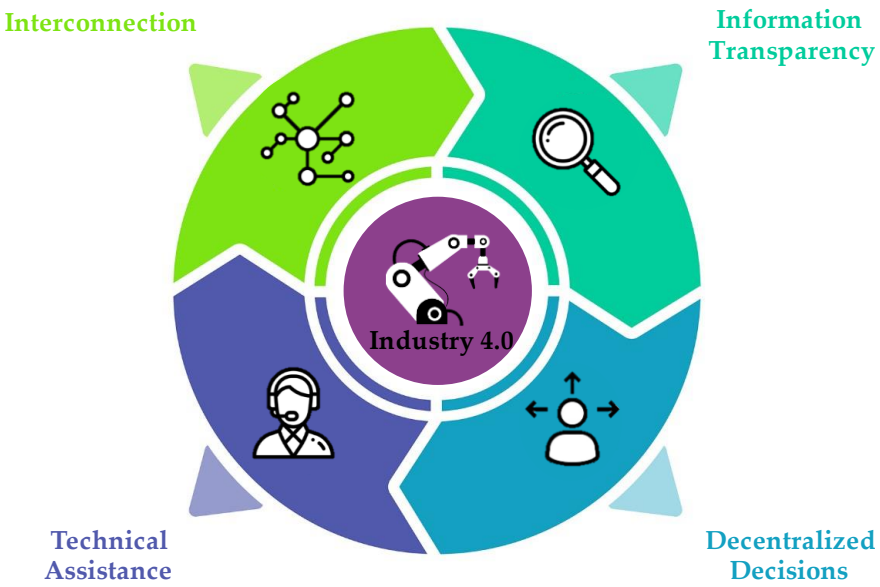

Figure 1.2. The architecture of Industry 4.0.

2.1.2. Industry 4.0 leads to changing work roles and evolution of the occupational safety and health concept

Besides the economically measurable success brought by the application of the 4.0 approach to the manufacturing system, it is now necessary to understand how I 4.0 has impacted and still continues to impact the type, quality and quantity of work and, consequently, the lives of the workforce.

Autonomous process optimizations and independent decision-making procedures, together with advancing computerization imply a reorganization of the work pyramid [15]. A targeted and extensive planning of the production line (ensured by the huge amount of data from the machines) makes the worker's presence on site often unnecessary, so foresting flexible working conditions and improved life balance [16], [17]. Also, ever more digital factories exploit industrial robots instead of human personnel to perform dangerous or tiring tasks (e.g., manual lifting and carrying), leading employees to quit risky and routinary manual roles [18]. In this frame, collaborative robots (cobots) are becoming increasingly popular [19]. Indeed, workers start devoting themselves to performing more intellectual and supervisory positions. This entails that employees are exposed to more challenging and mentally stimulating problems and that

they can perform creative and diverse activities promoting their own self-development [20]. In this respect, due to a decreasing in manual and physical labor which is replaced with computer work, the working class is less subjected to traumatic risks but is adopting even more sedentary behaviors. As consequence, sedentary-related diseases such as low back pain and cardiovascular issues are becoming increasingly widespread across the working population [21]. Moreover, risks related to the psychological sphere should not be underestimated since decision-making positions involve greater mental load and pressure, which can eventually lead to depressive moods [22].

In this context, a large space has been carved out for the concept of occupational health and safety. Based on a new approach to risk management, innovative methods have been adopted to make workers safer and healthier by monitoring both the working environment in which the operators are immersed and the workers themselves. Regarding the control of the working environments, several technologies are used starting from the most common gas and chemical detectors. Also, industrial machines can be equipped with interconnected sensors that detect faults and lead to a rapid resolution if a malfunction occurs [23]. Moreover, in the case of cobots, such sensors not only allow for self-monitoring, but can also investigate the operating environment to become aware of their surroundings in order to safely interact with the operators with whom they share the workspace [19]. Based on this, Gisbert et al. [24] pointed out that the creation of a technological platform capable of remotely controlling the industrial machinery through feedback acquired from a network of sensors could be the next step in improving occupational risk management.

Regarding the monitoring of the workers' health status, new technologies have brought useful tools for real-time detection of changes in environmental or physiological factors which would be predictor of the occurrence of dangerous situations. More in detail, personal protective equipment incorporating technology that can detect the presence of risk factors (e.g., excessive noise, temperature changes, open flames, presence of toxic gases or chemicals, etc.) is widely used [23]. However, this equipment detects only exogenous factors coming from the environment, while in recent times interest is turning towards monitoring parameters originating from the worker. In fact, early and continuous risk assessment can be achieved through the use of smart WDs embedding sensing technology capable to collect physiological variables related to the subject's phyco-physical well-being. Indeed, respiratory frequency, heart rate, temperature and information regarding the body positioning in the space are useful to identify sudden anomalies such as dyspneas, hearth failures, heat strokes or falls [20]. This approach is particularly successful since it is worker-centered and provides an all-round check on his/her status regardless of the presence of environmental risk factors, thus allowing preventive measures to be taken to avoid hazards occurrence [25].

2.2. The Smart Healthcare era: a clinical revolution driven by technological advancement

The 21st century was marked by enormous social changes, the most significant of which is an expanded life expectancy [26]. Better hygiene conditions, public sanitation and improved attention in leading a healthy and active lifestyle are just some of the factors which played a key role in in achieving greater longevity. In these regards, recent studies conducted by the Department of Economic and Social Affairs of the United Nations emphasize that the percentage of the people whose age is above 65 years will reach the 16% of the worldwide population in 2050, increasing by 6% with respect of 2022. Also, for the first time in human history, by 2050 the population of over-65s will be twice the number of both the pre-school children and children under the age of 12 [27]. While extending the population's life expectancy is one of the primary objectives of a developed nation as it is deeply correlate to an attained condition of high wellness and social welfare [28], [29], it also source of major challenges. In fact, as a consequence of an ageing population, there is an increasing incidence of age-related disorders. In addition to common conditions related to the normal ageing (e.g., hearing and vision loss) the occurrence of age-related chronic diseases (such as cardiac and neurological disorders, osteoporosis, respiratory complications, diabetes, reduced motility and more) is becoming increasingly frequent [30], [31]. The treatment of chronic diseases is time-consuming and extremely expensive, as well as burdening the national health system and increasing insurance costs. Moreover, the traditional hospital-centric patient management based on doctor-patient direct relationship is no longer capable of sustaining the rising demand of medical support, pushing the system to the brink of collapse [32].

On these grounds, in the last few decades a modernization and digitization of the healthcare system have been carried out with the aim of decentralizing the role of the hospital and placing greater emphasis on patient self-monitoring [33]. Indeed, by taking advantage of the new technological breakthroughs, it has been possible to shift the medical care approach to a smarter one, giving rise to Smart Healthcare (SH) [32]. SH relies on the use of novel technologies and IT innovations (such as advanced sensing systems, IoT, BDA, CC etc.) for remotely monitoring patient's state oh health and constantly sharing their data with clinicians, who can make diagnoses remotely, or choose to receive the patient by appointment. SH also promotes the decentralization of the medical care from the hospital to several clinical sites interconnected and distributed over the territory which deliver personalized health services focused on the needs of the patient. More in practice, the new SH paradigm of patient management aims to achieve the following goals: *i)* transition from a disease-centered medical model to a patient-centered one; *ii)* distribution of health assistance on the territory, *iii)*

promotion of remote monitoring and assistance to the patient and *iv)* improvement of preventive healthcare [32]. In few words, SH offers tailor-made patient service through continuous remote monitoring, fast data sharing and consultation with clinicians and customized treatments, with de benefit of reducing associated costs and time and limiting hospital crowding [7].

In the following subparagraphs, the technologies the SH system relies on are illustrated. Also, the 4.0 novel healthcare architecture is presented.

2.2.1. The Smart Healthcare key technological players

As illustrated in the previous section, the SH system rests deeply on the various sophisticated technologies and advanced IT breakthroughs brought by the I 4.0 revolution. For better comprehension, the main technological solutions exploited in this context are listed below:

1) *Wearable technology and implantable sensors*: WDs of various shapes and types embedding sensing elements together with high technological implantable sensors offer real-time monitoring of the patient's state of health via detection of vital physiological variables (e.g., respiratory rate, cardiac rate, blood pressure, glucose levels, etc.) [7], [33];

2) *Cloud platforms*: the patient's data retrieved by the WDs and implantable sensors are recorded and stored in remote cloud platforms real-time where they can be consulted and check [34], [35];

3) *Big data analytics algorithms*: BDA-based approach to data analysis is a crucial requirement to manage the statistical evaluation of a massive quantity of data [34], [35];

4) *Artificial intelligence and machine learning algorithms*: AI and machine learning algorithms (together with the statistics provided by BDA-based algorithms) are of prominent importance to make decisions in the light of the data analyzed. This is even more important aiming the promotion of a remote diagnosis service [35];

5) *Simulation, modeling and virtualization*: Simulations and computational models make it possible to assess the performance of health systems management, enabling structural changes [36].

2.2.2. The 4.0 paradigm redesigns the architecture of the healthcare system

Depending on where healthcare services are delivered, two main settings can be identified in the SH scenario: the domestic setting and the clinical setting. In this framework, it can be observed that the three main tasks to be performed by the health service (i.e., prevention, diagnosis and treatment of the human diseases), which were previously only supported by the hospital, are now carried out in both domestic and clinical settings [37]. To enable this, the new SH architecture is highly hierarchical and composed of several actors [33], as illustrated in Figure 1.3 and described below:

Domestic Setting: the domestic environment is where remote monitoring and virtual diagnosis, as well as home care services take place. The main actors of this setting are the users which can be, for example, elderly individuals with reduced mobility or chronic diseases [38], or people undergoing home rehabilitation after a hospital discharge [39], [40]. Remote monitoring, in fact, permits to continuously assess and control the patients' state of health, enabling quick intervention in the event of a sudden injury (e.g., stroke or fall) or to evaluate the goodness of the recovery pathway. Patient monitoring is made possible by the use of smart WDs which collect real-time data that are stored in the cloud and made available to the doctors. In this way, it is possible to obtain direct feedback from the clinician and constant follow-up without the need to visit the hospital [41]. Moreover, the clinician's constant feedback can motivate the patient to regularly perform the rehabilitation exercises or can be an incentive to follow a healthier and more active lifestyle. This setting is particularly relevant as it offers personalized and tailored care to the patient in the comfort of his/her own home environment, also limiting the number of hospital admissions with consequent improvement of the hospitalized patient management, reduction in waiting times and facility costs.

Clinical Setting: the main players of this scenario are multiple and are all those large and small clinical facilities, located across the territory, that are headed by the central healthcare center (i.e., the hospital). Rural, urban, regional healthcare centers are clinics offering a differentiated range of health services driven by high qualified personnel with diversified medical backgrounds. These centers deal with medical services at a lower level, decentralizing the figure of the hospital as a single entity providing services in order to limit its burdening. As consequence, hospitals will be able to focus on more intensive treatments, giving priority to the care of more serious and severe patients. Thanks to the SH management, which is largely supported by a highly computerized and IT-based network that allows interconnection between different clinical facilities, medical staff are able to provide optimal treatment and care to the patient [42]. In

addition, doctors themselves rely on the support of technologies that assist them in performing surgical operations (e.g., surgical robots), clinical exams (e.g., latest generation computed tomography, echographs, etc.) and in the choice of therapies (e.g., AI and machine learning-based tools), thus limiting the human error [43].

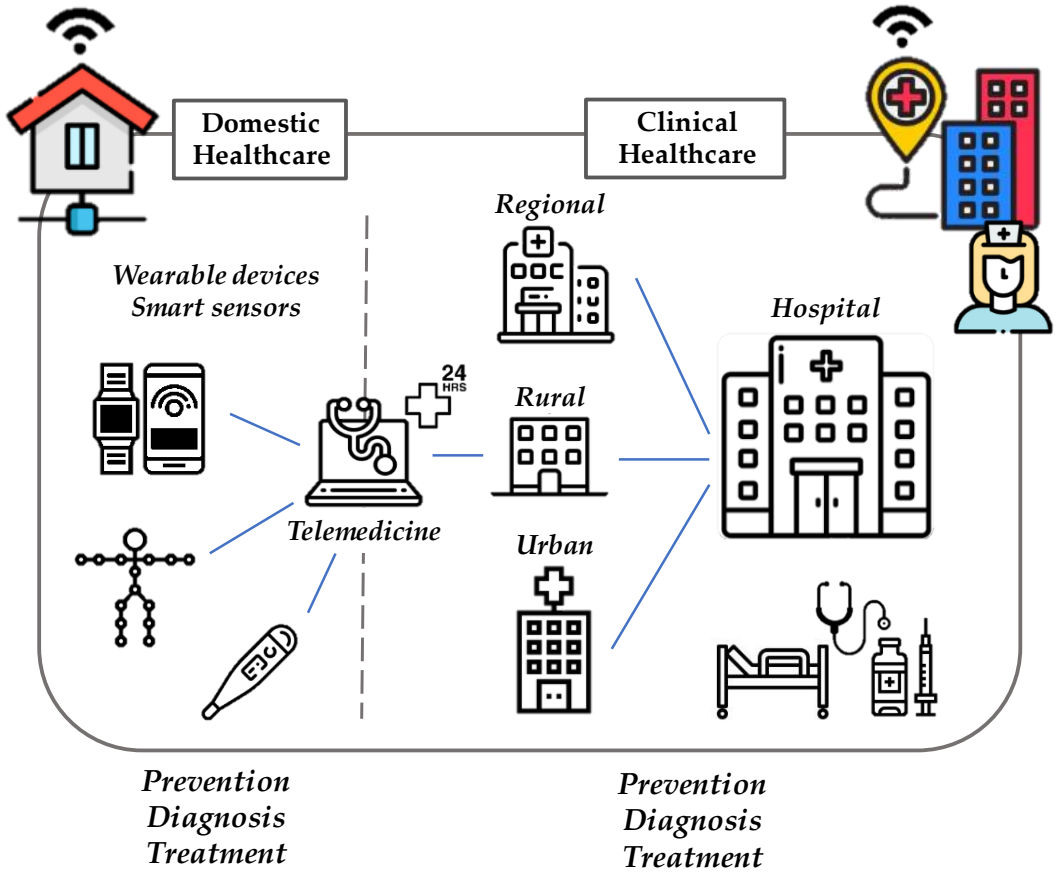

Figure 1.3. The architecture of the Smart Healthcare system.

3. The role of the wearable devices in 4.0 occupational safety and Smart Healthcare

The 21st century technological advances boosted popularity of WDs since their use has become an integral part of our everyday life, deeply changing our quotidian [44]. The WDs market is flourishing more than ever, presenting an almost unlimited range of models. Nowadays, each of us owns at least one of these devices among smartwatches, fitness wristbands, smart glasses, which provide us with information on our lifestyle and related to our physical state anywhere and anytime [45]. Apart from the everyday life, it is clear that WDs have played a relevant role in both the fields of occupational health and safety, and healthcare.

In fact, as also pointed out in the previous paragraphs, WDs are becoming part of the everyday life of workers. These systems can help preventing musculoskeletal diseases by improving user's posture in different working conditions, such as sitting (in the case of video terminal job), standing and handling heavy objects. Furthermore, the monitoring of physiological parameters helps to identify stress-correlated disease. This topic, although not sufficiently considered, is of paramount importance as a state of excessive mental load is usually accompanied by a lowering of work performance and an increase in the probability of incurring accidents in the workplace [46], [47]. However, although useful, the daily usage of wearable devices may also encounter some difficulties in this area. In fact, in the workplaces some particularly rigid, bulky or, in general, poorly fitting systems may not be easily accepted as they could restrict the user's range of motion.

Also, several are the benefits brought by the use of WDs in the healthcare sphere. In fact, multiple studies proved that the use of such systems is of great encouragement to patients in maintaining a healthy and active lifestyle [48], [49], monitoring, for example, the diet [50] or sedentariness [51]. Since continuous feedback can be obtained both from the device and the doctor (via telemedicine), the user is typically more proactively involved in rehabilitation process, not skipping exercise sessions. WDs are also largely exploited for real-time monitoring of patients in domestic environments to control a recovery course and intervene promptly in case of sickness [48]. In fact, in order to avoid hospitalization or depriving the elderly patient from the comfort of his or her own home, in some cases it is preferable to adopt a home course. On the other hand, this approach may not be successful for those patients who are older and therefore more reluctant to use new technologies. In addition, it is not uncommon for patients to unproperly wear the devices causing data loss or data corruption.

In the following sections, emphasis will be placed on the physiological variables of greatest interest in establishing the health status of patients or workers. The essential characteristics that a WD must fulfil will then be examined, and a brief description of the most used sensing technologies for wearables will be given.

3.1. The investigated physiological variables

There are many physiological variables in the medical literature that are directly related to a person's state of health, as sudden changes in these values can be linked to states of risk, disease, discomfort or distress [52]–[54]. However, with the aim of remotely monitoring the patient/worker in the SH and I4.0 context, a non-invasive approach to measurement (i.e., using non-invasive devices) was required. As consequence, in this section more stress will be placed on parameters classified as "physical" (i.e., detectable through non-invasive measurement approaches), while biochemical ones will not be mentioned.

Among others, respiratory rate (RR) and heart rate (HR) are of fundamental importance in determining a subject's state of health. Moreover, they are some of the easiest parameters to retrieve by means of WDs.

RR is considered to be one of the most informative physiological variable as it is highly sensitive to physical and emotional stress [55], [56]. In the medical practice, RR monitoring is highly used to predict the occurrence of adverse events such as cardiac arrest [57] or myocardial infarction, as well as it is used to check the improved health of in-patients [58]. Also, since it is extremely sensitive to states of psychological distress, it can be a useful ally in detecting stress-related discomfort conditions both in workers exposed to weight responsibilities and long-term patients. Another variable of interest is HR, which is closely associated with oxygen uptake, as it is sensitive to training-induced adaptations both at rest and during exercise. Together with RR, it is used to monitor psychophysiological stress and adverse health conditions, for example elevated resting heart rate is an independent risk factor for cardiovascular as well as all-cause mortality, and a prognostic factor in patients affected by coronary disease [59].

In addition to these two, although not strictly a physiological variable, also body motion (BM) (in terms of movement of specific body parts with respect to the body and movement of the body through the surrounding environment) is highly investigated. In fact, being able to monitor the movement of a joint can help both the patient and the clinician to identify an incorrect rehabilitation task execution, while keeping their tracking helps to verify the patient's improvement over time. In addition, controlling correct posture when lifting and handling loads can prevent the onset of musculoskeletal disorders [60], [61]. However, given the increasingly sedentary working environment, controlling the correct maintenance of sitting posture has also become of prominent importance [62].

3.2. Design consideration for wearability

To realize a WD, it is first necessary to identify the possible positioning sites on the user's body according to the variable (among those presented in the previous section -

RR, HR and BM) to be retrieved. In Figure 1.4, areas of the body in which each of the three above-mentioned variables can be measured according to [63] are shown.

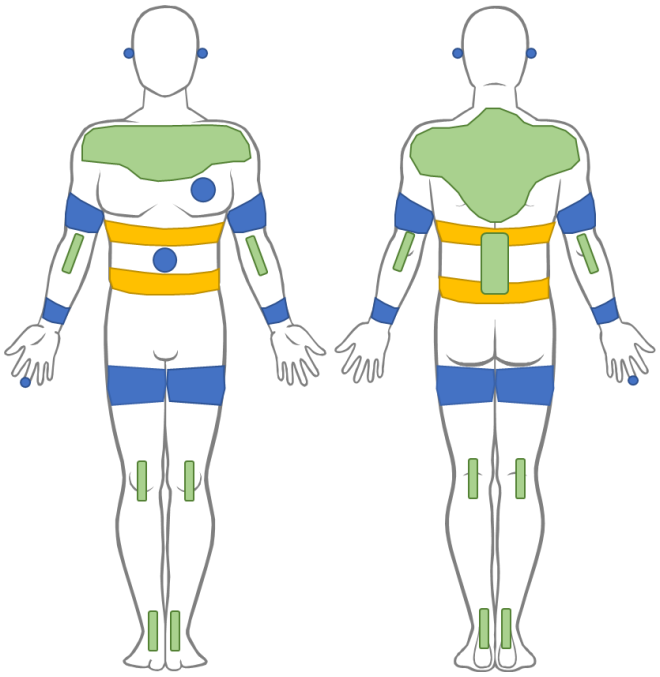

Figure 1.4. Positioning sites of the human body to retrieve RR (in yellow), HR (in blue) and BMs (in green) variables.

A prototype design process must then be carried out taking into account certain characteristics that the device must respect in order to ensure user acceptability. In an extensive literature review work, Genaro et al. [64] identified up to twenty principles that a WD must comply with, however the main characteristics taken into account by the manufacturers are considered to be the following:

1) *Comfort*: it is defined as freedom from pain and distress after a prolonged use of the wearable [65]. The concept of comfort must be taken into account in the process of finding the proper shape and material for the device. It also involves acceptable temperature at the skin interface and no movement constrains [66];

2) *Ergonomy*: in order to be compliant with the user's body, the WD must be ergonomic, that is it must adapt to the body anatomy [67];

3) *Unobtrusiveness and Weight Distribution*: the device must not impede the natural motility of the body or burden the user with loads [63]. The consequence of this requirement is the increasing miniaturization of the technology, and the study of which body areas better bear the loads;

4) *Reliability*: this word embodies the concepts of security, precision and effectiveness [65];

5) *Wearability*: combines the already described concepts of comfort, ergonomy and unobtrusiveness with the features of ease of wearing and aesthetics [68].

Over the last decades, a wide range of WDs have appeared on the market showing different functionalities and wearing options. The most frequently used are sensorized accessories (e.g., smartwatches, wristbands, smart glasses, jewelry, etc.) and smart garments (e.g., smart textiles, T-shirts, etc.) [69]. Nevertheless, considering both the abovementioned requirements and the clinical and occupational contexts of applicability, in recent years more and more space has been given to the production of flexible WDs made of soft materials [70]. In fact, their high flexibility and stretchability allow for good adaptation to the body anthropometry and no reduction in range motion, making these systems extremely comfortable and compliant. In addition, most of them are composed of polymeric materials that render them soft to the touch and suitable to be placed in direct skin contact, hided under ordinary clothes.

3.3. The sensing technology behind flexible wearable devices

As indicated in the previous section, since wearables research field has been recently moving towards the production of flexible systems, an overlook of the sensing technologies supporting this process will be given.

Strain sensors are extensively employed in this context as they allow the RR, HR and BM to be easily detected by means of the transduction of mechanical deformation into electrical signals [71]. Strain sensors are mainly classifiable into resistive and capacitive ones, although there are several other types. Soft flexible sensors can then be produced by means of different materials, such as low dimensional carbons (such as graphene [72] and nanotubes [73]), nanowires [74], nanoparticles [75] and their structures, or incorporating lightweight and thin resistive/conductive fabrics into silicone (e.g., Ecoflex and Dragonskin) or rubber -based matrices. Although popular, these sensors are not free of drawbacks. In fact, most of them are composed of conductive films and dielectric layers that make them incompatible for use in the presence of electromagnetic fields (which is likely, for example, in healthcare).

A possible solution to these limits is given by the utilization of an alternative strain sensing technology based on fiber optics: the fiber Bragg grating (FBG) sensors. In fact, in recent times, FBGs are gaining ever more acceptance due to their valuable features such as electromagnetic immunity, intrinsic electrical safety (as FBGs are empowered by light) and high sensitivity to strain. Also, extremely reduced size and weight, high flexibility and multiplexing capability allow for easy insertion into flexible substrates [76]–[78].

Chapter 2 – Fiber Bragg grating sensors for monitoring respiratory rate and body movements

1. Fiber Bragg grating sensors: measurement principle and metrological properties

In recent decades, FBGs have become increasingly popular for RR and BMs detection applications due to their unique properties such as small size, electromagnetic compatibility, high sensitivity and multiplexing capability. This paragraph provides an analysis of the FBGs' working principle and metrological features, together with the operating principles underlying the existing types of interrogation units. In this paragraph, parts of the work [79] which the PhD candidate has co-authored have been freely extracted.

1.1 Theoretical background

The FBG is a wavelength-selective fiber components and implements an in-fiber resonator concept, similar to notch filters in electronics [80]–[82]. An FBG is a modulation of the effective refractive index (η_{eff}) of the core of an optical fiber. In its simplest configuration (which is called "uniform FBG" [80]), the spatial periodicity (Λ) of the η_{eff} modulation is constant along the fiber core length. FBGs resonates at the so-called Bragg wavelength, λ_B. In fact, once illuminated by a broadband light sourced by an optical interrogator unit, most of the light spectrum passes through the grating, except for a small amount, which is centered around λ_B (i.e., reflected spectrum of light) and back-reflected to the source. λ_B can be defined as [81], [82]:

$$\lambda_B = 2 \cdot \eta_{eff} \Lambda \tag{2.1}$$

The spectrum of an FBG can be computed through the coupled mode theory [81], which studies the waves coupled forward and backward into the grating. The reflectivity $R(\lambda)$ of an FBG having total length L and refractive index modulation amplitude $\delta\eta_{eff}$, at each wavelength λ, can be expressed as follows [81], [83]

$$R(\lambda) = \frac{sinh^2\left(L\sqrt{k^2+\sigma^2}\right)}{cosh^2\left(L\sqrt{k^2-\sigma^2}\right) - \frac{\sigma^2}{k^2}} \cdot \Lambda \tag{2.2}$$

where the term $\sigma(\lambda)$ contains the wavelength dependence:

$$\sigma(\lambda) = \frac{\pi}{\lambda}\delta\eta_{eff} + 2\pi\eta_{eff}\left(\frac{1}{\lambda} - \frac{1}{\lambda_B}\right) \tag{2.3}$$

The grating strength and the maximum reflectivity can be defined as atanh^2(kL), where kL is a unitless parameter, and depend on the FBG fabrication method. In fact, phase-mask inscription [84] and direct inscription [85], [86] can implement strong gratings with kL usually within 1 to 3 value, while draw-tower inscription methods achieve low-reflectivity gratings with kL < 0.5 [87].

While the spectral features of a single FBG can be entirely encoded in its geometrical and fiber properties, the key aspect of an FBG element in sensing applications is its narrow bandwidth, which is in general reported as a full-width half-maximum (FWHM) bandwidth [80]. For an FBG having kL value ranging from 0.5 to 3 (the typical values in FBGs), the FWHM of the grating ranges from 0.15 nm to 0.38 nm: hence, the FBG acts as notch resonator, with a very narrow spectrum. This way, it is possible to stack multiple gratings in the same fiber, all having different λ_B values: this approach, labeled wavelength-division multiplexing (WDM), allows simultaneously detecting multiple gratings, up to several tens, all inscribed in the same fiber in a single array. As a plurality of FBGs can be inscribed on the same fiber, and it is possible to interrogate simultaneously multiple fibers, significant sensing networks can be obtained. In this framework, FBGs have the capability not only to detect physical parameters, but also to localize their detection in a specific point of the fiber, identifying their spatial distribution [88].

Figure 2.1 (a) shows the spectral characteristics of FBG elements.

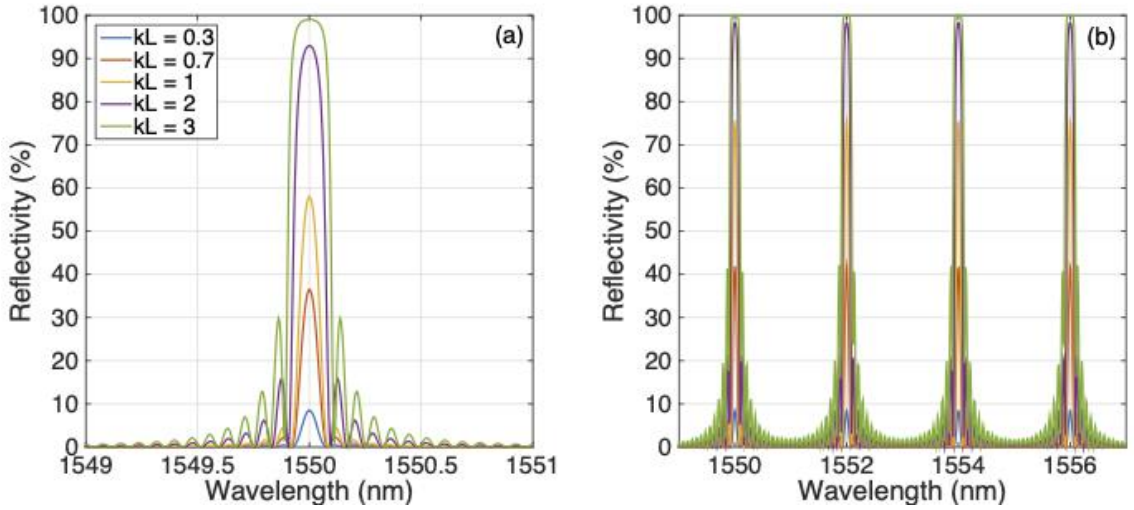

Figure 2.1. Reflection spectra of FBGs, simulated using the coupled mode theory, for different grating strength (kL) values. (a) Single FBG at 1550 nm; (b) Array of 4 FBGs at 1550-1556 nm with 2 nm spacing.

An FBG behaves as a narrow reflective filter, having reflectivity that ranges from 8% to 99% as the kL coefficient rises from 0.3 to 3. The main spectral lobe defines the bandwidth reflected by the FBG, while the spectral lobes that appear on the side of the grating have a progressively lower amplitude. The spectrum of a 4-element FBG array is shown in Figure 2.1 (b); by choosing an appropriate spacing between adjacent λ_B values (2 nm typically [88]), it is possible to have an almost perfect spectral separation between each element, hence implementing a WDM scheme.

1.2 FBGs for strain and temperature measurements

FBGs are excellent instruments for strain and temperature measurements since the sensitivity to strain and temperature is encoded directly in the λ_B. In fact, when a strain variation ($\Delta\varepsilon$) and/or a temperature variation (ΔT) are applied to the FBG, a shift in the reflected spectrum is obtained, with consequent λ_B shift ($\Delta\lambda_B$), as depicted in Figure 2.2. $\Delta\lambda_B$ can be expressed as [81]:

$$\Delta\lambda_B = 2 \cdot \left(\Lambda \frac{\partial \eta_{eff}}{\partial \varepsilon} + \eta_{eff} \frac{\partial \Lambda}{\partial \varepsilon} \right) \Delta\varepsilon + 2 \cdot \left(\Lambda \frac{\partial \eta_{eff}}{\partial T} + \eta_{eff} \frac{\partial \Lambda}{\partial T} \right) \Delta T \qquad (2.4)$$

Moreover, the Equation 2.4 can be written as a linear combination of strain sensitivity (S_ε) and temperature sentitivity (S_T) as shown in the following:

$$\Delta\lambda_B = S_\varepsilon \Delta\varepsilon + S_T \Delta T \qquad (2.5)$$

In FBG sensing networks operated in WDM, the strain or temperature values are estimated by monitoring the $\Delta\lambda_B$ from the reference position, knowing S_ε and S_T through a previous calibration or from datasheet values. The value of the sensitivity terms depends on the fiber material, and on the wavelength of operation. For FBGs on glass or ormoceramic fibers operating in the near infrared (around 1550 nm), the strain sensitivity is around 1 pm·$\mu\varepsilon^{-1}$, while the thermal sensitivity is around 10 pm·°C^{-1} [80]–[82]. On the contrary, for plastic fibers the thermal sensitivity is around -50 pm·°C^{-1} to -200 pm·°C^{-1} [89].

The dual strain/temperature sensitivity is both an advantage and a disadvantage of this sensing technique. On one side, since the system exhibits a similar response to strain and thermal variations, it is important to provide either a temperature-compensation method or a technique to isolate strain events from thermal methods. A possible method is to use a loose FBG, decoupled from any strain, as a temperature sensor, and then using this temperature reading to compensate thermal variations from the strain sensors [90], [91]. Also, in the analysis of pulsatile strain waveforms (as in the case of respiratory waveforms), another method is to isolate the contributions of respiratory patterns, having frequency contributions higher than 0.2 Hz, from temperature variations having frequency << 0.1 Hz through the use of digital bandpass

filters [78] under the assumption, where possible, that temperature variations occur at a much slower rate than strain events. In fact, in applications where an extremely rapid temperature change can occur (e.g., during intense physical activity or in a non-thermoregulated environment) such a solution would prove fallacious. However, since the sensitivity terms are both linear for a very high range of strain and temperature variations, this ensures that a compensation is always accurate, and the sensors are stable over long-term operation.

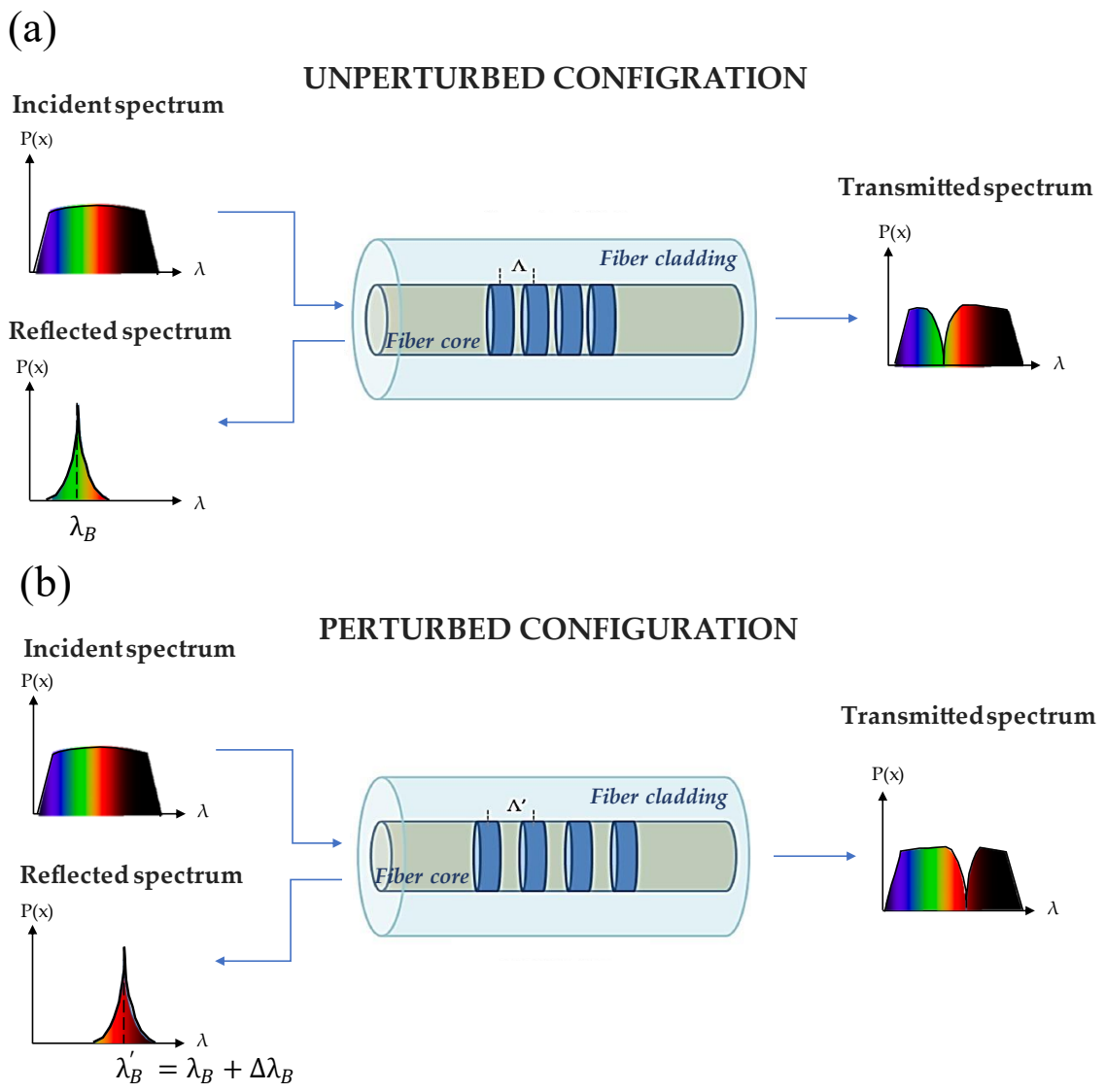

Figure 2.2. Representation of the working principle of an FBG sensor. The incident broadband spectra of light, the transmitted spectra and the reflected spectra whose peak is centered at the Bragg wavelength (λ_B) are shown. In (a) it is reported the unperturbed FBGs' configuration, while the perturbed configuration is shown in (b), where the strain and/or temperature variations caused a shift in the reflected spectrum ($\Delta\lambda_B$).

1.3 Operating principles of optical interrogator units

FBG sensors inscribed within an optical fiber are read by the optical interrogation units, that are devices which supply a light source to the FBG sensors and read their output expressed as $\Delta\lambda_B$. Interrogation units are capable to interrogate multiple fibers simultaneously. Although several methods have been proposed based on one or two wavelengths monitoring, the most common techniques for the interrogation of FBGs is based on the detection of the whole FBG spectrum, in a wide range of wavelengths [92]. The methods used in most interrogation systems are sketched in Figure 2.3.

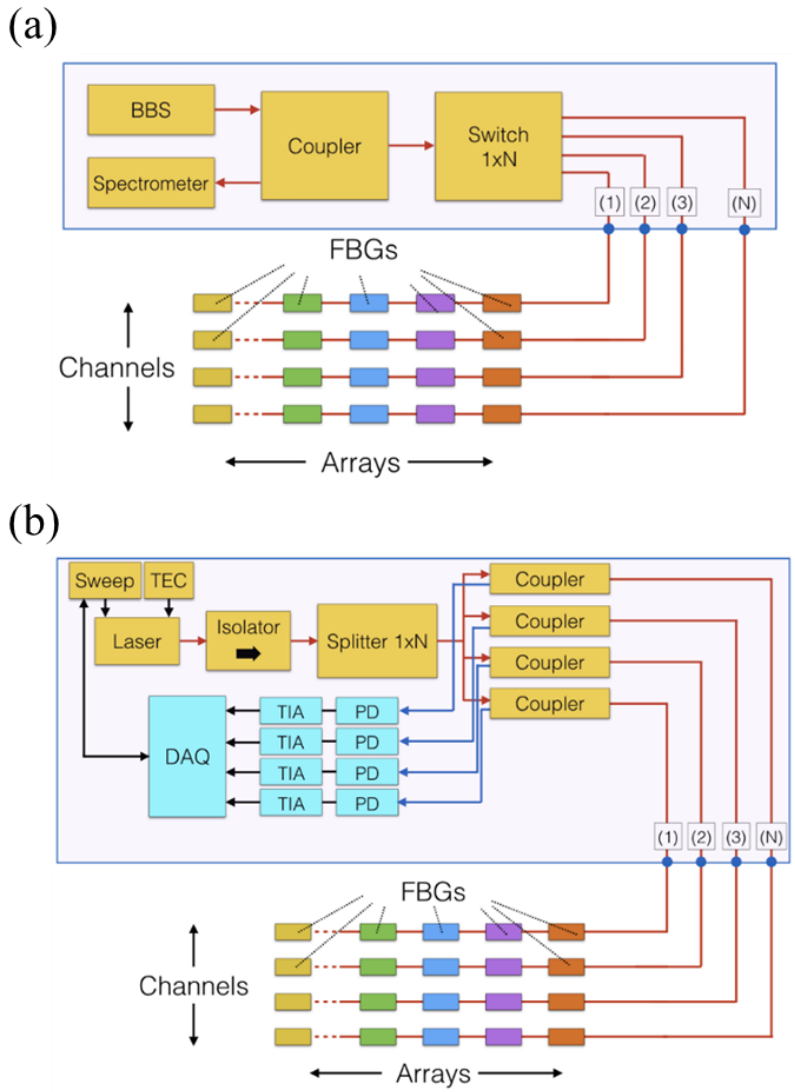

Figure 2.3. (a) Schematic of an FBG interrogation system based on a broadband source (BBS) and a spectrometer; a switch 1xN multiplexes in time domain N channels, each hosting an FBG or FBG array in WDM; (b) Schematic of an FBG interrogation based on a swept laser and a series of photodetectors, with the laser is controlled by a sweep function generator. The N channels are physically separated by a 1xN splitter.

The first method, shown in Figure 2.3 (a), makes use of a broadband source (BBS), and a spectrometer for detection. The BBS is usually a superluminescent LED, matching the bandwidth of the spectrometer; the two devices are interconnected with a coupler of circulator, routing the spectrum reflected by the FBG arrays to the detector. A switch 1xN can be used to multiplex N channels in the time domain, commuting between multiple output fibers; this approach combines WDM with TDM, to arrange sensor networks spaced in wavelength and time. The method based on spectrometer has several advantages in terms of portability, power consumption, and cost; as shown in previous works, a spectrometer-based interrogator can be packaged in a portable battery-powered device [93].

The second method, integrated in several commercial devices, aims at detecting FBG spectra on a denser wavelength grid (below 10 p), is called swept-lased method. The system is based on a swept laser, either implemented as a laser controlled by a thermo-electric controller (TEC) and a sweep function generator, as illustrated in Figure 2.3 (b), or as a Fabry-Perot laser tuned by an acousto-optic filter [94]. In this system, the channels are physically split and simultaneously detected, by means of a 1xN splitter and N couplers, routing the light to the N channels. The detector is based on a photodiode (PD) followed by a variable-gain transimpedance amplifier (TIA). The data acquisition (DAQ) system synchronizes the readout from all photodetectors with the sweep function generator. This method leads to a device that is bulkier, more expensive, and with limited field operativity due to the need to mains power supply, however it has better precision thanks to the narrow wavelength grid and 1 kHz speed thanks to the rapid wavelength scans, regardless of the number of channels.

2. Measurement principle of systems based on FBGs for monitoring respiratory activity

This paragraph is devoted to display the main techniques used to detect RR and BMs variables starting from the breathing activity by means of the FBG sensors. In this paragraph, parts of the work [79] which the PhD candidate has co-authored have been freely extracted.

2.1. Introduction to respiratory mechanics

Breathing (or ventilation) consists in recalling and expelling air into and from the lungs to promote carbon dioxide (CO_2) and oxygen (O_2) gas exchanges. More precisely, at the alveoli site, CO_2 is released while O_2 diffuses into the bloodstream.

The breathing process is composed of two different phases, which are described below [95], [96]:

1) *Inspiration, or inhaling*: it is the phase in which air enters the lungs. Inspiration is promoted by the contraction of the principal (the diaphragm and external intercostal muscles) and accessory (the scalene and the sternocleidomastoid) inspiratory muscles. The diaphragm flattens while ribs and sternum are elevated, thus increasing the volume of the thoracic cavity and, as consequence, of the lungs. As lungs' volume increase, a drop in pressure occurs. Pressure inside the lungs is lower than in the external environment, recalling the air. The air enters the nose/mouth, runs through larynx and pharynx, and reaches the lungs.

2) *Expiration, or exhaling:* in this phase the air is expelled from the lungs to the external environment. Expiration can be both passive and active. In the case of passive exhalation, the lowering of the volume of the thoracic cavity is given by the relaxation of the main respiratory muscles coming to their resting position. Moreover, active exhalation occurs when also the abdominal, sternocleidomastoid and internal intercostal muscles are involved by active contraction (e.g., during forced breathing or asthma cases). The pressure increases in the lungs becoming greater than in the external environment, forcing the air to flow outside going backwards through the airways.

During the respiratory process, the air undergoes transformations in the thermohygrometric conditions [97]. Outside air is inhaled at room temperature (which is about 23 °C) and relative humidity (RH) ranging between 40% and 80%, but as it passes through the airways it is humidified and heated. This difference is significant as air is exhaled at body temperature (i.e., around 37 °C) and saturated by vapor (i.e., RH = 100%) [98]. In Figure 2.4, the two phases of the respiratory mechanics and the thermohygrometric conditions of inhaled/exhaled air are represented.

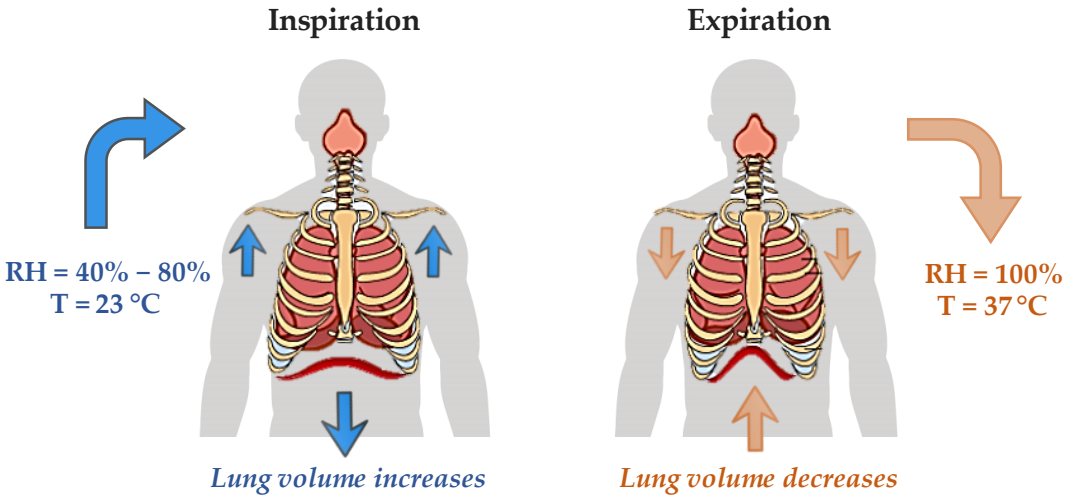

Figure 2.4. Schematic of the respiratory mechanics and thermohygrometric characteristics of the inhaled and exhaled air are shown for the two breathing phases.

Based on this knowledge, in the following subsections the description of the most popular FBGs-based techniques for monitoring RR and, more in general, respiratory parameters are reported. In Subsection 2.2.1 the technique based on the monitoring of the chest wall movements caused by the respiratory activity is shown. Subsection 2.2.2 focuses on the estimation of the respiratory parameters exploiting the difference in RH between inspiratory and expiratory air. In Subsection 2.2.3 the technique based on monitoring the respiratory airflow has been described. Particular attention will be focused on the working principle of these solutions.

2.1.1. FBG-based system for respiratory monitoring via chest wall displacements

During quiet breathing, the rib cage undergoes displacements of 3-5 mm in the ventral part and 1-2 mm in the lateral parts but can reach much greater shifts for heavy breathing [99], [100]. Being able to monitor the chest circumference changes occurring during breathing can be crucial to understand respiratory mechanics better. FBGs are highly suitable for this purpose. Often, solutions based on the encapsulation of FBGs in soft materials (e.g., silicone rubbers) are preferred to improve the robustness of the system and to improve the adherence to the chest wall. When the substrate undergoes a deformation, the strain is transmitted to the FBGs that experience a $\Delta\lambda_B$. Although $\Delta\lambda_B$ is caused by both strain and temperature variations (please refer to Equation 2.5), in this context, the $\Delta\lambda_B$ can be considered caused only by strain, since the contributions given by temperature variations are negligible (as pointed out in Subsection 1.2). As consequence, $\Delta\lambda_B$ can be obtained as follows:

$$\Delta\lambda_B = S_\varepsilon \Delta\varepsilon \tag{2.6}$$

The maximum and minimum deformation of the sensors corresponds to the end of the inspiratory and expiratory phases, respectively. Therefore, considering the elapsed time between two consecutive maxima (i.e., two consecutive inspiratory ends) or minima (i.e., two consecutive expiratory ends) is possible to estimate the respiratory period and so the RR.

In Figure 2.5, a representation of the working principle of this technique is reported, together with an example of the obtained $\Delta\lambda_B$ trend in time, showing the minimum and maximum peaks corresponding to the end of expiration and inspiration phases, respectively.

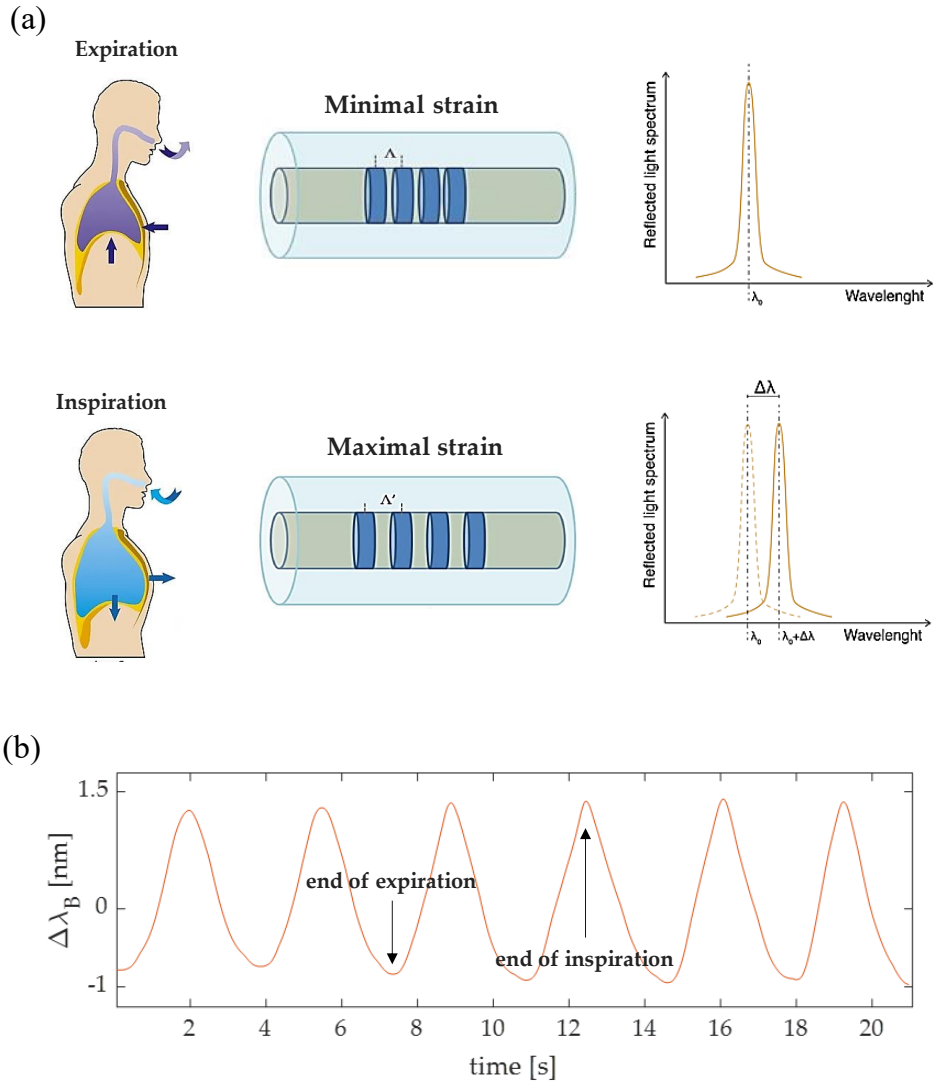

Figure 2.5. (a) Representation of the working principle of the technique for RR monitoring based on the measurement of the chest wall displacements occurring during the breathing activity. In the expiration phase the sensor undergoes minimum deformation, while in the inspiration phase

a maximal sensors deformation occurs. In (b) an example of $\Delta\lambda_B$ trend in time is given, showing minimum and maximum peaks corresponding to expiration and inspiration phases, respectively.

2.1.2. FBG-based system for respiratory monitoring via difference of thermohygrometric conditions between inspiratory and expiratory airflow

During the breathing activity, the airflow is inspired at environmental temperature and humidity while is expired at body temperature and full saturated of water. The difference in the content of water vapor and so in RH can be exploited to discriminate the inspiratory from the expiratory phase.

Although the description of the FBGs' principle of work and Equation 2.4 highlight the sensitivity of FBGs to only strain and temperature, solutions based on FBGs for measuring RH have been investigated [101], [102]. To make an FBG sensitive to RH, the sensing part is coated by hygroscopic polymers. Several coatings, that can be roughly divided into synthetic polymer coatings (e.g., polyimide and polymethyl methacrylate), natural polymer coatings (e.g., agar and agarose), and other material coatings (e.g., ORMOCER), have been investigated [101]–[103]. These materials absorb/desorb water vapor for RH increase/decrease with a consequent volume increase/decrease.

Thus, two contributions cause an increment of $\Delta\lambda_B$ when expired gas hits the sensing element for two reasons: *i)* the positive temperature change from inspired to expired air and *ii)* the positive RH change from inspired to expired air with consequent swelling of the coating and so the strain of the grating.

Modeling a functionalized FBG as an infinitely long rod made of two bonded materials (i.e., the coating and the fiber silica) and assuming the behavior of both the materials linear, isotropic and elastic so causing linear transmission of the volumetric changes of the matrix on the grating in terms of longitudinal ε, Equation 2.4, can be rewritten as the following [104]:

$$\Delta\lambda_B = S_{RH}\Delta RH + S_T\Delta T \tag{2.7}$$

with S_{RH} the sensitivity to ΔRH, expressed in nm·%$^{-1}$.

In many applications the ΔT contribution is deemed negligible and the $\Delta\lambda_B$ can be considered product of the sole ΔRH. Moreover, RR and its subcomponents (i.e., inspiratory time and expiratory time) can also be investigated by exploiting FBGs sensitivity to ΔT. As the temperature increase/decrease, FBG sensors undergo a shift to higher/smaller λ_B values ($\Delta\lambda_B$), so ΔT can be obtained by dividing $\Delta\lambda_B$ by the temperature sensitivity coefficient. The temperature difference between the inhaled and the exhaled air may allow estimating RR.

In contrast to what was said for the chest wall displacements, in this configuration the maximum FBG deformation is retrieved at the end of the expiratory phase, while the minimum deformation is given at the end of the inspiratory phase. Once again, RR can

be obtained considering the inverse of the period (which is the elapsed time between two consecutive maxima or minima). A representation of the working principle and the $\Delta\lambda_B$ evolution in time is given in Figure 2.6.

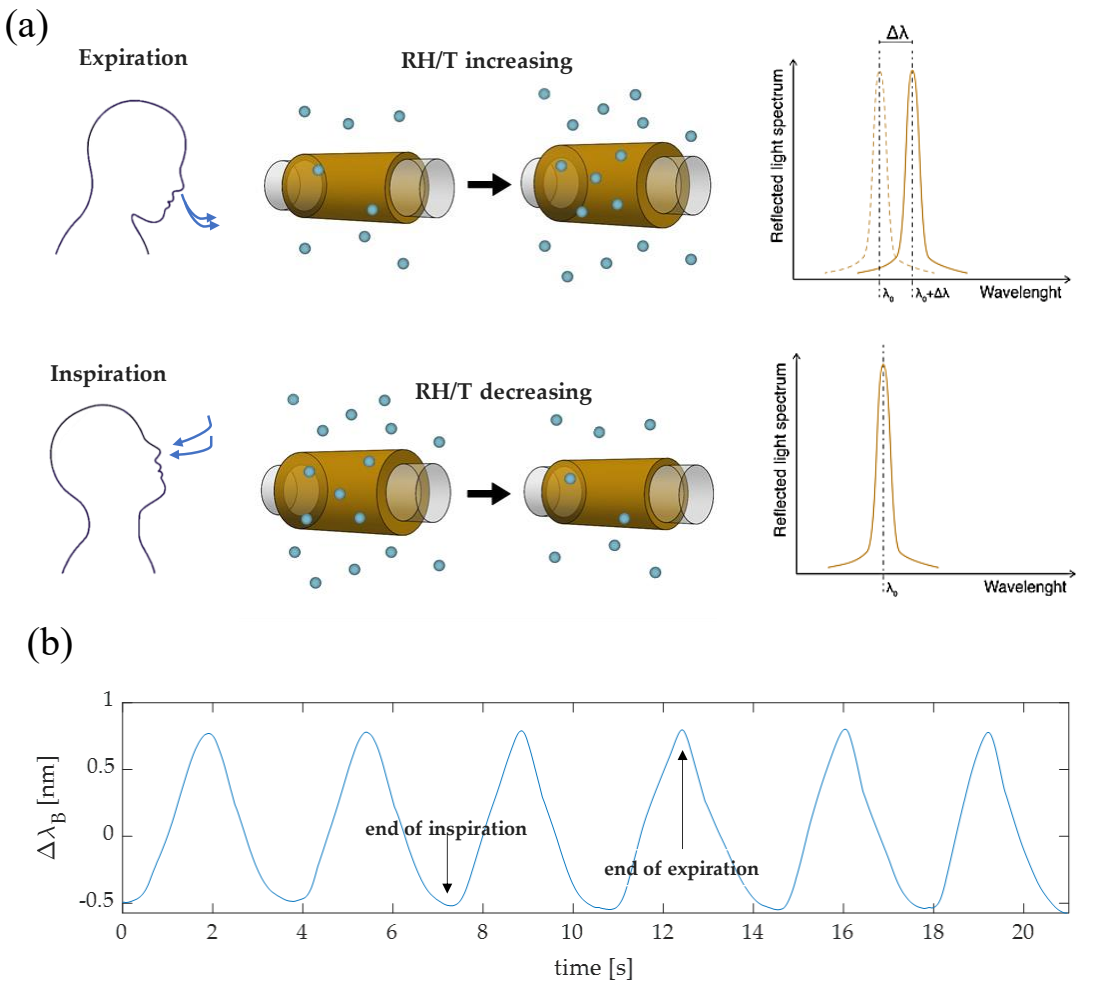

Figure 2.6. (a) Representation of the working principle of the technique for RR monitoring based on the difference of thermohygrometric conditions between inspiratory and expiratory airflow. In the expiration phase the sensor undergoes maximum deformation, while in the inspiration phase a minimal sensors deformation occurs. In (b) an example of $\Delta\lambda_B$ trend in time is given, showing minimum and maximum peaks corresponding to inspiration and expiration phases, respectively.

2.1.3. FBG-based system for respiratory monitoring via breathing airflows

This technique exploits FBGs to directly measure inhaled and exhaled airflows and takes advantage of the high sensitivity to the strain of the FBGs. In this case the FBGs, usually embedded in highly flexible membranes or diaphragms, are subjected to the

direct flow of air inhaled and exhaled through the nose or mouth. As consequence, the sensors undergo deflections and compressions causing $\Delta\lambda_B$ which is the larger, the greater the flow of exhaled/inhaled air. As for chest wall movements, also in this case $\Delta\lambda_B$ can be considered product of the sole $\Delta\varepsilon$ contribution (please refer to Equation 2.6). Again, RR can be retrieved considering the inverse of the breathing period. In figure 2.7 the working principle is shown, together with an example of the $\Delta\lambda_B$ trend in time [105].

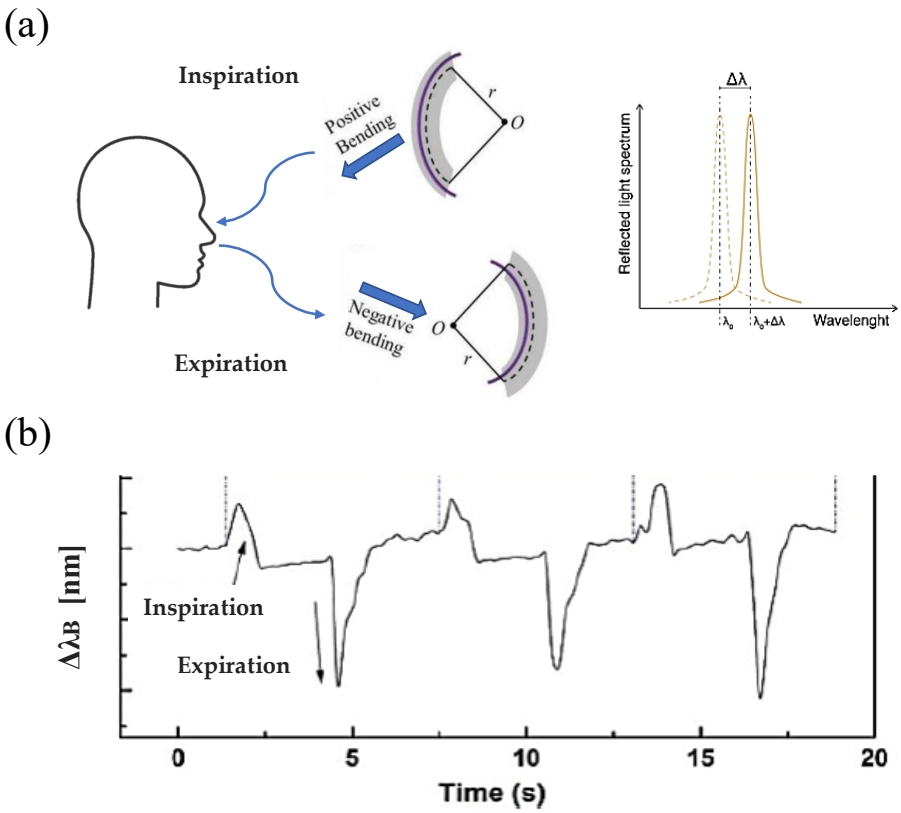

Figure 2.7. (a) Representation of the working principle of the technique for RR monitoring based on the direct measurement of inspiratory and expiratory airflow. In (b) an example of $\Delta\lambda_B$ trend in time is given, showing minimum and maximum peaks corresponding to expiration and inspiration phases, respectively. Adapted from [105].

3. Measurement principle of systems based on FBGs for monitoring body movements and posture

This paragraph is devoted to display the main techniques used to monitor body movements and discriminate the sitting postures starting from the movement of the different body districts by means of the FBG sensors.

2.2. Introduction to body movements mechanics

Humans are capable to reproduce an extended variety of posture and movements by controlling body's structures through the generation of forces. The main actor in this activity is the musculoskeletal system, consisting of muscles, bones, tendons and ligaments.

Given the high number of movements/postures the human body can reproduce, it is needed to define to them starting from a reference position, also known as the anatomical position: the body has an upright posture, the upper limbs along the hips, palms facing forward, head erect, face forward, the lower limbs stretched out in contact with each other, the feet resting fully on the ground and parallel to each other. In this position, a main tern of perpendicular planes (see Figure 2.8) can be identified [106]:

1) Sagittal plane: or medial plane, is the plane of symmetry that divides the body into its left and right parts;
2) Frontal plane: is the vertical plane perpendicular to the sagittal plane, passing through the body's center of gravity;
3) Axial plane: or transversal plane, is the horizontal plane passing through the center of gravity of the body.

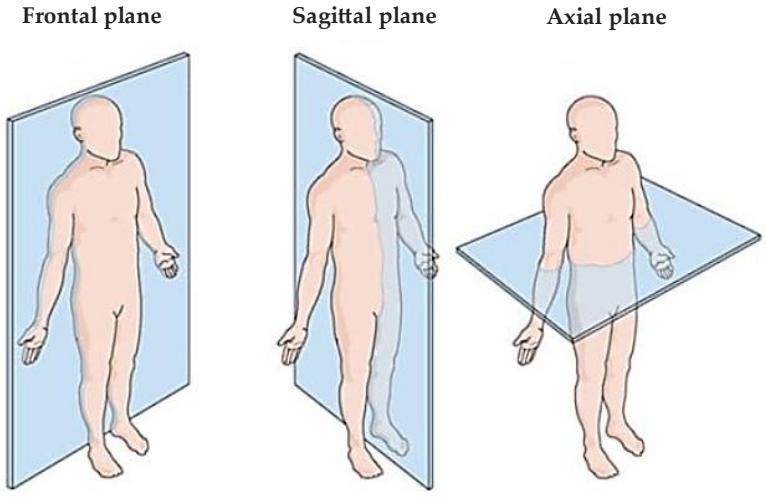

Figure 2.8. Representation of the three planes of the human body.

The movements which can be executed by the body segments are accounted as rotation around cardinal axis are classified with reference to anatomical position [106]:

1) flexion/extension: is the rotation around an axis parallel to the sagittal plane;
2) abduction/adduction: is rotation around an axis parallel to the frontal plane;
3) intra/ extra rotation: is rotation around a vertical axis;
4) plantarflexion/dorsiflexion: are respectively extension and flexion of the foot;
5) pronation/supination: rotations around to the long axis of the hand or foot.

In Figure 2.9, some examples of body movements of flexion/extension, adduction/adduction and rotation are represented for several body segments.

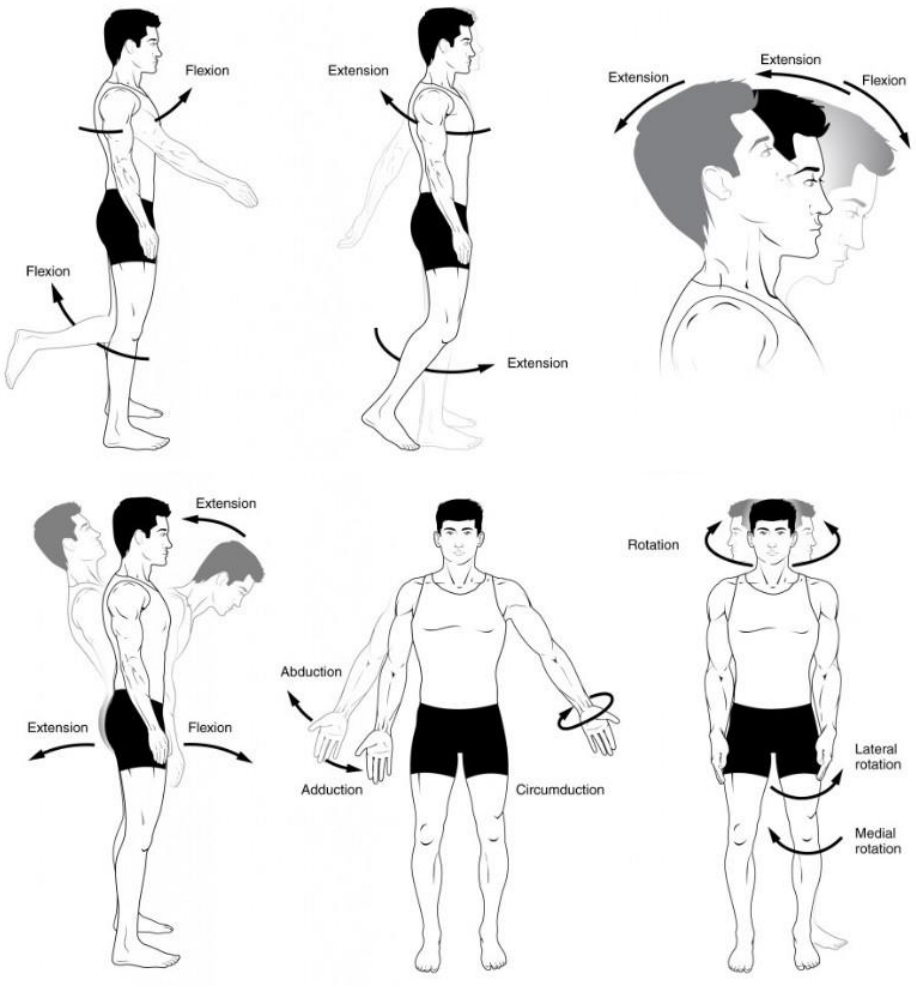

Figure 2.9. The movements of flexion/extension, adduction/adduction and rotation.

Movement originates from the rotation of body segments around the body joints (or articulations). Depending on whether the movement is performed around one, two or three axes, the body joint responsible for the movement will have one, two or three

degrees of freedom [107], [108]. For example, the knee joint can only perform the flexion-extension movement, so it only has one degree of freedom. The ankle, on the other hand, in addition to flexing and extending, can also invert and evert, thus gaining two degrees of freedom. The hip joint, on the other hand, has three degrees of freedom, as it can perform flexion and extension, adduction and abduction, and internal and external rotation.

2.2.1. FBG-based system for body movements and sitting posture monitoring

During the execution of a movement, a distortion of the surrounding tissues such as ligaments, muscles and skin is produced in the area of interest. Sites of particular interest are the body joints because they are the anatomical structures that separates two or more adjacent elements of the musculoskeletal system and that permits the movement of a body segment with respect to another. It is on the joints that most of the strain is concentrated. Therefore, being able to monitor the $\Delta\varepsilon$ occurring while changing a posture or performing a movement can be pivotal to establish the nature of the movement. To do so, FBGs are a viable option.

For these applications, FBG sensors are usually encapsulated into soft flexible matrices, both to improve their robustness and ensure compliance with the body anthropometry. They are applied, directly to the skin or with the help of bands or special garments, on the area of the body whose displacement is to be measured, longitudinally to the direction of movement. For example, on the back area for posture detection or in correspondence of a particular joint (e.g., knee) to monitor the extent of a movement (e.g., flexion and extension). Due to the movement, the skin undergoes deformations, the strain is transmitted to the soft matrix and, as consequence, to the FBG, resulting in $\Delta\lambda_B$. Once again, in case of thermoregulated environment and light physical activity, for this applications temperature variations could be considered negligible due to a much slower dynamic with respect to body movements. As consequence, $\Delta\lambda_B$ can be obtained as indicated in Equation (2.6).

Through $\Delta\lambda_B$ analysis, it is possible, for example, to distinguish the flexion-extension movements. In fact, flexion leads to greater $\Delta\varepsilon$, resulting in $\Delta\lambda_B$ maxima, while extension results in $\Delta\lambda_B$ minima. In Figure 2.10, the flexion-extension movements of the knee joint (a) and back (b) are shown, together with a corresponding $\Delta\lambda_B$ trend in time.

Nevertheless, it should be pointed out that this approach allows a movement to be correctly recognized only if it is performed along a single axis.

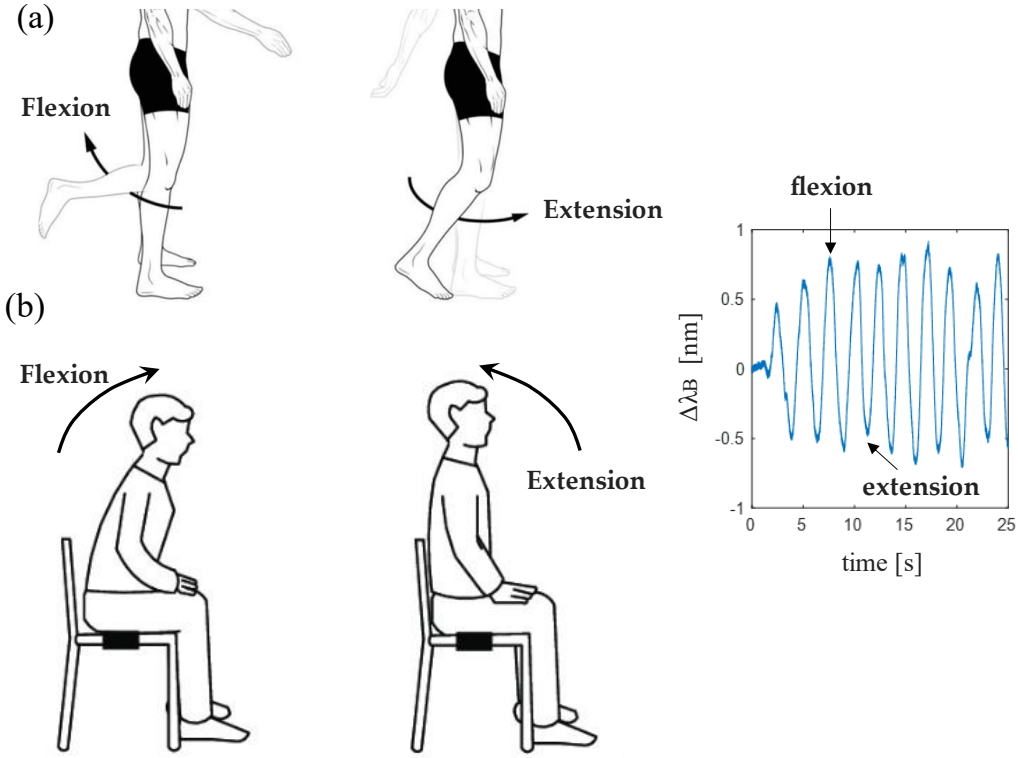

Figure 2.10. The movements of flexion/extension of knee joint (a) and back (b). On the right, an example of $\Delta\lambda_B$ trend, showing minimum and maximum peaks corresponding to extensions and flexions, respectively.

Chapter 3 – Solutions based on FBG technology for respiratory rate, body posture and movement monitoring: a literature overview

1. FBG-based solutions for respiratory rate monitoring

Techniques used to measure directly inhaled and exhaled airflows are the most popular to assess respiratory health. Indeed, the most common approach used as a screening test is the spirometry, which measures the inhaled and exhaled volume or flow of air as a function of time during breathing [109]–[111]. However, such systems are often impractical to be used outside the clinical setting, especially for prolonged periods of time. In fact, they are generally fitted with a disposable cardboard mouthpiece that must be inserted in the subject's mouth. This mouthpiece tends to deteriorate with use and creates feelings of mouth fatigue and discomfort for the user. Another valuable option is represented by motion capture (MoCap) systems which are, to date, one of the leading and most reliable instruments to evaluate the respiratory biomechanics of patients [112]. However, the need for equipped spaces and qualified operators, the application of photo-reflective markers to the subjects' torso, as well as the high costs of infrared cameras and dedicated software have limited the usage of this technology to hospital or ambulatory scenarios.

Current research has attempted to solve these drawbacks by exploiting the excellent features of FBG technology to offer innovative solutions for continuous, non-intrusive and comfortable respiratory monitoring, also in harsh environments such as in presence of electromagnetic interferences (e.g., during magnetic resonance imaging -MRI- routines).

In the following sections, an in-depth study on the state of the art of the proposed FBG-based solutions was made, dividing them into non-wearable and wearable systems. In this paragraph, parts of the work [79] which the PhD candidate has co-authored have been freely extracted.

1.1. Non-wearable systems

Non-wearable system embedding FBG sensors aiming at investigating the breathing patterns are mainly used to monitor the subjects in static conditions, such as during sleep, during the execution of medical exams (e.g., magnetic resonance imaging -MRI- or computed tomography -CT-routines) or while sitting. These solutions typically come

as pads made by different materials (e.g., Plexiglass or resins) or cushions to be placed under the user's back. In fact, such devices exploit the pressures induced on FBGs by the vibrations caused by breathing activity. Although some solutions are effective, their use is limited to clinical and static scenarios. Hereafter some examples are reported.

The work of Dziuda and colleagues [113], [114] focused mainly on the development of a system for respiratory monitoring of subjects performing MRI routines. The system was composed of an FBG attached to the central part of a Plexiglass plate (whose dimensions were 95 mm x 220 mm x 1.5 mm) with epoxy glue. This device was designed to be placed between the back of the patient undergoing MRI and the mattress of the MRI machinery to allow the vibrations resulting from the respiratory activity to be transferred to the sensor. The device was preliminarily tested on three volunteers lying in a hospital bed by interposing it between the user's back and the mat [113]. From the obtained data, it was clearly possible to depict the respiratory cycle by identifying the inspiratory phase with the increase of $\Delta\lambda_B$ and the expiratory phase with the decrease of $\Delta\lambda_B$. An experiment was also carried out on 12 subjects in MRI environment (Achieva 1.5 T MRI scanner by Philips) by testing the device's capability in retrieving RR against a reference system (i.e., respiration bellows) [114]. The FBG's output was denoised (by applying a 250-sample averaging), RR were calculated and compared with the values retrieved by the reference system, finding a mean relative error <7%.

A similar approach was used by Fajkus et al. who in [115] presented a plexiglass pad 40 mm x 15 mm x 0.3 mm with an FBG attached at its center with epoxy adhesive. The performances of this system in retrieving respiratory pattern were compared to the ones of a soft device which came as a rectangular-shaped (60 mm x 30 mm x 5 mm) polydimethylsiloxane (PDMS) matrix holding an FBG and intended to be worn at chest level secured by an elastic belt. The presented system reported slightly inferior performances in RR monitoring since it showed 0.36% lower accuracy than that of the WD.

Always remaining within the scope of monitoring respiration in lying patients, Hao and his coworkers [116], [117] fabricated a smart bed by integrating 12 FBG sensors forming a 3 x 4 matrix array on the bed surface. The bed surface was then covered with the mattress. Every FBG was embedded into a curved structure made of carbon fibers which is elastic and allows the sensor to deform but at the same time prevents it from breaking. The system was tested by 10 subjects which assumed six different sleeping positions. Data were analyzed and RR values ranging from 10 bpm and 25 bpm were obtained, which are in line with values reported in the literature for adults sleeping.

Dziuda's research group in [118], [119] explored a new field of application by proposing a smart cushion for RR monitoring to be applied on the back of chairs or vehicle seats. In [118] a first prototype was created by equipping an inflatable cushion with a single FBG attached with epoxy glue at its center. Seven healthy subjects used the cushion for 60 s in presence of a benchmark. The signal was filtered (i.e., low-pass-filter with 1.8 Hz of cutoff frequency) and the RR were extracted with a maximum relative error of 14%. A step forward was made in [119] where two FBGs were used to

instrument the cushion and were placed one at its center and one laterally. Once again, the system was tested on seven volunteers and RR was calculated with a smaller error (i.e., 12%).

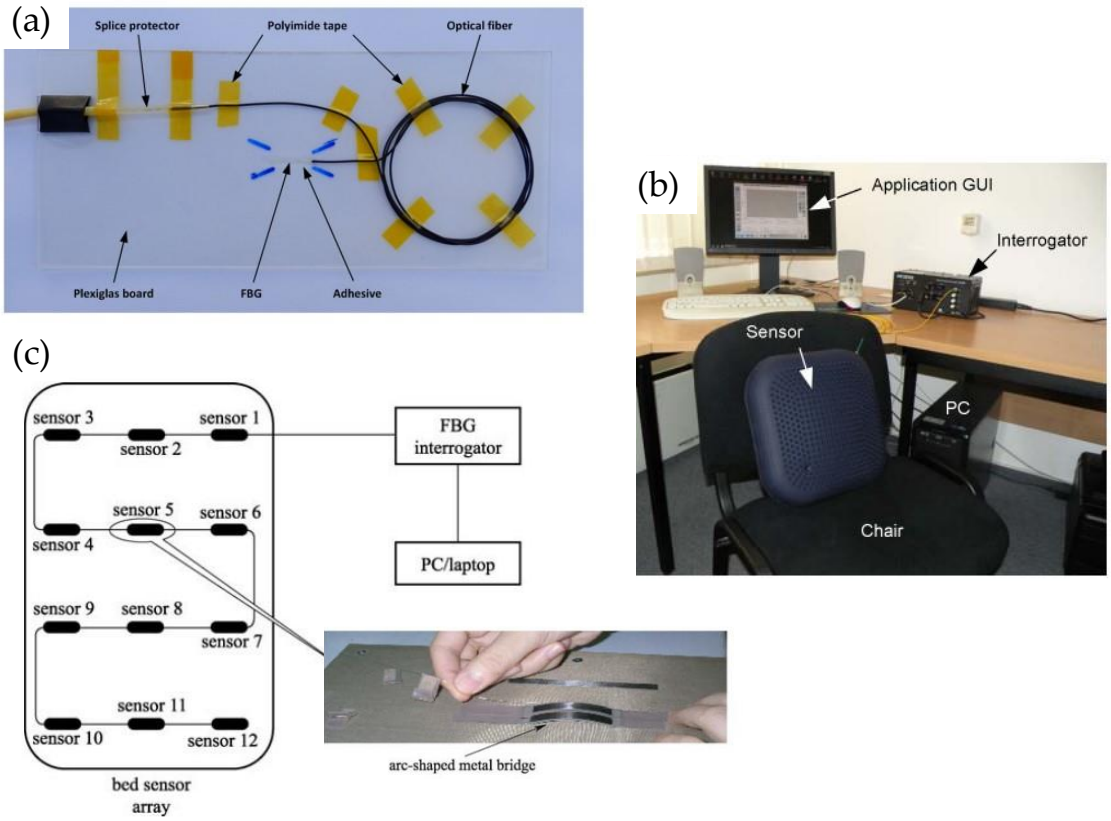

Figure 3.1. Examples of some of the non-wearable systems depicted. In (a) the Plexiglass plate equipped with the FBG sensor for MRI routines presented by Dziuda et al. (adapted from [5][6]). In (b) the cushion realized by Dziuda et al. (adapted from [118]). In (c) the smart bed fabricated by Hao et al. (adapted from [116], [117]).

1.2. Wearable systems

A hot spot of current research is represented by smart systems based on FBG technology intended to be worn by the users. Fabrics, T-shirts or, more in general, garments can be made "smart" by the direct integration of FBG sensors or application of flexible sensors which can be made of soft materials or 3D printed. Also, accessories commonly used in clinical settings such as surgical masks, PVC masks and nasal oxygen cannulas and spirometers equipped with FBG sensors can be useful tools for investigating the breathing pattern of subjects. Such devices are usually well accepted by users as they are easy to wear and typically non-intrusive. Also, allow free movement of the subjects during monitoring.

In the following subsections, an overview on the current state of the art of these devices is given.

1.2.1. FBG-based systems for respiratory monitoring via chest wall displacements

The wearable solutions for respiratory monitoring based on chest wall displacements can be divided into three main categories: smart textiles, soft flexible sensor and 3D printed sensors.

Are defined as "smart textiles" all those fabrics in which the FBGs, and more generally the optical fibers which embed them, are sewn, knitted or glued directly to the garment [120], as shown in Figure 3.2 (a). The development of such solutions has found wide application as FBG sensors are particularly suited to these uses. In fact, due to their lightness, flexibility and small size, FBGs are ideal sensors to be exploited [121]. Several works presenting innovative smart textiles integrating FBGs for respiratory monitoring are described in Subsection 1.2.1.1.

Soft flexible sensors are preferred in all the applications where the FBG undergoes greater deformations. Generally, these sensors consist of a matrix of flexible material (usually silicone rubbers) into which the optical fiber is inserted following determined geometries [122]. These sensors are usually attached to garments, bands or other accessorizes by means of various anchoring systems (such as Velcro stripes, buttons, etc.). The manufacturing of soft flexible sensors is more elaborated and time consuming with respect to the smart textiles as the fabrication typically requires the following steps, shown in Figure 3.2 (b): *i)* design and printing of the cast that typically consists of two parts: one smooth and one with a protrusion to create the groove in which the optical fiber has to be inserted; *ii)* first pouring of the liquid silicone material into the cast and curing of the material to form the first matrix layer; *iii)* insertion of the fiber optic following the groove created with the addition of glue if needed; *iv)* second pouring of the liquid silicone to create the second layer and curing and *v)* removal of the final sensor from the cast. Some examples of soft flexible prototypes based on FBG technology are reported in Subsection 1.2.1.2.

In the last years, growing interest has been shown in the 3D printing technique giving light to a new generation of FBG-based sensors [123]. Compared to the soft flexible sensors, 3D sensors' production is faster and more automated. In fact, the production steps are: *i)* design of the sensor; *ii)* printing of the first layer, *iii)* positioning of the fiber optic and *iv)* printing of the second layer. The four steps for the production of the 3D printed sensors are reported in Figure 3.2 (c). Moreover, as the printing process is fully automated, such sensors present a higher reproducibility [124]. In Subsection 1.2.1.3. an insight into the proposed 3D printed sensors for RR monitoring is given.

In Figure 3.2 a representation of the three aforementioned categories of wearable sensors and their fabrication techniques is reported.

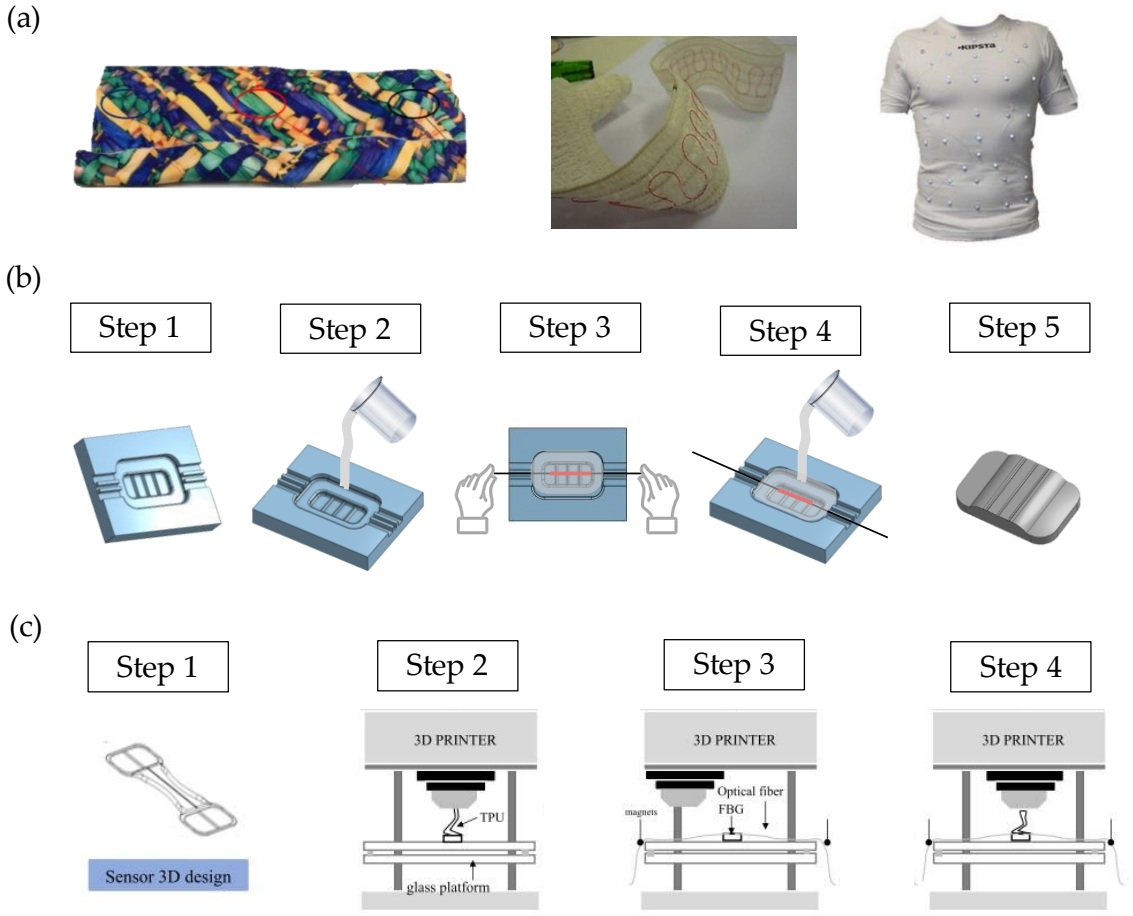

Figure 3.2. Representation of the three categories of wearable sensors. In (a) smart fabrics in which optical fibers are woven (first and second pictures) and glued (last picture) are depicted (adapted from [125][126], respectively). In (b) and (c) are depicted the steps composing the fabrication process of the soft flexible sensors and 3D printed sensors, respectively (adapted from [127], [128], respectively).

1.2.1.1. Smart textiles

In the framework of an ambitious project (i.e., OFSETH), Grillet et al. [129] presented an elastic belt made by an elastic textile above which a fiber optic (enclosed into a coating) was fixed by sewing it to the fabric and adding glue to the extremities. The fiber optic was made of silica and embedded a single FBG. The design of the system, although basic, avoids the total transmission of the strain to the FBG in order to prevent its damage. The system's feasibility to measure strain values, and consequently RR, has been assessed by means of a tensile machine equipped with a load cell. The mechanical characterization was performed by investigating the sensor response to deformation and the FBG output trend in time during 10 strain cycles at maximum strain of 5% with respect to the initial length. The response of the sensor was linear up to 40% of the textile elongation with no corruption of the fiber optic. Also, the system was capable of

following cyclic deformations, showing its applicability in detecting respiratory movements.

A different design for fiber integration into textiles was explored in [125],[130] by De jonckeere and co-workers. In the activities of the same project, an unobtrusive device based on FBG technology capable of monitoring thoracic respiratory displacements has been investigated. The fiber optic was sewed and glued onto a fabric band following a curved path to minimize the risk of breakage. Once again, the linear behavior to strain deformation (i.e., from 0.1 % up to 5% in elongation without degradation of the optical fiber), as well as the high stability and reproducibility of the device was assessed by means of a mechanical respiratory simulator. Moreover, the sensor presented a sensitivity of 0.32 $nm \cdot \%^{-1}$ (no uncertainty reported). Furthermore, a preliminary test on healthy volunteers was performed. Although the experiments have not been executed in the presence of a benchmark system, the thoracic displacements given by inhalation and exhalation were clearly identifiable from the FBGs outputs, making the smart device suitable for detecting respiratory phases.

An amount of novelty was brought by Ciocchetti et al., who designed a light and unobtrusive respiratory monitoring smart textile MRI compatible [131]. The wearable consists of a commercial t-shirt equipped with a single fiber optic housing two FBGs 10 mm in length. The FBGs were glued on the tissue with silicone rubber. The sensors' positioning was guided by previous experiments carried out with the use of an optoelectronic system (OEP) that revealed the chest landmarks in which the highest displacements are experienced during breathing. Then, a preliminary test was carried out by four healthy volunteers who were asked to perform two sessions of normal breathing for 60 s each while wearing the smart garment in the presence of the OEP system. The sensitivities of the FBGs were 0.66 $nm \cdot L^{-1}$ and 0.35 $nm \cdot L^{-1}$ (no uncertainties reported), respectively. A Bland-Altman analysis showed a good accuracy (i.e., < 0.045 s) in discriminating the time interval between two consecutive inhalations.

Starting from this, Massaroni and his research group increased the number of FBGs embedded into the T-shirt to improve the performances of the systems. In [132] and [133] a multi-sensors smart T-shirt embedding six FBGs in the frontal area was presented. Three FBGs were positioned on the right side and three on the left side, identifying three areas of the torso (i.e., pulmonary rib cage, abdominal rib cage and abdomen compartments). A further step forward was made in [126], [134] in which the FBGs were increased to 12, also covering the back of the shirt for total torso monitoring. Preliminary assessments on volunteers showed the possibility of detecting the respiratory pattern either from the sum signal of all FBGs, or by using the signal of the sensors belonging to each torso compartment. No substantial difference in device performance was noted with female volunteers, thus showing good device fit in both male and female subjects [134]. Also, experiments conducted on patients undergoing MR procedures showed that such wearables were capable of detecting RR with good accuracy (i.e., 0.29 bpm of maximum error was calculated). However, data processing was required to separate the respiratory contribution from the cardiac one.

In [135] Ogawa and co-workers proposed a system composed of two separated FBGs attached to surgical tape for RR evaluation. The sensors were tested on a healthy volunteer who was asked to breathe normally for 180 s, placing one sensor at the carotid artery level and the second in correspondence of the tricuspid valve. The results demonstrated the feasibility of distinguishing the respiratory component of the signal from the cardiac ones by applying a digital low pass filter with cutoff frequency of 0.2 Hz. Also, the system showed good agreement with the reference device in the detection of respiratory acts.

A similar approach was used by Koyama et al. [136] who studied the strain induced on the body areas by the respiratory cycle using two FBG sensors applied on different parts of the body. An FBG was preliminarily assessed proving its ability in detecting RR against a sensor used as reference. Then the first FBG was always kept in abdominal position as benchmark for the respiratory activity, while the second was positioned in different zones such as wrist, elbow, shoulders and chest. The abdominal area has proven to be the best positioning for controlling respiratory activity. The shoulder and chest area also provided usable signals, while elbow and wrist detection failed.

Issatayeva et al. proposed in [137] two smart elastic bands to be worn at chest and abdomen levels. Each band consisted of a central elastic part and two lateral rigid parts; an optical fiber containing five FBGs sensitive to chest variations is inserted in the central part. The FBGs were not fixed to the tissue to be free to elongate. The sensors were preliminarily characterized to retrieve S_ε and S_T, obtaining values of 1.03 pm $\cdot\mu\varepsilon^{-1}$ and 10.2 pm $\cdot°C^{-1}$, respectively (no uncertainties reported). The performances of the system were assessed on two volunteers breathing normally during sitting, lying, staying and running activities. As expected, the most challenging condition proved to be running as the signals were affected by massive motion artefacts. However, the breathing signals were reconstructed with promising results in all the stance by summing the outputs of the 10 FBGs.

Lastly, Defrianto and co-workers [138] proposed the use of an elastic band equipped with a both a single-mode fiber (SMF) and a FBG-based fiber attached following a sinusoidal macro bending pattern to experimentally relate the amount of air inspired/expired in/from the lungs with the deformation experienced by the chest walls. Seven people were tested on normal breathing conditions while wearing the device and the different chest circumference variations were calculated for each subject. Based on these data, an airflow model and a finite element model of the lungs were developed.

In general, all the proposed systems, some more than others, showed good performance in detecting movements related to the respiratory activity. No degradation or rupture of the optical fiber was reported. However, it remains clear that such configurations (in which the fiber is glued, sewn or woven into tissues) have inherent fragility. Some of the described solutions are reported in Figure 3.3.

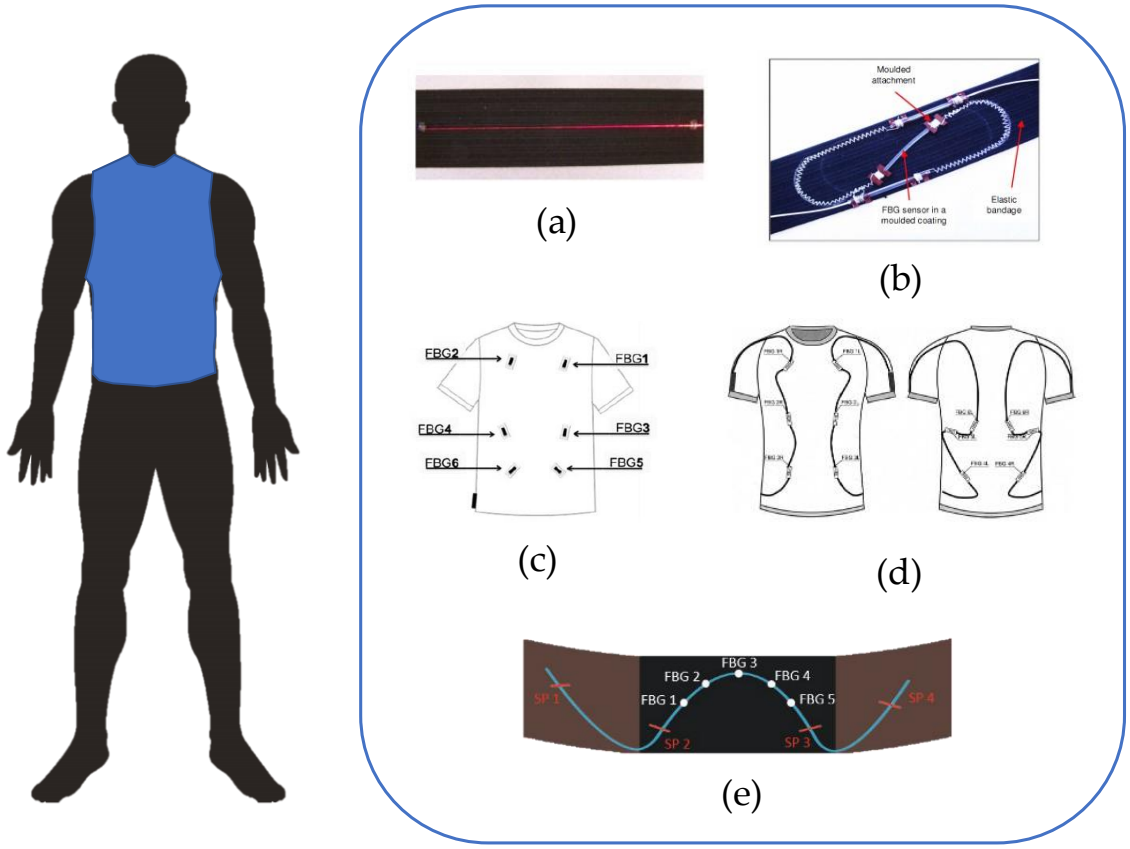

Figure 3.3. Collection of some of the smart textiles described and area of the human body suitable to their application. In (a) the solution proposed by Grillet et al. (adapted from [129]), in (b) the elastic band developed by De jonckeere et al. (adapted from [125], [130]). In (c) and (d) the smart T-shirt created by Massaroni and co-workers embedding 6 (adapted from [132], [133]) and 12 FBG (adapted [126], [134]), respectively. In (e) the elastic belt presented by Issatayeva et al. (adapted from [137]).

1.2.1.2. Soft flexible sensors

Da Silva et al. [139],[140] proposed a smart soft sensor equipped with Velcro stripes enabling easy attaching and removing at the chest level. The sensor was composed of two overlapping layers of PVC containing at their center an optical fiber (with a single FBG embedded) in a sinusoidal path. This configuration increased the fiber robustness while maintaining its flexibility. The prototype was tested against a benchmark system (i.e., Zephyr BioHarness) on 12 volunteers performing normal breathing tasks in standing position. A filtering stage (band-pass digital filter, cutoff frequencies of 0.1 Hz – 0.4 Hz) was applied to the signal to separate the respiratory component from the cardiac one and the RR was estimated for all subjects. Also, the relationship between the FBG output and the change in chest circumference due to the breathing activity was established.

In the same year, the same research group [141] proposed a large-area soft sensor based on FBG technology to be integrated into a corset, covering the whole garment surface. The sensor was composed of a polychloroethanediyl (PVC) matrix of 400 µm in thickness in which a fiber optic containing two FBGs was enclosed. The sensing system was tested using a tensile machine, showing a S_ε = 0.8 pm· µε^{-1} (no uncertainty reported). The system was then assessed on 12 healty subjects showing its feasibility for RR evaluation purposes after the use of digital filters to eliminate the component attributable to the cardiac activity.

Fajkus et al. in [142] and Nedoma et al. in [143] proposed a new soft sensor for RR evaluation by encapsulating an FBG sensor into a polydimethylsiloxane (PDMS) elastomer substrate. The sensor was in the shape of a rectangular probe. The probe was firstly tested on a single subject breathing normally in three static positions (i.e., standing, laying on the back and sitting upright) showing its capability in retrieving RR. An evolution of this soft sensor was reported in [144] by the same research group. This time, two FBGs were encapsulated in a PDMS rectangular matrix. A preliminary characterization to temperature variation showed an increase in the S_T of FBGs after encapsulation in PDMS. Then the probe was fixed at the chest level of 10 volunteers (both males and females) with the help of an elastic band. A time domain and frequency domain analysis were performed to retrieve RR. The maximum relative error of 5.41% was observed, probably due to the presence of motion artefacts not attenuated by the use of a signal filtering step.

In [145] Chethana and co-workers proposed a soft sensor with a brand new design to increase the sensitivity of the FBG to the chest-wall displacements. In fact, an FBG is attached to a silicone diaphragm which is, in turn, inserted inside a PVC dome structure. The outer dome ensures stable positioning on the subject's chest, while the inner diaphragm accompanies the movement of the FBG as it is deformed by respiratory activity. The system, tested on four lying subjects, showed good performances in retrieving RR.

A significant step forward has been made in [146], [147] by Lo Presti et al., who fabricated two flexible sensors each embedding an FBG into a rectangular silicone (i.e., Dragon Skin silicone rubber) patch that can be fixed onto an elastic band. Such a structure improves the sensor robustness and its compliance with the body. Promising results in estimating RR were obtained as the mean absolute percentage error was ≤ 1.97% during quiet breathing. The system capability to detect RR during sports activities was then assessed on two professional archers [147]. The aforementioned systems were designed to be used both in clinical settings (i.e., respiratory rehabilitation process or during MRI exams) and during sport and exercise.

Few years later, Lo Presti and co-workers [148] made a marked enhancement in this field by presenting a new soft sensing system with improved shape. The sensor came as a multilayered structure formed by a silicone rubber substrate in a bone shape embedding a single FBG at its center. This shape enabled the breathing-related strains to focus on the FBG. The structure was then layered between two fabric liners to impart

a skin-like softness improving the acceptability to the user. The metrological assessment of the smart patch was then held retrieving S_ε = 0.10 nm·mε^{-1}, S_T = 0.01 nm· °C^{-1} and S_{RH}= 0.0002 nm·RH^{-1}. A feasibility assessment on nine volunteers was performed for eupnea and tachypnea breathing in three positions (i.e., standing, lying and sitting). Maximum RR error values of 0.10 bpm and 0.14 bpm were calculated in standing position for eupnea and tachypnea breathing, respectively.

An amount of novelty was finally brought by Li and colleagues in [149]. The proposed sensor had a rectangular silicone rubber substrate which enclosed a fiber optic containing two FBGs. The FBGs were positioned at the two edges of the rectangle and embedded into two protective sleeves not to be deformed, while the fiber optic connecting them was embedded in the rectangle with a Ω-shape pattern. This time, the breathing signal was obtained by considering the light power fluctuation caused by deformation of the non-sensorized portion of the optical fiber due to the chest-wall displacements. The sensor's resistance was tested in several challenging working conditions (i.e., a deformation > 30% was applied, it was curved up to 120° and bended multiple times around objects of different radii −4.7 mm the smallest one−, it was soaked and exposed to water drops) never deteriorating the signal. Also, the applicability of the presented sensor to evaluate respiratory patterns was assessed testing it on a healthy volunteer performing tachypnea and eupnea breathing trials.

The wearable systems reported in this subparagraph have taken a step forward in terms of fiber reinforcement by inserting the sensing part into polymer matrices of various shapes. This choice also makes it possible to minimize heat exchange between the sensing element and the subject's skin. However, some systems flaw in terms of wearability as they are bulky and may be difficult for a user to accept. Some of the described solutions are reported in Figure 3.4.

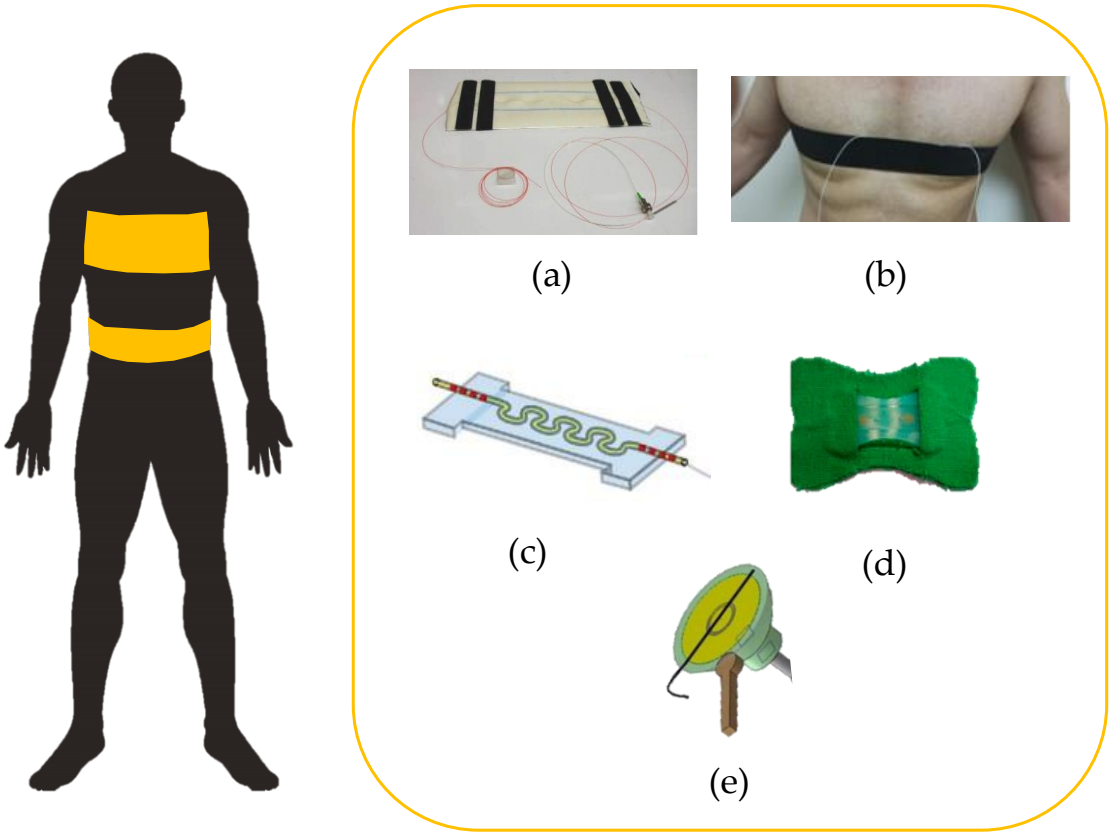

Figure 3.4. Collection of some of the soft flexible sensors described and area of the human body suitable to their application. In (a) the solution proposed by Da Silva et al. (adapted from [140]), in (b) the elastic band developed by Fajkus et al. (adapted from [144]). In (c) the sensor made by Li et al. (adapted from [149]) and in (d) the smart patch created by Lo Presti and co-workers (adapted from [148]). In (e) the instrumented silicone diaphragm presented by Chethan et al. (adapted from [145]).

1.2.1.3. 3D printed sensors

An amount of novelty has been brought in this field from the fruitful collaboration of two research groups. In [150] Tavares et al. presented a first prototypes of sensors for respiratory monitoring made by 3D printing and integrating an FBG. The sensors came as rectangular-shaped structures (i.e., 30 mm x 40 mm) made of printable material (Flexible by Avistron, Bergheim, Germany) holding at their center a 10 mm length FBG. A total of six prototypes were produced: three with a thickness of 2 mm at 100%, 60% and 20% infills, and other three with 3 mm thickness at 100%, 60% and 20% infills. All the samples were assessed by means of an actuator capable to reproduce movements mimicking in amplitude and frequencies the chest-wall movements related to both the breathing and cardiac activity. Results shown that the 2 mm thick sensor with 20% infill had the best performances. Also, the sensor was tested against a reference (i.e., BioHarness by Zephys) on three volunteers wearing the sensor at the chest level with

the help of an elastic band. The volunteers were asked to breath normally while lying. A filtering step was employed to separate the respiratory and cardiac contributes. RR was calculated and matched with the values retrieved by the benchmark.

In [128] Lo Presti et al. moved a step forward with the sensor's design. In fact, they changed the manufacture material (i.e., TPU 95 A) and presented a rectangular shape which is thinned in the central part (in correspondence of the FBG's location) to maximize the strain in that site. In addition, two 3D printed loops have been added at the edges of the structure for easy attachment of the elastic band to be tightened around the user's chest. They fabricated four sensors which differed in the infill percentages (30% and 60% infills values) and infill paths (triangle and gyroids). The responses of the sensors to strain, temperature and humidity were investigated, together with the hysteresis error. Highest S_ε and lower hysteresis errors (i.e., 3.9 nm·mε^{-1} and 5.6% at 12 bpm and 11.9% at 70 bpm, respectively) were reported for the sensor with 30% infill and triangle infill path. This sensor was then assessed on a volunteer while performing eupnea and tachypnea breathing, showing that the respiratory acts were clearly identifiable during both the breathing conditions.

Such solutions are extremely innovative and give the chance of minimizing the sensor encumbrance as they allow the optical fiber to be inserted inside substrates with low thickness. In addition, the almost fully automated fabrication process by means of the 3D printer allows the fiber to be placed into the substrate with great precision. On the other hand, this methodology is still at the beginning of its development, so the literature still lacks real tests on subjects in different application scenarios.

The described solutions are reported in Figure 3.5.

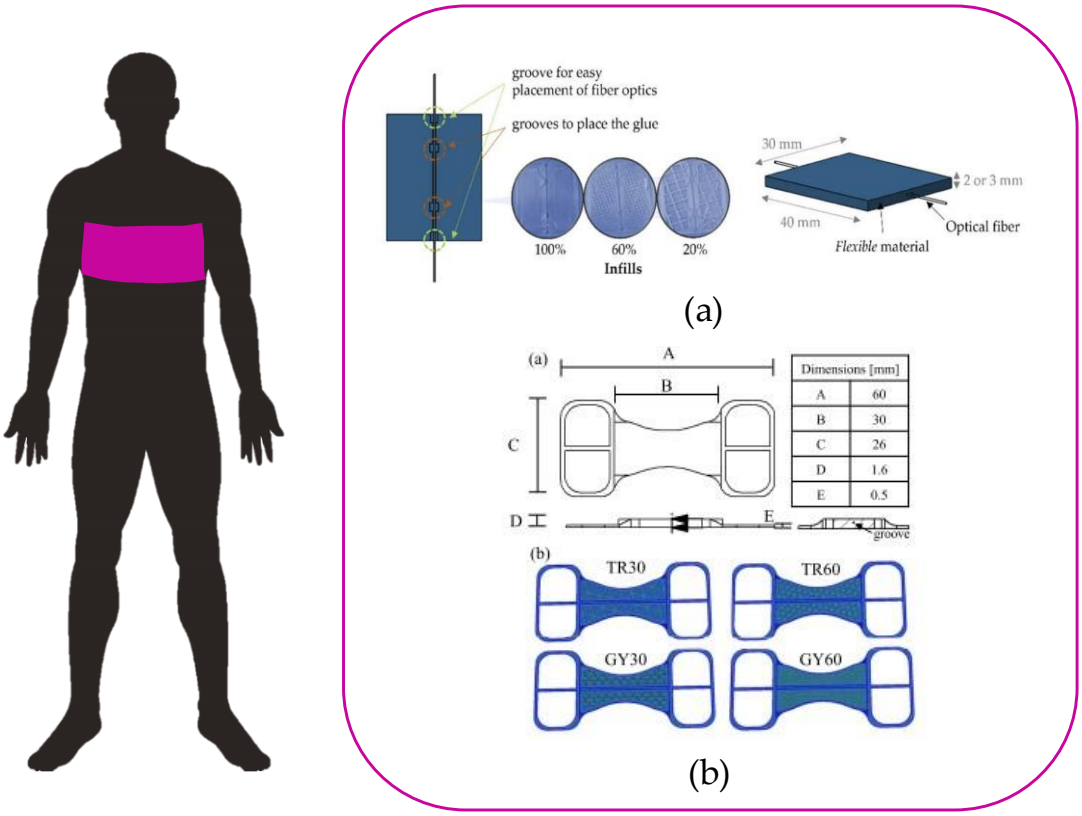

Figure 3.5. Collection of some of the 3D printed sensors described and area of the human body suitable to their application. In (a) the solution proposed by Tavares et al. (adapted from [150]). In (b) the 3D sensors presented by Lo Presti and co-workers (adapted from [128]).

1.2.2. FBG-based systems for respiratory monitoring via difference of thermohygrometric conditions between inspiratory and expiratory airflow

Different solutions have been proposed to monitor ventilatory variables, and some of these have been tested on volunteers during breathing. In [151]–[154] an FBG functionalized with agar has been used to develop a needle-like probe that was tested during mechanical ventilation [151]–[153], and on 9 volunteers during quiet breathing [154]. The performance was assessed in terms of RR estimation and was compared with the RR set on the mechanical ventilator in [152] and with the RR estimated by a spirometer in [154]. In both cases, the results were promising in terms of percentage error (i.e., <3%).

In [155], a tilted FBG was made sensitive to RH by deposition of graphene oxide. The proposed system was not assessed on humans, but the good static (e.g., of 18.5 $pm \cdot \%RH^{-1}$ and 0.027 $dB \cdot \%RH^{-1}$ in the range of 30%–80% RH) and dynamic characteristics (e.g., response time ~42 ms) make the sensor suitable for breath monitoring.

In [156], Liang et al. presented a novel wearable system for respiratory monitoring that consists of a commercial face mask equipped with a couple of FBGs. One sensor was directly connected to the mask (active FBG) while the other was at room temperature, working as a temperature reference. The active FBG was so exposed to warm and cold air during exhalation and inhalation phases, respectively. Two sequences of regular and heavy breathing were performed for 30 s and the sensor capability to follow a 30 bpm (with bpm is intended breathing per minute that is a unit of measurements popular in respiratory monitoring) breath rate was assessed. Moreover, the device showed a linear response over a 15 °C – 20 °C range of temperature.

A similar approach was presented by Nedoma et al.[157] who proposed an oxygen mask equipped with a FBG sensor for respiratory monitoring during MRI routines. The FBG was encapsulated within a cylindric support directly inserted into the oxygen mask and so exposed to ΔT. The system was tested by six subjects executing MRI exams showing the advantages of the brought by the method compared to other methodologies commonly used in MRI (e.g., limited bulkiness and elimination of motion artefacts caused by devices placed on the abdomen). For the same scenario of use, the same research group proposed in [158] a nasal oxygen cannulas holding an FBG sensor as an alternative to oxygen masks. Following the same working principle, once again RR detection was assessed in MRI environment on ten volunteers. The accordance of the proposed sensor with two reference devices placed at chest and abdominal levels in evaluating RR was analyzed via Bland-Altman analysis, reporting a total relative error <5%.

Nasal oxygen cannulas and masks were also subjects of the research of Sinha et al. [159]. Also in this case, commercial cannulas and masks were equipped with FBGs. In this case, the devices were assessed on 15 subjects under controlled bradypnea, eupnea and tachypnea breathing regimes (i.e., 5 bpm, 12 bpm and 30 bpm, respectively) by asking them to breath following a digital metronome. Also, a trial performing shallow breathing was performed by each of the subjects. RR was extracted from the $\Delta\lambda_B$ signal with mean accuracy of 88.1%.

Gautam et al. in [160] described the realization and the assessment of an oxygen mask equipped with an FBG and a BME 280 module, both sensitive to ΔT. A comparison between the performance of the FBG and electronic module in RR retrieving was carried out. Five volunteers breathed normally while wearing the mask. High accordance between the two devices was observed, testified also by the overall percentage error of 5.29% across the five subjects. Also, the FBG response times to ΔT were 1.82 times faster in rise and 5.1 times faster in decay than the response times shown by the electronic module.

A light WD exploiting a single FBG was presented by Manujło et al. [161]. A first comparison between the sensor and an electronic LM35 integrated circuit in measuring static temperatures was made. Although the FBG presented a not perfectly linear response, RR could be successfully calculated as it is obtained comparing relative ΔT rather than absolute values. Then, the systems were tested by placing the sensors under

the subjects' nose during quiet breathing. Results showed that the electronic circuit sensitivity was higher, but both the sensors were able to discriminate inhalations and exhalations.

Both Hernandez et al. [162] and Morgan et al. [163] presented two WDs for respiratory monitoring capable of detecting RH and temperature variations simultaneously. In [162], a sensor probe was made by covering the tip of an optical fiber, which embeds an FBG, with 23 PAH/SiO2 layers whose refractive index changes with RH. In [163], a further step forward was made by adding an ulterior FBG, which works as temperature reference and incorporating the sensitive system into a respiratory mask, so enhancing the design and fitting. The presence of the FBG is targeted for ΔT detection, but also for calculating the absolute humidity (AH). In fact, AH can be obtained comparing ΔT and the RH values detected by the PAH/SiO2 film. The system was tested into a mechanical ventilator, confronting its performance with that of two thermocouples and a humidity sensor. Experiments showed a relatively small sensitivity to RH (i.e., -1.4·10-12 W· %RH^{-1}), an FBG sensitivity value of 10 pm·°C^{-1} and assessed the system feasibility to measure ΔT and RH together, so allowing estimating RR.

The described devices are interesting and innovative as they offer an alternative to elastic bands to be worn around the torso for controlling breathing activity. This is most useful in those cases where the user resents possible chest constriction. On the other hand, masks and nasals can only find real application and acceptance in a clinical setting. Some of the described solutions are reported in Figure 3.6.

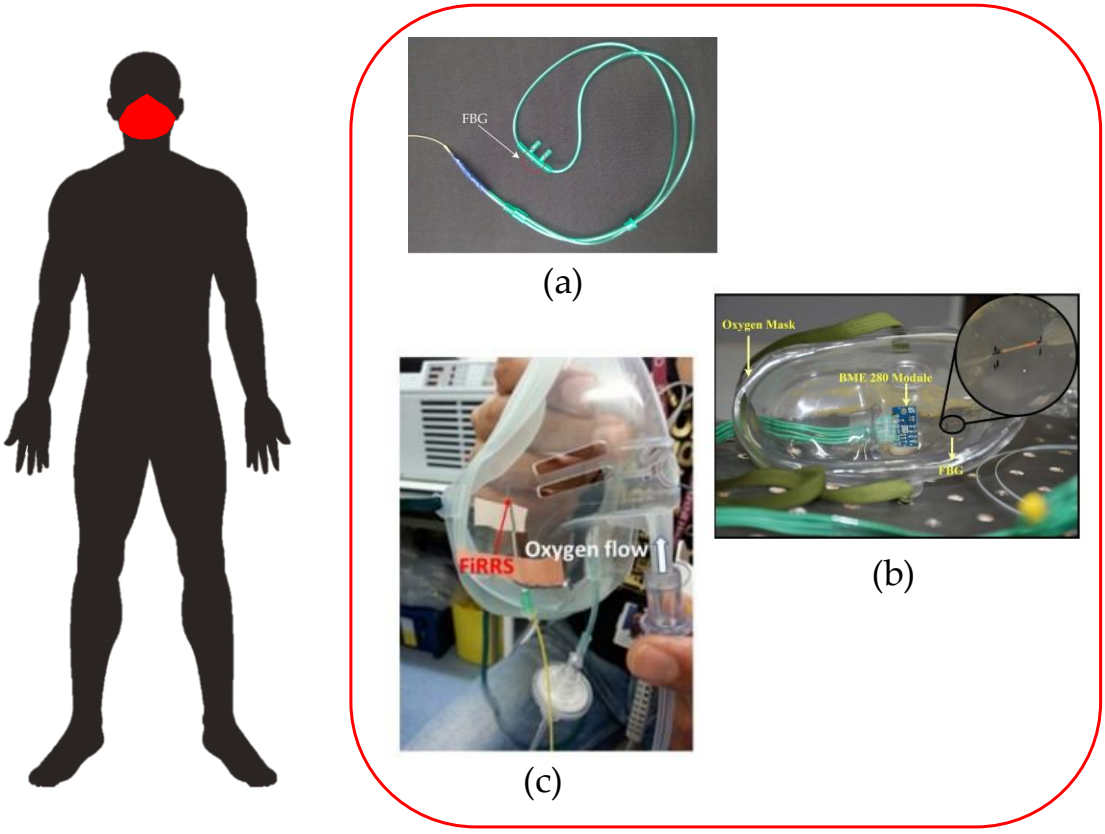

Figure 3.6. Collection of some of the solutions for respiratory monitoring via difference of thermohygrometric conditions between inspiratory and expiratory airflow and area of the human body suitable to their application. In (a) the instrumented cannula proposed by Fajkus et al. (adapted from [158]). In (b) and (c) the oxygen masks proposed by Gautam et al. (adapted from [160]) and Sinha et al. (adapted from [159]), respectively.

1.2.3. FBG-based systems for respiratory monitoring via breathing airflows

Among several techniques used to design spirometers and flowmeters (in Seventies Hayward found more than 100 types on the market [164]), different configurations based on FBGs have been investigated.

In [165], a spirometer based on the strain of an FBG due to respiratory air has been developed and tested on volunteers. Results in terms of some crucial respiratory parameters (i.e., forced expiratory volume in the first second – FEV1, forced vital capacity -FVC-, and peak expiratory flow -PEF-) were compared to a commercial spirometer used as reference and showed promising results.

In [105], basing on the same principle, Pant and co-workers designed a new device made of soft foam rubber to be worn on the nose. Two FBGs were applied at the extremities of the device, one at each nostril, to flex with the air passage. 10 subjects tested the device in eupnea breathing trials. The respiratory periods of each subject

were evaluated and were in line with what has been reported in the literature for eupnea breathing.

More recently, Nepomuceno et al. [166] integrated two FBG directly into a 3D printed component of the spirometer. One FBG is enclosed into a needle and is used to compensate the temperature effect, while the second FBG is, in turn, free to be deformed by the air flows passing. The experimental assessment was performed on a volunteer by evaluating the FVC, FEV1, PEF and FEV1/FVC parameters, showing good agreement between the proposed device and the electronic flowmeter taken as benchmark.

In recent times, the increase in the use of surgical masks due to the covid-19 pandemic led Das et al. [167] to design a surgical mask for RR monitoring purpose with an FBG incorporated into a silicone diaphragm mounted on the vent valve. The study shown the applicability of this approach as the output given by the sensor could clearly depict the breathing pattern. In fact, outward deflection of the sensor due to exhaled air caused an increase $\Delta\lambda_B$, while the inward deflection due to inhaled air was responsible for a decrease in $\Delta\lambda_B$.

An interesting solution investigated by several authors is the development of a hot wire anemometer using two FBGs [168]–[171]. The principle of work of this type of sensor is underpinned by the phenomenon of heat transfer. Usually, the sensing part is heated by an external energy source. When the airflow hits the sensing element, there is heat exchange. The equilibrium temperature or the energy used to maintain the sensing element at a constant temperature can be used as an indirect measure of the airflow velocity. Finally, the flowrate can be estimated by the velocity. In [168]–[171], the sensing part consists of one or more FBGs heated by a laser source, which makes them similar to a hot wire anemometer. Experiments show the valuable characteristics of high sensitivity at low flowrate which can be crucial in respiratory monitoring. All these sensors were not used in clinical trials, although the working principle and the performance foster future experiments in a real scenario.

Once again, such solutions are an alternative to the most canonical smart textiles. Nevertheless, in a scenario other than clinical, I would see such solutions applied with difficulty given the impracticality of using systems such as the mask or flowmeter in everyday life.

Some of the described solutions are reported in Figure 3.7.

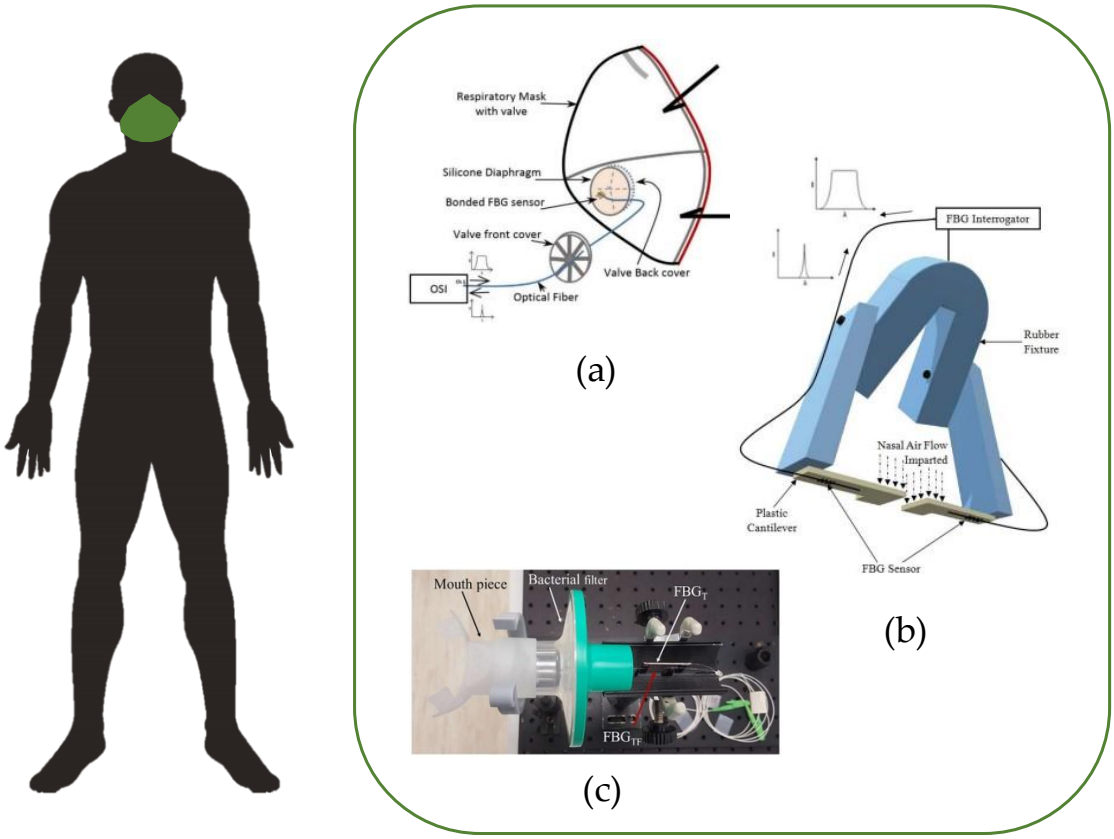

Figure 3.7. Collection of some of the solutions for respiratory monitoring via breathing airflows and area of the human body suitable to their application. In (a) the surgical mask proposed by Das et al. (adapted from [167]). In (b) the solution presented by Pant and co-workers (adapted from [105]) and in (c) the spirometer equipped with two FBGs by Nepomuceno et al. (adapted from [166]).

2. FBG-based solutions for body movement monitoring: joint motion and posture evaluation

Body motion sensing has been deeply investigated since is a source of a great deal of information for the study of disabilities, the development of rehabilitation techniques or, more simply, for the identification of the most common postural attitudes in sitting or standing positions to prevent the occurrence of musculoskeletal diseases [172]. Limbs' orientation and joint angle variations have been extensively explored by means of different tools, the most common of which are inclinometers and goniometers [107], [173]–[175] and inertial sensors [259]. However, the use of such mechanical and rigid instruments can result often impractical, given the particular anatomical structure of many joints (which permit more than one degree of freedom in movement) or the curved surfaces of some body areas (such as the back). Indeed, goniometers offer accurate monitoring of a few joint districts, and the quality of the measurements strictly depends on the operator's skills and experience, since the procedure is carried out manually. On the other hand, inertial sensors may manifest inaccuracy in detecting slow movements. Moreover, the usage a limited number of inertial sensors often causes a low spatial resolution in the movement reconstruction.

Given this, camera-based systems played an important role in this field as well, but, as expected, mainly for research purposes and relegated to laboratory environments [176]–[178]. In fact, as also pointed out for respiratory monitoring, MoCap systems are extremely expensive and unfeasible to use in everyday settings (e.g., working environments or home settings) due to need for dedicated space and operators.

In this background, the research has moved more and more towards the development of viable alternatives and in the last twenty years smart WDs have gained momentum as represent a good option for body motion monitoring allowing free movements without being an impediment to the subject. Also in this context, FBG sensors have gained large acceptance as they are highly integrable in fabrics, tissues and soft matrices and have high sensitivity to strain, a key feature to be exploited for joint monitoring. However, albeit to a much lesser extent, non-wearable FBG-based alternatives have also been proposed for BMs monitoring purposes in more static conditions (such as during sleep or for monitoring sitting or static standing postures).

This paragraph is devoted to display the solutions currently proposed to detect body movements by means of the FBG sensors' integration, once classified as non-wearable and wearable systems.

2.1. Non-wearable systems

Several research groups have focused their efforts on finding innovative solutions exploiting the FBGs' sensitivity to pressure in order to improve and facilitate the care of the bedridden or disabled patient. In this respect, Abro and co-workers [179] designed a smart bed to identify the patient's sleeping postures. Two pressure sensing elements were created by enclosing two FBGs into a 3D printed disk (i.e., PLA plastic material) by means of the fusion deposition printing technique. The pressure sensors were then calibrated by applying a vertical load form 0 N to 350 N in six steps for six times with the help of a tensile tester machine. The sensors showed the following sensitivity values: 0.00053 nm $\cdot N^{-1}$ and 0.00012 nm $\cdot N^{-1}$. Also, 13.3% of maximum measurement error was found for vertical loading and unloading tests. The sensors were then glued to a thin foam foil at 200 mm of distance to each other. The system was then placed under a mattress, in its center zone. An assessment test was conducted on a male volunteer getting four different lying postures, maintaining each of them for 10 s. The two FBGs showed different $\Delta\lambda_B$ for each posture, thus providing the possibility to distinguish the four lying positions.

Starting from this, a further step forward has been taken by Fook et al. [180] who proposed both a smart bed and chair to provide monitoring of the patient's lying and sitting postures, respectively. 5 mm long FBG sensors were embedded in arcuate reinforcement structures composed of carbon fibers. Such pressure sensors showed good linearity when calibrated to pressure. The sensors were applied to the bed wooden structure by forming a 6 x 7 matrix and to the chair seat forming a 3 x 2 matrix. Experiments showed that by applying a baseline pressure value, it was possible to determine whether the patient was sat or stood up from the chair. On the other hand, the use of the smart mattress provides a more precise indication of the position assumed by the patient. In fact, by analyzing the data provided by the 42 FBGs, it was possible to classify five postures: turn left, turn right, sit up, lie down and get out of the bed.

In [181], Tavares and co-authors presented a wheelchair equipped with six FBG-based pressure cells to identify maximal pressure areas in the disabled patient's seat in order to avoid incorrect postures often responsible for ulcers. The pressure cells consisted of six FBG encapsulated at the center of six epoxy resin cylinders, 20 mm in diameter. The sensors were characterized to pressure starting from 0 Pa to 319 kPa for three times, showing sensitivity values ranging from 9.5 pm $\cdot kPa^{-1}$ to 18.7 pm $\cdot kPa^{-1}$. The cells were then applied in six sites of the wheelchair: right and left scapular zone, right and left ischiatic zone, and right and left heel zone. A test was performed on a volunteer who was asked to assume nine different positions. Results proved the capability of the system to discriminate the nine postures thanks to the different output of each FBG. In addition, it was investigated whether the ΔT could affect the performance of system by adding two temperature sensors (i.e., two FBG inserted into plastic cannulas) in the

scapular and ischiatic area. No error was induced by the T increase on the posture assessment.

Finally, to check the correct distribution of body weight, the postural stability and, in turn, to detect the possible development of musculoskeletal diseases, a sensorized plantar platform was developed by Prasad and colleagues [182]. The platform was composed of two Perspex foils enclosing six FBGs, three placed on the right half (each covering the fore-, mid- and hind- foot plantar area of the right foot, respectively) and three on the left half (each covering the fore-, mid- and hind- foot plantar area of the left foot, respectively). Ten subjects were asked to stand on the platform for 30 s while wearing an accelerometer as reference. The data provided by the platform made it possible to determine the plantar strain distribution. Also, the postural stability has been investigated in terms of plantar strain variance with good agreement with the benchmark device.

In Figure 3.8, a representation of the systems described is given.

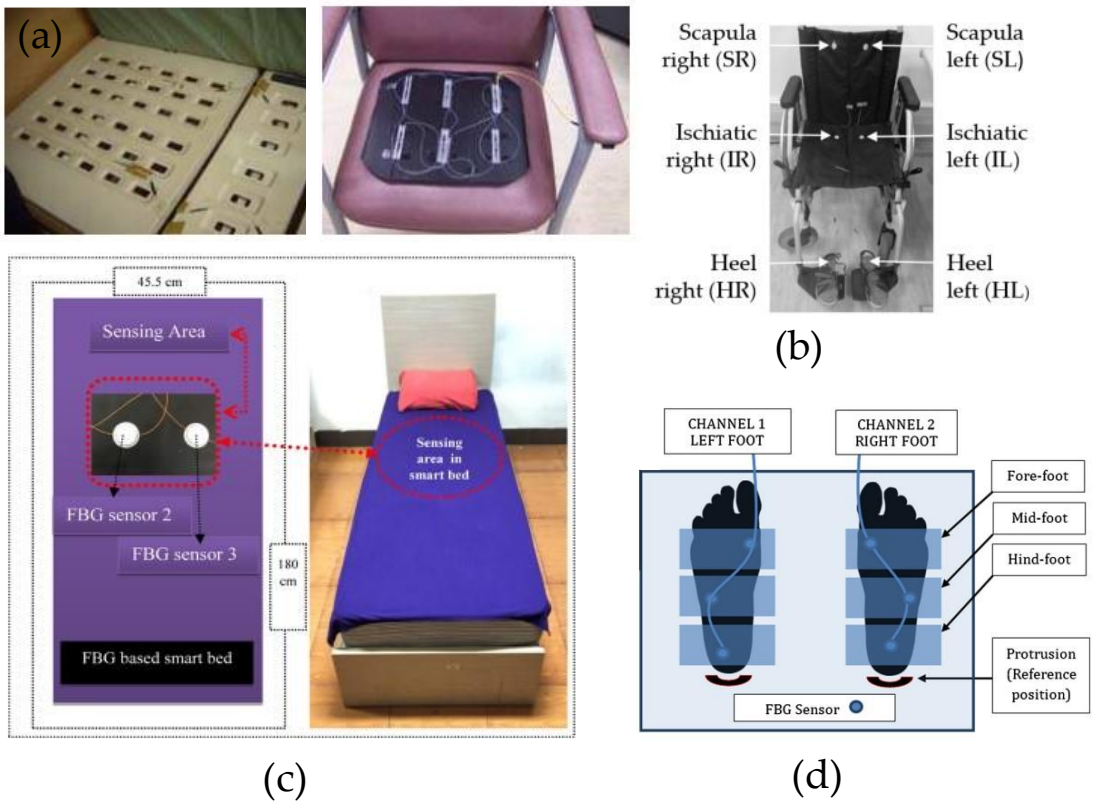

Figure 3.8. Representation of the non-wearable systems for posture and movement detection described in the section. In (a) the smart bed and chair equipped with the FBG-based sensors presented by Fook et al. (adapted from [180]). In (b) the wheelchair realized by Tavares et al. (adapted from [181]). In (c) the smart bed fabricated by Abro et al. (adapted from [179]) and in (d) the FBG-based plantar platform designed by Prasad and co-workers (adapted from [182]).

2.2. Wearable systems

With greater advancement in technologies, research in the context of wearable systems for monitoring body movement and posture based on FBG sensing technology has undergone a major acceleration. In fact, in this field, even more so than in respiratory monitoring, the onset of new 3D printing technologies, the discovery of extremely strong fabrics and textiles, as well as innovative flexible and stretchable materials has boosted the spread of novel highly reliable measurement systems resistant to the extreme deformations caused by body motions. Also in this case, FBGs are integrated into textiles and fabrics, making gloves and knee braces “smart”, or directly inserted into 3D printable structures. Also, FBG-based soft flexible sensors are applied to common accessorizes such as knee pads and elbow bands to assess their angle variation. In the following subsections, an overview on the wearable systems devoted to body motion and posture monitoring is given, again classifying the proposed solutions into smart textiles, soft flexible sensors and 3D printed sensors.

2.2.1. Smart textiles

Da Silva and co-workers in [183] designed a novel glove based on FBGs for hand gesture recognition. In order to detect the flexion/extension movement of the 14 phalanx joints present in the hand, 14 FBGs multiplexed along a single fiber optic were enclosed into two flexible polymeric foils following a curvilinear path in correspondence of each joint. Such design allows the fiber to withstand the deformation caused by the flexion/extension movement (> 14% of $\Delta\varepsilon$). The foils were then sewed on a commercial glove. The glove was characterized in respect to the fingers’ flexions and extensions. In fact, a test was performed by asking a volunteer to wear the device and open and close the hand repeatedly, in presence of a reference device to assess the angles of hand joints motions. The sensorized glove determined the 14 joint angles with maximum error of 2° in a motion range of 0° - 90°.

Still remaining on the hand gesture, also Lin et al. [184] fabricated a FBG-based glove but implementing a different approach for sensor integration. A commercial glove was used where each phalanx was covered by a piece of rectangular sponge 10 mm thick. On each piece of sponge fiber optic was glued containing two or three FBG sensors, depending on the number of joints in the phalanx. A calibration process was carried out to relate the FBGs output to the degrees of angle motion. $\Delta\lambda_B$ showed linear behavior until the fingers close into a fist. In that last phase $\Delta\lambda_B$ assume non-linear trend. A cubic spline interpolation proved to be the most suitable interpolation to fit the finger posture motions of six postures.

The joints of the limbs are the subject of equally interesting studies. Both Rocha et al. [185] and Dominguez et al. [186] focused their attention on the knee joint. The system proposed by Rocha and co-authors [185] comes as an elastic knee brace upon which a foil of PVC embedding a single FBG is applied with the help of metallic pressure

buttons. The PVC foil permits the strain transmission to the FBG without damaging it. This system was intended to be worn on the knee to distinguish the flexion and extension movements. The system was tested by a subject running and walking at several speeds, for 10 s of data recording. Raw data showed $\Delta\lambda_B$ increase for flexion and decrease for extension movements. Also, $\Delta\lambda_B$ trends were smoother at higher speeds. On the contrary, Dominguez et al. [186] developed a sensor by applying a FBG on a stripe of Kinesio tape to be attached directly to the user's skin at the knee level. The sensor was calibrated performing different angular motions (i.e., from 5° to 60°) for three times guided by a goniometer. The $\Delta\lambda_B$ showed an exponential dependence with the applied angle, probably given by the tissue elasticity. Moreover, the system was assessed during a walk by a volunteer for a total of seven gaits, which could be clearly identified in their flexion/extension phase from the FBG output. Also, in a single gait, it was possible to detect the seven phases which compose the gait cycle.

Moreover, in [187] Butt and co-workers developed a smart insole to collect data of the plantar pressure distribution as support for an ambitious study. In fact, those data were matched with those retrieved by an electroencephalogram to predict the brain signals corresponding to three postures (i.e., sitting, standing and walking) by means of AI algorithms. The smart insole came as a commercial insole made by polyethylene foam 5 mm thick and equipped with three FBG sensors at different plantar zones: front, middle and back plantar. The outputs of the three FBGs had different trends depending on the position assumed by the subjects. In sitting position, no change in $\Delta\lambda_B$ was observed, while in standing position there were minimal $\Delta\lambda_B$ due to the weight displacement on the plantar. During the walk, on the other hand, it was again possible to recognize the gait phases progression.

Summing up, the described WDs represent working solutions for the detection mainly of hand, ankle and knee movements. However, all the devices described are particularly bulky. In fact, because body movements imply a wider range of motion than the chest displacements caused by the respiratory activity, it is necessary to reinforce the fiber by inserting it into thicker or larger substrates.

In Figure 3.9, an outlook on some of the proposed solutions is displayed.

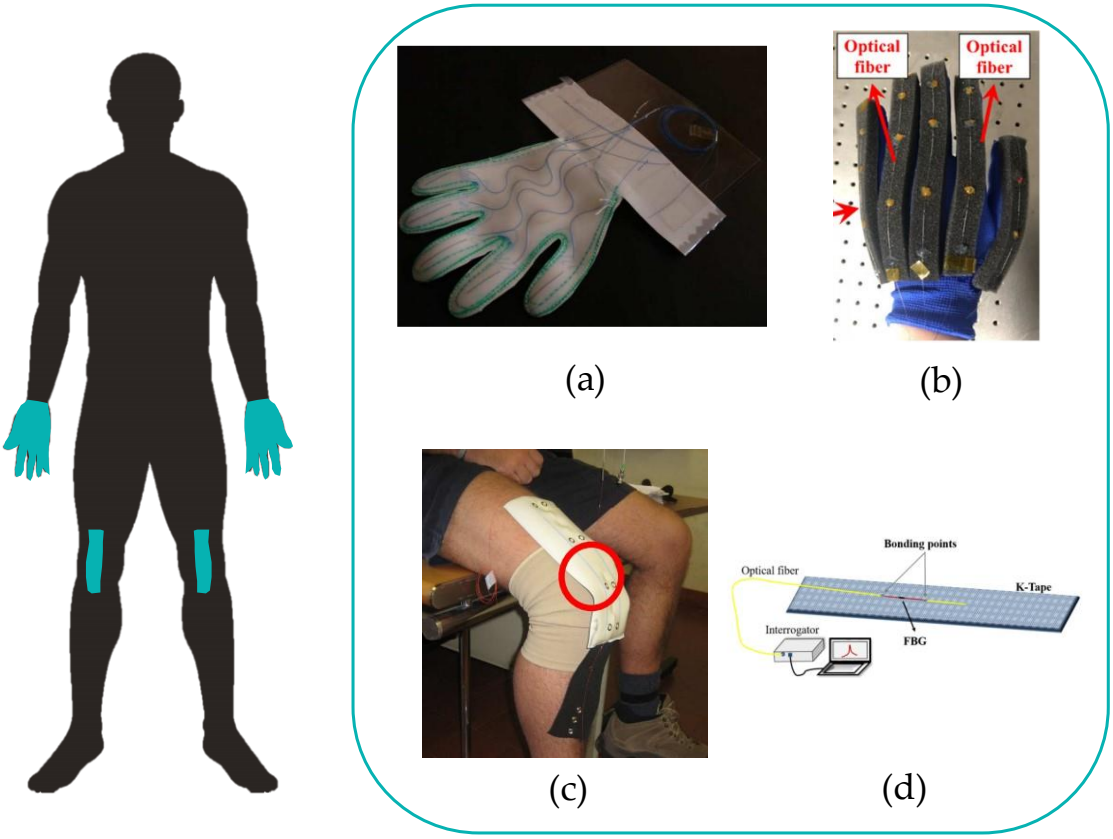

Figure 3.9. Collection of some of the described smart textiles for motion and posture monitoring and area of the human body suitable to their application. In (a) and (b) the smart gloves proposed by Da Silva and co-workers (adapted from [183]) and Lin et al. (adapted from [184]), respectively. In (c) and (d) the solutions presented for knee flexion/extension detection by Rocha et al. (adapted from [185]) and Dominguez et al. (adapted from [186]), respectively.

2.2.2. Soft flexible sensors

Jang and his research group [188] proposed three different FBG-based sensors to identify the three different movements executable by the arm by means of the shoulder and elbow joints (three degrees of freedom are permitted). The three sensors were divided into: *i)* "shape sensor" (to be applied on the shoulder) which monitored the arm orientation; *ii)* "angle sensor" (to be applied to the elbow) which detected the angle variation, and *iii)* "twist angle sensor" (to be applied to the elbow and shoulder) which detected the twisting movements. Each sensor presented a different structure to maximize the output of the embedded FBG given the motion. The shape sensor consisted in three fiber optics (with multiple FBGs each) inserted into a 300 µm in diameter polyamide tube. The angle sensor consisted of a 150 mm wide x 250 µm thick matrix of epoxy resin embedding at its center a single fiber optic holding several FBGs. Lastly, the twist angle sensor came as a rigid tube housing a fiber optic arranged in a spiral holding a single FBG. The accuracy of the three sensors were evaluated. Average

error < 1.98 mm was made by the shape sensor in detecting arms' orientation in 3D space. Angle error < 0.2° was committed by the angle sensor, while the twisting angle showed a resolution of 0.47° in measuring rotation angles.

A different approach was applied by Abro et al. [189] in the production of a FBG-based smart belt for knee posture identification. An FBG sensor was fixed over a rectangular-shaped silica gel substrate whose dimensions were 3 mm x 6 mm x 25 mm and covered with a PVC strip. This sensing structure was secured at its edges to a belt to be tied around the knee. The functionality of the device has been tested in both static (the subject moved from stand to seat position in three steps and kept each position for 10 s) and dynamic experiments (the subject was asked to run). The system showed a sensitivity of about 0.03 nm/°. A further step forward has been made by the same research group in [190]. In this work they explored the functioning of the smart belt at different body joints such as fingers, wrist and elbow. Linear increase in the FBG's output was always obtained by varying the angle of each investigated joint from 0° to 120 °. However, experiments carried out dynamic conditions (i.e., running trials) showed that knee movements are the most suitable to be detected by this system.

Still on the topic, in [191] Resta and co-workers fabricated two soft sensing elements by encapsulating a 1 mm length FBG into two silicone rubber matrices with rectangular shape (dimensions: 50 mm x 30 mm x 10 mm for the bigger sensor and 40 mm x 30 mm x 10 mm for the smaller ones). Their strain sensitivity was investigated by applying a maximum deformation of 2% and the S_ε values of 3.944 nm ·mm^{-1} and 2.897 nm ·mm^{-1} were calculated. The soft sensors were then applied to the upper part of a knee pad. The system was then tested by a subject walking on a treadmill at three speeds. For both the soft sensors, flexion/extension movements caused maximum/minimum strains which corresponded to the maximum/minimum points in $\Delta\lambda_B$ trends.

The same operating principle was exploited by Domingues and colleagues [192] to produce a novel system for plantar flexion/extension recognition. An FBG was enclosed into a rectangular epoxy resin substrate. At the edges of the substrate two 3D printed PLA adapters were glued. The adapters were designed to link to two sockets to be secured to some stripes of Kinesio tape which was attached to the dorsum of the foot. The FBG was subjected to maximal strain during plantar flection. The system's calibration was performed and a sensitivity of 0.041 nm/° was assessed. Also, the performance of the system during walking was investigated: similar trends were identified for all the gait cycles, and in every gait, it was possible to distinguish both the stance and the swing phases.

An attempt was made by Kim and colleagues in [193] to fabricate a novel wearable solution to determine the hand posture in real-time. The system was composed of five finger modules which could be regulated in length to adapted to the user's hand size. Each module came as a silicon spring structure to be fixed to the finger which enclosed an FBG fixed to a polyurethane polyhedron structure in correspondence of the central phalange. The modules were characterized to bending by performing bending tests with the help of a stepping machine until reaching an angle of 90° for 10000 times. FBGs'

showed linear behavior and high accuracy in performing the measurements. The average error among all joints occurring in measuring the fingers' angles was 0.47° ± 2.51° with a MAE of 1.63° ± 1.97°.

Lastly, Guo et al [194] proposed a soft flexible sensor based on FBG technology suitable for monitoring multiple joints. The sensor was a rectangular-shaped substrate (15 mm x 10 mm x 2 mm) made of polydimethylsiloxane in which a fiber optic (holding a single FBG) was placed with curved path. The sensor was highly stretchable (until 50% of deformation), flexible and transparent. This system was tested applied upon different garments (i.e., on a knee band and on a glove) or directly to the skin (i.e., on the neck and on the wrist) with the help of some chirurgical tape to assess its capability to evaluate the angle variation of different body articulations. In all these application, flexion and extension movements could be clearly identified by the sensor output over time. In fact, once again, flexion movements led to maximum sensor's deformation which corresponded to $\Delta\lambda_B$ peaks. On the contrary, extensions were traceable to the minimum $\Delta\lambda_B$ points.

The insertion of the optical fiber into soft matrices is presented as a winning strategy to reinforce the sensing element and enhance its thermal insulation, not losing the flexibility which allows freedom of movement to the user. However, in very few studies trials have been carried out on volunteers, so the real ease of use of such systems has not been proven.

In Figure 3.10, some of the proposed devices are shown.

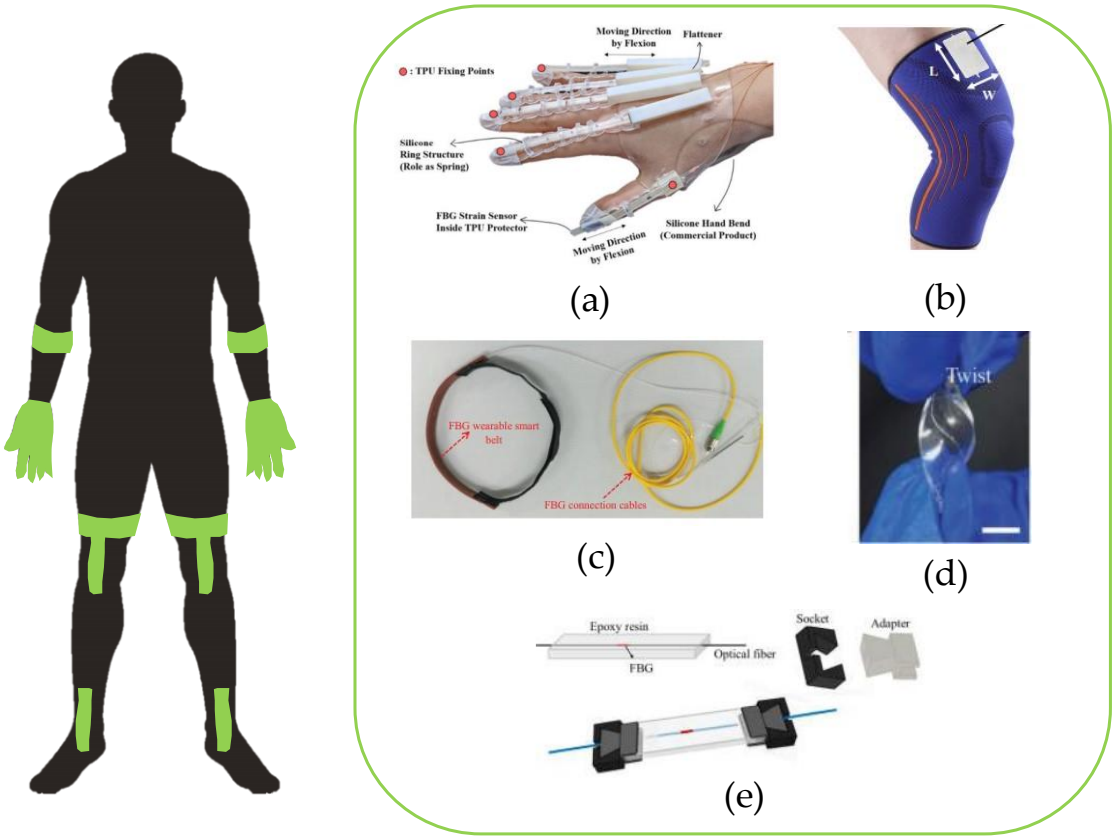

Figure 3.10. Collection of some of the described soft flexible sensors for motion and posture monitoring and area of the human body suitable to their application. In (a) the modular solution proposed by Kim and colleagues (adapted from [193]) for finger joint motion detection. In (b) the sensorized knee pad fabricated by Resta et al. (adapted from [191]) and in (c) the knee belt proposed by Abro et al. (adapted from [189]) are shown. In (d) the high stretchable sensing element presented by Guo and co-workers (adapted from [194]) is reported. In (e) the system for plantar flexion/extension monitoring designed by Domingues and colleagues (adapted from [192]) is shown.

2.2.3. 3D printed sensors

Cheng-Yu et al. [195] presented an innovative solution for both elbow and joint movements monitoring. The research group fabricated via fusion mold 3D printing technique two elastic rings of PLA which enclosed a fiber optic with a single FBG each. The two smart rings were designed to be worn 50 mm below the joint elbow and few centimeters above the knee. This design permitted to exploit the expansion/reduction of muscles size during movements to strain the FBGs and, in turn, to obtain $\Delta\lambda_B$. A first test was executed to assess the ring's capability to display increase/decrease in elbow angle. A subject was instructed to wear the ring and maintain seven band elbow angles (i.e., 0°, 15°, 30°, 45°, 60°, 75° and 90°) maintaining each position for 15 s. This ring shown 0.0056 nm/° of measurement sensitivity, 0.18° of minimum resolution and 9.5% of maximum error at 90°. A similar experiment was conducted to test the smart ring for

the knee angle monitoring. A sensitivity of 0.0276 nm/° and resolution of 0.39° were found. Both the rings demonstrated to be valid tools for joint angle detection purposes.

This proposal is a novelty in the field of 3D printed sensors. The chosen design limits the encumbrance and allows stable fixation to arms and legs for monitoring the subject's movements at two different joint sites. However, tests should be carried out on volunteers by reproducing daily motor activities to verify the real usability in terms of comfort.

A picture of the presented system is shown in Figure 3.11.

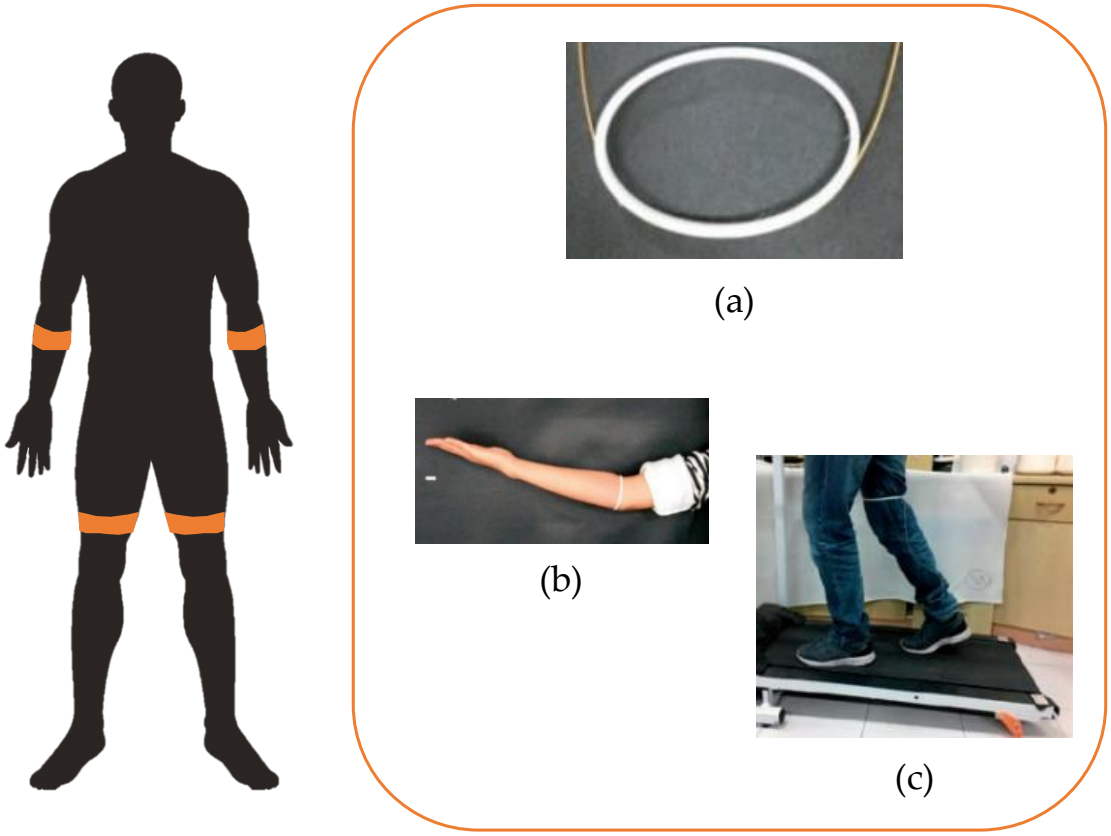

Figure 3.11. Representation of the described smart rings for elbow and knee angle monitoring presented by Cheng-Yu (adapted from [195]) and area of the human body suitable to their application. In (a) the rings design, in (b) and (c) their application to the elbow and knee, respectively.

Chapter 4 – Design and development of novel wearable systems based on FBG technology for respiratory rate, body movement and posture monitoring

1. FBG-based smart wearable solutions for respiratory rate monitoring

In this paragraph, the design and development of two WDs for respiratory activity monitoring are described. In particular, the first device is equipped with soft flexible sensing elements embedding FBG sensors to monitor RR via chest wall displacements. The second one is instead a system integrating an FBG functionalized in agarose substrate to be placed at the nostrils levels, which exploits the variation in thermo-hygrometric conditions of the respiratory flow to discriminate inspiratory and expiratory breathing phases. Their assessment on volunteers is also reported.

1.1. Elastic bands instrumented with four soft flexible FBG-based sensing elements for chest-wall displacements detections

This system is composed of four flexible dumbbell-shaped sensing modules anchored to two elastic bands for chest-wall displacement detection. The system is light and easy to wear and can be adapted to any anthropometry. This device is intended to be used for respiratory monitoring in both occupational and clinical environments. In fact, its assessment has been performed on employees performing active and static working activities and patients whose respiratory pattern could be affected by disabilities (i.e., hemiplegic patients).

In this section, parts of the works [196]–[198] which the PhD candidate has co-authored have been freely extracted.

1.1.1. Design and manufacturing process

A representation of the wearable system is given in Figure 4.1 (a). The wearable system comes as two elastic modules to be worn around the chest and abdomen, each of which consists of two parts: a stretchable element and a sensing element.

The stretchable element is a 1 m-length elastic band (50 mm of width) with two Velcro® straps at the ends to be adaptable to different anthropometric characteristics.

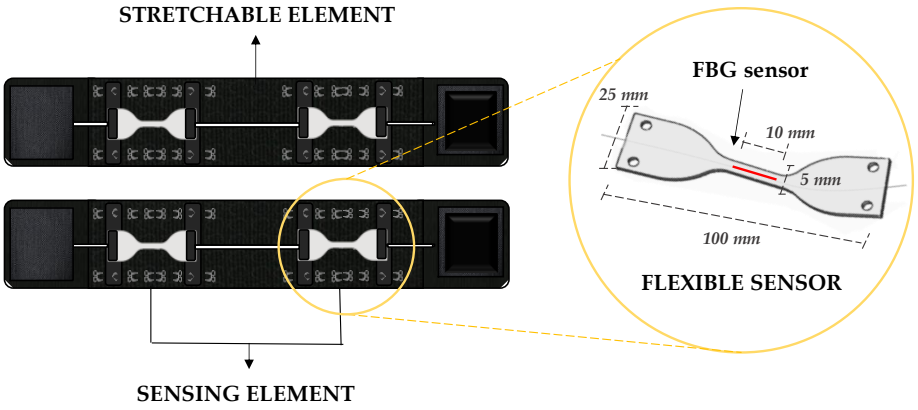

(a)

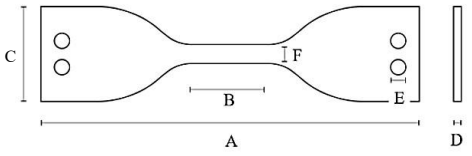

A - Overall length [mm]	B – Narrow portion length [mm]	C – Ends width [mm]	D – Thickness [mm]	E – Holes diameters [mm]	F- Narrow portion width [mm]
100	21	25	2	3	5

(b)

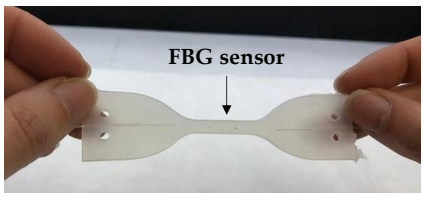

(c)

Figure 4.1. Representation of the wearable system. In (a), an insight into the wearable system is given, showing the two stretchable elements (which come as two elastic bands), each of which is equipped with a sensing element composed by two flexible sensors. In addition, a magnification of a flexible sensor is reported on the right. In (b), a schematic representation of the nominal geometric characteristics of the custom flexible sensors is given. A photo of the flexible sensor is shown in (c), illustrating the position of the FBG.

The sensing element consists of two multiplexed flexible sensors. Each flexible sensor (FS) comes as a commercial polyimide (PI) -coated fiber optic (developed by Broptics Technology Inc.) holding a 10-mm length FBG sensor encapsulated into a dumbbell shaped-flexible matrix. The λ_B of the FBG sensors were 1549 nm and 1557 nm respectively for each pair to avoid overlap. The choice of PI as fiber coating is motivated by the higher flexibility and handiness of PI-recoated optical fiber than the acrylate-recoated one [199]. Moreover, Dragon Skin™ 20 silicone (produced by Smooth-on Inc.)

was chosen as casing material because it is very flexible and highly stretchable [200]. Regarding the size and shape of the encapsulating matrix, the design has been guided by the international standard ISO 37:2017 (Tensile Stress-Strain Properties of Vulcanized or Thermoplastic Rubber) [201]. Among various specimen size included in the standard ISO 37:2017, Type 1A (Figure 4.1 (b) and (c)) has been chosen to enhance the FS's sensitivity to uniaxial ε and ensure the well-anchorage of the sensors on the elastic bands through the dumbbell extremities (which improves the adhesion of the FBG to the band and, in turn, its compliance with the rib cage deformation). The silicon matrix was designed with overall dimensions of 100 mm x 22 mm x 2 mm and narrow portion dimension of 21 mm x 5 mm x 2 mm in the conformance with specimen size Type 1A in [201]. On each end, two 3mm-diameter holes interspaced by 5 mm allow the FS to be quickly bonded to a garment. In this way, no matrix cracks and lacerations occur because of the implementation of a bonding mechanism (e.g., the use of automatic buttons) after the polymer vulcanization.

The main steps of the manufacturing process are as follows:

1) the FBG sensor was positioned between two matching 3D printed molds designed into a dumbbell shape in a sandwich construction;
2) the silicone was fabricated by mixing Dragon Skin™ 20 (A and B bi-component, at a 1:1 ratio);
3) the mixture was placed inside a degassing pot connected to diaphragm pump for making a bubble-free casting;
4) the mold was clamped to an inclined surface at an angle of 60° to the horizontal plane, and the silicone was poured into the mold through an injection port;
5) the FS was removed from the mold after the polymer curing which lasted 4 h at room temperature (as suggested on the technical data sheet of the material).

The anchorage of each FS to the band is achieved by means of the anchorage system depicted in Figure 4.2.

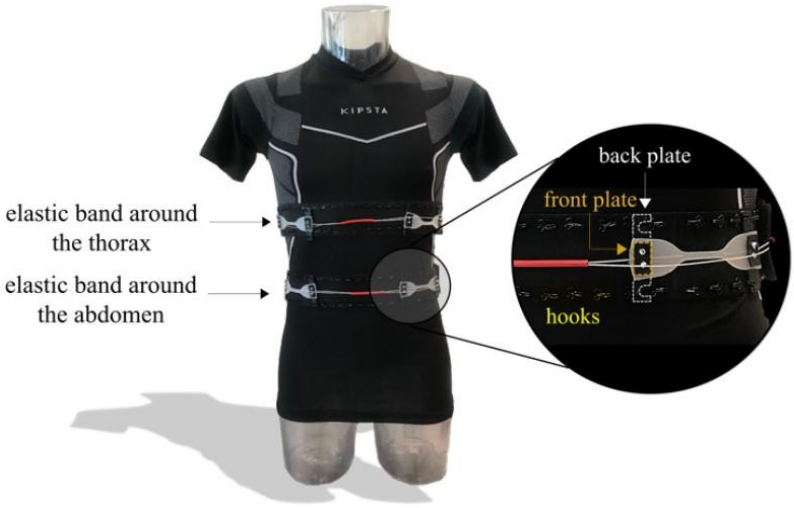

Figure 4.2. The wearable system with a zoomed detail of the anchoring system. The front rectangular plate is highlighted, the back-pad plate with U-shaped loops in dotted line, hooks in yellow.

The anchorage system is composed by four hooks handsewn on the fabrics and two rectangular pad plates with two loops each. The rectangular-shaped pad plates are provided (55 mm x 10 mm x 2 mm) with two u-shaped loops (3 mm of diameter) to join a hook couple. The hooks-and-loops anchoring system allows the FS to be placed on the band along a specific direction after its dressing around the chest (i.e., on the thorax and the abdomen). The locking of the FS to the pad plates is performed by clamping the matrix ends of each sensor between the pad plate in contact to the back surface (back pad plate in Figure 4.2) of the sensor, and an additional smaller rectangular plate (21 mm x 10 mm x 2 mm) on the front (front plate in Figure 4.2).

1.1.2. Metrological characterization

The S_ε was evaluated considering that when the subject inhales, the diaphragm contracts and the stomach inflates, so the FS that is positioned on the chest is strained. Conversely, during the exhalation, the diaphragm expands, the stomach depresses, and the sensor is compressed. Simultaneously, in the scenario of interest, the sensor can work at different environmental conditions, so that the temperature effects were also taken into account, and $S_T$was obtained. Lastly, considering the repetitive inward and outward chest movements during breathing, the hysteresis error (expressed in terms of percentage, $\%h_{err}$) was calculated.

1.1.2.1. Response to strain

One of the four nominally identical FSs was calibrated by performing tensile testing using the tensile testing machine (Instron 3365) to apply controlled ε values (from 0% to 2.5%) in a quasi-static condition (at a low displacement rate of 2 mm·min^{-1}). The static assessment of the flexible FBG sensor was executed by positioning the dumbbell-shaped specimen between the lower and the upper clamps of the machine (please, refer to Figure 4.3 (a)), at room temperature. A total of ten repetitive tensile tests were carried out, straining up the specimen to 2.5% of its initial length (l_0) (see Figure 4.3 (b)). The term l_0 is defined as the initial free matrix length between the clamps. The maximum ε value of 2.5% was chosen to cover the working range experienced by the FS in the application of interest (in accordance with the results of a preliminary test). The strain applied by the tensile machine on the FS was recorded at the sampling frequency of 100 Hz. At the same time, the $\Delta\lambda_B$ of the encapsulated grating was collected by the optical spectrum interrogator (si425, Micro Optics Inc.) at the sampling frequency of 250 Hz. The calibration curve ($\Delta\lambda_B$ vs. ε) was obtained by processing the collected data through a custom algorithm in MATLAB R2019b. The average value of $\Delta\lambda_B$ and the repeatability of the system was determined by calculating the related uncertainty across the ten tests by considering a t-student reference distribution with nine degrees of freedom and a level of confidence of 95%. To find out the S_ε, the best fitting line of the calibration curve was calculated, and its angular coefficient was calculated. Results showed an S_ε value of 0.08 nm·mε^{-1} and an excellent agreement between the experimental data and the linear fitting (Figure 4.3 (c)), as confirmed by the high value of the coefficient of determination (R^2 >0.998).

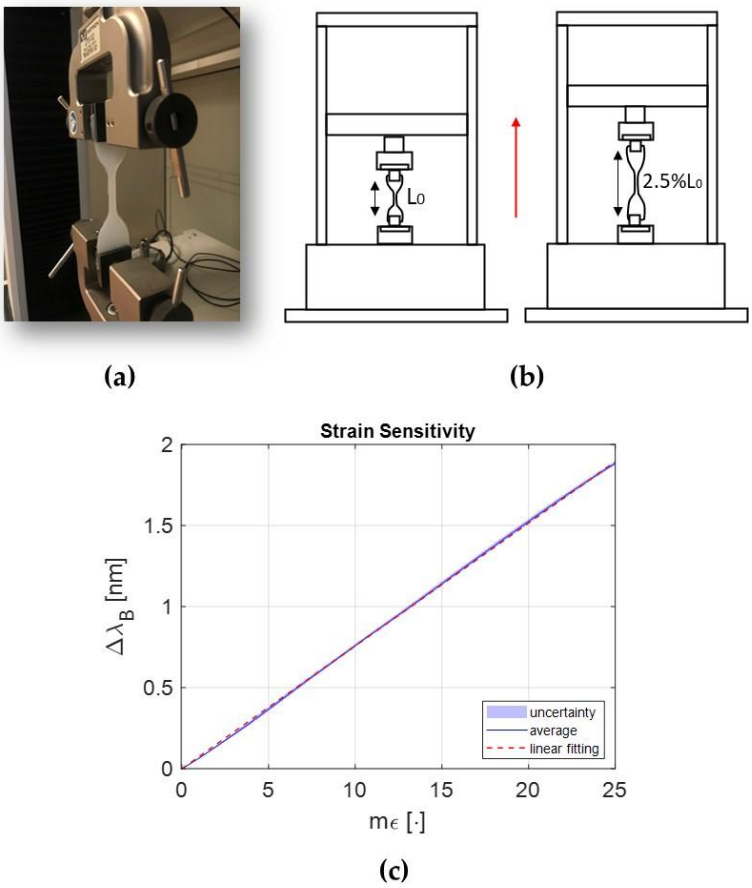

Figure 4.3. In (a) the positioning of the flexible sensor between the clampers of the tensile machine is shown. In (b) a representation of the tensile test is depicted. In (c), the average $\Delta\lambda_B$ vs. mε (in blue line), the uncertainty (in shadow blue), and the best fitting curve (in red dotted line).

1.1.2.2. Response to temperature influence

The effects of T were investigated to retrieve S_T. The specimen was placed inside a laboratory oven (PN120 Carbolite®) using a thermocouple probe (EL-USB-TC-LCD, EasyLog, Lascar Technology) as a reference. In the experiment, both the sensors were rapidly exposed to a T increment of 20°C (from 20°C to 40 °C). In this case, the maximum T value was chosen in accordance with the application of interest. When the highest T value was reached, the oven was switched off, and both sensors were kept inside all night long. It allows a quasistatic T decrement to the room temperature without any perturbation. The $\Delta\lambda_B$ values were collected by the optical spectrum interrogator at 1 Hz and the reference ΔT values by the thermocouple at 10 Hz, respectively. The calibration curve ($\Delta\lambda_B$ vs. ΔT) was obtained by processing the collected data in MATLAB and S_T as the angular coefficient of the best fitting line (see Figure 4.4). Results showed an S_T of 0.008 nm·°C^{-1} and a high agreement between experimental data and the linear fitting (R^2 >0.998).

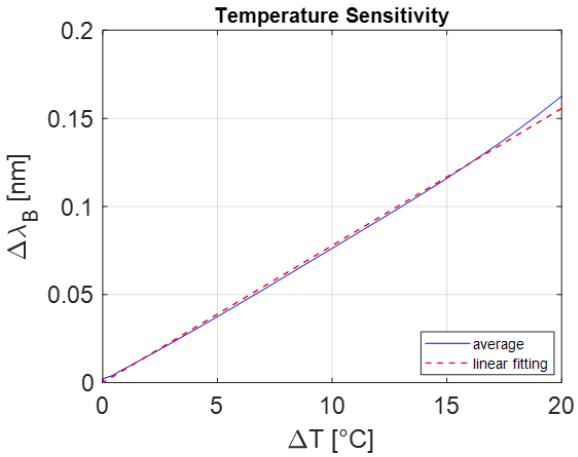

Figure 4.4. The average $\Delta\lambda_B$ vs. ΔT (in blue line) and the best fitting curve (in red dotted line).

1.1.2.3. Hysteresis loops

A total of ten repeated hysteresis loops were performed at three different velocities simulating RR values of 12, 24, and 36 breaths per minute (bpm), respectively. During each cycle, the dumbbell-shaped specimen was positioned between the clamps, and strained and unstrained, repeatedly. The $\Delta\lambda_B$ values were collected by the optical spectrum interrogator at the sampling frequency of 250 Hz while the tensile testing machine (Instron 3365) loads and displacements at the sampling frequency of 100 Hz. The $\%h_{err}$ of each test was calculated starting from the difference between value of wavelength changes during the ascending and descending phases (i.e., $\Delta\lambda_B^{up}(\varepsilon) - \Delta\lambda_B^{down}(\varepsilon)$) of each loop at the same ε (expressed in %); then, the maximum value of this difference was computed and divided by the $\Delta\lambda_B^{full-scale}$ of each loop as:

$$\%h_{err} = \frac{max\left[\Delta\lambda_B^{up}(\varepsilon) - \Delta\lambda_B^{down}(\varepsilon)\right]}{\Delta\lambda_B^{full-scale}} \cdot 100 \qquad (4.1)$$

Results showed maximum $\%h_{err}$ of 14.8%, 15.0%, and 15.9% for velocities mimicking RR values of 12 bpm, 24 bpm, and 36 bpm, respectively (see Figure 4.5 (a), Figure 4.5 (b) and Figure 4.5 (c), respectively).

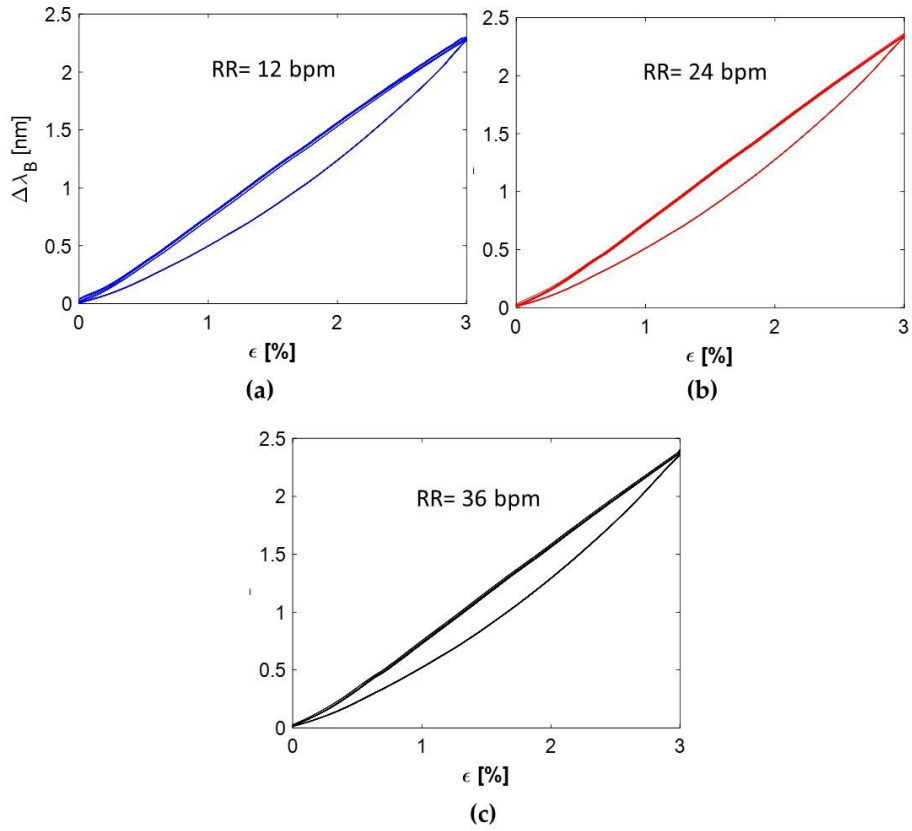

Figure 4.5. In (a) the hysteresis cycles at 12 bpm (in blue), in (b) at 24 bpm (in red) and in (c) at 36 bpm (in black) are reported.

1.1.3. Experimental assessment

In this section, the assessment of the wearable system in retrieving RR is described. The device was tested in occupational and clinical settings.

1.1.3.1. Assessment in occupational settings

In this subsection, the wearable system was tested in RR retrieving on volunteers simulating different working conditions. The choice to test the device in occupational environments is driven by the awareness that RR is a valuable indicator of the psychological load and fatigue state of workers and, more in particular, it is one of the most precise indicators of several stressing conditions such as excessive cold, heat, hypoxia, pain, and discomfort which can be related to working environments [56]. Protocols mimicking both active real-life tasks (e.g., handling loads, walking, standing up and sitting down, etc.) and static working tasks (e.g., videoterminal work) were carried out and described in the following subsections.

1.1.3.1.1. Active working activity scenario

A) Experimental setup and protocol

The assessment of the wearable system was performed in different scenarios mimicking real occupational activities on ten healthy volunteers. The volunteers have the following age and anthropometric features expressed as mean ± standard deviation: age of 28 ± 4 years old, height of 165 ± 9 cm, body mass 61.5 ± 10.5 kg, and chest circumference 87.7 ± 9.7 cm.

Each volunteer was invited to wear a tight shirt and stand still while an operator helped him/her to wear the wearable system. The two stretchable elements were tightened with some Velcro strips around the subject's torso in thoracic and abdominal positions, respectively. Then, two sensing elements (each of which embeds two FSs) were securely anchored upon the two elastic bands via the adjustable systems of hooks fixed at the extremities of the sensors, as depicted in Figure 4.2. The experimental setup is shown in Figure 4.6. An FBG interrogator (Hyperion si255, Micron Optics) was used to collect FBGs' outputs at the sampling frequency of 100 Hz. To assess the performances of the wearable system, a flowmeter (SpiroQuant P by EnviteC, Honeywell) was used as reference instrument, which allows transducing the flowrate in a pressure drop. The flowmeter has been coupled with a differential pressure sensor (163PC01D36, Honeywell) which transduces the pressure drop into a voltage. This voltage was then recorded using a custom electronic board embedding a 12-bit analog-to-digital converter (ADC MAX 1239 by Maxim), a microcontroller (STM32F446RET by STMicroelectronics), and a Bluetooth module (SPBT2632C2A by STMicroelectronics) for wireless data transmission at 100 Hz. The box containing the pressure sensor and the data acquisition board was placed in the sternal position with some stripes of bi-adhesive polymeric tape, and the flowmeter was placed at the volunteer's mouth with the help of a commercial breathing mask.

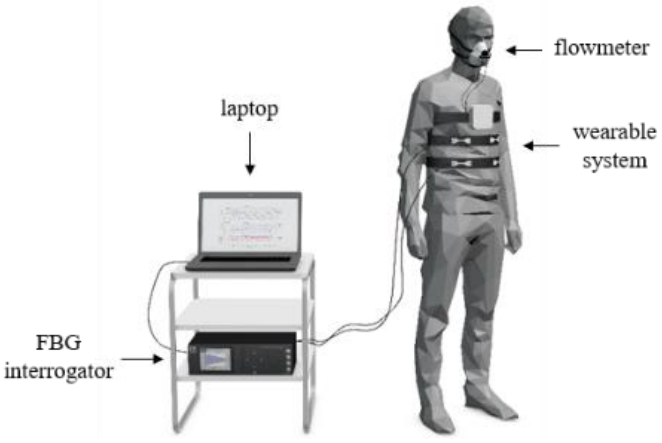

Figure 4.6. The experimental setup used for all the proposed protocols.

To pilot the experimental protocol, two Graphical User Interfaces (GUIs) were developed in LabVIEW (National Instruments, TX, USA). The first GUI was used to synchronize and save the outputs readout of the wearable system, namely the FBGs, and the benchmark, namely the flowmeter. The other GUI has been implemented to make the experiment clearer to the participant and improve engagement during the test, guiding the subject to perform the current task associated with an image, as a virtual instructor. The subject was then instructed on the movements to be executed and invited to follow the sequence of images displayed in the GUI.

The protocols used are detailed below and represented in Figure 4.7:

1) 1st protocol: 60 s of eupnea and 60 s of tachypnea, both in standing, sitting and supine static postures;
2) 2nd protocol: 120 s of self-paced walking;
3) 3rd protocol: cyclical changes of three different postures (i.e., standing, sitting and supine), keeping each position for 30 s;
4) 4th protocol: isolated upper limbs and trunk movements (i.e., frontal bending of the trunk, maximum right torsion of the trunk, maximum left torsion of the trunk, maximum arms up, lateral lifting of the arms and frontal lifting of the arms), keeping each position for 10 s;
5) 5th protocol: combination of different upper limbs and trunk movements consecutively performed (i.e., starting from a standing position, grab a target item laterally placed on the ground -on the left and on the right-, move it frontally on a rack and then replace it back on the ground), repeating each cycle four times.

The experimental design of the presented protocol aimed at assessing the ability of the sensing system in tracking the subjects' breathing activity in selected static and dynamic conditions characterizing working settings. Specifically, trial 1 aims at evaluating RR in the absence of body motions, while trials 2, 3 and 4 aim at estimating RR during the execution of dynamic tasks. Finally, trial 5 aims at investigating the performances of the wearable in a real working scenario, mimicking some typical working tasks. The protocol STUCBM 27/18 OSS received the approval of the ethical committee of Università Campus Bio-Medico di Roma.

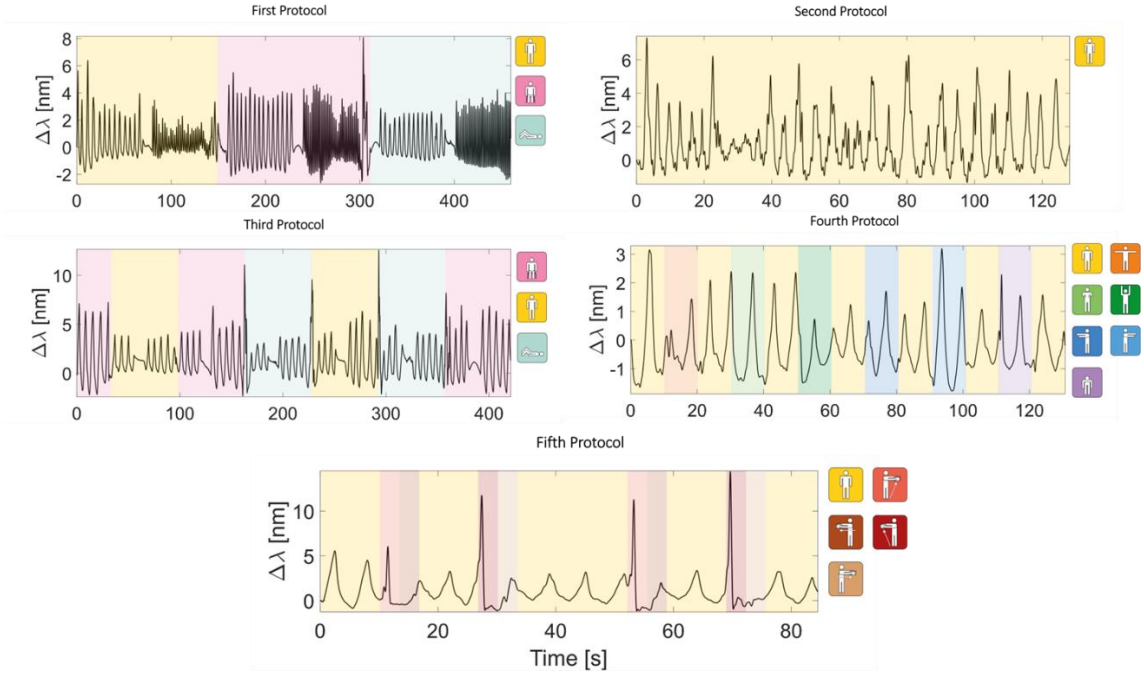

Figure 4.7. The five designed protocols and the related $\Delta\lambda_B$ trend in time. Each box is colored as the icon representing the activity performed by the volunteer during the execution of the protocol. The activities are: standing (yellow icon), sitting (pink icon), supine (azure icon), walking (dark yellow icon), lateral lifting of the arms (orange icon), front lifting of the arms (light green), maximum arms up (dark green), maximum right torsion of the trunk (blue icon), maximum left torsion of the trunk (light-blue icon), front bending of the trunk (purple), lifting an item from the ground on the left (dark pink icon), moving the item from left to right (brown icon), lifting an item from the ground on the right (bordeaux icon) and moving the item from right to left (light brown icon).

B) Data analysis and results

The acquired data have been processed offline in MATLAB environment. Firstly, the flowmeter signals were filtered with a 3rd order Butterworth bandpass filter (0.05 Hz and 2 Hz of low and high cut-off frequencies, respectively). The four FBGs data were summed together and filtered with the same bandpass filter used for the flowmeter. The RR values were estimated by identifying the inspiratory maxima peaks. Given the variability of the respiratory ranges within each trial, the identification of maxima peaks has been performed by considering a moving time window of 15 s for each sampling point (see Figure 4.8 (a)). Then the reciprocal of the averaged time differences between consecutive peaks was calculated, thus obtaining $RR^{ref}(i)$ and $RR^{FBG}(i)$ both the reference and the wearable systems in each i-th time window (see Figure 4.8 (b)). Finally, $RR^{ref}(i)$ and $RR^{FBG}(i)$ were averaged obtaining $\overline{RR^{FBG}}$ and $\overline{RR^{ref}}$ for each protocol. To assess the overall performance of the system for each protocol we also

calculated the mean $\overline{RR^{FBG}}$ and $\overline{RR^{ref}}$ among all volunteers. Results are listed in Table 4.1.

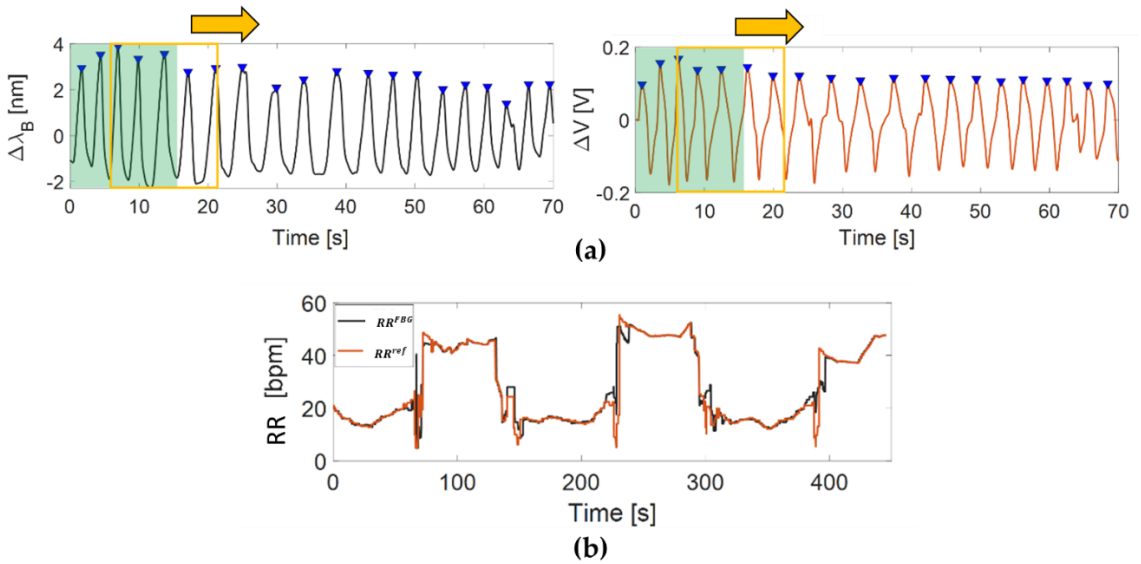

Figure 4.8. (a) Maxima peaks identification (blue triangles) considering a time window of 15 s (green area) moving along the signals at every sampling point (yellow framed window area). The black trend on the left represents the FBGs output signal and the red trend on the right represents the reference flowmeter signal. (b) Estimated RR trends representing $RR^{ref}(i)$ (red line) and $RR^{FBG}(i)$ (black line).

To evaluate the performance of the proposed WD compared to the reference instrument, the percentage error (%E) has been computed as in the following equation

$$\%E = \frac{\overline{RR^{FBG}} - \overline{RR^{ref}}}{\overline{RR^{ref}}} \cdot 100 \tag{4.2}$$

The average %E and the absolute percentage error ($\%E_{abs}$) have been computed for each subject and protocol (see Table 4.1). In contrast to other works, the error was here evaluated taking into account the average RR values (i.e., $\overline{RR^{FBG}}$ and $\overline{RR^{ref}}$). This choice has been made to get a general quantitative overlook on the system's ability in retrieving RR and a quick evaluation on its overestimation and underestimation.

The proposed wearable system showed proper match with the reference instrument as testified by both the $\overline{RR^{ref}}$ and $\overline{RR^{FBG}}$ values shown and the %E values (see Table I). Indeed, the %E was lower than 5% in all volunteers but one (i.e., the volunteer 2 during the third protocol, in which the error was of 9.9%). The last row of Table I shows the values of $\overline{RR^{ref}}$ and $\overline{RR^{FBG}}$, %E and $\%E_{abs}$ resulted by averaging out volunteers' data for each protocol. Regarding the average errors, %E ranged from -0.33 % and 3.38 %, while $\%E_{abs}$ from 1.0 % and 4.2%.

Table 4.1. Average estimated Respiratory Rate values, %E and $\%E_{abs}$ obtained from the data analysis. S_{mean} represents the calculated parameters averaged among all volunteers.

	First Protocol				Second Protocol				Third Protocol			
Volunteer	F_{FBG} [bpm]	F_{REF} [bpm]	%E [%]	$\%E_{abs}$ [%]	F_{FBG} [bpm]	F_{REF} [bpm]	%E [%]	$\%E_{abs}$ [%]	F_{FBG} [bpm]	F_{REF} [bpm]	%E [%]	$\%E_{abs}$ [%]
S1	37,8	38,8	-2,5	2,5	24,7	24,2	2,1	2,1	18,0	17,1	5,0	5,0
S2	28,2	27,9	1,0	1,0	23,5	22,7	3,2	3,2	19,3	17,6	9,9	9,9
S3	21,0	21,0	-0,2	0,2	23,1	22,4	3,1	3,1	12,4	12,1	2,4	2,4
S4	25,0	24,8	0,5	0,5	23,1	22,3	3,2	3,2	19,7	19,0	3,6	3,6
S5	20,8	19,9	4,6	4,6	25,5	24,5	4,1	4,1	17,5	16,7	4,7	4,7
S6	23,0	22,4	2,7	2,7	26,0	24,7	4,9	4,9	20,0	21,0	-4,5	4,5
S7	30,2	30,3	-0,4	0,4	26,7	26,1	2,2	2,2	18,6	18,6	0,1	0,1
S8	26,8	26,5	1,1	1,1	23,2	22,1	5,1	5,1	19,5	18,5	5,0	5,0
S9	29,6	29,6	-0,1	0,1	23,0	22,2	3,6	3,6	16,5	16,0	3,1	3,1
S10	25,9	25,2	2,8	2,8	23,2	22,7	2,2	2,2	16,8	16,2	3,7	3,7
S_{mean}	26,8	26,6	1,0	1,6	24,2	23,4	3,4	3,4	17,8	17,3	3,3	4,2

	Fourth Protocol				Fifth Protocol			
Volunteer	F_{FBG} [bpm]	F_{REF} [bpm]	%E [%]	$\%E_{abs}$ [%]	F_{FBG} [bpm]	F_{REF} [bpm]	%E [%]	$\%E_{abs}$ [%]
S1	18,7	18,6	0,8	0,8	17,3	17,5	-1,3	1,3
S2	17,7	17,3	2,2	2,2	17,9	17,9	0,0	0,0
S3	15,3	15,0	1,6	1,6	16,1	16,0	0,6	0,6
S4	17,4	17,3	0,6	0,6	17,3	17,0	1,5	1,5
S5	17,3	17,0	1,6	1,6	17,0	16,6	2,6	2,6
S6	18,1	18,0	0,6	0,6	17,6	18,0	-1,9	1,9
S7	19,4	19,3	0,5	0,5	18,3	18,0	1,3	1,3
S8	18,0	17,7	1,7	1,7	17,8	18,1	-1,5	1,5
S9	17,5	17,5	0,2	0,2	17,0	17,2	-1,1	1,1
S10	17,2	17,2	-0,4	0,4	16,6	17,2	-3,5	3,5
S_{mean}	17,6	17,5	1,0	1,0	17,3	17,3	-0,3	1,5

1.1.3.1.2. Sedentary working activity scenario

In this case, the WD was assessed on two volunteers in a more static occupational scenario and for long-term acquisitions. Taking into account the excellent performance obtained by testing the device under more active and challenging occupational conditions (see previous section), it was deemed appropriate in this case to use a single elastic band equipped with two FSs for the benefit of greater user comfort. Also, the performance of the system in RR monitoring was investigated by following a single- and multi- sensor configuration to check whether the number of sensors affects the system performance.

A) Experimental setup and protocol

Two videoterminal workers (both males) were enrolled as volunteers. The subjects were invited to seat and wear the FBG-based wearable system and the BioHarness (BH) devices (the Zephyr™ BioModule and Strap commercialized by Medtronic, Nederland)

used as gold standard. Each volunteer was invited to perform a self-induced apnea of 10 s and then to breath normally for about 40 min while executing videoterminal tasks. During the trial, both the wearable system (equipped with two flexible sensors hereafter named as FS1 and FS2) and the reference system were worn around the torso, one beneath the other. The FSs' outputs were collected at a sampling rate of 1 kHz by means of an FBG interrogator (si255, Hyperion platform, Micron Optics, USA) while the BH data (i.e., respiratory waveform at 25 Hz) were stored on board. A representation of the experimental setup is given in Figure 4.9.

Figure 4.9. Representation of the experimental setup: (a) the FBG interrogator, (b) the elastic band instrumented with two flexible sensors and (c) the laptop dedicated to the acquisition of data from the interrogator.

B) Data analysis and results

Raw data acquired by the FBGs-based system (FS1, FS2 and FS_{tot} signals) and the BH were synchronized by means of the apnea performed by the volunteers at the beginning of the acquisition. All the signals were windowed by splitting them into 40 windows lasting 60 s each and the power spectral density (PSD) was computed for every window. The dominant frequency (i.e., f_0 that is the frequency where the maximum peak of the PSD is located) was saved and used to estimate RR value window-by-window (see Figure 4.10). The estimation of RR values was then executed by converting the 40 values of f_0 from the PSD computed on the windowed signals into breaths per minute (bpm) by multiplying for 60.

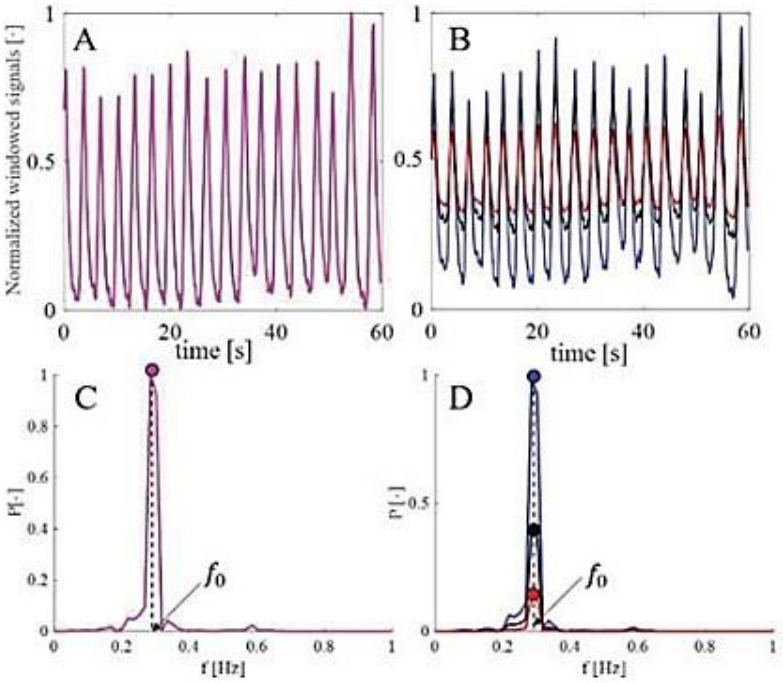

Figure 4.10. (A) 60s-lasting window of BH signal (magenta line); (B) FS1, FS2 and FS_{tot} signals (black, red and blue lines respectively); (C) PSD of the windowed BH signal; (D) PSD of FS1, FS2, FS_{tot} (black, red and blue lines respectively).

Then, the performance of the proposed system was assessed by comparing the RR values obtained considering the single- (i.e., obtained by analyzing the signal of FS1 and FS2) and multi-sensor configurations (i.e., obtained by analyzing FS_{tot}) to the ones from BH. The mean absolute error (MAE) was calculated considering the three above-mentioned cases as follows:

$$MAE = \frac{1}{n}\sum_{i=1}^{i=n}\left|RR_i^{FBG} - RR_i^{BH}\right| \tag{4.3}$$

Results showed the system capability of working during a prolonged acquisition (i.e., 40 min) in a real everyday working scenario. The high mechanical coupling between the wearable and the users' chest is verified by the high capability of the proposed system to replicate the trend in time of the reference instrument. Indeed, apnea stages and maximal inspirations are clearly visible on the signals collected by both the wearable and the BH as shown in Figure 4.11, where three windows of the signal related to one of the two volunteers are reported, both for the FSs and the BH. For instance, window 2 (Figure 4.11 (a) and (b)), window 27 (Figure 4.11 (c) and (d)) and window 40 (Figure 4.11 (e) and (f)) are reported for BH (magenta waveform), FS1 (black waveform), FS2 (red waveform) and FS_{tot} (blue waveform).

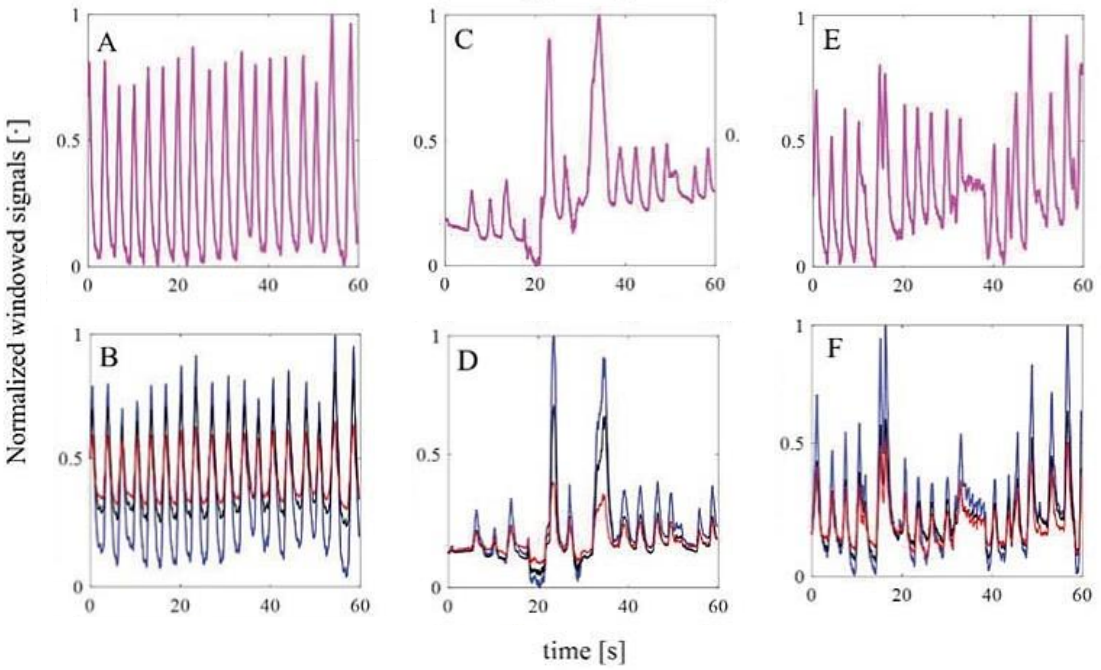

Figure 4.11. Three windows of signals related to volunteer 2. Window 2 of BH (A) and FSs (B); window 27 of BH (C) and FSs (D); window 40 of BH (E) and FSs (F); In (A) and (B) a regular respiration pattern is shown, in (c) and (D) some maximal inspirations and in (E) and (F) regular pattern intervalled by an apnea stage are reported.

The presence of some apnea stages (please refer to Figure 4.11 (E) and (F)) justifies values of RR lower than 8 bpm reported in Figure 4.12 in which the values of mean RR window-by-window for FS1 (black bars), FS2 (red bars), FS_{tot} (blue bars) and BH (magenta bars) are shown for volunteer 1 and 2.

Lastly, the discrepancy between the two measuring systems by using a single-and a multi-sensor configuration approach is listed in terms of MAE in Table 4.2.

Table 4.2. MAE values retrieved for the single- and multi-sensor configuration.

	MAE [bpm]		
	FBG1	**FBG2**	**FBG_{tot}**
volunteer 1	0.24	0.48	0.24
volunteer 2	0.77	0.99	0.52

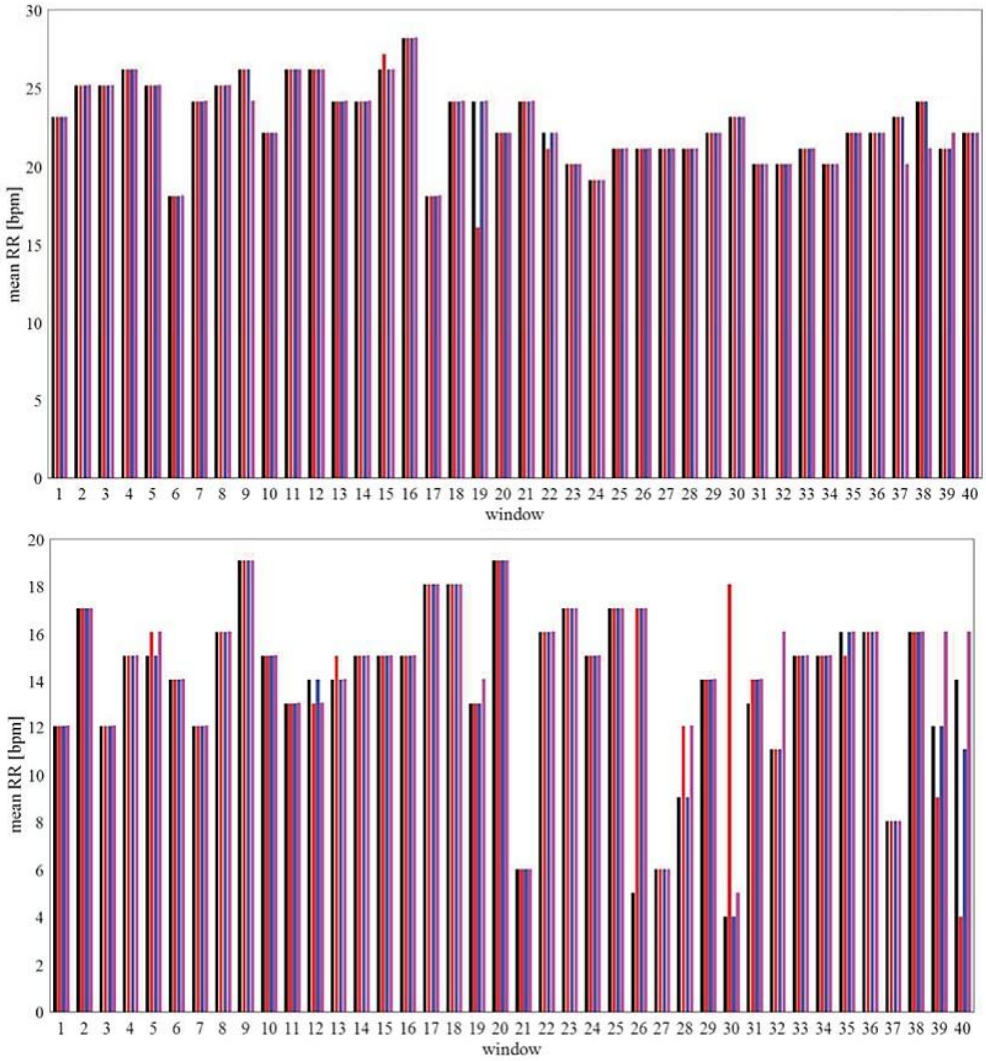

Figure 4.12. The bar plot of volunteer 1 (on the top) and volunteer 2 (in the bottom). The RR value averaged over each window are shown for FS1, FS2, FS_{tot} and BH in back, red, blue and magenta bars, respectively.

1.1.3.2. Assessment in clinical setting

In this section, the assessment of the presented FBG-based wearable system in clinical setting is presented. In particular, hemiplegic volunteers were enrolled in the study. The choice of this experimental population was made because breathing diseases are extremely common in hemiplegic patients as respiratory muscle impairment provokes altered RR, which is the more altered the more extensive the disability [202]. Also, in the most severe subjects, paradoxical motion of the chest wall paretic side, results in breathing discoordination and asynchronous respiratory movements between torso compartments [203]–[206]. As a consequence, being able to monitor RR and assess the presence of respiratory asynchronies could be of paramount importance to define hemiplegics' health status.

In the following sections, an assessment in RR retrieving and a preliminary investigation on the system's capability to detect respiratory asynchronies between torso compartments is reported.

A) **Experimental setup and protocol**

Seven post-stroke hemiplegic patients being treated at the Physical and Rehabilitation Unit of Fondazione Policlinico Universitario Campus Bio-Medico were recruited from the research volunteer database. The informed consent form was read and signed by all the participants. All patients fulfilled the inclusion criteria, i.e., an established post-stroke hemiplegia diagnosis and absence of cognitive limitations preventing comprehension of the experimental protocol. The features of the population that took part in the study are reported in Table 4.3, together with the related Fugl–Meyer Assessment Upper Extremity score [207] to quantify the upper body disability extent.

Table 4.3. Features of the enrolled hemiplegic volunteers.

# Volunteer	Age [y.o.]	Sex	Affected Side	BMI [kg·m^{-2}]	UE-FMA [1]
1	73	Male	Left	34.6	37
2	62	Male	Left	26.7	32
3	46	Female	Right	19.3	33
4	64	Male	Right	32.7	43
5	33	Female	Left	19.1	55
6	55	Male	Right	17.4	50
7	43	Male	Left	27.6	34

[1] Fugl–Meyer Assessment Upper Extremity score.

A representation of the experimental setup is given in Figure 4.13 (a). Each participant was asked to wear a tight shirt and sit on a stool. Then, the operator helped the subject to wear the wearable system as depicted in Subsection 1.1.3.1.1. Considering the torso divided into the four macro-areas depicted in Figure 4.13 (b) (i.e., right and left thorax—TR and TL, respectively—and right and left abdomen— AR and AL, respectively), an FS was placed in correspondence to each area. 40 photoreflective hemispherical markers with a diameter of 12 mm were applied to the patient's torso, 20 on the front and 20 on the back, as depicted in Figure 4.13 (c). The used marker protocol is an enhancement of the one presented by Ferrigno et al. [208], exploiting 32 markers for thoraco-abdominal kinematic detection and compartmental respiratory volume evaluation. A stereophotogrammetric MoCap system was exploited as a reference device for chest wall kinematics and respiratory activity. The system (BTS DSmart, produced by BTS Bio-Engineering S.r.l., Milan, Italy) consists of eight cameras, installed at approximately 2 m from the stool, four forward and four rearward, as shown in Figure 4.13 (a). The trajectories of the markers were collected with a sampling rate of

60 Hz by means of the tracker software provided by BTS (BTS, Bioengineering S.r.l., Milan, Italy). An optical interrogation unit (si255, developed by Micron Optics Inc., Atlanta, GA, USA, wavelength range of 1460–1620 nm) was employed to interrogate the FBGs contained in the FSs. The interrogation unit supplies the sensors with broadband polarized light and collects the $\Delta\lambda_B$ values at a 1 kHz sampling rate.

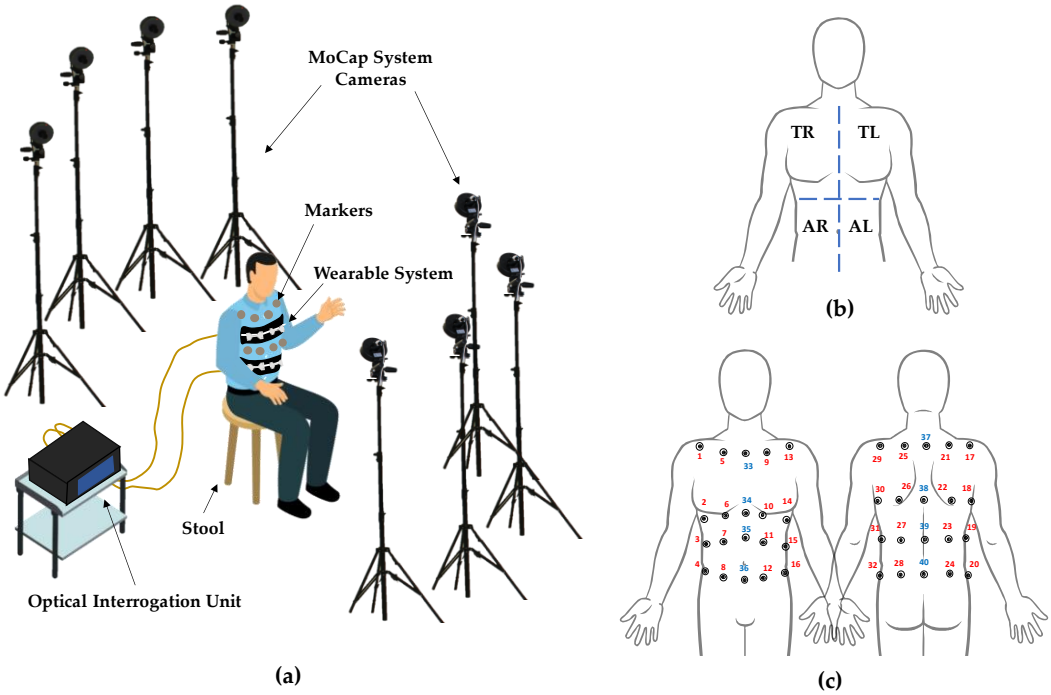

Figure 4.13. In (a) the experimental set-up, composed of a stool, the eight cameras of the motion capture system, the reflective markers, the wearable system, and the optical interrogation unit, is depicted. In (c), the four macro-areas (right thorax—TR, left thorax—TL, right abdomen—AR, and left abdomen—AL) into which the torso is subdivided are displayed. In (d), the positioning of the 40 reflective markers on the subject's torso is shown.

The volunteer was instructed on the experimental protocol, which consisted of two trials:

1) Trial 1: 5 s of apnea followed by 40 s of eupnea, maintaining the upright sitting position with the hands resting on thighs;
2) Trial 2: 5 s of apnea followed by 30 s of tachypnea (to the best of each subject's ability), maintaining the upright sitting position, hands resting on thighs. The design of the presented protocol was conceived to assess the ability of the wearable system to monitor the respiratory activity of the hemiplegic patients in two ordinary breathing conditions (i.e., eupnea and tachypnea).

The experimental protocol was designed to meet the patients' capacities and preserve their health status. The study protocol was approved by the Ethics Committee

of Università Campus Bio-Medico di Roma (protocol code ST-UCBM 27.2(18).20 OSS), in conformity with the percepts of the Declaration of Helsinki.

B) Data analysis and results

i) Assessment of the Wearable System in Respiratory Rate Estimation

Data obtained by the four FSs of the wearable system and MoCap were processed in the MATLAB environment (MathWorks Inc., Natick, MA, USA). Markers' data were analyzed to retrieve the total respiratory volume (V_{TOT}) and the respiratory volumes related to the four torso areas (i.e., V_{TR}, V_{TL}, V_{AR}, and V_{AL}). In particular, the chest wall volume was derived by the 3D marker coordinates by using the geometric model reported in [209]. Also, signals retrieved by the FSs placed in TR, TL, AR, and AL will be hereafter named as FS_{TR}, FS_{TL}, FS_{AR}, and FS_{AL}, respectively.

FS_{TR}, FS_{TL}, FS_{AR}, and FS_{AL}, and V_{TOT}, V_{TR}, V_{TL}, V_{AR}, and V_{AL} were synchronized by means of the first maximum peak occurring after the 5 s apnea. To eliminate information content not exclusively related to the respiratory activity, a first-order Butterworth passband filter was applied with a cutoff frequency of 0.01–1 Hz to eupnea signals (i.e., Trial 1) and 0.01–2 Hz to the tachypnea signals (i.e., Trial 2). An example of the data retrieved for a volunteer is given in Figure 4.14.

Both for the MoCap and the wearable system, the signals related to the thoracic, abdominal, plegic, non-plegic, and all four torso areas were obtained as follows:

i. Thoracic compartment signal: sum of the signals related to the TR and TL (i.e., FS_{TR} + FS_{TL} for the wearable system and V_{TR} + V_{TL} for the MoCap);
ii. Abdominal compartment signal: sum of the signals related to the AR and AL (i.e., FS_{AL} + FS_{AR} for the wearable system and V_{AR} + V_{AL} for the MoCap);
iii. Plegic compartment signal: sum of the thoracic and abdominal signals related to the affected side of each patient;
iv. Non-plegic compartment signal: sum of the thoracic and abdominal signals related to the non-affected side of each patient;
v. Summed signal: sum of all four torso areas' signals (i.e., FS_{TR} + FS_{TL} + FS_{AB} + FS_{AL} for the wearable system and V_{TOT} for the MoCap).

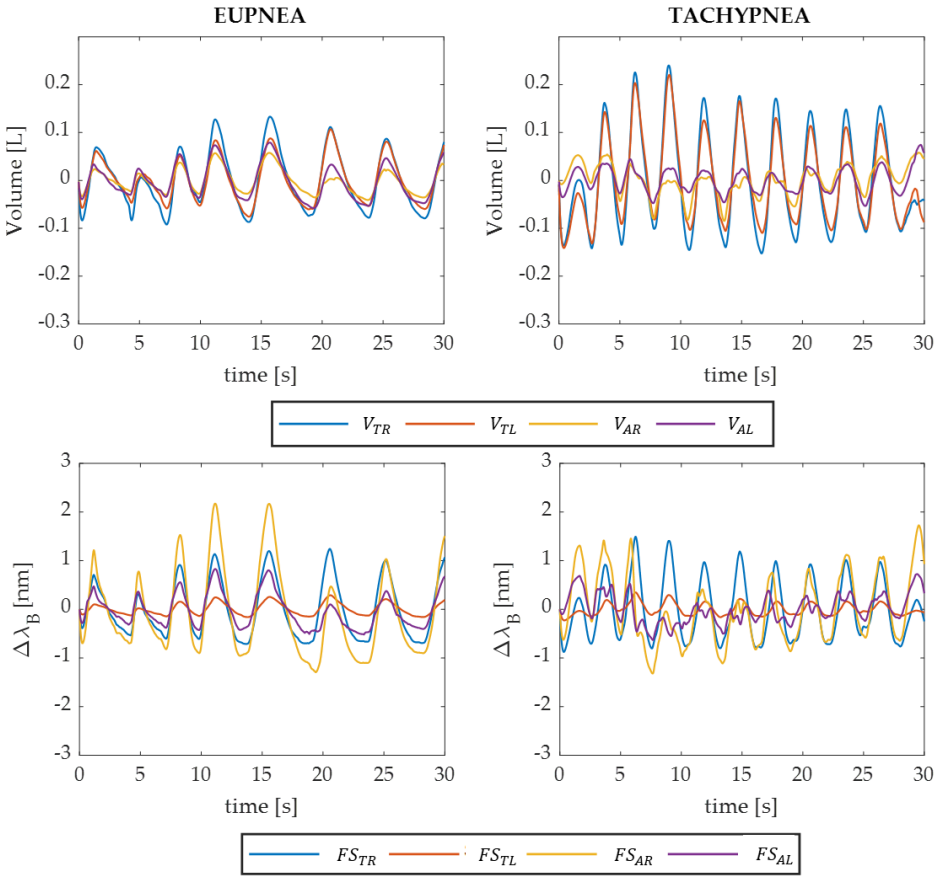

Figure 4.14. Example of the respiratory signals retrieved by the MoCap (upper graphs) and wearable system (bottom graphs) during 30 s of eupnea and tachypnea trials (left and right columns, respectively) performed by a patient. In blue, orange, yellow, and purple are shown the signals related to the TR, TL, AR, and AL compartments, respectively (i.e., V_{TR}, V_{TL}, V_{AR}, and V_{AL} for the MoCap and FS_{TR}, FS_{TL}, FS_{AR}, and FS_{AL} for the wearable system).

For each of the five signals obtained for every volunteer in eupnea and tachypnea, RR was estimated via a breath-by-breath approach. A single breathing act is the portion of signal enclosed between two consecutive minima. The i-th respiratory period (T_{ri}) related to the i-th breath was retrieved as the time elapsed between two consecutive maximum peaks (expressed in s), both for the wearable system and the MoCap $T_{ri}^{wearable}$ and T_{ri}^{MoCap}, respectively). Thus, the related i-th RR values were obtained ($RR_{ri}^{wearable}$ and RR_{ri}^{MoCap}) as the reciprocal of the respiratory periods multiplied by 60 (as expressed in breaths per minute - bpm).

To quantify the accordance between the wearable system and the reference device in RR evaluation, Bland–Altman analysis [210] was carried out, providing the mean of differences (MOD) and the limits of agreement (LOAs) expressed as MOD ± 1.96 SD (where SD is the standard deviation). The Bland–Altman graphs obtained for the four compartments (i.e., thoracic, abdominal, plegic, and non-plegic) and summed signals related to the eupnea (Trials 1) and tachypnea (Trial 2) are shown in Figures 4.15 and

4.16, respectively. MOD values and the values of the span between the LOAs (i.e., ΔLOA calculated as 2· 1.96 SD) are reported for each graph.

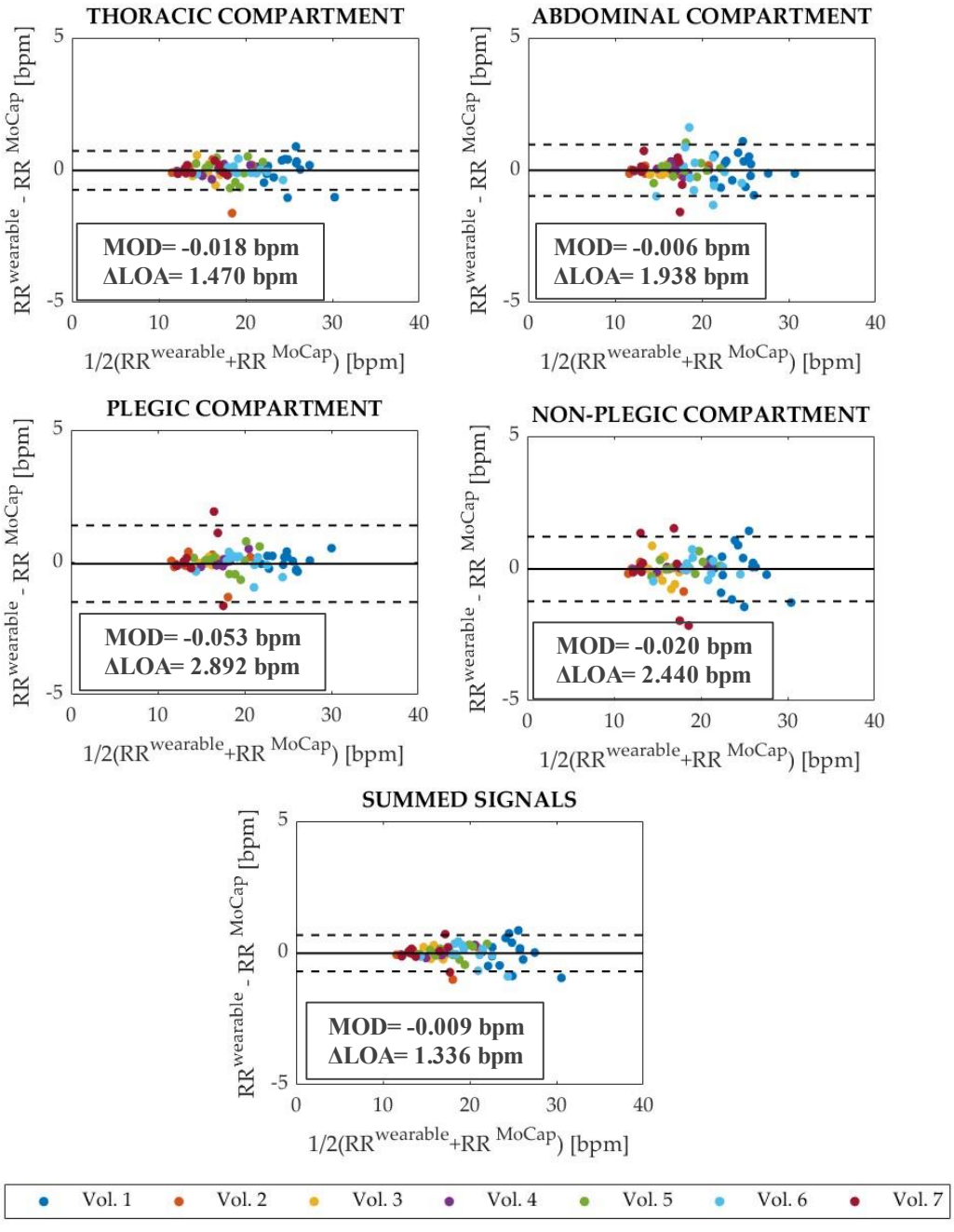

Figure 4.15. Bland–Altman plots showing the bias between $RR_{ri}^{wearable}$ and RR_{ri}^{MoCap} calculated from the thoracic, abdominal, plegic, and non-plegic compartments' data and the summed signals retrieved during the eupnea trials (Trials 1). The MOD and ΔLOA are reported on each graph. In addition, MOD is represented with black solid lines, while ΔLOA is the span comprised between the two black.

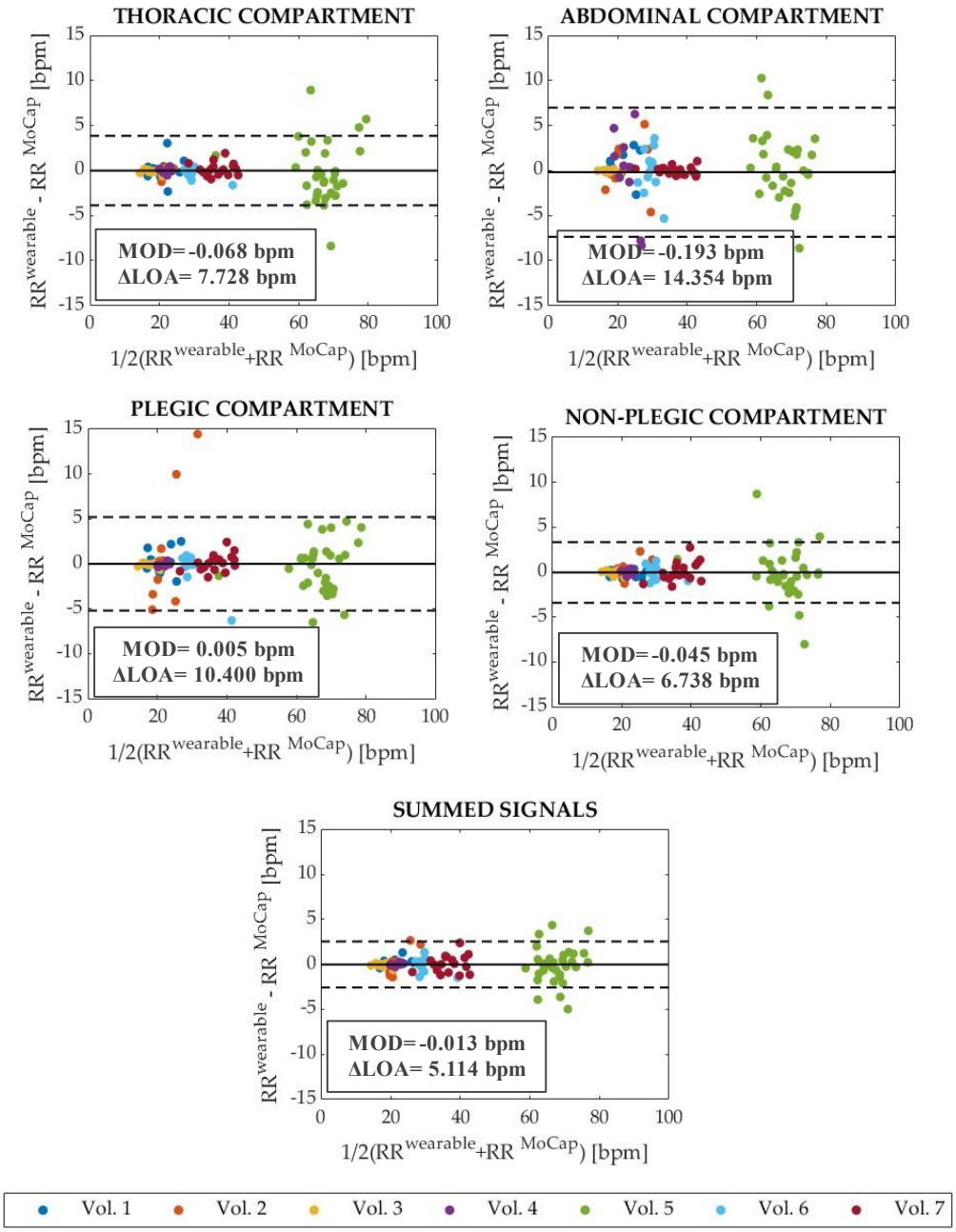

Figure 4.16. Bland–Altman plots showing the bias between $RR_{ri}^{wearable}$ and RR_{ri}^{MoCap} calculated from the thoracic, abdominal, plegic, and non-plegic compartments' data and the summed signals retrieved during the tachypnea trials (Trials 2). The MOD and ΔLOA are reported on each graph. In addition, MOD is represented with black solid lines, while ΔLOA is the span comprised between the two black.

MOD values are almost comparable in all compartments and summed signals in eupnea, while they present a higher value in the abdominal compartment in tachypnea. In both eupnea and tachypnea, ΔLOAs are always lower for the summed signals.

The mean absolute percentage error (MAPE) was also calculated to determine the error committed by the wearable system in evaluating RR as

$$MAPE_{RR} = \frac{1}{n}\sum_{i=1}^{n}\frac{\left|RR_i^{wearable} - RR_i^{MoCap}\right|}{RR_i^{MoCap}} \cdot 100 \quad (4.4)$$

where $RR_{ri}^{wearable}$ and RR_{ri}^{MoCap} are the RR calculated for the i-th breathing act from the wearable system and MoCap data, respectively, and *n* is the number of respiratory acts identified in each signal. The $MAPE_{RR}$ values related to all five analyzed signals are reported in Table 4.4 for every volunteer in eupnea (Trial 1) and tachypnea (Trial 2), and for all the volunteers together (considering the vectors in which the RR values of all subjects are concatenated).

Table 4.4. $MAPE_{RR}$ [%] values reported for every volunteer in eupnea (Trial 1) and tachypnea (Trial 2).

Trial 1—EUPNEA					
# Volunteer	$MAPE_{RR}$ [%] Thoracic	$MAPE_{RR}$ [%] Abdominal	$MAPE_{RR}$ [%] Plegic	$MAPE_{RR}$ [%] Non-Plegic	$MAPE_{RR}$ [%] Summed
1	1.51	1.93	0.86	2.57	1.60
2	1.78	0.72	1.91	1.28	1.15
3	1.47	0.78	0.62	2.79	1.08
4	0.69	0.69	0.79	0.37	0.52
5	2.03	1.58	1.87	1.11	1.08
6	0.73	3.45	1.46	1.35	1.34
7	1.07	2.66	6.09	5.23	1.52
All	1.32	1.77	1.81	2.08	1.22
Trial 2—TACHYPNEA					
# Volunteer	$MAPE_{RR}$ [%] Thoracic	$MAPE_{RR}$ [%] Abdominal	$MAPE_{RR}$ [%] Plegic	$MAPE_{RR}$ [%] Non-Plegic	$MAPE_{RR}$ [%] Summed
1	4.25	5.76	5.68	1.91	2.06
2	1.31	8.63	18.55	3.33	4.41
3	1.08	0.89	0.87	1.13	1.00
4	0.97	14.36	1.05	1.04	0.52
5	3.93	5.60	3.38	2.97	2.18
6	1.70	5.46	2.44	2.17	1.94
7	1.39	0.97	1.87	2.22	1.94
All	2.45	5.61	4.30	2.33	2.06

In eupnea (Trial 1), the maximum MAPE among all the volunteers is reported for the non-plegic compartment (i.e., 2.08%), with MAPE values for individual subjects ranging from 0.37% (volunteer 4, non-plegic compartment) to 6.09% (volunteer 7, plegic compartment). In tachypnea (Trial 2) a general slight increase in the MAPE values is observed and the maximum value among all the volunteers is obtained for the abdominal compartment (i.e., 5.61%). Peak values of 18.55% (volunteer 2, plegic compartment) and 14.36% (volunteer 4, abdominal compartment) were achieved in two individuals due to the poor quality of the retrieved breathing signals. Moreover, the best performance was given by the summed signal in both the eupnea and tachypnoea trials, presenting values of 1.22% and 2.06% for MAPE calculated on all the volunteers, respectively. Consequently, considering that the lowest MAPE overall and the ΔLOA

values retrieved from the Bland–Altman analysis were always obtained for the summed signals, it can be assumed that among the five proposed, the summed signals are the most suitable for RR estimation.

ii) Explorative Investigation on Respiratory Asynchronies between Compartments

Breathing discoordination between compartments due to rib cage muscle weakness can cause a phase shift between the related respiratory signals— that is, the more pronounced it is, the more severe the asynchrony [203]–[206]. The phase shift is commonly quantified by means of the phase angle (Φ) retrieved via the loop technique using Lissajous figures [211]–[213].

An explorative investigation via the loop technique was performed to assess the capability of the wearable system to detect the presence of phase shifts. The analysis was carried out comparing the respiratory signals of the thoracic and abdominal compartments, and plegic and non plegic-compartments, retrieved for different volunteers in the tachypnea trials. Referring to the comparison between the thoracic and abdominal compartments, the two best signals representing six consecutive and homogeneous respiratory acts were chosen among all the volunteers and were identified for volunteers 3 and 5. The signals were then plotted in time. In Figure 4.17 (a) (referring to volunteer 5), it is possible to observe that the signals are out-of-phase as the thoracic anticipates the abdominal one, while in Figure 4.17 (c) (referring to volunteer 3), the two signals are in-phase. The related Lissajous figures were obtained by plotting the two respiratory signals against each other (i.e., thoracic signal on the y-axis and abdominal signal on the x-axis). For each loop (which corresponds to a single respiratory act), the Φ_i was calculated as follows [211]:

$$\Phi_i = \sin^{-1}\left(\frac{m_i}{s_i}\right) \tag{4.5}$$

where m_i is the maximum distance of the i-th loop projection on the x-axis, while s_i is the distance of the loop projection on the x-axis at 50% of the thoracic signal. Φ was retrieved for each volunteer as the average value of all Φ_i.

Values of Φ = 11.2° (see Figure 4.18 (b)) and Φ = 2.7° (see Figure 4.17 (d)) were obtained for the first and second volunteers, respectively.

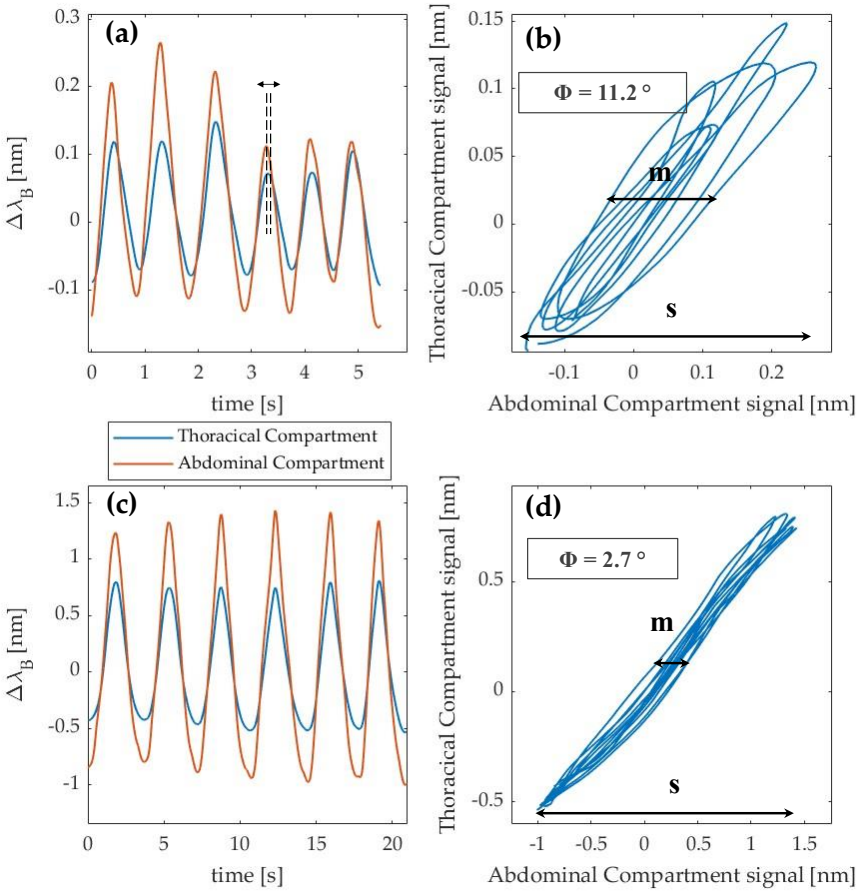

Figure 4.17. Phase shift analysis between thoracic and abdominal compartments. Plots of thoracic and abdominal compartments' signals in time for two different subjects are shown in (a,c). In (a), a phase shift is shown, while in (c), no significant shifts are visible. Lissajous figures of the out-of-phase (b) and in-phase (d) signals are reported, together with the related phase angle value.

The same analysis was performed for the plegic and non-plegic compartments, choosing the signals retrieved for volunteers 3 and 4. In Figure 4.18 (a) (referring to volunteer 3), out-of-phase signals are shown (i.e., the plegic precedes the non-plegic signal), while in Figure 4.18 (c) (referring to volunteer 4), in-phase signals are represented. Once again, Φ was calculated, obtaining Φ = 11.6° (see Figure 4.18 (b)) and Φ = 2.3° (see Figure 4.18 (d)).

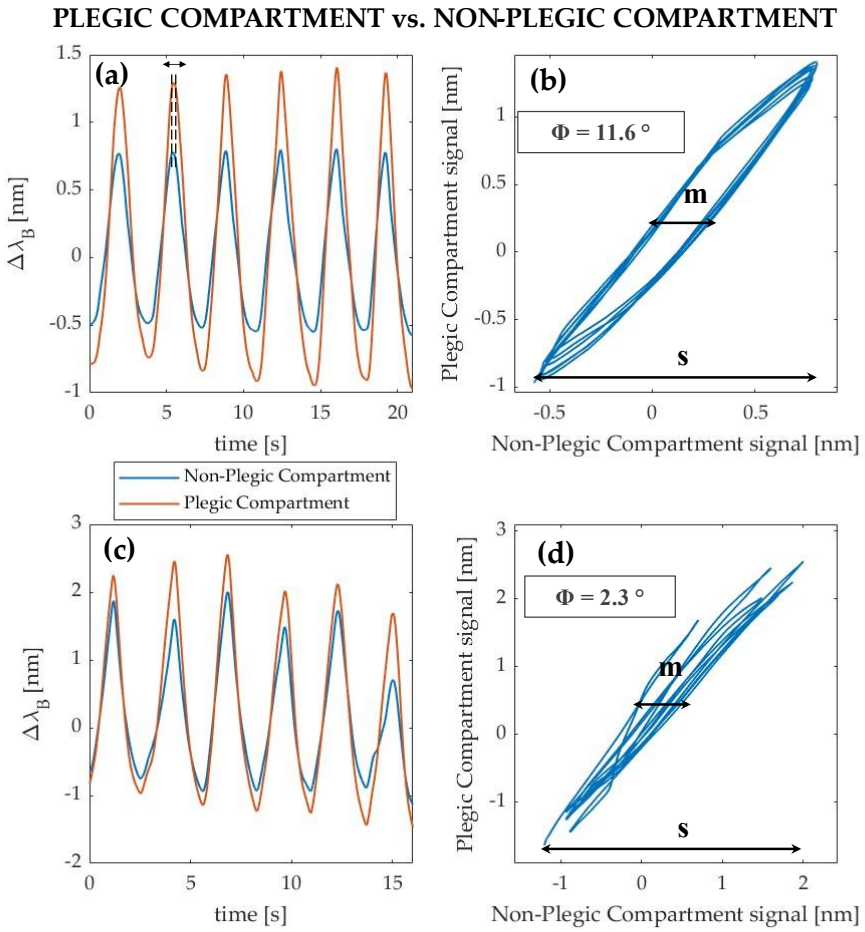

Figure 4.18. Phase shift analysis between plegic and nonplegic compartments. Plots of plegic and non-plegic compartments' signals in time for two different subjects are shown in (a,c). In (a), a phase shift is shown, while in (c), no significant shifts are visible. Lissajous figures of the out-of-phase (b) and in-phase (d) signals are reported, together with the related phase angle value.

1.1.4. Discussions

A wearable system composed of two elastic bands instrumented with four dumbbell-shaped flexible sensors based on FBG technology intended to be worn around the torso (at chest and abdomen level) was developed for RR monitoring via chest-wall displacements.

In terms of characteristics of the flexible sensors, the linear response to ε, with an S_ε of 0.08 nm·mε^{-1}, suggests a good bonding between the polymer matrix and the fiber optic. The low value of S_ε than the one of a bare FBG are related to the silicone-dampened effect in transmitting tension applied on the matrix surface into grating ε. Regarding the sensor response to ΔT, an S_T value slightly lower than the nominal one of a bare FBG (i.e., 0.008 nm·C^{-1} vs. 0.010 nm·C^{-1}). The influence of T during RR monitoring can be considered negligible as the dynamic of the phenomenon for three reasons: *i)*

the environments in which the experiments were carried out were temperature-controlled, so substantial temperature fluctuations occurred; *ii)* the sensing elements were attached to elastic bands fixed to the clothed subject, thus never in direct contact with the subject's skin, and *iii)* under these conditions, if ever a temperature change occurred, it would have a very slow dynamics compared to the dynamics of the respiratory act, so it would be eliminated via digital filtering. The $\%h_{err}$ values obtained from the dynamic response of the flexible sensor to applied repetitive ε at velocities mimicking RR values (i.e., 12 bpm, 24 bmp, and 36 bpm) are in all cases ≤ 15.9%. The $\%h_{err}$ values, albeit non negligible, are acceptable if compared to what present in the literature and considering the method applied to retrieve RR. Indeed, since RR is evaluated by assessing the time interval between one signal peak and the consecutive one, $\%h_{err}$ does not affect consistently the RR measurement. As consequence, the suitability of the proposed sensors for monitoring RR in eupnea, tachypnea and bradypnea respiratory conditions is guaranteed.

In the literature, some studies proposed FBGs housed into flexible matrices, but only a few works proposed the sensing element metrological characterization in terms of its static and dynamic responses. In [141]–[143], [146], [147] WDs consisting in elastic bands equipped with rectangular-shaped FBG flexible sensors for cardiorespiratory monitoring were proposed. Results showed values of S_ε and S_T comparable with the ones assessed for the dumbbell-shaped flexible sensor. Higher $\%h_{err}$ values in [146], suggest a higher energy dissipation in the rectangular-shaped flexible sensor than in the dumbbell-shaped one. This proves that the dumbbell shape allows a better adhesion of the sensing part to the elastic band, a well-anchorage of the sensors through the wider matrix ends, a well-compliance to the chest wall deformation and the optimization of the tensile strength concentration in the narrow portion of the flexible matrix.

The presented wearable system was assessed in occupational (by simulating both static and active working activities) and clinical scenarios, always showing good agreement with the reference instruments. The wearable was firstly assessed on ten healthy volunteers by simulating typical working conditions obtaining a maximum %E of 5% for a mean RR of 20 bpm (which correspond to about 1 bpm). In [147] a similar system was proposed and tested on archers for respiratory and cardiac monitoring. The performance of the flexible rectangular-shaped sensors in [147] is slightly higher than the ones of the wearable system proposed in this study (in the worst case, %E <1.97 % vs. 5%) but the scenario of interest is different as this precision sport requires stable chest maintenance and slow breathing. In contrast, the developed system was tested during more challenging working activities where breathing-unrelated movements occur and may affect its performances.

Regarding the wearable assessment in the static working scenario, results showed that the system was able to measure RR with lower error (maximum MAE = 0.52 bpm in eupnea, which is about 2.5% of %E) than the previous case. This was to be expected

given the less challenging conditions, but it is worth emphasizing that this result was achieved using only two of the four FSs. Also, although tested on only two subjects, this result is competitive with respect to other proposed systems. For instance, in [119], an FBG sensor has been embedded into a cushion positioned between the back of the person and an office chair to monitor the respiratory activity while sitting at a desk. The proposed device was compared to a reference instrument obtaining a maximum %E of 12%. Lastly, the device was assessed in a highly challenging scenario, i.e., on hemiplegic volunteers, always showing good results, such as MAPE errors for the summed signals of 2.06% and 1.22% in tachypnea and eupnea breathing, respectively, that are in line with what reported in the literature for RR evaluation. Errors detected in tachypnea are generally higher compared to those retrieved for eupnea, as tachypnea is a challenging respiratory condition for hemiplegic subjects, who may have used trunk compensatory movements to sustain the breathing effort, thus increasing the committed error. Moreover, the different severities of disability reported by the patients (evidenced by the different Fugl-Meyer indices) can explain the interindividual variability in the errors observed. However, the shown errors were always <6%, which can be comparable to those present in the literature.

Compared to the most popular and established technologies for respiratory monitoring in clinical settings which are represented by MoCap and flowmeters, the developed WD provides multiple advantages in terms of wearability, encumbrance, costs, and comfort. Considering in particular the last target population that the assessment focused on, the device presented a marked improvement in terms of fit and practicality also compared to smart T-shirts [126], [132]–[134]. Indeed, T-shirts can be difficult to wear among individuals with limited limb motility, such as people affected by hemiplegia. Additional concerns may occur as a single size could not be fit to all the anthropometries. Moreover, the particular cleaning process required to sanitize the garment without damaging the embedded sensors may represent an additional limit in T-shirts' usability. On the contrary, the proposed system, allows for easier dressing of the subject, while the modular anchorage system guarantees good fitting to any physicality. In addition, since the FSs are removable, the elastic bands can be cleaned following ordinary washing routines. Focusing on elastic bands, several devices designed to be worn around the chest and embedding a single sensor have been presented [137], [142], [146], [147]. Compared to these solutions, the presented system allows data acquisition in four areas of the torso, which is of prominent importance given the examined population. In fact, as is widely reported in the literature [203]–[206], hemiplegic subjects may develop paradoxical motion of the respiratory muscles, often resulting in breathing discoordination between compartments. As testified by the results obtained by the explorative investigation of breathing discoordination between compartments, such device could be a useful instrument to better understand the respiratory biomechanics of people affected by hemiplegia.

1.2. Wearable device instrumented with an FBG functionalized in agarose layer

This system comes as a wearable accessorize whose sensing part (composed by an FBG integrated into an agarose substrate) is intended to be positioned at the nostrils. This system can be used in working settings (as valid alternative to the system described in the previous section), but it is particularly suitable to be exploited during MRI exams, thanks to the absence of metallic parts and intrinsic electromagnetic compatibility of the FBG sensor. Moreover, its open design permits patients not to amplify feeling of claustrophobia and discomfort that a confined environment such as an MRI machine might cause.

In this section, parts of the work [214] which the PhD candidate has co-authored have been freely extracted.

1.2.1. Design and manufacturing process

The proposed WD is a measurement system for RR evaluation trough the ΔRH of the nasal airflow. To accomplish this task, the FBG was functionalized by using a hygroscopic material (i.e., 1 wt% agar) whose volume changes in accordance with the content of water vapor of the surrounding air. The design of the proposed WD was driven by requirements of comfortability, unobtrusively, and MR-compatibility. It consists of two parts: Block A which is the sensitive part, and Block B which is the supporting one (see Figure 4.19 (a)). The Block A should be placed below the nostrils and the PVB tube of Block B over the head and tightened by an adjustable piece at the back (see Figure 4.19 (b)). The Block A was fabricated as follows:

1) a commercial FBG sensor (λ_B of 1533 nm, grating length of 10 mm, At Grating Technologies) was encapsulated into a custom silicone brick (50 mm x 10 mm x 2 mm) made of Dragon SkinTM 20 (Smooth-On, USA), except for the grating (bare volumeof 15 mm x 3 mm x 1.5 mm). The silicone rubber was cured for four h at room temperature, as suggested by the technical bulletin;
2) 1 wt% solution of agar (commercialized by Sigma-Aldrich) was prepared by dissolving agar powder in distilled water at T $\sim$ 85 ◦C. Then, the 1 wt% agar solution was deposited on the grating and the drying process lasted 24 hours, at room temperature.

Regarding the Block B, two 3D-printed sliding covers of Polylactic acid (PLA) were used to connect the block A to a flexible polyvinylchloride (PVC) tube by a heat-shrink sheath made of Polyethylene (PE).

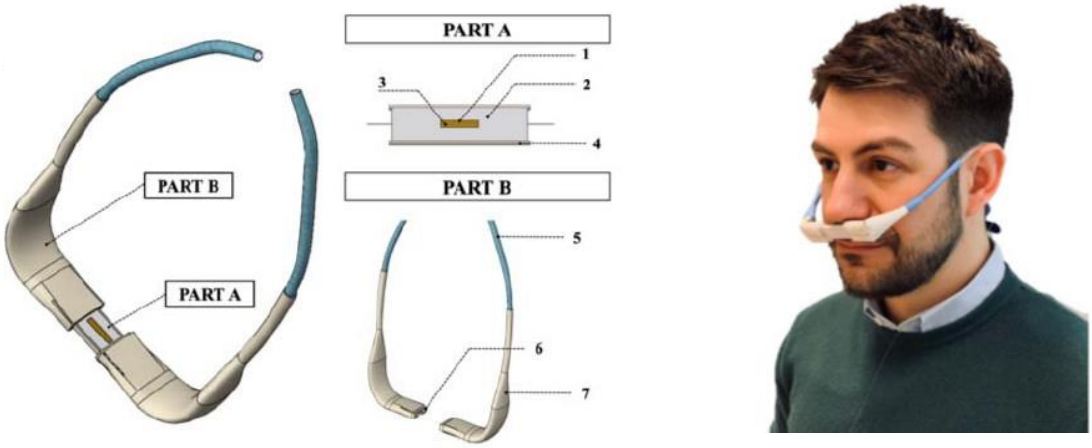

Figure 4.19. (a) The MR-compatible wearable device. The Block A shows the FBG (1), the agar-based matrix (2), the Dragon-Skin brick (3) and the PLA-based case (4). Block B shows the sliding covers (5), the heat-shrink sheath (6), and the flexible tube (7). (b) A photograph of the device worn by a user.

1.2.2. Metrological characterization

The sensitivity of the system to ΔRH (which is S_{RH}) and its step response were investigated.

1.2.2.1. Response to relative humidity variation

The static response of the system to ΔRH was investigated by positioning the Block A inside a custom-made climatic chamber. The RH in the chamber changed very slow in time so that sensor response can be considered as static. A capacitive RH sensor (HIH 4602A, Honeywell International Inc, USA, repeatability ± 0.5%) was used as reference instrument for the RH while a temperature probe (EL-USB-2-LCD. Temp & RH Data Logger, Easylog) for registering ΔT (and confirm the negligibility of ΔT during the test). The FBG output was collected by an optical sensing instrument (si255 based on HYPERION platform, Micron Optics, USA) at 100 Hz, the output of the RH reference system by data acquisition board (NI DAQ USB-6009, NI Instruments) at 100 Hz, and the ΔT values by the mentioned device at 1 Hz. The RH values inside the chamber ranged from RH∼10% to RH∼75%: the air was humidified by forcing the airflow inside the humidification chamber of a heated humidifier (MR850, Fisher & Paykel Healthcare) and dehumidified bypassing the humidifier and delivering dry airflow at 1 L·min^{-1} by a mass flow controller (EL-Flow, Bronkhorst High-Tech) directly within the climatic chamber.

The collected data (i.e., the FBG output and the reference RH sensor output) were synchronized over time and retrieved to obtain the $\Delta\lambda_B$ vs. ΔRH curve. The best-fitting line was calculated, and the S_{RH} value estimated as its slope (i.e., 0.016 nm·%$^{-1}$). Figure

4.20 (a) and (b) shows the trends of ΔRH and $\Delta\lambda_B$ vs. time, respectively, during the whole experiment that lasted approximately 15 min. Figure 4.20 (c) shows the response of the system ($\Delta\lambda_B$ vs. ΔRH) obtained after the synchronization of the two curves reported in 4.20 (a) and (b).

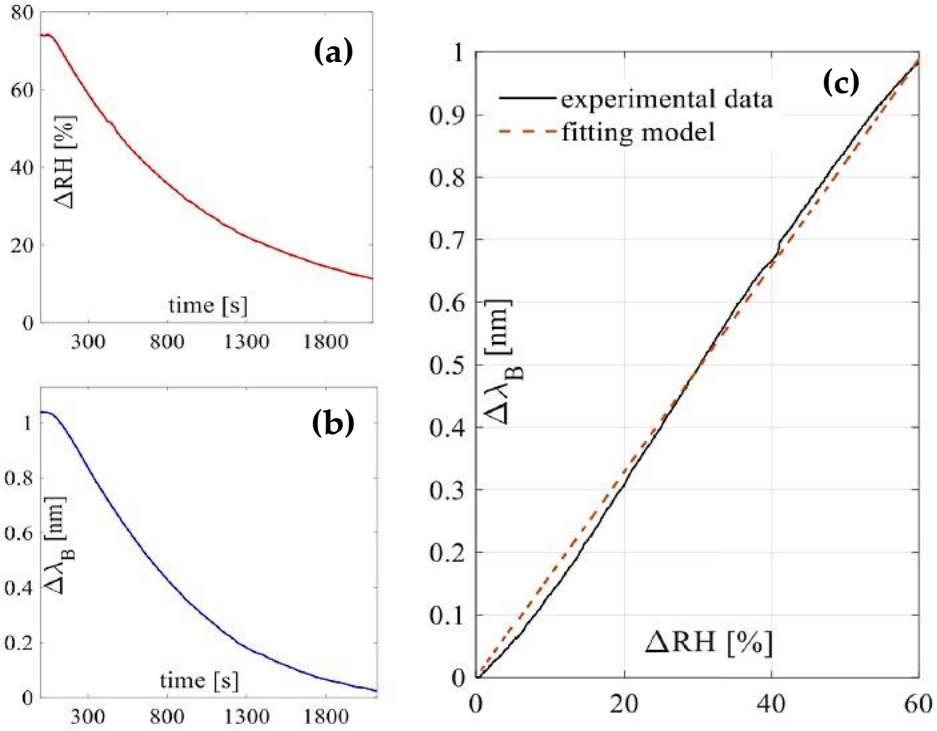

Figure 4.20. In (a) and (b) the ΔRH and $\Delta\lambda_B$ trends in time, respectively. In (c) the $\Delta\lambda_B$ vs. ΔRH curve with the best fitting line.

1.2.2.2. Step response

The same setup described in the previous subsection was used to investigate the step response of the system, and to estimate the response time; only the humidifier was removed. The step-change was applied by forcing dry airflow inside the climatic chamber and when RH value was < 10%, the chamber was quickly opened, and the sensor suddenly exposed to room conditions (RH∼50 % and T∼24 ◦C).

The output of both the proposed system (i.e., $\Delta\lambda_B$) and the reference sensor (ΔRH) vs. time are shown in Fig. 4.21 (a). Then, an exponential fitting was executed, taking into account that an FBG functionalized by a hygroscopic matrix can be modeled using as an infinitely long rod made of two bonded materials (i.e., the polymer coating and the fiber silica). The mass transfer inside the matrix, which coats the grating, can be modeled assuming the matrix made of two layers (i.e., the surface and the inner layers) with two different response times (i.e., τf and τs, where τf < τs) [215]. The step response of a functionalized FBG can thus be described as below by means of two exponential terms:

$$\Delta\lambda_B^{norm} = 1 - \left(wf \cdot e^{-\frac{t}{\tau f}} + wt \cdot e^{-\frac{t}{\tau s}}\right) \quad (4.6)$$

with $\Delta\lambda_B^{norm}$ the normalized $\Delta\lambda_B$, wf and wt the weights of the surface and the inner layers. The exponential fitting reported in Equation 4.6 using wt = wf = 0.5 was applied to the data of the proposed system to calculate the response time (see Figure 4.21 (b)). From this analysis τf and τs values (i.e., 44.4 s and 111.7 s, respectively) were obtained. To assess the response time of the system, a different approach was exploited based on the use of the error fraction of the system's output [216]. Using this approach, the value of the response time (τ_{63}) is 72.4 s.

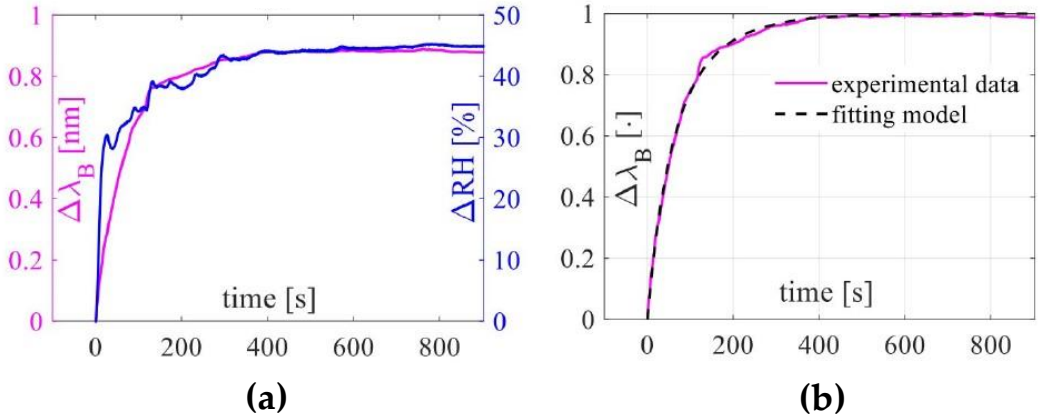

Figure 4.21. The response to the step changes. (a) ΔRH (blue line) and $\Delta\lambda_B$ (magenta line) over time. (b) the best fitting exponential model of the normalized $\Delta\lambda_B$ signal.

1.2.3. Experimental assessment

A pilot study was performed on six healthy volunteers to assess the feasibility of the WD for RR monitoring.

A) Experimental setup and protocol

An 8-cameras motion capture system (D-Smart, BTS Bioengineering S.p.A., Milan, Italy) was used to record reference respiratory waveforms. Six volunteers (3 males and 3 females, age 25-31 years, body mass 48-85 kg, and height 163-182 cm) were enrolled in the study. On the torso of each participant, 32 IR-photo-reflective spherical markers (with a diameter of 15 mm) were positioned according to the protocol reported in [209]. The MoCap records the trajectories of markers to indirectly estimate RR starting from the chest wall volume [217]. The sampling frequency was 60 Hz. Each participant was invited to sit and wear the custom WD. While wearing the device, each participant performed a single trial which consists of three main phases: *i)* 10 s of apnea followed by 30 s of slow breathing (sb); *ii)* 10 s of apnea followed by 30 s of normal breathing (nb) and *iii)* 10 s of apnea followed by 30 s of fast breathing (fb). During the protocol execution, a metronome was used to control the sb, nb, and fb.

The output of the FBG-based sensing element was recorded by an optical interrogator (si255 based on Hyperion platform, Micron Optics, USA) at 100 Hz. Figure 4.22 (top and bottom) shows the outputs collected on a volunteer using the WD and the MoCap system, respectively. After 10 s of apnea (reported using a black line in Figure 4.22), the phases of sb (green line), nb (blue line), and fb (red line) lasting 30 s are also clearly discriminated by both the proposed system and the reference one. Between each phase there are 10 s of apnea which can be identified by an interval of time where the systems' output is almost constant (shown in black line).

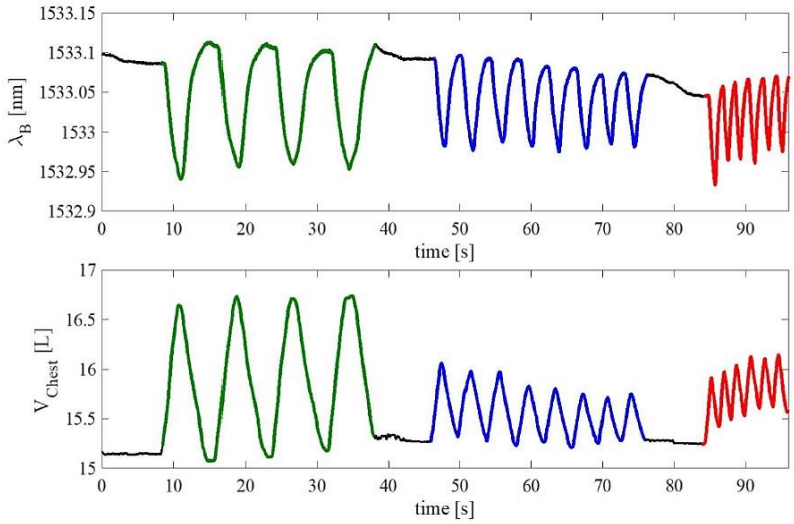

Figure 4.22. Results collected during the experiments on one of the volunteers: in the top image, output of the wearable system (λ_B) and in the bottom image output of the MoCap system (V_{Chest}). The green line is related to the sb stage, the blue one to nb stage, and the red one to the fb stage. In black, the apnea stages.

B) Data analysis and results

For each volunteer, the collected data were analyzed in MATLAB environment. Firstly, the data collected by both the WD and the reference one was split into three signals according to the breathing stages performed by each volunteer. A 3rd order Butterworth low pass filter was applied with 2 Hz of cut-off frequency for signals collected during sb and nb, and 5 Hz of cut-off frequency for the one related to fb. All the signals were then normalized between 0 and 1 and a custom algorithm, described in detail in [218] was used to perform the peak detection on the normalized signal. Since each maximum peak corresponds to the end of each inspiration, the time elapsed between consecutive peaks was calculated and considered equal to th-respiratory period, T_R. The breath-by-breath RR was estimated as $60/T_R$ (expressed in breaths per minute, bpm).

The agreement between the breath-by-breath RR values estimated by the WD and the ones by the reference system was evaluated considering all the three breathing

stages (nb, sb, and fb). Mean percentage error (MPE) and Bland-Altman analysis were performed. The MPE was calculated as follows and the values were reported in Table 4.5:

$$MPE\% = \frac{1}{n}\sum \frac{RR^{wearable} - RR^{MoCap}}{RR^{MoCap}} \cdot 100 \tag{4.7}$$

Table 4.5. MPE values.

	MPE [%]					
	Vol 1	**Vol 2**	**Vol 3**	**Vol 4**	**Vol 5**	**Vol 6**
sb	-0.48	-0.61	0.49	-1.06	-0.17	-2.29
nb	-0.06	0.01	0.15	0.05	0.22	0.27
fb	-0.17	-0.20	1.38	-0.39	-0.43	-1.55

Regarding the Bland Altman analysis, the LOAs and MOD were calculated, according to [210]. In Figure 4.23, the Bland-Altman plots for each breathing conditions are reported, together with the MODs and ΔLOAs values.

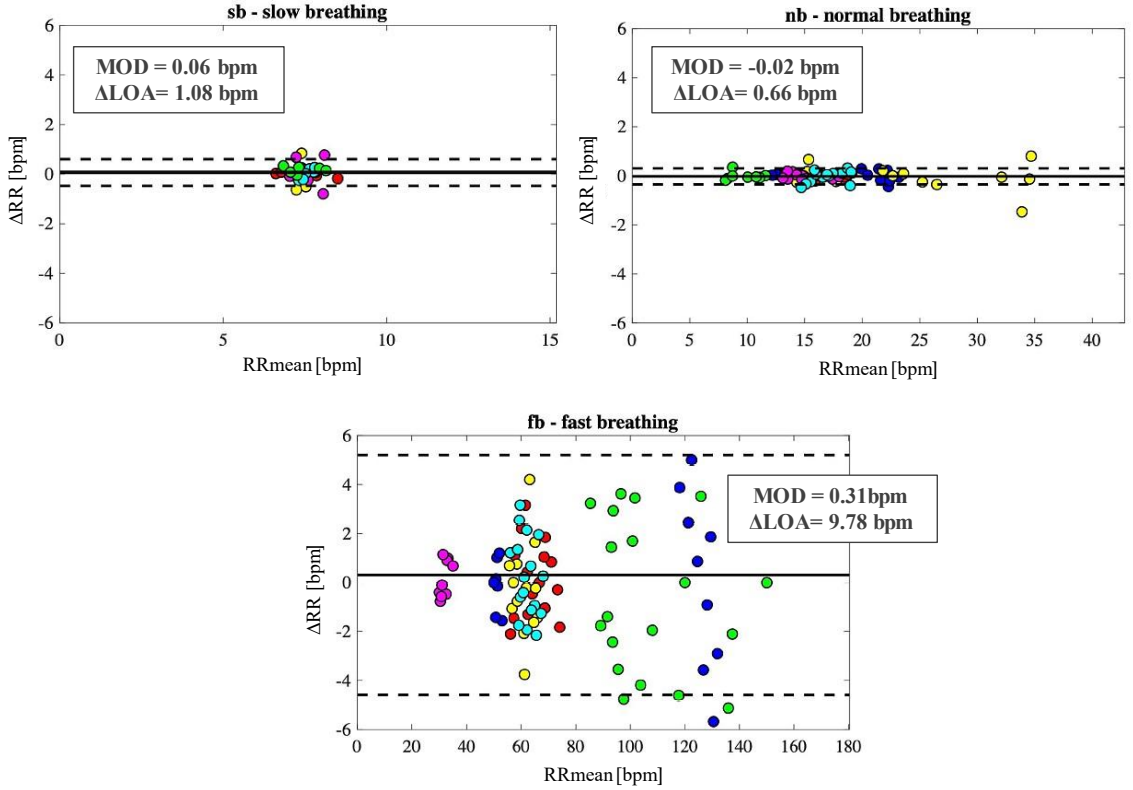

Figure 4.23. Bland-Altman plots related to sb breathing, nb breathing, and fb. Each color represents one volunteer. The continuous black line is the MOD while the dashed lines delimitated the LOAs interval. Also, the corresponding MODs and ΔLOAs values are reported.

1.2.4. Discussions

The unique design and the mechanical simplicity make the proposed wearable comfortable and unobtrusive for the user. Moreover, the use of polymer-based materials for the coating, the use of one FBG, and the absence of metallic parts make the device both biocompatible and MR-compatible. Results of metrological characterization showed an S_{RH} value of 0.016 nm·% $^{-1}$ and a τ_{63} value of 72.4 s. Results of the assessment test showed high performances in detecting RR.

Regarding wearable systems for RR monitoring based on FBG, only a few systems working on respiratory airflow have been reported. In [152], [153] a probe consisting of a metallic needle holding a FBG functionalized with agar reported a S_{RH} of 0.01 nm·% $^{-1}$ in the RH range from 25 % to 60 % and 0.006 nm·% $^{-1}$ in the RH range from 60% to 95%, and a τ_{63} of 90 s. Also, a percentage error < 2.07% [152] was observed and 2% of maximal MPE value for the assessment during mechanical ventilation at imposer frequency (i.e., 24 bpm) [153]. The solution proposed increases S_{RH} and improves τ_{63} with respect to [152], [153], also with better performances in RR estimation (maximum MPE 0.27% vs. 2.07%). Moreover, compared to the FBG-based sensing probe inserted into a surgical mask presented in [162], [163], the design of the proposed wearable enhance the acceptability of the user as results less invasive. In fact, facial masks may lead to intolerance, claustrophobia, and facial discomfort especially during long term monitoring. In [158] a system consisting of an FBG incapsulated into a nasal cannula reported during laboratory tests MPE < 5%, MOD values ranging from 0.048 bpm to 0.212 bpm, and LOAs maximum span of 4.617 bpm. Comparted with this, the presented wearable system showed better performance in the RR monitoring during nb, confirmed by both MPE values (≤0.27%) and Bland-Altman analysis (MOD values of -0.02 bpm and LOAs span of 0.66 bpm), with the added advantage of being less invasive as it does not require insertion into the nostrils.

2. FBG-based smart wearable solutions for trunk movements detection

FBGs are highly strain-sensitive with intrinsic fragility, so they have been mostly used for the detection of shallow motions (i.e., respiratory- and cardiac- related displacements) or limited joints excursion. In this paragraph, for the first time, three configurations of WDs integrating FBG sensing technology devoted to the detection of wide-range back movements are shown. All the proposed solutions involve embedding FBG sensors within polymer matrices to ensure robustness and durability of the sensing elements.

Focus is given to the evolution of the soft flexible sensors' design, as it led to the integration of the FBGs into silicone substrates of different shapes to maximize their performance and make the sensors resistant even when exposed to significant deformations. Also, the design process to make these wearables accepted to be used in several occupational and clinical contexts is described. In addition, the feasibility assessment of each wearable on a target experimental population related, once again, to both work and clinical settings is reported.

2.1. Smart T-shirt instrumented with two soft flexible patches

In this section, a preliminary analysis is described to verify the feasibility of two soft flexible sensors based on FBG technology applied on a commercial T-shirt to retrieve the wide movements of the back. In particular, the assessment of the smart T-shirt in detecting flexion and extension (F/E) dorsal back movements was carried out.

In this section, parts of the work [219] which the PhD candidate has co-authored have been freely extracted.

2.1.1. Design and manufacturing process

The proposed smart T-shirt, as shown in Figure 4.24 (a), is a tight elastic T-shirt equipped with two custom flexible patches, each containing a saleable FBG sensor (λ_B values of 1545nm and 1541 nm, grating lengths of 10 mm, and reflectivity of 90% AtGrating Technologies, China). The aforementioned patches are made of silicone rubber (i.e., Dragon Skin 20, Smooth On, Inc. USA) and rectangular- shaped with dimensions of 90 mm x 24 mm x 1 mm. These polymeric matrices incapsulate the gratings improving their flexibility and robustness.

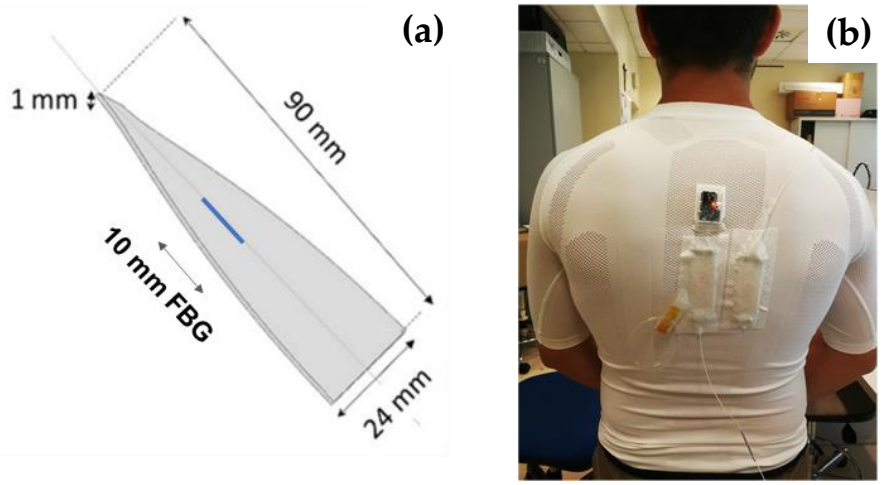

Figure 4.24. The sensing elements and the wearable system. (a) Geometrical features and dimensions of the rectangular-shaped silicone patches embedding the FBGs; (b) The two patches fixed upon the elastic t-shirt.

The manufacturing process of the flexible patches consists of the main steps reported below:

1) Two rectangular-shaped plastic molds, whose dimensions are 90 mm x 24 mm x 1 mm, were created with Onshape® design software and realized by the 3D printing process [30] ('Ultimaker 2+', Ultimaker B.V., Utrecht, The Netherlands);
2) The FBG were placed at the midsection of the custom-made plastic molds. The extremities of the optical fiber were then passed inside the lateral grooves and delicately fixed with the help of some adhesive tape in order to keep the fiber adequately tight;
3) Dragon SkinTM20 silicone rubber parts A and B were mixed 1A:1B by volume ratio (as indicated in the technical bulletin). Then, an amount of 10% in volume of liquid thinner was added to reduce the viscosity of the compound. The mixture was well stirred in order to allow the complete blending of all the components;
4) The compound was put into a vacuum chamber and let degas for few minutes in order to obtain an opalescent fluid with no presence of gas bubbles;
5) The degassed mixture was slowly poured into the molds until their full filling;
6) The mixture was let polymerize for a curing time of four hours at room temperature;
7) Once solidified, the flexible rectangular-shaped (i.e., 90 mm x 24 mm x 1 mm) flexible patches were extracted from the molds. The excess of polymeric material was removed by mean of a cutter and the edges were refined.

A representation of the fabrication process is given in Figure 4.25.

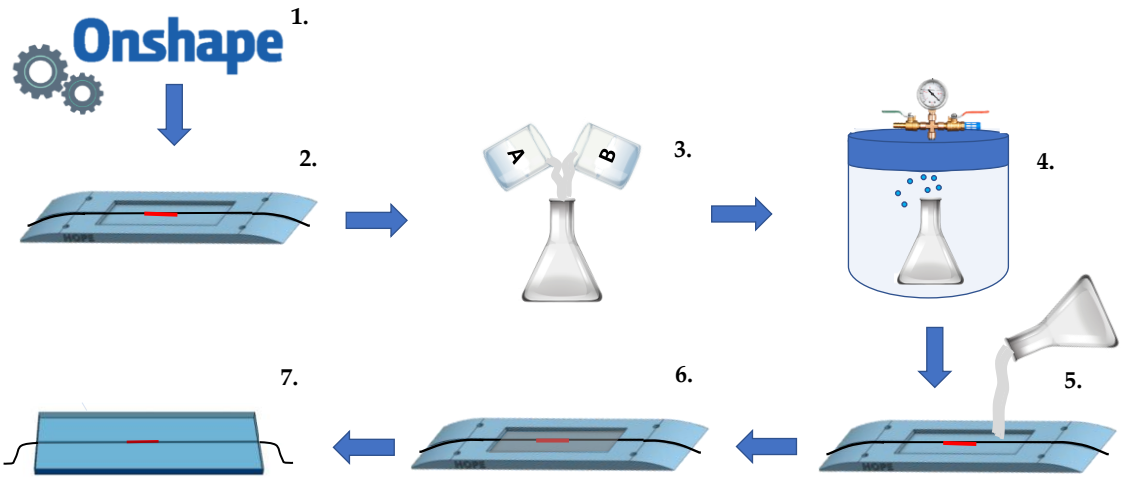

Figure 4.25. Main steps of the manufacturing process of the two flexible patches embedding an FBG sensor.

2.1.2. Metrological characterization

As the flexible patches are placed on the T-shirt in correspondence of the back, they undergo deformation during trunk movements of flexion and extension. As consequence, the S_ε of the FBGs-based patch was evaluated and described in the following section.

2.1.2.1. Response to strain

The response of the sensing element to strain was assessed by fixing the silicone patch between the tongs of the machine at room temperature. Strains starting from 0% up to 2% in length (i.e., the maximum strain - $\varepsilon\%_{max}$) were applied at a load speed of 3mm· min^{-1} to simulate quasi-static tensile conditions. This trial was performed four times to assess its repeatability. The FBG output was recorded by an optical interrogator (si425, Micro Optics Inc. USA) at the sampling frequency of 250 Hz. The strain and force values applied to the silicone patches by the traction machine were collected at the sampling frequency of 10 Hz.

The collected data were analyzed in MATLAB environment. The trends of both ε and $\Delta\lambda_B$ over time are shown In Figure 4.26 (a) and (b), respectively. The calibration curve ($\Delta\lambda_B$ vs. ε) was obtained as the best fitting line considering the average value of $\Delta\lambda_B$ calculated across the four tests vs. ε. The related uncertainty was estimated by multiplying the standard uncertainty with a coverage factor (k=3.1824) obtained considering a t-student distribution with three degrees of freedom and a confidence level of 95%. Results showed a S_ε value of about 0.10 nm·mε^{-1} (see Figure 4.26 (c)). The

agreement between the proposed linear model and the experimental data was confirmed by the high values of the obtained correlation coefficient (i.e., $R^2 > 0.99$).

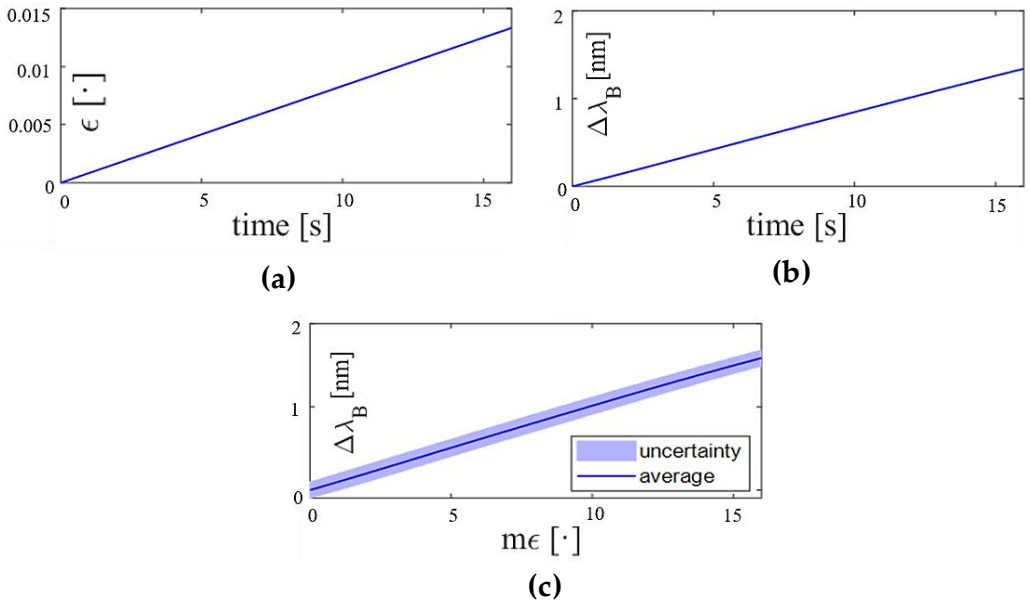

Figure 4.26. (a) Trend in time of ε, (b) Trend in time of $\Delta\lambda_B$ and (c) the best fitting line of the calibration curve obtained considering the average value of $\Delta\lambda_B$ vs. ε (blue line) and the uncertainty (purple shadow).

2.1.3. Experimental assessment

The assessment of the smart T-shirt was carried out on six healthy volunteers to verify its capability to detect F/E movements of the back.

A) Experimental setup and protocol

Six volunteers (three males and three females), whose anthropometric features are 173.67 cm ± 2.61 cm height, 69 kg ± 5.65 kg body mass and 96.34 cm ± 3.27 cm chest circumference, were enrolled in the study. Each volunteer wore the T-shirt, and the two flexible patches were fixed in the central zone of the dorsal part of the back (between the thoracic vertebrae T5 and T9) with a skin-friendly polyacrylate tape (i.e., 100% polyester, Curafix® H, Lohmann & Rauscher, Switzerland). One patch was positioned above the spine while the second one at about 1cm to the right of the vertebral column. Both the patches were adherent to the t-shirt textile and compliant with the dorsal curvature. A MIMU system (SensorTile STEVAL STLKT01V1) was also fixed upon the shirt to acquire reference position data related to F/E movements in the sagittal body plane, at the sampling frequency of 100 Hz. An optical spectrum interrogator (si255, Micro Optics Inc. USA) was used to simultaneously collect the output of the two FBG-based patches at the sampling frequency of 1 kHz.

Each subject was asked to perform two trials of four consecutive dorsal flexions and four consecutive extensions. A 15 s-lasting stasis was performed between each trial. A representation of the protocol is shown in Figure 4.27. Afterwards, the positions of the two patches were inverted and each volunteer was asked to perform the same protocol again. An overall of 16 repetitions was carried out by every volunteer.

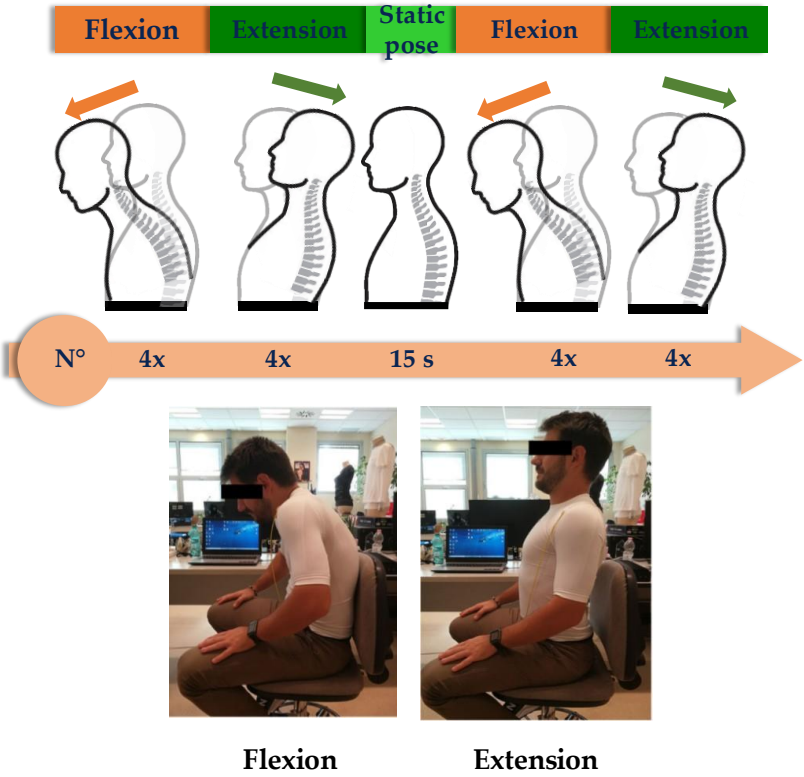

Figure 4.27. Representation of the experimental trial (upper image) and flexion and extension movements performed by the volunteers (bottom image).

B) Data analysis and results

The collected data were analyzed in MATLAB environment. For each trial, the signals output of both the FBGs and the MIMU system were synchronized, normalized, and plotted over time. The output changes related to flexions and extensions for each volunteer were distinguished and identified with orange and green rectangles, respectively (see Figure 2.28). A good match between the signal trends in time estimated by the FBGs and the reference instrument was found.

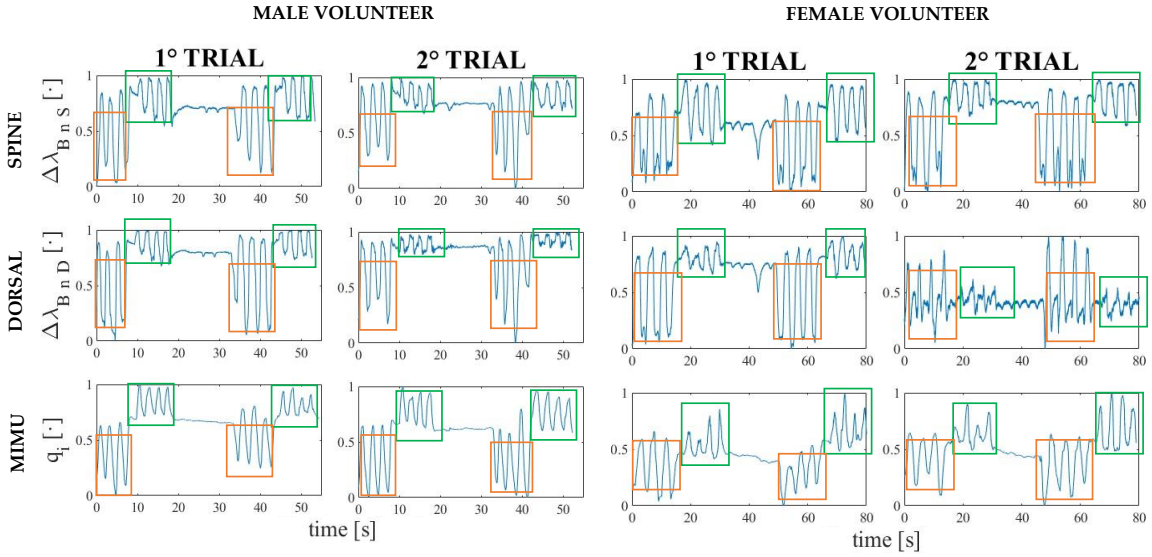

Figure 4.28. Example of an experimental dataset collected for a male (on the left) and a female (on the right) volunteer. In the first column the outputs of the two FBGs (reported in $\Delta\lambda_{B\,n\,S}$ and $\Delta\lambda_{B\,n\,D}$, for the one positioned on the spine and the one on the dorsal right area, respectively) and the MIMU (expressed as q_i) related to the first trial are shown. In the second column the outputs related to the second trial are shown. In the orange and green rectangles, flexions and extensions are highlighted respectively.

2.1.4. Discussions

In the literature, only few studies investigated the use of fiber optic-based wearables for detecting back dorsal F/E movements [220]–[222]. In all these works, no FBG-based smart textiles have been devised to detect dorsal F/E. In this study, a first attempt was made to investigate if such technology, strengthened by integration into polymeric matrices, would be a suitable option to detect such a wide range of motion.

Taking inspiration from what already present in the literature for the monitoring of different joint movements [189]–[192], [194], a polymeric matrix with rectangular shape (dimensions of 90 mm x 24 mm x 1 mm) was chosen to integrate the FBG. Two flexible patches were obtained, with linear response to strain (as testified by the $R^2 < 0.99$) and good strain sensitivity (i.e., S_ε=0.10 nm ·mε^{-1}). The high value of S_ε suggests a tight adhesion of the gratings into the silicone substrate that ensures a good transmission of the strain applied on the silicone surface to the sensing elements.

The sensorized patches were fixed above a commercial T-shirt on specific points of the dorsal area (i.e., over the spine and 1 cm on the right of the spine) making the proposed system easy to wear, comfortable, compliant with the natural spine curvatures and adaptable to any type of body-shape (prior use of a suitable T-shirt size) if compared to the solution proposed in [220]–[222]. Results of tests performed on the healthy volunteers showed that all the FBGs trends in time agree with the trend of the reference, with no data loss or patch breakage caused by excessive stress. This proven

that the insertion of FBGs within flexible matrices is a winning strategy to adopt to monitor even wide-range movements such as back F/E. This awareness guided the design and development of the WDs described in the following sections.

2.2. Elastic wearable system equipped with a rectangular-shaped soft flexible sensing element

Building on the knowledge gained in the preliminary assessment reported in Section 2.1, a novel wearable system was developed which could fulfill the following aims: *i)* to be easily worn by the user, also upon ordinary clothes; *ii)* to strengthen the sensing element. Consequently, as elastic structure to be anchored to the user's garments was realized. The sensing element was retained in the rectangular shape but, compared to the two patches, was reduced in size and thickened to stiffen a bit more the FBG sensing part. In addition, the soft sensor is intended to be applied to the wearable structure instead of being directly attached to the T-shirt, in order to dissipate a part of the mechanical strain provoked by F/E motions. This system is meant to distinguish flexion-extension back movements to assess the right sitting posture in sedentary videoterminal workers.

In this section, parts of the works [223], [224] which the PhD candidate has co-authored have been freely extracted.

2.2.1. Design and manufacturing process

The proposed WD consists of two parts: a flexible FBG-based sensitive element and an elastic wearable structure. An image of the wearable system is shown in Figure 4.29 (upper image).

The elastic wearable structure is a wearable support composed by two elastic bands stitched orthogonally together by hand. The first band was designed to be worn on the worker's right shoulder and solidly anchored at the subject's garments by means of two clips. The second band works like an elastic belt that, once secured with some Velcro® stripes around the subject's waist, ensures the adherence of the system to the back. The system is adjustable in length, so that it can be worn by subjects with di different anthropometric characteristics.

The flexible sensing element was produced by encapsulating a commercial optical fiber embedding an FBG (grating length of 10 mm, λ_B of 1556.97 nm and reflectivity of 90%; AtGrating Technologies, China) into a silicone substrate (Dragon SkinTM20, Smooth-On, Inc., Macungie, PA, USA) whose dimensions are 55 mm x 20 mm x 2 mm. The production method is the same as described in the previous Section 2.2.1. The

silicone rubber constitutes a highly flexible and stretchable support base that improves the FBG in robustness avoiding breakages. The high flexibility of the sensor is exhibited in Figure 4.29 (bottom image) where the twisting, bending, folding and stretching capabilities of the element are shown.

The flexible sensing element is fixed upon the back part of the structure (where the two elastic bands cross) with a double-sided adhesive tape for fabrics to be compliant with the physiological lumbar curvature.

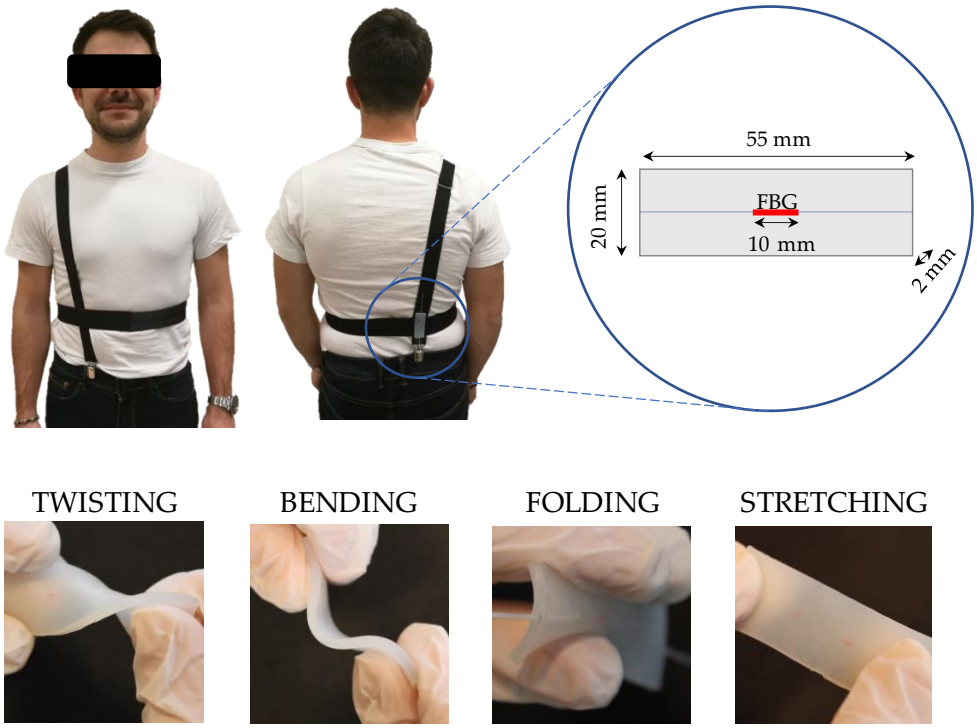

Figure 4.29. The device worn by a volunteer with a magnification on the flexible sensing elements presenting is features is shown in the upper image. In the bottom images, the flexible element in twisting, bending, folding and stretching configurations.

2.2.2. Metrological characterization

The flexible sensing element undergoes elongation/compression when F/E movements occur. Indeed, the response of the sensing element to strain was investigated and reported in the subsection below.

2.2.2.1. Response to strain

A set up constituted by a fiber optic interrogator (Micron Optics si255, Micron Optics Inc., Atlanta, GA, USA) and a tensile testing machine (Instron 3365A, Instron, Norwood, MA, USA) was used to estimate the response to strain of the flexible sensor. A tensile test was performed on the flexible sensor at room temperature and quasi-static conditions (i.e., low load speed). The flexible element was lengthened at 2 $mm \cdot min^{-1}$ of

load speed, by 2% with respect to its initial length. The output data given by the tensile machine (i.e., ε, time, applied force and elongation) were collected by a personal computer at a sampling frequency of 10 Hz, whereas the FBG output data were collected by the fiber optic interrogator at a sampling frequency of 100 Hz. The whole process was executed 10 times in order to evaluate the repeatability of the response. All the data were exported and analyzed in MATLAB (MathWorks® Inc., Natick, MA, USA) environment. The calibration curve (represented with its expanded uncertainty in Figure 4.30 (a)) was calculated as the best fitting line considering the average value of $\Delta\lambda_B$ obtained across the ten trials over ε (Figure 4.30 (b)). Considering a t-student distribution with nine degrees of freedom and 95% of confidence level, it was possible to evaluate the expanded uncertainty as the product of the standard uncertainty and the coverage factor k (i.e., 2.262). The high repeatability of the system was assessed and confirmed by the slight value of the expanded uncertainty. Furthermore, the S_ε = 0.20 nm·mε^{-1}, was calculated as the slope of the calibration curve. The correlation coefficient (R^2) was then evaluated. Its high value (i.e., >0.99) confirms that the behavior of the experimental data agrees properly with the linear model.

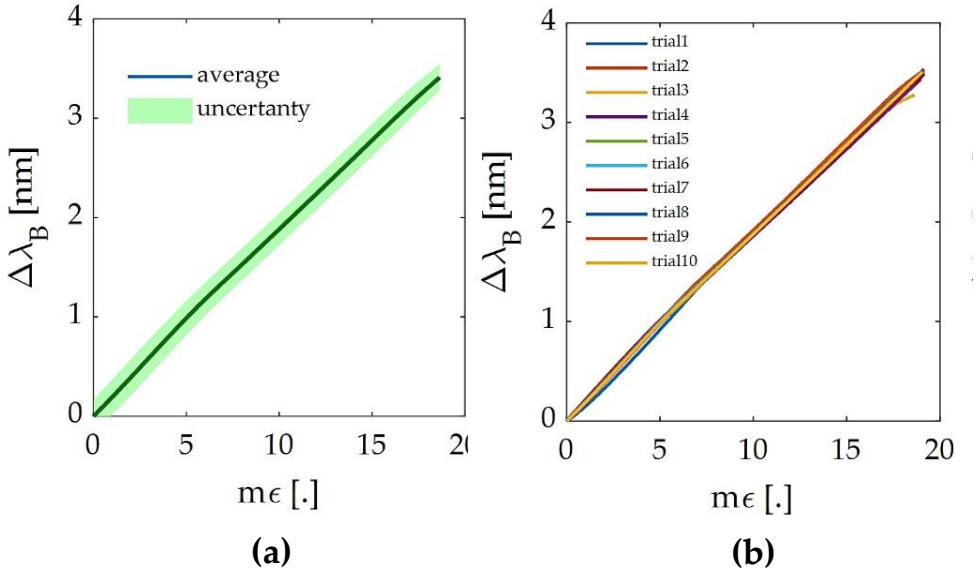

Figure 4.30. Response to strain of the sensing element. (a) Trend of the calibration curve (blue curve) and its uncertainty (green shadow). (b) $\Delta\lambda_B$ vs. ε obtained across the ten trials.

2.2.3. Experimental assessment

Experimental trials were carried out on a group of volunteers to investigate the ability of the proposed WD to monitor the low back F/E movements.

A) Experimental setup and protocol

Four healthy volunteers (two males and two females) with no history of back disorders were enrolled. The main population characteristics, expressed as mean ± standard deviation, are: age of 28.4 ± 0.5 y.o., height of 175.2 cm ± 4.4 cm, body mass 67 kg ± 11.7 kg, and chest circumference 94.4 cm ± 9.5 cm. Each subject wore the elastic structure over a tight T-shirt and was invited to sit on a stool placed at the center of the four-camera MoCap recording area (about 3 m^3 of calibrated volume) and maintain a straight posture. In line with the protocol proposed in [225] by Chockalingam et al., 11 photo-reflective passive markers with a diameter of 18 mm were positioned on specific body landmarks (i.e., C7, T1, T4, T7, T10, L1, L3, L4, L5, right and left shoulder) by means of a bi-adhesive tape (see Figure 4.32 (a)). The FBG-based flexible sensor was then fixed with bi-adhesive tape for textiles upon the elastic wearable structure, in correspondence with the lumbar area between the subject's L1 and L5 lumbar vertebrae, as shown in Figure 4.31 (a).

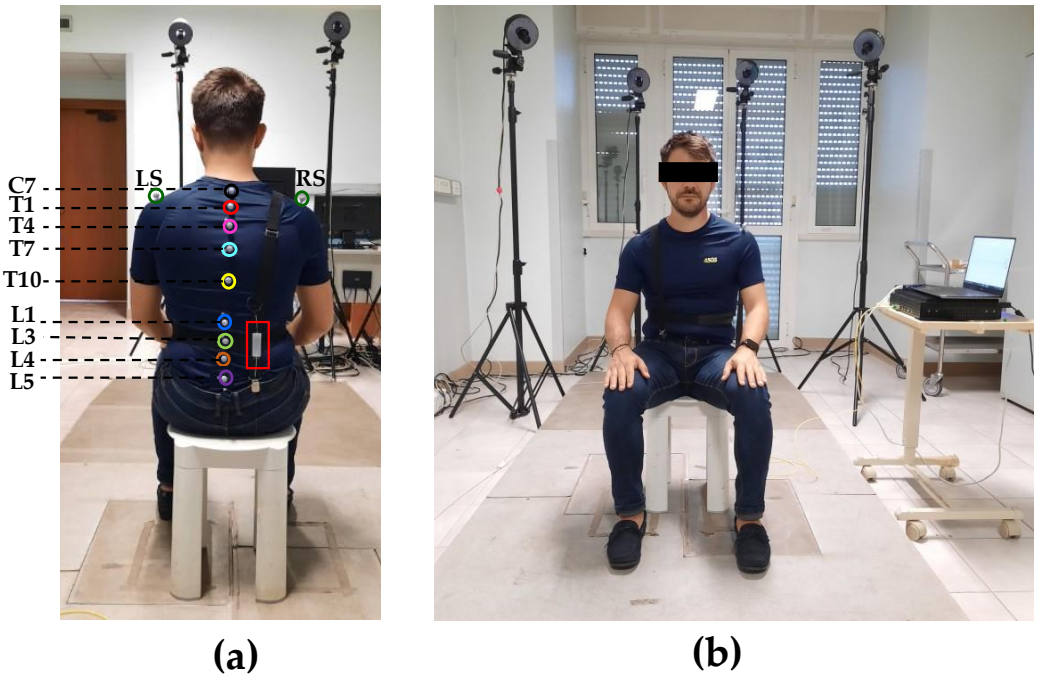

Figure 4.31. Experimental set up. (a). Back view showing the posterior part of the wearable device and the positioning of the flexible sensor (red rectangle) and the photo-reflective markers; (b). Frontal view showing the anterior part of the wearable device, the MoCap cameras, the optical interrogator and the laptop.

The volunteer was instructed to follow the protocol that consisted in executing four consecutive back flexions followed by four consecutive extensions, for two time and for an overall of 16 F/E movements per trial. Each volunteer repeated the protocol twice; a total amount of 8 trials was collected. During the trials, the outputs of both the wearable

system and the MoCap system were acquired. An optical spectrum interrogator (si255, Micron Optics Inc., Atlanta, GA, USA) was used to collect the FBG outputs at a sampling rate of 100 Hz, while the positions in time of the photo-reflective markers were collected by the MoCap at the sampling frequency of 60 Hz and processed with a dedicated software (i.e., OEP-Smart, BTS Bioengineering Corp., Milan, Italy) to obtain the trajectories of the F/E movements. The entire experimental set-up is shown in Figure 4.31 (b).

B) Data analysis and results

Per each trial, from markers' trajectories the distance between markers L1 and L3 ($d_{L3\text{-}L1}$, see Figure 4.32) was calculated as in the following formula:

$$d_{L3-L1} = \sqrt{((x_{L3} - x_{L1})^2 + (y_{L3} - y_{L1})^2)} \quad (4.8)$$

where x_{L3} and x_{L1} are the x-axis coordinates of L3 and L1, respectively and y_{L3} and y_{L1} the y-axis coordinates. The $\Delta d_{L3\text{-}L1}$ was then calculated as

$$\Delta d_{L3-L1} = d_{L3-L1} - d_{L3-L1}|_{t=0} \quad (4.9)$$

This value allowed to quantify the relative distance between L1 and L3 (expressed in cm) during F/E movements.

Considering one trial, the first maximum peaks recognized both on the $\Delta\lambda_B$ and on the $\Delta d_{L3\text{-}L1}$ signals were used to synchronize the WD and the MoCap. Then, the $\Delta\lambda_B$ and $\Delta d_{L3\text{-}L1}$ data recorded during the first flexion movement were used to calibrate the WD output for reconstructing the L1-L3 displacements from $\Delta\lambda_B$ (to obtain $\Delta d_{\Delta\lambda}$).

Since the linear relationship between the ε and the $\Delta\lambda_B$ (see Figure 4.30), a least-squares linear regression was carried out to accomplish this task, considering the $\Delta d_{L3\text{-}L1}$ as predictor variables and $\Delta\lambda_B$ as response variables as in Equation (4.10),

$$y = \alpha + \beta x + \zeta \quad (4.10)$$

where α is the y-intercept (fixed at 0), β the slope (or regression coefficient), and ζ the error term. To quantify the goodness of regression, the coefficient of determination (R^2) was calculated. The obtained calibration coefficient β was then applied to the whole signal $\Delta\lambda_B$ to obtain $\Delta d_{\Delta\lambda B}$ signal as in the following equation:

$$\Delta d_{\Delta\lambda B} = \beta\, \Delta\lambda_B \quad (4.11)$$

To quantify the difference between the distance $\Delta d_{L3\text{-}L1}$ and the reconstructed distance $\Delta d_{\Delta\lambda B}$ the MAE ($MAE_{\Delta d}$) coefficient was calculated as in the following equation:

$$MAE_{\Delta d} = \frac{\sum_{i=1}^{N} \left| \Delta d_{\Delta\lambda_B} - \Delta d_{L3-L1} \right|}{N} \quad (4.12)$$

Additionally, the lumbar angle (θ) was calculated considering the trajectories of L1, L3 and L4 as shown in Figure 4.32. In particular, θ was obtained as the angle among two vectors ($\overrightarrow{L1L3}$ and $\overrightarrow{L3L4}$) at each instant:

$$\theta = \cos^{-1}\left(\frac{\overrightarrow{L1L3} \cdot \overrightarrow{L3L4}}{\left\|\overrightarrow{L1L3}\right\| \cdot \left\|\overrightarrow{L3L4}\right\|}\right) \quad (4.13)$$

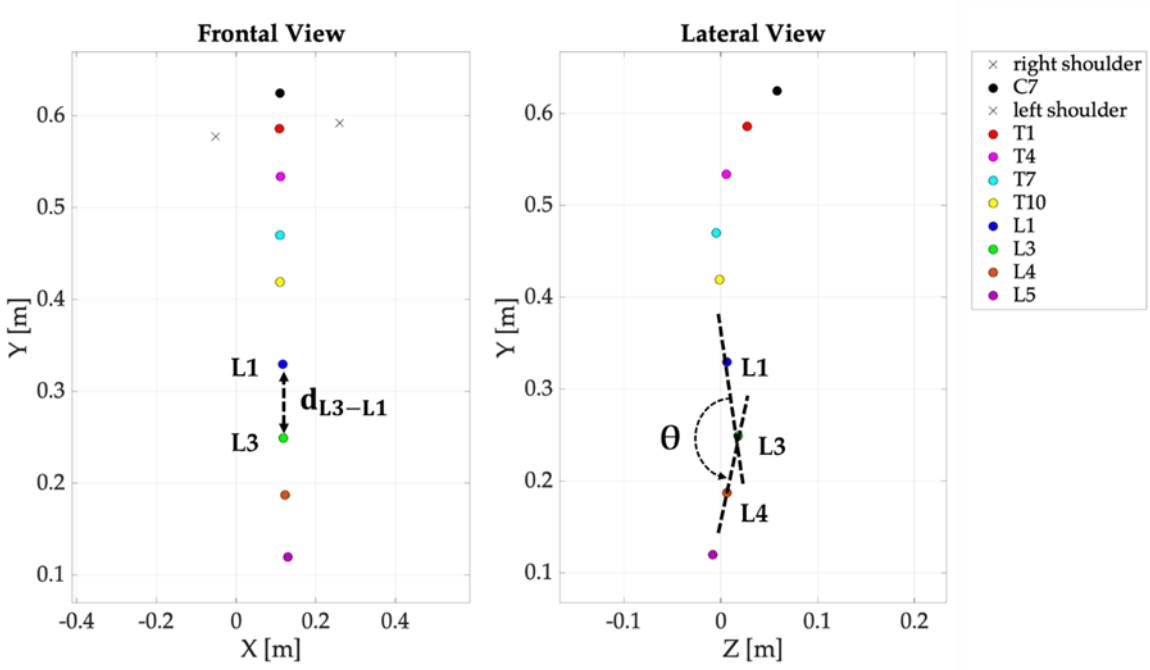

Figure 4.32. The distance d_{L3-L1} (left image) and the lumbar angle ϑ (right image) retrieved from markers' trajectories.

In Figure 4.33 the trends in time of the wearable output ($\Delta\lambda_B$), the distance between L1 and L3 ($\Delta d_{L3\text{-}L1}$), and the lumbar angle (θ) evaluated for each trial are reported. It is possible to observe that the FBG and the reference system outputs show great agreement. Eight flexions (i.e., the signal peaks) and extensions (i.e., the signal valleys) can be counted, with a total amount of 16 F/E movements for each trial, as expected. The widest $\Delta\lambda_B$ excursion that occurs during the trials is about 2 nm. Table 4.6 summarizes the β regression and the R^2 coefficients related to the regression procedures.

Table 4.6. Calibration coefficient β used to reconstruct $\Delta d_{\Delta\lambda B}$ from $\Delta\lambda_B$, R^2 coefficients resulting from the linear regression between $\Delta d_{L3\text{-}L1}$ and $\Delta\lambda_B$ and $MAE_{\Delta d}$ values used to quantify the difference between the distance Δd_{L3-L1} and the reconstructed distance $\Delta d\ \Delta\lambda_B$.

Trial	#1	#2	#3	#4	#5	#6	#7	#8
β [cm·nm^{-1}]	1.38	2.10	2.78	1.08	1.43	0.32	1.45	1.84
R^2	0.92	0.78	0.89	0.66	0.91	0.93	0.88	0.88
$MAE_{\Delta d}$ [cm]	0.33	0.18	0.21	0.14	0.14	0.07	0.28	0.29

As shown in the table, the β differs trial by trial from 0.32 cm·nm^{-1} to 2.78 cm·nm^{-1}; all the R^2 values denote moderate to good quality of regression. Also, Table 4.6 reports the range of $\Delta d_{L3\text{-}L1}$ calculated from data recorded by the MoCap together with the $MAE_{\Delta d}$. The maximum value of $MAE_{\Delta d}$ was 0.33 cm (about 16% on the $\Delta d_{L3\text{-}L1}$ amplitude of 2.02 cm).

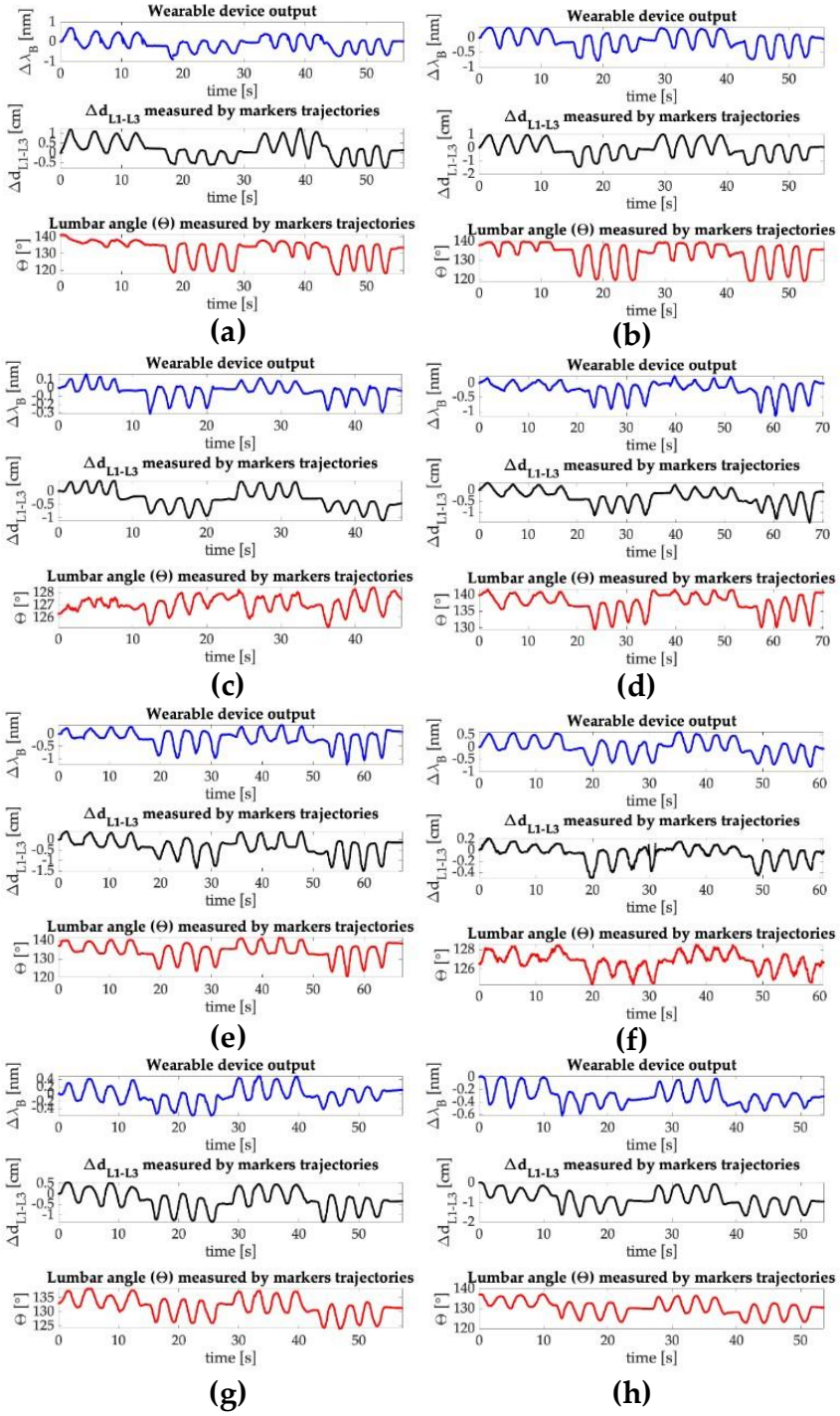

Figure 4.33. The wearable output ($\Delta\lambda_B$), the distance between L1 and L3 (Δd_{L3-L1}) and the lumbar angle (ϑ) trends obtained per each trial. (a): Trial 1; (b): Trial 2; (c): Trial 3; (d): Trial 4; (e): Trial 5; (f): Trial 6; (g): Trial 7; (h): Trial 8.

2.2.4. Discussions

The presented device is composed by a custom-made comfortable elastic structure and a flexible sensing element made of a commercial FBG housed into a rectangular-shaped silicone matrix. The flexible element response to strain was assessed showing S_ε=0.20 nm· mε^{-1} (which is comparable to the $S_\varepsilon$of the soft sensing elements devoted to joint motion detection present in the literature [189], [191], [192], [194]). Then, the feasibility assessment of the WD in measuring F/E in the sagittal body plane was experimentally executed on a small population of volunteers, in presence of the MoCap. Good accordance between FBG and MoCap trends were retrieved, and F/E movements are clearly distinguishable. $MAE_{\Delta d}$ were calculated and quite wide ranges of values were observed (i.e., ranging from 0.07 cm to 0.33 cm), which can be attributable to the sliding of the photoreflective markers and the wearable from their initial placement while performing the experimental routines. In fact, although arrangements were made to maintain as much as possible the initial positioning of the setup (e.g., the shirt was tight and fixed by the elastic structure of the wearable, while the wearable was firmly hooked to the user's pants) and the range of motion of the performed movements was not wide, nevertheless, an inherent error caused by the slippage of the setup from the initial position cannot be excluded. Also, the intra and inter subject variability of the sensor positioning could cause the low value of R^2 obtained for the 4th volunteer (i.e., 0.66) the wide dispersion of the β values (i.e., from 0.32 cm· nm^{-1} to 2.78 cm ·nm^{-1}). However, a calibration process to be performed at the beginning of each trial would help minimize these undesired effects.

In the literature, no wearables exploiting FBG technology for back movements monitoring are presented. However, some WDs incorporating other technologies [226], [227] have been proposed, but proven to be excessively cumbersome, especially for long-term use in the scenario of interest. On the contrary, the lightness and compactness of the proposed system permit its usage for the entire working day. Also, smart T-shirts have been proposed [220], but the availability of only few sizes limits their usability on a wide range of population with different anthropometric characteristics and gender. In contrast, thanks to the adjustable elastic wearable structure, the presented device can be regulated to fit any anthropometry. Moreover, it can be worn over any garment which is particularly useful in work environments where a particular dress code is required.

However, an improvement in terms of a better and firmer integration of the sensing element upon the wearable is foreseen in order to minimize the errors committed in displacements evaluations. Also, new methodologies to ensure a better anchorage of the elastic structure and firm sensor positioning will be evaluated.

2.3. Wearable system composed of multiple soft flexible sensing elements for large-area movements detection

To minimize the errors caused by the slipping of the wearable system described in Section 2.2, the approach to directly apply the sensing elements to the users' skin was chosen. In addition, the number of the sensing elements was increased to provide monitoring of the entire back area and not just a single point. As consequence, in this section a flexible WD consisting of seven modular soft sensing elements to be applied along the entire back is presented. As attached to the skin, this time, the soft polymer matrix in which the FBG is embedded presents an advanced shape to better distribute strain. This device was designed to detect compensatory trunk movements (CTMs) that patients affected by hemiplegia might perform while executing rehabilitation tasks.

In this section, parts of the work [127] which the PhD candidate has co-authored have been freely extracted.

2.3.1. Design and manufacturing process

The wearable system is a 1m-length multi-point sensing device designed to be placed along the back spine. The device consists of a commercial fiber optic array with seven multiplexed gratings (λ_B values ranging from 1512 nm to 1559 nm, gratings length of 10 mm, and reflectivity of 90%, AtGrating Technologies) 100 mm interspaced from each other with an FC/APC optical connector at the fiber end. Each FBG is enclosed into a soft silicon matrix (Dragon SkinTM30, Smooth-On, Inc., Macungie, PA, USA) to comply with the physiological back curvature. As a result, seven identical soft sensing elements (SSEs) were developed, named SSE1, SSE2, SSE3, SSE4, SSE5, SSE6 and SSE7, from the farthest to the nearest to the optical connector (see Figure 4.34 (a)).

Each SSE (whose rendering and features are reported in Figure 4.34 (b)) comes as a structure formed by two superimposed polyhedra with rectangular bases and rounded corners. The lower polyhedron (30 mm x 20 mm x 3 mm) contains an FBG placed at 2 mm from the bottom in its central section. This portion provides a wide adherence area to ensure reasonable compliance with the skin as is intended to be bonded to the subjects' back through biocompatible double-sided tape. A smaller polyhedron (20 mm x 10 mm x 2 mm) presenting three parallel grooves (0.4 mm deep) on its surface is placed above the FBG and centered to the lower polyhedron. Such extrusion both strengthens the sensor by preventing fiber damages caused by excessive traction in the central area and avoids undue deformations by distributing the surface tensile stress by means of the grooves. The fiber portion between two consecutive SSEs is held in small flexible plastic tubes (8 tubes in total). The small tubes improve the robustness of the portions of optical fiber that are not encapsulated into the silicone matrices. Moreover, these portions allow the sensors arrangement at specific anatomical landmarks, thus respecting inter-subject anthropometric variability.

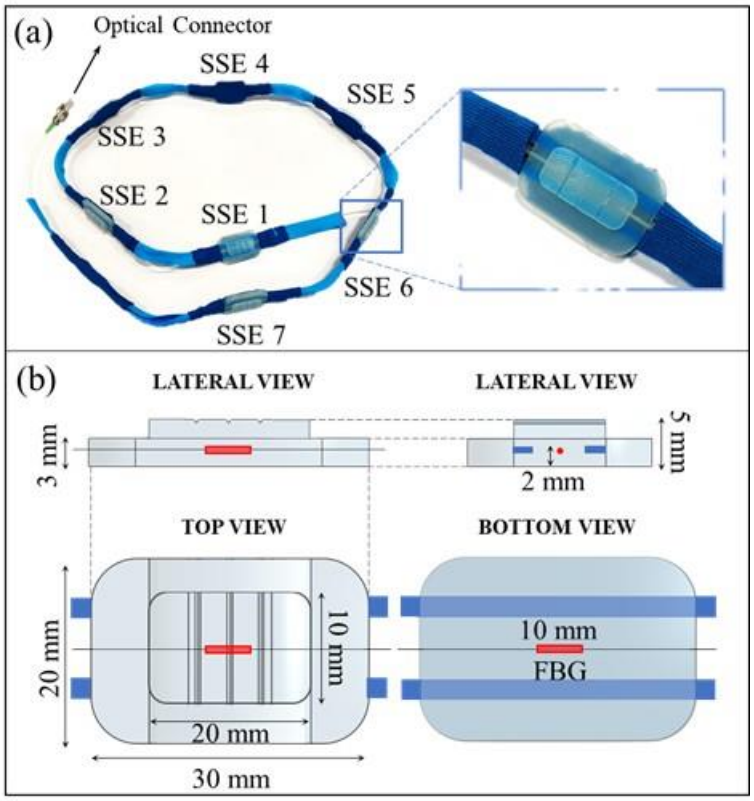

Figure 4.34. The wearable system. (a) A picture of the wearable system (on the left), together with a close-up view of one of the seven identical sensing elements (on the right); (b) Rendering and features of the sensing elements shown in lateral, top and bottom views.

The steps followed to manufacture the wearable system are represented in Figure 4.35 and detailed below:

1) Seven identical plastic molds created with a design software (OnShape®, PTC, Boston, MA, USA) were 3D printed by Ultimaker 2+ (Ultimaker B.V., Utrecht, The Netherlands). The molds were positioned in succession and 100 mm apart, then fixed to the working surface with double-sided tape;
2) eight small plastic tubes were inserted along the fiber optic (between the FBGs and at the extremities) to strengthen the exposed portions of the fiber. The fiber optic was inserted into the molds, passing through the lateral grooves and being careful to place each FBG at the midsection of the corresponding mold. The extremities of the fiber were then slightly pulled and secured with some adhesive tape to keep the FBGs properly tight. Two strips of kinesio tape 2 mm wide (ALPIDEX, BB Sport GmbH & Co KG., Töging am Inn, Germany) were placed parallel to the fiber optic and fixed into the dedicate housings of each mold, in order to toughen the system;
3) part A and part B of a bi-component silicone rubber (Dragon SkinTM 30, Smooth-On, Inc., Macungie, PA, USA) were blended with a volume ratio of 1A:1B (as recommended in the technical bulletin [29]) together with 10% in volume of

liquid thinner (Silicone ThinnerTM, Smooth-On Inc., Macungie, PA, USA). The mixture was let degassing into a vacuum chamber for few minutes until the complete removal of air bubbles;

4) the mixture was poured into each mold and let curing at room temperature for 24 hours. Once cured, the sensing elements were gently pulled out from the molds. Additional kinesio tape was used to cover the portions of the optical fiber which were not encapsulated into the polymeric substrates.

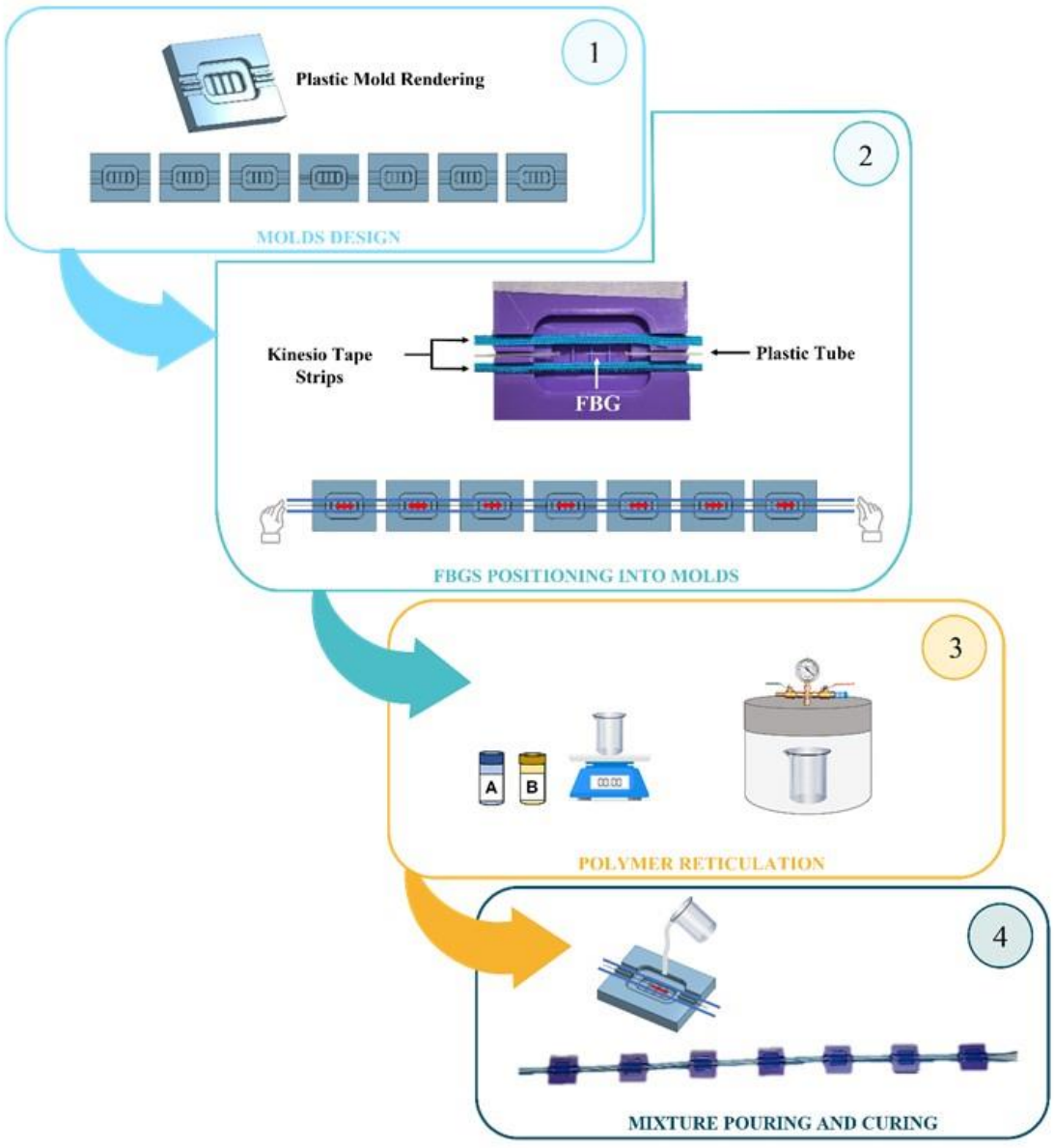

Figure 4.35. Diagram showing the manufacturing process of wearable system.

2.3.2. Metrological characterization

In the present application, the proposed wearable system is intended to be used as a strain sensor for detecting the back movements of the enrolled subjects. Hence, a metrological characterization was carried to estimate the S_ε of each SSE. Although the experiments were carried out at constant room temperature, once the flexible matrices have been attached to the skin, slightly ΔT may occur at the skin-matrix interface. Therefore, the SSEs responses to ΔT were also investigated.

2.3.2.1. Response to strain

The response to ε of the SSEs was evaluated by using a tensile testing machine (Instron 3365A, Instron, Norwood, MA, USA, repeatability ± 0.15%) at quasi-static conditions (i.e., 2 mm·min^{-1} of elongation speed) and room temperature. Each SSE was positioned between the machine clampers and fixed to the edges of the polymeric substrate (see Figure 4.36 (a)). The SSE was strained nine times (to ensure event repeatability) from 0% to 0.5% of ε with respect to its initial length to cover the ε range that could be experienced by the sensor in response back movements. Values of ε were collected at a sampling frequency of 10 Hz, while the FBGs outputs were recorded by an optical interrogator (si255 Hyperion Platform, Micron Optics Inc., Atlanta, GA, USA) at 100 Hz.

Data processing was executed in MATLAB environment (MathWorks® Inc., Natick, MA, USA). For each SSE, the mean value of $\Delta\lambda_B$ and the expanded uncertainty were calculated across the nine tests. The expanded uncertainty was obtained as the standard uncertainty multiplied by the coverage factor (k = 2.30), considering a t-student distribution with eight degrees of freedom and a confidence level of 95%. The calibration curve was estimated as the best fitting line of the average $\Delta\lambda_B$ over ε and S_ε as the slope of the best fitting line. The high values of correlation coefficients (R^2 > 0.99 for all the SSEs' calibration curves) ensured agreement between the experimental data and the linear model. Figure 4.36 (b) shows the calibration curve one of a single SSE (i.e., SSE2), while the S_ε values of all the SSEs are listed in Table 4.7. The different S_ε numerical values are attributable to the fabrication process which is manually executed. In fact, although the manufacturing was carried out with the utmost carefulness, it cannot be excluded that slight differences in the tensioning of the fiber during its positioning into molds and variations in the bonding strength at the fiber-polymer matrix interface during the curing might be occurred in each SSE.

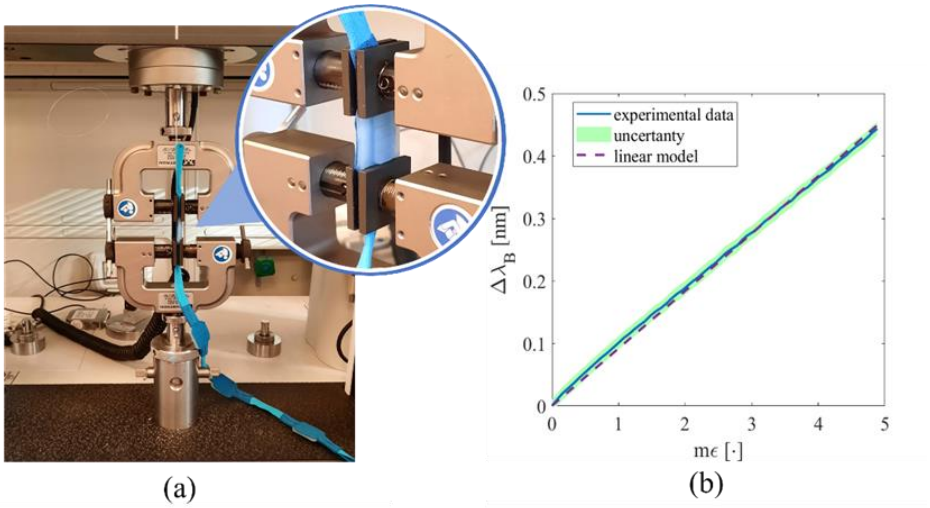

Figure 4.36. Response to strain of the SSEs. (a) The testing machine and a zoom of the sensing element placed between the two clampers. (b) The calibration curve $\Delta\lambda_B$ vs. mε of SSE2 given as an example. The mean experimental $\Delta\lambda_B$ signal is shown in blue line, the uncertainty in the shadowed green area, and the linear model in the dotted purple line.

2.3.2.2. Response to temperature influence

The influence of T on SSEs output was evaluated by placing the wearable system within a laboratory oven (PN120 Carbolite®), as shown in Figure 4.37 (a), and exposed to T changes from 26 °C to 50 °C to extensively covering the working range of SSE. Reference values of T were collected by a thermistor (EL-USB-TP-LCD, EasyLog, Lascar Technology) and the output of SSEs by the FBG interrogator (FS22, HBM FiberSensing). A sampling frequency of 1 Hz was set for both the devices. All the $\Delta\lambda_B$ values range from ~0 nm up to 0.43 nm when exposed to T ranging between 26 °C to 49 °C. To extract the calibration curve (see Figure 4.37 (b)), the $\Delta\lambda_B$ of each SSE was plotted against ΔT (blue line) and the best fitting line was computed (dotted orange line).

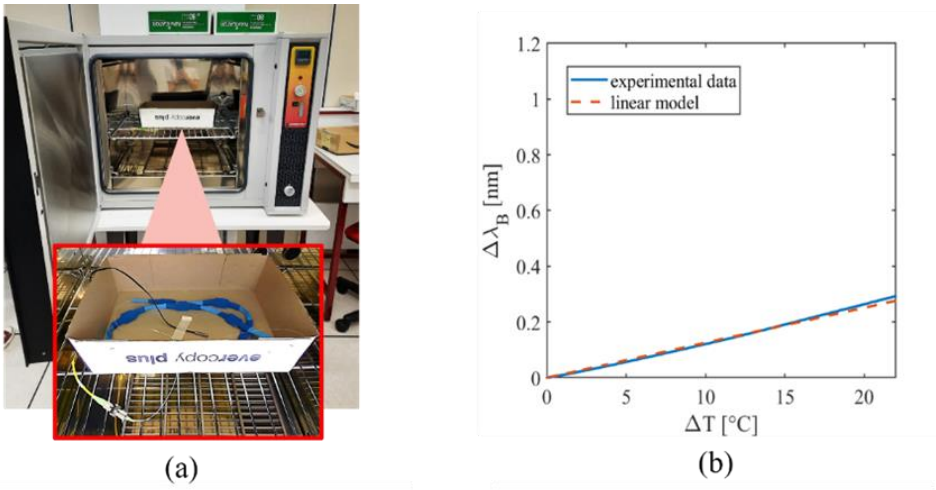

Figure 4.37. Response to temperature of the SSEs. (a) The laboratory oven and a zoom of the wearable system placed between inside the oven. (b) The calibration curve $\Delta\lambda_B$ vs. ΔT of SSE2

given as an example. The experimental $\Delta\lambda_B$ signal is shown in blue line while the linear model in the dotted purple line.

The S_T value of each SSE was obtained as the slope of the best fitting line and listed in Table 4.7.

Table 4.7. Values of the. Sε and S_T obtained for the seven SSEs

# SSE.	Sε [nm·mε^{-1}]	S_T [nm·°C^{-1}]
SSE1	0.21	0.015
SSE2	0.09	0.013
SSE3	0.05	0.012
SSE4	0.05	0.013
SSE5	0.06	0.014
SSE6	0.04	0.014
SSE7	0.06	0.015

Results showed S_T values similar to a bare FBG (i.e., 0.01 nm·°C^{-1}) and a negligible influence of T on the SSEs output during the experimental phase. Therefore, no changes in the thermal expansion of the polymer matrices occur. Indeed, in each trial (described in the following sections), typical every-day life tasks are replicated. The whole test sequence lasts about 20 min per patient. Therefore, the thermal stability at the matrix-body interface due to the body thermoregulation, as well as the smooth environmental ΔT which may occur in the scenario of interest, led to a negligible T influence on the SSE output.

2.3.3. Experimental assessment

The wearable system was a preliminary assessed on healthy subjects to verify its capability in detecting CTMs. Then, experimental trials were conducted on hemiplegic patients in a real clinical rehabilitation scenario. All subjects have read and signed informed consent. The study protocol was approved by the Ethics Committee of Università Campus Bio-Medico di Roma (protocol code ST-UCBM 27.2(18).20 OSS) and in accordance with the guidelines of the Declaration of Helsinki.

2.3.3.1. Experimental trial on healthy volunteers

A) Experimental setup and protocol

An explorative test was performed on 10 healthy volunteers (whose features are: five males and five females, all right-handed, age 25.2 ± 3.57 y.o., height 170.2 cm ± 9.59 cm, and body mass 63.4 kg ± 10.69 kg).

Participants were invited to sit on a stool, bare-chested or (in the case of female subjects) wearing a track top. The wearable system was applied on the back of each subject with hypoallergenic biocompatible tape on the user-facing side. SSE5 was placed

on the T12 vertebra, which identifies the point of inversion of the thoracic and lumbar curves, thus subdividing the back into upper and lower portions. SSE1 and SSE7 were then placed on the C7 and L3 vertebrae, respectively. Then, SSE2, SSE3 and SSE4 were equidistantly placed between SSE1 and SSE5, while SSE6 was fixed between SSE5 and SSE7. All sensors were then secured to the skin with an extra piece of Kinesio tape that is designed to stay in place all day, also during sweating. A stereophotogrammetric MoCap (BTS D-Smart, by BTS Bio-Engineering S.r.l., Milan, Italy) was used to quantitively measure the tridimensional movements of the upper part of the participants' body. Four cameras were installed behind the seated subject at ~2 m, and four in front of the volunteer. Fourteen spherical markers (12 mm in diameter) stuck attached with hypoallergenic tape were used and placed upon each SSE (M1, M2, M3, M4, M5, M6, and M7), on the right and left acromions (RA and LA, respectively), elbows (RE and LE, respectively) and wrists (RW and LW, respectively), and on the moving object (OBJ). The positioning of SSEs and markers is depicted in Figure 4.38.

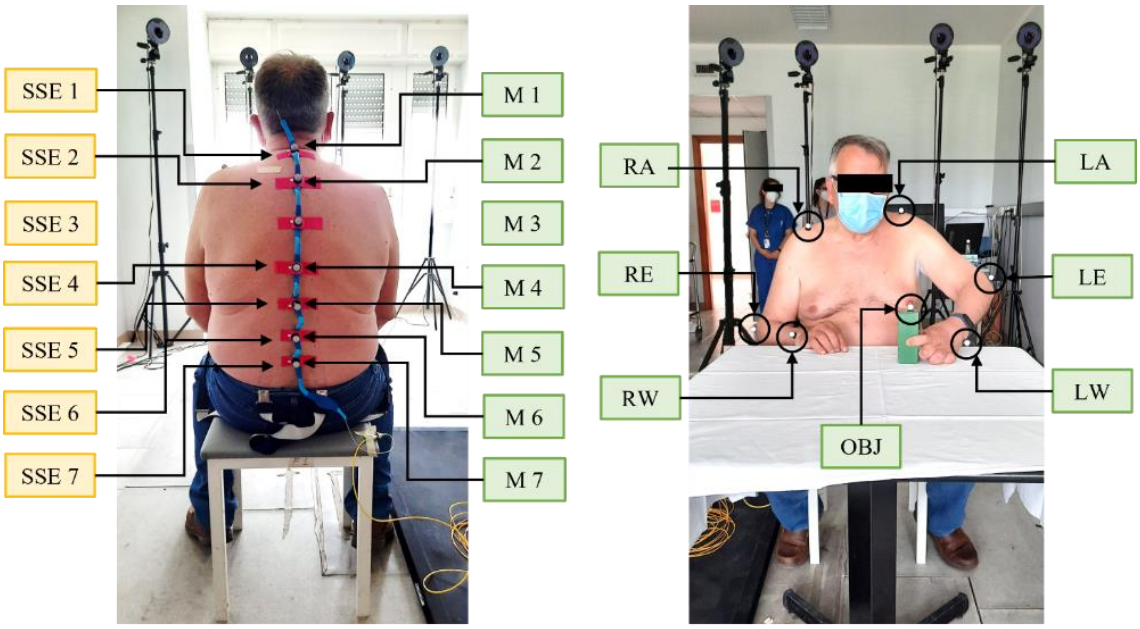

Figure 4.38. Soft sensing elements (yellow box texts) and markers (green box texts) positioning on a volunteer.

Also, in Figure 4.39 (a) and (b), the experimental setup is represented.

Participants were instructed on the experimental protocol, which consisted in sitting at a table while wearing the wearable system and moving an object (i.e., wooden polyhedron 10 x 15 x 5 cm) across the table's surface. The following three tasks (see Figure 4.39 (c)), which are representative of typical everyday life actions, were performed:

1) Forward Movements (FM): move the object back and forth by executing a flexion-extension movement of the arm;
2) Lateral Movements (LM): move the object right and left, keeping the arm outstretched;
3) Circular Movements (CM): move the object performing circular motions.

For each of the three tasks, all participants performed two rounds (i.e., Round 1 and Round 2), each consisting of 10 repetitions using the dominant arm. In Rounds 1, the volunteers executed the repetitions by avoiding the trunk recruitment, while in Rounds 2, the subjects performed the same repetitions by eliciting CTMs which typically occur in the presence of hemiplegia. More specifically, in Rounds 2 each volunteer was invited to self-maintain a stable upper limb pose while performing the task to promote trunk involvement (in line with [228]).

During the protocol execution, wearable system's data were collected by means of an optical interrogator (si255, Micron Optics Inc., Atlanta, GA, USA) at 1 kHz of sampling rate, while the 3D markers' trajectories were recorded with BTS Tracker software (by BTS Bioengineering S.r.l., Milan, Italy) at 60 Hz of sampling rate.

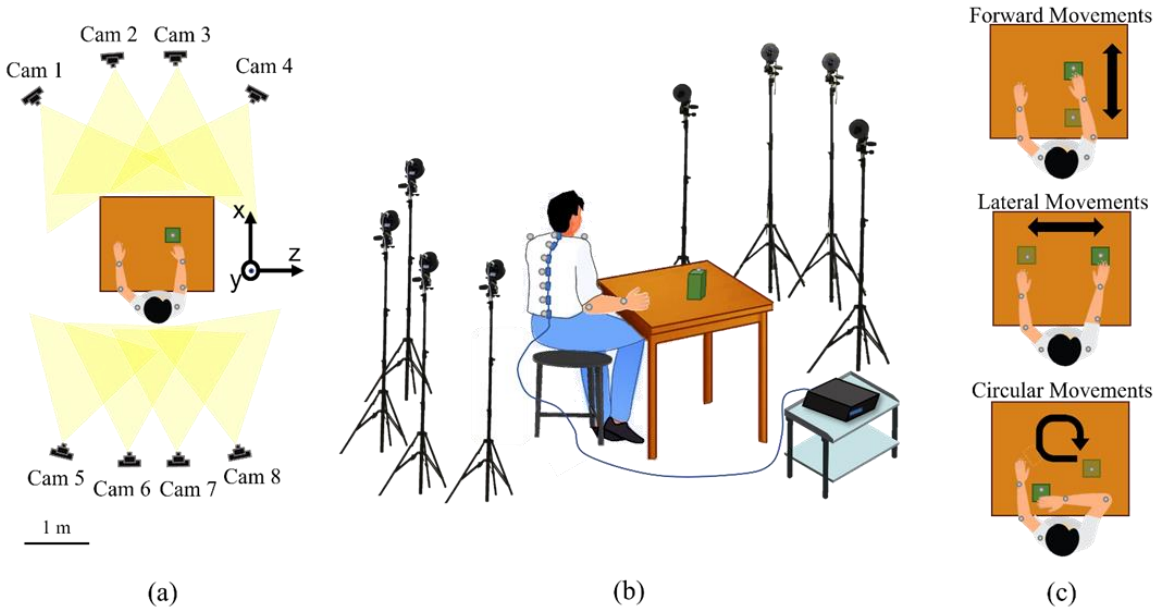

Figure 4.39. Experimental setup and protocol. (a) Upper view showing the positioning of the eight cameras and the reference axes. (b) The experimental set-up showing the subject's positioning, the MoCap system, the wearable system, and the spectrum interrogator. (c) Illustration of the three tasks per-formed during the protocol.

B) Data analysis and results

Experimental data were processed in MATLAB environment (MathWorks® Inc., Natick, MA, USA). MoCap was used as a reference instrument to determine the magnitude of the trunk involvement and, in turn, the presence of CTMs. Raw trajectories of all the markers in all the planes (sagittal plane x-y, transversal plane y-z, and frontal plane x-z) were recorded. In each trial, the marker positioned on the object was used to subdivide the recorded trace into ten signals related to the performed movements. The movement of the object is a periodic signal. The minimum points represent the instants in which the object is at the minimum distance from user, while the maximum points those in which the object is at the maximum distance from the user. A complete movement was considered as the signal between two consecutive minima points. As a consequence, 10 movements per each trial were identified and the seven markers' trajectories on x, y, z axes were segmented into 10 windows. For each window, the relative marker displacement amplitude was calculated as the difference between the max value and the min value of the displacement. Hence, ten values were obtained per each marker and per each axis considering each trial. The median value over the ten movements was calculated to obtain the median relative displacement (R) of all the markers along x (Rx), y (Ry), and z (Rz) directions separately. The Rx, Ry, Rz are considered index of trunk displacement along the three axes: the higher the value of R, the higher the trunk involvement.

Figure 4.40 (left column) shows the box plots obtained grouping all the R data gathered by different subjects. In each box plot, the median and the interquartile range (IQR) quantify the magnitude and inter-subject variability of the trunk involvement. As expected, Rx, Ry, and Rz values corresponding to each spinal marker are always greater in Rounds 2 (presence of CTMs) than in Rounds 1 (without CTMs). In all the tasks, the median values of R registered from the seven markers are approximately one order of magnitude greater than those in Round 1 in all the axis. Moreover, it is worth noting that during the FM and LM tasks, larger Rx and Rz values occurred, respectively. The lowest values are related to Ry in all tasks. registered from the seven markers are approximately one order of magnitude greater than those in Round 1 in all tasks.

From the output of each SSE, the ε trends in time were retrieved for all the SSEs as $\varepsilon = \Delta\lambda_B/S_\varepsilon$. In Figure 4.41 (a), an example of the output obtained by one of the seven SSEs is reported. To quantify the ε experienced by each SSE during trunk displacements, for every subject we evaluated the standard deviation (SD) over the ten repetitions of each task. Then, for each SSE and task, we calculated the mean value of the SDs across the 10 healthy volunteers. In Figure 4.41 (b), the mean SDs of SSEs (from 1 to 7) are reported for the three tasks considering both Rounds 1 and 2. In all the trials, each SSE showed higher SD values in Rounds 2 than in Rounds 1, confirming the presence of CTMs.

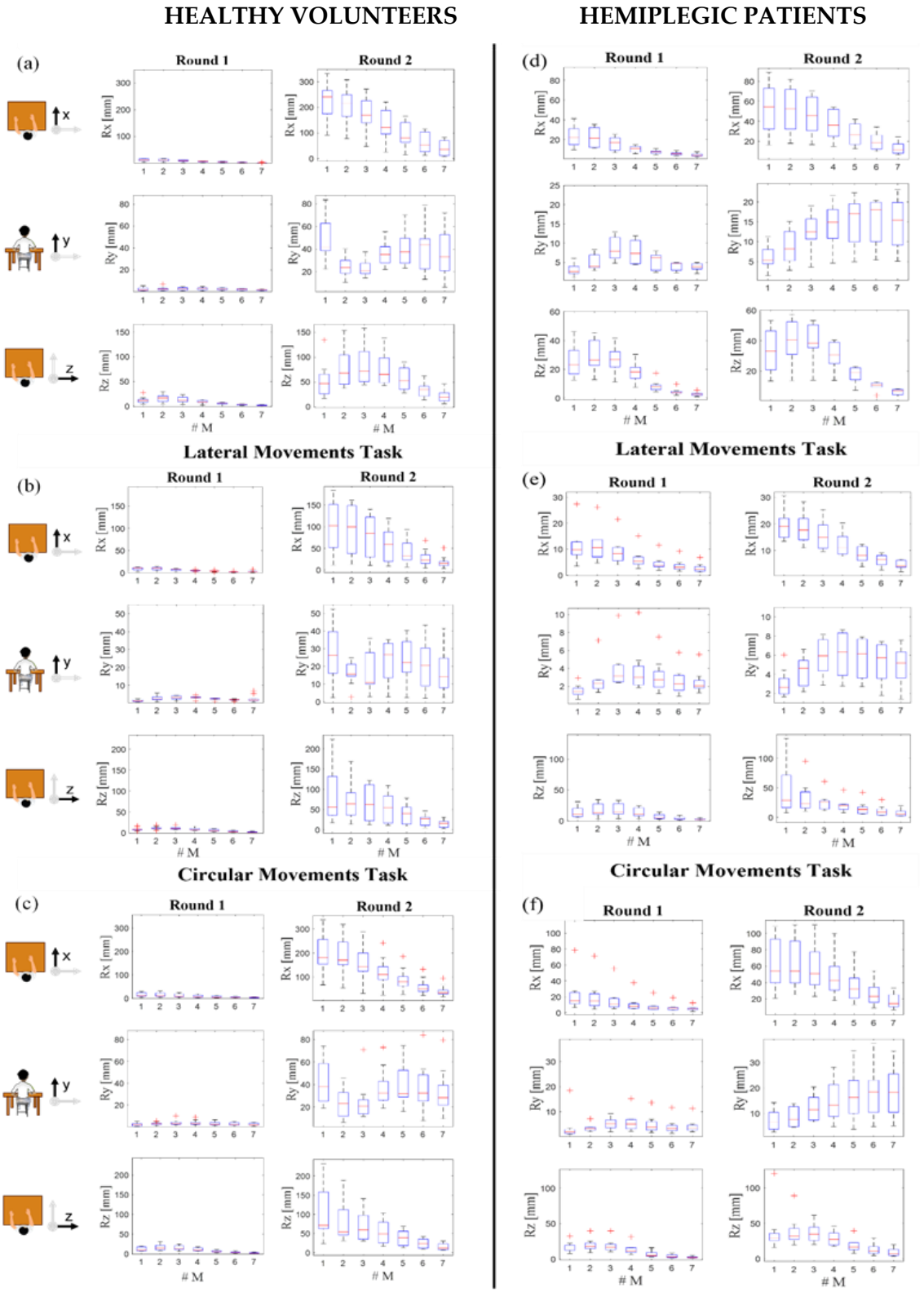

Figure 4.40. Relative displacements of the 7 MoCap markers (#M) placed on the spline along x (Rx), y (Ry) and z (Rz) axes during the three tasks (forward movements in (a) and (d), lateral movements in (b) and (e) and circular movements in (c) and (f)) performed by the healthy volunteers (left column) and hemiplegic patients (right column) in presence (Round 1) and absence (Round 2) of CTMs. Data are expressed as median, IQRs and outliers.

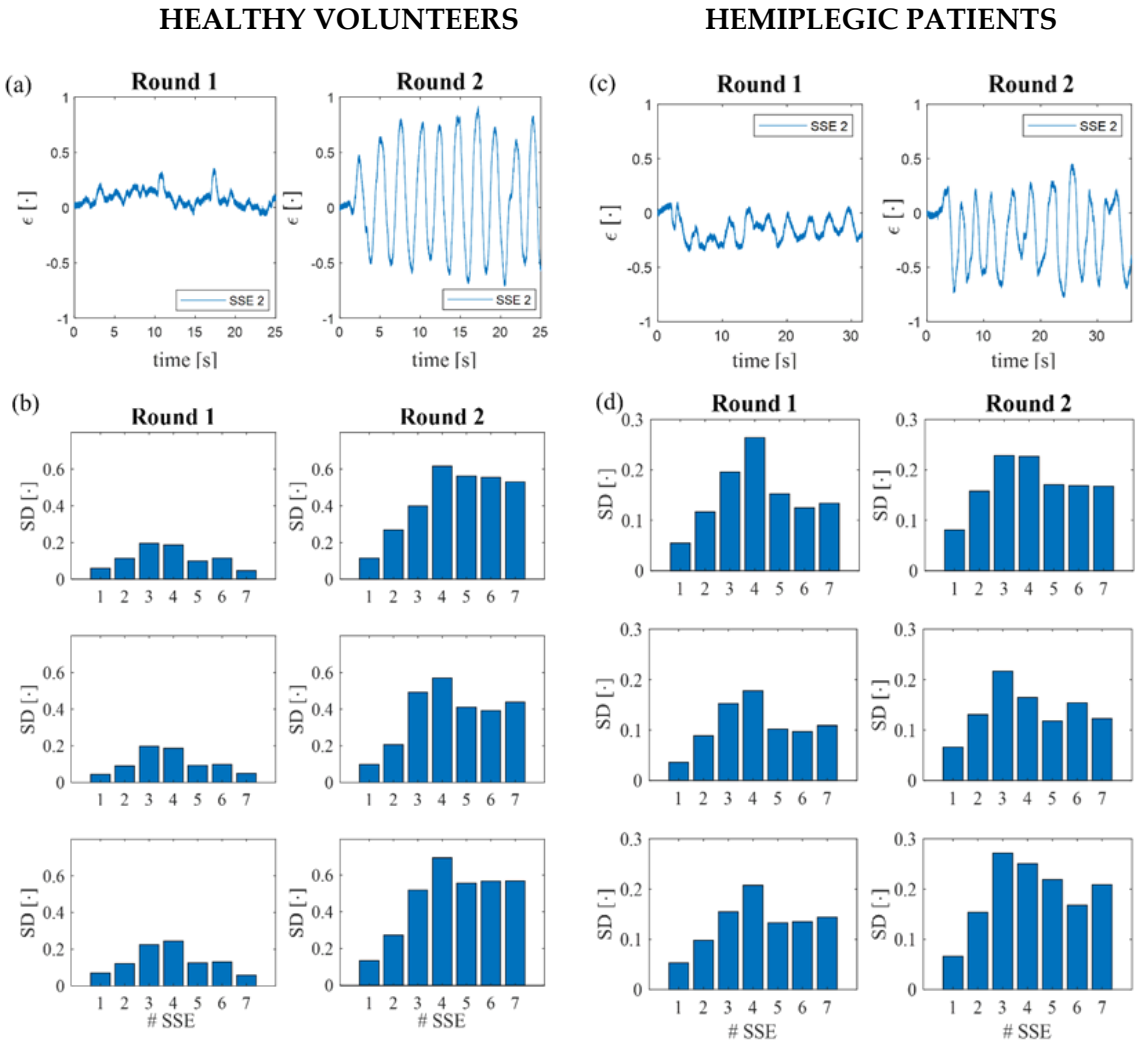

Figure 4.41. Example of the ε trends in time retrieved by SSE 2 during the execution of CM task performed by a healthy volunteer (a) and a hemiplegic patient (c) in Round 1 and Round 2. Mean SD values calculated for the 7 SSEs (# SSE) during the three tasks performed by the healthy volunteers (b) and hemiplegic patients (d) in Round 1 and Round 2.

2.3.3.2. Experimental trial on hemiplegic patients

Having preliminarily verified the system capability to detect CTMs on healthy volunteers, an assessment was performed on post-stroke hemiplegic patients.

A) Experimental setup and protocol

Participants were recruited from a research volunteer database produced by the Physical and Rehabilitation Unit of Fondazione Policlinico Universitario Campus Bio-Medico. A number of eight hemiplegic patients (whose features are shown in Table 4.8) has been enrolled. Inclusion criteria were: *i)* acquired diagnosis of stroke, *ii)* absence of cognitive deficits and *iii)* score of the Fugl-Meyer Assessment Upper Extremity Scale of Motor Impairment (i.e., the most used rating scale to measure post-stroke disability

extent [207]) ≥ 10 [229]. This value was identified as the minimum value to guarantee residual upper limb functionality to perform the required tasks.

Hemiplegic patients were instructed to perform the same experimental protocol executed by the healthy volunteers, but this time using the unaffected arm in Rounds 1 and the hemiplegic arm in Rounds 2.

Table 4.8. Features of the hemiplegic patients.

# Patient	Age [y.o.]	Sex	Affected Side	Height [cm]	Body Mass [kg]	UE-FMA *
1	55	Male	Left	170	74	11
2	73	Male	Left	175	106	37
3	63	Male	Right	175	88	43
4	33	Female	Right	168	54	55
5	63	Male	Left	170	79	32
6	47	Male	Left	184	86	24
7	55	Male	Right	168	49	50
8	43	Male	Left	165	75	34

* Fugl-Meyer Assessment Upper Extremity score.

B) Data analysis and results

The Rx, Ry, and Rz medians and the IQRs values obtained by the MoCap data are shown in Figure 4.40 (right column). As for the healthy volunteers, the Rx, Ry, and Rz values corresponding to each marker (from M1 to M7) during the three tasks are always higher in Rounds 2 (i.e., affected arm and presence of CTMs) than in Rounds 1 (i.e., unaffected arm and absence of CTMs). As before, it is possible to state that the lowest values are related to Ry in all the tasks. Instead, during the execution of FM and LM tasks, larger Rx and Rz values occurred, respectively.

Regarding the wearable system, ε trends in time were obtained for all SSEs (in Figure 4.41 (c) an example is given). In Figure 4.41 (d), the SDs calculated for all the SSEs are reported for the three tasks grouped in Rounds 1 and 2. Each SSEs showed higher mean SDs in Rounds 2 than in Rounds 1 considering all the three tasks, except for the values obtained from SSE4 during the performance of FM and LM tasks. In fact, SSE4 presented mean SD values of 0.264 and 0.178 in Rounds 1 of FM and LM, respectively, and of 0.227 and 0.165 in Rounds 2 for FM and LM, respectively.

2.3.4. Discussions

The presented system is a novel WD composed of seven FBG-based SSEs which enable reliable and multi-point monitoring of trunk movements for CTMs detection in post-stroke upper limbs patients.

The manufacturing of the WD and the SSEs' response to ε and ΔT were described, showing S_ε values (i.e., ranging from 0.04 nm·mε^{-1} to 0.21 nm·mε^{-1}) comparable to those retrieved in the literature for soft flexible sensors [189][194][192][191] and S_T value close to that of a bare FBG. A demonstration of the SSEs' high sensitivity to ε is given by

the capability of the wearable system to perceive even the smallest trunk deformations during the exercises performed by hemiplegic patients. The feasibility of the proposed device to detect CTMs was firstly proven on ten healthy volunteers in the presence and absence of trunk recruitment, and then on eight hemiplegic patients using the affected and unaffected arms. In accordance with the MoCap, the wearable system demonstrated its ability in detecting CTMs.

To date, several WDs have been proposed for monitoring joint movements [189]–[192], [194]. These solutions mostly come as belts or knee bands which are equipped with a single FBG-based soft sensor, that led to a lack in spatial resolution in the movement's reconstruction. On the contrary, compared to these devices, the multi-sensor configuration exploited in this wearable enables measurements at different spine levels enabling the monitoring of a large area such as the back. Moreover, the positioning of multiple, freely placeable SSEs allows the system to adapt to different anthropometries. Also, the SSEs redundancy which ensures continuous monitoring even in the event of failure of a sensing element. Furthermore, the application of the SSEs directly on the back makes the device unobtrusive, not limiting the patients' normal motility. In fact, elastic bands and belts can create feelings of constriction and discomfort in disabled patients, limiting their range of movements.

Lastly, to the best of our knowledge, the presented wearable is the first one based on multiple soft sensors embedding FBG technology and distributed along the whole spine whose purpose is to evaluate the trunk recruitment during post-stroke rehabilitation processes.

3. FBG-based smart wearable solutions for respiratory rate and posture monitoring

In this paragraph, the application of two FBG-based systems for the simultaneous monitoring of posture and respiratory activity is described for the first time. More precisely, two WDs already presented in the previous sections were assessed to define their capability to estimate RR and, at the same time, evaluate neck and trunk postures. Results of these tests are reported in the sections below.

The use of such systems in these terms was designed for the assessment of the presence of psychological (by means of RR detection) and muscular stress (by means of neck and trunk posture detection) in an occupational scenario, in order to prevent the onset of psychological discomforts and musculoskeletal diseases.

3.1. Soft flexible patches

The soft flexible patches presented in Section 2.1 are here applied in two sites of the neck area in order to assess their feasibility in retrieving both RR and neck F/E and axial rotation movements (ARm).

In this section, parts of the work [230] which the PhD candidate has co-authored have been freely extracted.

3.1.1. Experimental assessment

A) Experimental setup and protocol

To detect F/E movements, one flexible patch (hereafter named FBG1) was positioned in correspondence of the cervical spine segment C1–C7, along the longitudinal direction starting from C7. For the ARm monitoring, the second patch (hereafter named FBG2) was positioned on the right side of the neck, horizontally with respect to FBG1 starting from the center of C6, C7 (Figure 4.43 (a)). A polyacrylate bandage (100% polyester, Curafix® H, Lohmann & Rauscher, Padova, Italy) was used to allow a better adhesion and compliance to the skin. The positions were chosen to optimize the strain distribution along the FBG longitudinal direction. The F/E movements cause longitudinal strain on FBG1: its output increases during flexion, while decreases during extension (Figure 4.42 (b)). The ARm are mostly detected by the FBG2: its output increases during left rotations, while a decrease is experienced during the right rotations (Figure 4.42 (c)). Breathing monitoring is allowed by the neck muscles activity and cervicothoracic junction movements that strain both the FBGs. This phenomenon results in $\Delta\lambda_B$ pseudo-periodic oscillations, which allows estimating RR [231].

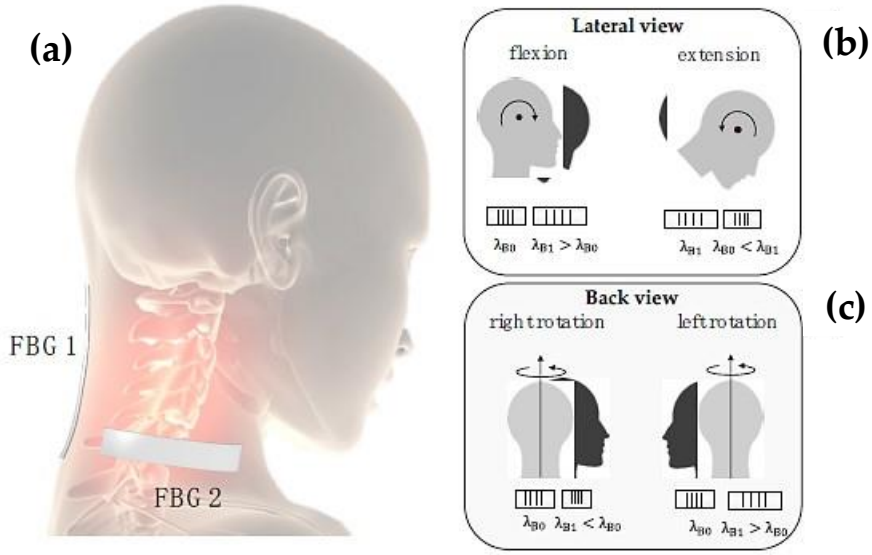

Figure 4.42. (a) Sensors' positionings on the neck of the user; (b) schematic representation of the FBG1 response to flexion-extension (F/E); (c) schematic representation of the FBG2 response to axial rotation (AR) movements.

The system was assessed on five healthy subjects (three males and two females) whose features are the following: age of 29.6 y.o. ± 5.35 y.o., height of 173.2 cm ± 6.82 cm, body mass of 80.4 kg ± 24.1 kg, neck circumference of 39.4 cm ± 4.8 cm.

Participants were asked to sit maintaining their feet on the floor, both hands on the knees, with hips and knees flexed at 90° (Figure 4.43 (a)). A MoCap system (Smart-D, BTS Bioengineering Corp., Milan, Italy) was used as a gold standard to assess the capability of the multi-parametric wearable system to discriminate F/E and ARm. Four spherical, infrared photo-reflective markers (15.2 mm in diameter) were placed on each subject as shown in Figure 4.44 (a) and (b). In particular, the first marker is placed on the forehead (marker P1 in 4.44 (a) and (b)), the second marker on the C7 spinous process (marker P2 in Figures 4.44 (a) and (b)), and the last two markers were placed in correspondence of the acromioclavicular joints (P3' and P3'' in 4.44 (b)). Eight cameras collected the trajectories of the markers at a sampling rate of 60 Hz. An FBG interrogator (si255 based on HYPERION platform; Micron Optics Inc., Atlanta, GA, USA) was used to record the FBGs output, at a sampling rate of 1 kHz.

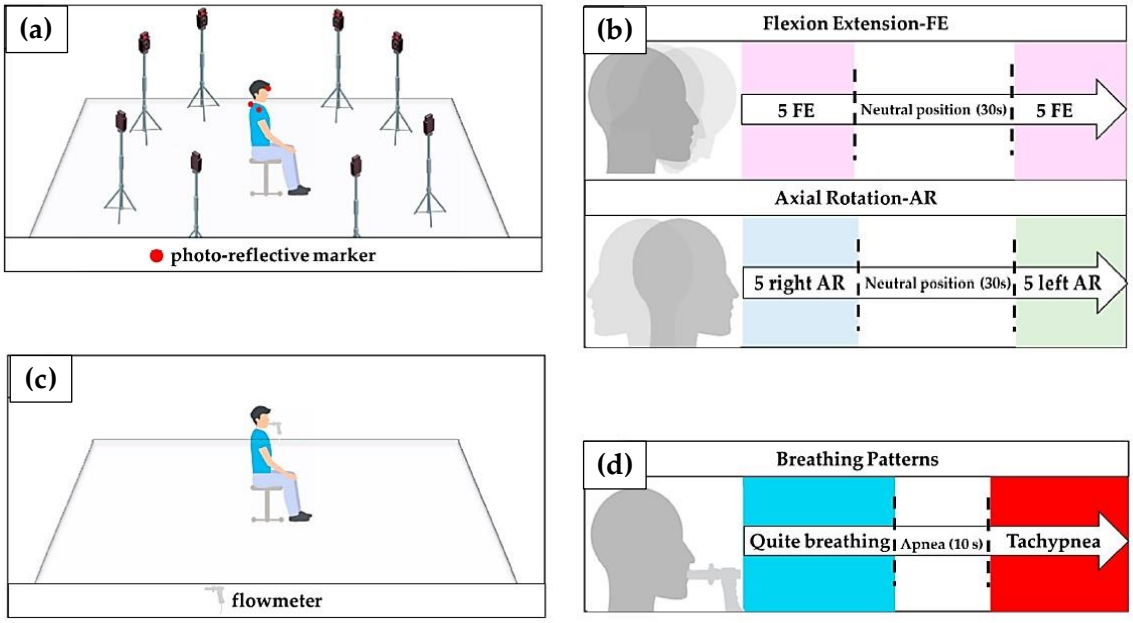

Figure 4.43. (a) Experimental set-up to assess the feasibility of the proposed system for monitoring neck movement; (b) experimental protocol for monitoring FE and AR movements; (c) Experimental set-up to assess the feasibility of the proposed system for respiratory frequency monitoring; (d) experimental protocol for RR monitoring.

After markers and FBG positioning, the protocol was explained to each subject. Participants started with the head and the neck in a neutral position and looking forward. Firstly, the participants were asked to perform F/E and ARm, simultaneously recorded by the wearable and MoCap systems. Each participant performed:

1) five F/E repetitions, followed by 30 s in the neutral position, and then five F/E repetition (Figure 4.44 (b), upper image);
2) five AR repetitions to the right, followed by 30 s in the neutral position, and then by five AR repetition to the left (Figure 4.44 (b), bottom image).

An additional trial was executed to assess the ability of the multi-parametric wearable system to monitor breathing activity. During this trial, a commercial flowmeter (SpiroQuant P, EnviteC, Alter Hozhafen, Wismar, Germany) connected to a differential pressure sensor (163PC01D75, Honeywell, Minneapolis, MN, USA) was used as a reference system (Figure 4.43 (c)). The output of the differential pressure sensor was collected through a DAQ (NI USB-6009, National Instrument, Rockville, MD, USA) and a custom Virtual Instrument developed in LabVIEW® environment, at the sampling frequency of 250 Hz. Participants were asked to ventilate into a mouthpiece while performing two breathing patterns: ten breaths of self-controlled quite breathing and

ten breaths of self-controlled tachypnea; a 10 s stage of apnea was performed between the two breathing patterns (Figure 4.44 (d)).

B) Data analysis and results

i) *Assessment of the wearable system in neck movements estimation*

The number of F/E and ARm repetition was calculated from the raw data collected by the MoCap and the wearable system. The 3D coordinates of the markers recorded by the MoCap system were used to carry out the reference signals by following the steps: *(i)* the F/E angle (α_{FE}) was estimated in the sagittal plane (i.e., y–z) as the angle between the vectors $\overrightarrow{P2P1}$ and $\vec{u}$ (same direction of the y-axis), as shown in Figure 4.44 (a); *(ii)* the ARm angle (θ_{AR}) was estimated in the transverse plane (i.e., x–z,) as the angle between the vectors $\overrightarrow{P2P3'}$ and $\vec{v}$ (the same trend may be obtained by considering the vectors $\overrightarrow{P2P3''}$ and $\vec{v}$), as shown in Figure 4.44 (b). The θ_{AR} decreases during the right rotation (clockwise) and increases during the left rotation (counterclockwise).

Regarding the wearable system, the analysis of the neck movements' detection was performed as follows: *(i)* the changes of FBG1 output were used to evaluate F/E movements since the chin lowered down toward the chest causes a longitudinal deformation of FBG1; *(ii)* the changes of FBG2 output were considered to evaluate ARm, as the right and left rotations of the head around its vertical line (y-axis in Figure 4.44 (a)) causes a longitudinal deformation of FBG2. Trends of signals collected by the MoCap system are shown in Figure 4.44 (c) and (d), and the ones collected by the wearable system are shown in Figure 4.44 (e) and (f).

To assess the capability of the proposed system to detect neck movements on different planes, the collected data were processed. Firstly, the outputs of both the wearable and the MoCap systems were normalized in amplitude and plotted over time to evaluate trend similarity between signals. Then, the F/E and ARm repetitions were detected by using a custom peak detection algorithm in MATLAB environment. F/E movements were identified by considering the maximum peaks of both MoCap and FBG1 signals: when α_{FE} increases during the neck flexion (signal provided by the MoCap) FBG1 is strained with a consequent increase of λ_B (Figure 4.44 (c) and (e)). Right ARm were detected by considering the minimum peaks of both MoCap and FBG2 signals: when θ_{AR} decreases during the right ARm (signal provided by the MoCap) FBG2 is compressed with a consequent decrement of λ_B. In contrast, left ARm were detected by considering the maximum peaks of both MoCap and FBG2 signals because when θ_{AR} increases during the left ARm (signal provided by the MoCap) FBG2 is strained with a consequent increment of λ_B (Figure 4.44 (d) and (f)).

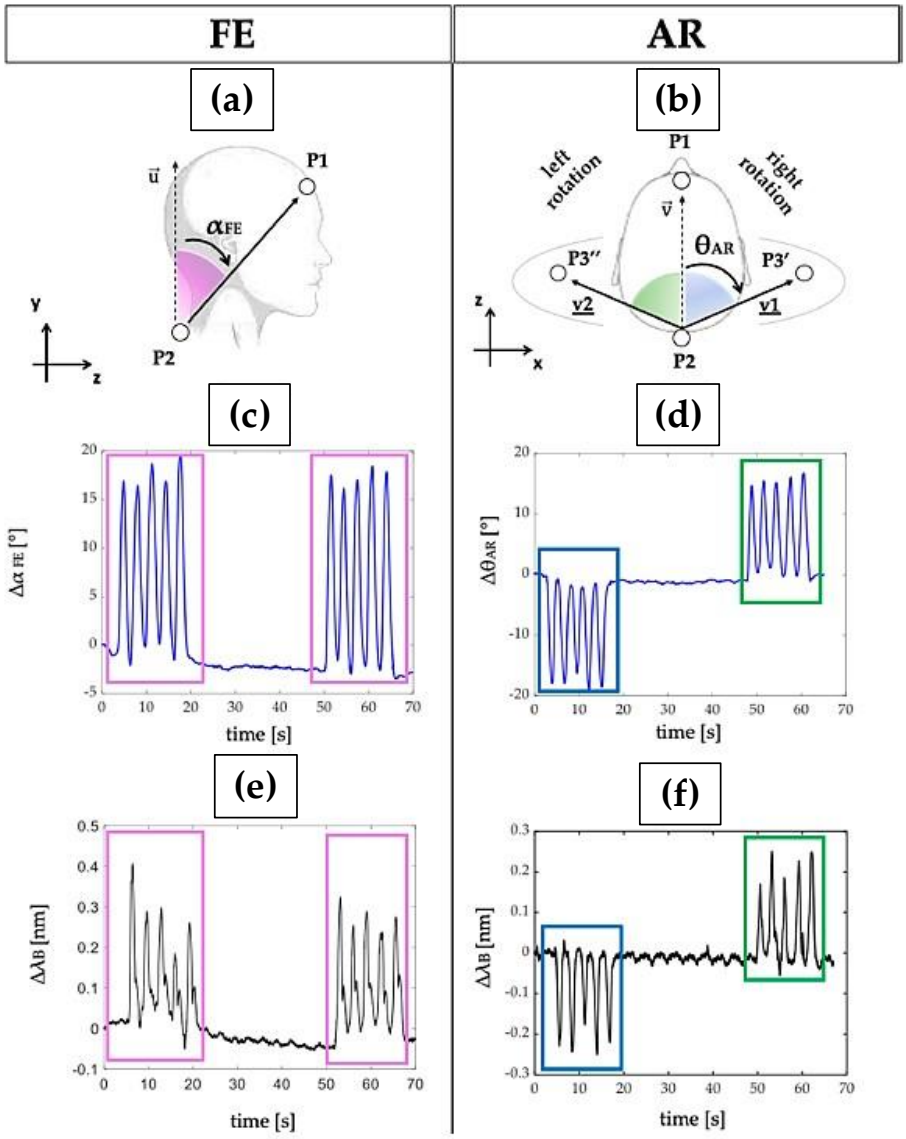

Figure 4.44. (a) The α_{FE} and (b) the ϑ_{AR} angles formed in the sagittal and transverse plane; (c) reference output changes over time during F/E and (d) ARm repetitions; (e) FBGs outputs changes over time during F/E and (f) ARm repetitions.

Results showed that the proposed wearable system was able to follow both F/E and ARm and detect the repetitions. The synchronized signals of both the FBGs and MoCap were plotted superimposed and shown in Figure 4.45. In particular, the wearable system showed good performance in detecting F/E and left ARm repetitions. In fact, it is possible to observe how the maxima of the peaks of the blue (i.e., MoCap) and black (i.e., FBG1) signals framed by the pink rectangles match. Also, $\Delta\lambda_B^{FBG2}$ patterns matched the MoCap ones during the left ARm repetitions (green boxes). On the contrary, $\Delta\lambda_B^{FBG2}$ pattern during the right ARm did not always match the reference signal (light blue box), as

evidenced by the fact that for some volunteers the signals are not overlapping and the peaks do not coincide (e.g., Volunteer 1).

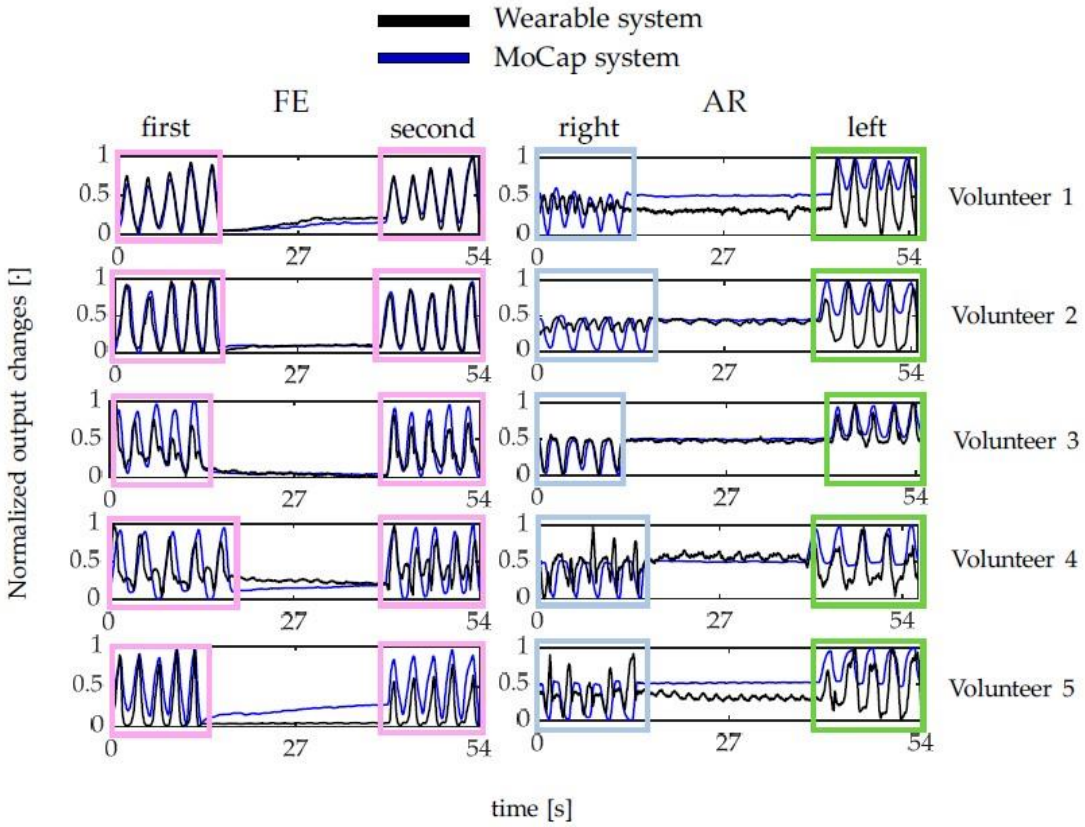

Figure 4.45. The output changes of both the wearable (black line) and the Motion Capture (MoCap) system (blue line) collected during F/E and AR repetitions.

ii) Assessment of the wearable system in respiratory rate estimation

The assessment of the proposed wearable system for the RR monitoring was performed by using the flowmeter as a reference instrument. The outputs of the wearable system and the flowmeter were normalized in amplitude and split into quiet breathing-related signals and tachypnea-related ones (i.e., $FBG1_{qb}$, $FBG2_{qb}$, $FLOW_{qb}$, $FBG1_{tc}$, $FBG2_{tc}$, and $FLOW_{tc}$), as shown in Figure 4.46 (a). The signals of both $FBG1_{qb}$ and $FBG1_{tc}$ were inverted since the FBG1 was compressed during the and tensioned during the expiration (this step was not implemented on the FBG2 output since its trend in time matches that of the reference system). A 3rd order Butterworth low pass filter was then applied on signals collected during quiet breathing (cut-off frequency of 0.5 Hz) and during tachypnea (cut-off frequency of 3 Hz). A PSD analysis was performed on the filtered signals and the maximum frequency (f_0) of both the reference and the wearable systems signals were evaluated (Figure 4.46 (b)). A peak detection was performed by

using findpeaks in MATLAB environment: the input parameter related to minimum peaks distance was set starting from the value of f_0 (Figure 4.46 (b)).

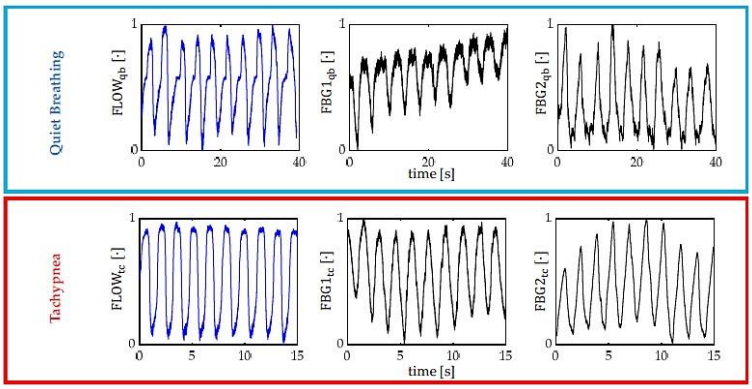

(a)

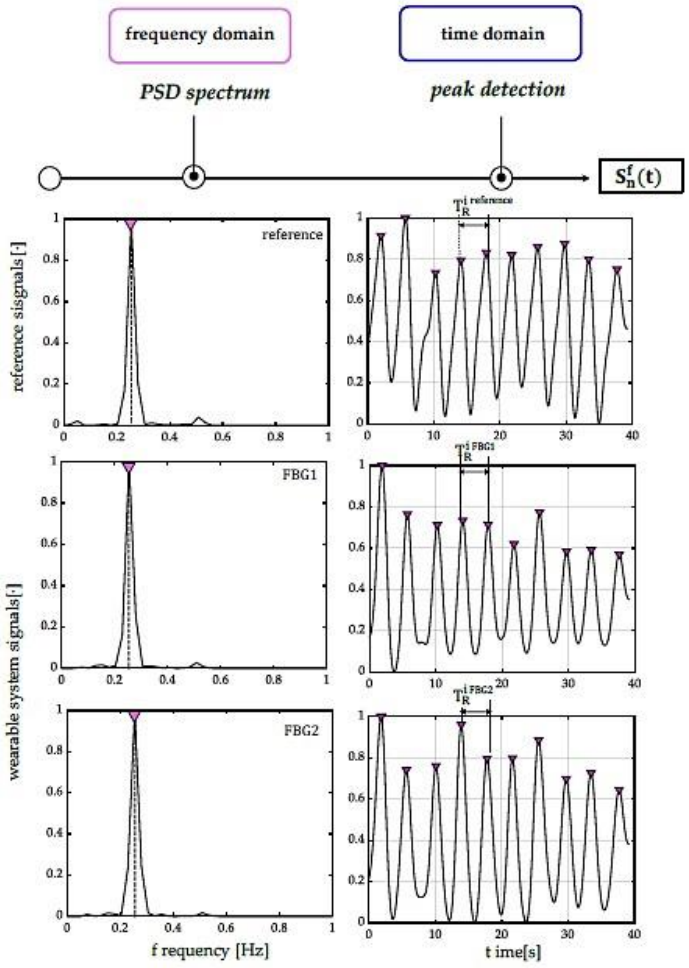

(b)

Figure 4.46. (a) Signals collected by the flowmeter (blue trend) and by the FBGs (black trend) during both quiet breathing (light blue box) and tachypnea (red box). (b) An example of signals processing performed for the RR estimation from data recorded by the flowmeter and the wearable systems, during quiet breathing. The power spectral density (PSD) spectra over frequency [Hz] and the peak detection over time [s] are shown for both the reference system and

the proposed wearable system based on two flexible sensors (FBG1 and FBG2). The $S_n^f(t)$ signals are filtered and normalized.

The respiratory periods of each breath (i.e., T_R^i) were computed as the time elapsed between two consecutive maximum peaks of the signal provided by FBG1, FBG2, and the flowmeter. The RR_i values during both quiet breathing and tachypnea were estimated as 60/T_R^i and expressed as breaths per minute (bpm).

The assessment of the wearable system in the RR estimation during both quiet and tachypnea breathing was performed using three parameters:

i) percentage error:

$$e_p[\%] = \frac{\overline{RR^{FBG}} - \overline{RR^{flow}}}{\overline{RR^{ref}}} \cdot 100 \tag{4.14}$$

where $\overline{RR}$ is the mean value of RR;

ii) absolute percentage errors for a breath-by-breath analysis:

$$\left|e_p^i\right|[\%] = \frac{\left|RR^{i\,FBG} - RR^{i\,flow}\right|}{RR^{i\,flow}} \cdot 100 \tag{4.15}$$

where $RR^{i\,FBG}$ and $RR^{i\,flow}$ are the values of the i-th RR estimated either by FBG1 or FBG2 and by the flowmeter;

iii) mean absolute percentage errors (i.e., MAPE) for a breath-by-breath analysis:

$$MAPE_{RR}[\%] = \frac{1}{n}\sum_{i=1}^{n} \frac{\left|RR^{i\,FBG} - RR^{i\,flow}\right|}{RR^{i\,flow}} \cdot 100 \tag{4.16}$$

All signals involved in the peak detection of the breathing analysis are shown in Figure 4.47. The peak detection allowed estimating RR in all volunteers but one (for FBG1 output changes of Volunteer 1 during both quiet breathing and tachypnea).

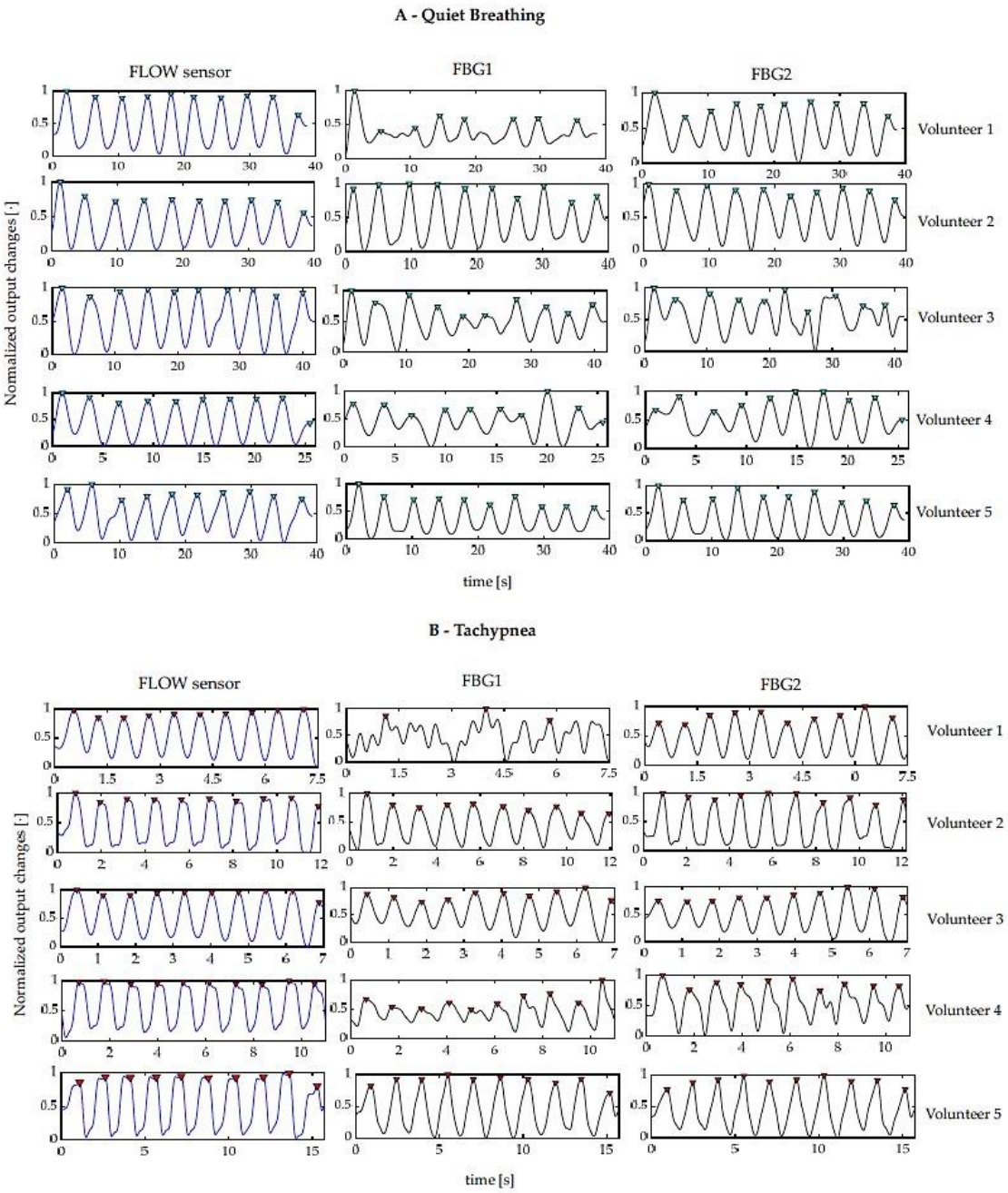

Figure 4.47. (A) signals collected by the flowmeter (blue line) and the FBGs (black lines) for each volunteer during quiet breathing and (B) during tachypnea. All the signals are synchronized, filtered, and normalized. The detected peaks are highlighted by using red markers.

The e_p, the MAPE and the $|e_p|$ values are listed in Table 4.9 and Table 4.10. The e^{FBG1} are always ≤1.53% and <0.71% whereas the e^{FBG2} ≤ 6.09% and ≤1.90%, during quiet breathing and tachypnea, respectively. The $MAPE^{FBG1}$ errors are always ≤12.87% and ≤5.86%, and $MAPE^{FBG2}$ always ≤15.36% and ≤4.90%, during quiet breathing and tachypnea, respectively. Data from FBG1 for Volunteer 1 were discarded.

Table 4.9. Mean RR values and percentage errors (e_P).

Quiet Breathing			
Volunteer	$\overline{RR^{FBG1}}$ [bpm]	$\overline{RR^{flow}}$ [bpm]	e_p^{FBG1} [%]
1	-	15.37	-
2	14.47	14.63	−1.09
3	14.36	14.14	1.53
4	22.36	22.09	1.22
5	15.15	15.22	−0.45
	$\overline{RR^{FBG2}}$ [bpm]	$\overline{RR^{flow}}$ [bpm]	e_p^{FBG2} [%]
1	15.30	15.37	−0.48
2	14.65	14.63	0.15
3	15.00	14.14	6.09
4	22.40	22.09	1.40
5	15.10	15.22	−0.79
Tachypnea			
Volunteer	$\overline{RR^{FBG1}}$ [bpm]	$\overline{RR^{flow}}$ [bpm]	e_p^{FBG1} [%]
1	-	83.62	-
2	48.65	48.80	−0.32
3	83.28	83.87	−0.71
4	54.53	54.58	−0.09
5	37.88	38.09	−0.56
	$\overline{RR^{FBG2}}$ [bpm]	$\overline{RR^{flow}}$ [bpm]	e_p^{FBG2} [%]
1	82.02	83.62	−1.90
2	48.46	48.80	−0.72
3	82.98	83.87	−1.05
4	54.99	54.58	0.75
5	38.01	38.09	−0.19

Table 4.10. Breath-by-breath absolute percentage errors, |ep|, and mean absolute percentage error (MAPE) values.

Quiet Breathing										
Volunteer	$\lvert e_p^{FBG1} \rvert$ [%]									**MAPE^{FBG1}** [%]
1	-	-	-	-	-	-	-	-	-	-
2	10.40	0.34	0.28	0.19	0.58	1.91	2.24	2.93	3.22	2.45
3	16.66	10.88	2.28	4.97	10.26	7.75	13.7	5.62	8.17	8.92
4	12.32	7.11	14.04	13.51	10.17	28.65	1.24	15.56	13.21	12.87
5	0.21	8.24	4.48	5.92	0.91	3.56	6.58	4.71	1.04	1.47
	$\lvert e_p^{FBG2} \rvert$ [%]									**MAPE^{FBG2}** [%]
1	5.28	3.76	0.20	2.18	4.75	4.19	1.33	4.92	4.33	3.44
2	2.69	0.86	2.06	1.14	0.97	2.09	0.19	6.76	4.42	2.36
3	29.36	12.12	4.05	3.63	17.35	27.82	8.21	15.75	19.93	15.36
4	15.34	16.03	4.22	0.85	7.36	3.46	3.33	0.16	1.35	5.79
5	2.53	1.52	0.95	1.95	~0	0.41	2.31	2.89	1.23	1.53

Tachypnea										
Volunteer	$\lvert e_p^{FBG1} \rvert$ [%]									**MAPE^{FBG1}** [%]
1	-	-	-	-	-	-	-	-	-	-
2	3.74	0.65	3.11	3.34	7.56	6.21	4.64	11.54	3.75	4.95
3	1.69	2.70	1.71	0.55	3.72	4.09	~0	5.82	1.16	2.38
4	2.95	9.77	4.48	18.86	0.37	1.46	1.44	5.35	8.10	5.86
5	0.52	1.06	0.77	1.84	0.50	0.73	0.24	1.31	2.11	1.01
	$\lvert e_p^{FBG2} \rvert$ [%]									**MAPE^{FBG2}** [%]
1	6.95	2.26	0.56	2.72	2.63	3.68	1.63	2.81	5.13	3.15
2	4.07	0.97	3.67	2.52	3.34	0.96	0.97	6.69	3.45	2.96
3	8.85	7.14	0.55	~0	1.12	1.14	0.55	1.11	7.41	3.10
4	6.41	2.47	9.92	5.24	5.43	2.11	6.23	6.29	~0	4.90
5	0.52	1.33	0.26	1.84	0.49	~0	1.72	1.02	0.72	0.88

3.1.2. Discussions

This study aims to verify the functioning of two smart patches previously presented in Section 2, Subsection 2.1 of this chapter in monitoring neck movements and RR at the same time.

The patches, here referred as FBG1 and FBG2, showed good performance in following both F/E and left ARm and detect the repetitions, while some limitations resulted in the right ARm detection. These findings could be explained considering different working conditions of FBG2 during ARm repetitions: the grating is tensioned during left ARm and compressed during right ARm. Therefore, the FBG2 compression during right ARm causes a partially adherence of this sensor to the neck surface. Also, the high sensitivity of the custom made flexible FBGs allows the monitoring of RR from the neck. Good accuracy was observed in terms of mean and breath-by-breath values in all trials but one (i.e., Volunteer 1) in which FBG1 failed, probably due to a poor sensor adherence to the user's skin. However, maximum MAPE values of 15.36% and 5.86% were retrieved during quiet and tachypnea breathing, respectively.

In the literature, there is no study in which a WD can simultaneously monitor neck posture and RR. Referring to neck movements' detection, wearable systems mainly based on electric sensors (e.g., inertial sensors [232], accelerometers [233], and piezoresistive sensors [234]) are proposed. However, some of them need a pre-calibration process [232], permit the detection of F/E movements only [233], or are cumbersome [234]. In contrast, the simple application of the two smart patches at two neck areas allows a non-invasive detection of the two joint movements (i.e., F/E and ARm), without the need for pre-calibration. Instead, for what concerns RR detection, there is a large number of FBG-based wearables, which mainly consist in elastic belts equipped with flexible sensors to be applied at the thorax [140], [144], or smart T-shirts [126], [132]. As already pointed out, the usage of predefined garments may be hardly acceptable, especially in those working context where employees need to assume a defined dress code. In this case the choice of applying the two patches in the neck area was motivated by the desire to propose a discrete system, with enhanced wearability and comfortability.

This is the first time that an FBG-based wearable system able to monitor neck movements and RR at the same time has been reported, which significantly expands the system's application possibilities. In this study, the contributions of respiratory activity and neck movement are analyzed separately, but future efforts could also focus on studying the cross-correlation between RR and neck movements on the sensors outputs in order to exploit the presented setup during the daily activities in workplaces. However, this should be considered as a first attempt toward the realization of a WD based on FBG sensing technology for posture and RR monitoring.

3.2. Wearable system composed of multiple soft flexible sensing elements for large-area detection

The multi-sensor wearable system presented in Section 2.3 is here exploited for both RR detection and sitting posture recognition of the three most common sitting postures – SPs (i.e., kyphotic, upright and lordotic posture).

In this section, parts of the work [235] which the PhD candidate has co-authored have been freely extracted.

3.2.1. Experimental assessment

A) Experimental setup and protocol

The experimental set-up (represented in Figure 4.48 (a)) is composed of the following elements:

1) The multi-sensor wearable system;
2) Stool, chair, and table: a stool between a chair and a table was used for seating the subject. The chair and table, positioned in front and behind the stool, respectively, supported the subject in performing the postures required by the protocol;
3) Optical interrogator and PC: an optical interrogator (si255, Micron Optics Inc., USA) was used to record the wearable system's outputs with a sampling frequency of 100 Hz. The data were real-time displayed on the PC monitor;
4) Reference device: the commercial instrument Zephyr BioHarness 3.0 (BH) (supplied by Medtronic, USA) was employed as a reference device to assess the respiratory activity and torso positioning regarding trunk tilt during the protocol execution. The breathing signal and torso inclination angle were collected with 25 Hz and 1 Hz sampling frequencies, respectively. The BH is a thoracic elastic belt embedding a strain gauge that is receptive to the chest wall displacements caused by the breathing activity and an electronic module including accelerometers for inclination assessment.

Ten volunteers (three males and seven females, whose anthropometric features are given as mean ± SD: age 27.1±2.6 y.o., body mass 60.7±8.3 kg, and height 168.7±7.0 cm) were enrolled in this study. Each volunteer was invited to sit on the stool, either bare-chested (males) or wearing a top (females). The wearable system was applied on the subject's back as shown in Figure 4.48 (b) and detailed in Subsection 2.3.3.1. (A). The BH was then worn at chest level.

The volunteer was instructed on the protocol. The subject was asked to breathe normally for 10 min in three different postures (see Figure 4.48 (c)): *i)* upright sitting (i.e., forming an angle of approximately 90° between legs and trunk, hands resting on

thighs), *ii)* kyphotic sitting (i.e., leaning forward and resting the forearms on the back of the chair) and *iii)* lordotic sitting (i.e., leaning backward, resting the elbows on the table). At the beginning and end of each of the three sitting postures, the subject performed 10 s of full-lung apnea to synchronize the instruments and easily split the respiratory signals acquired in the different postures.

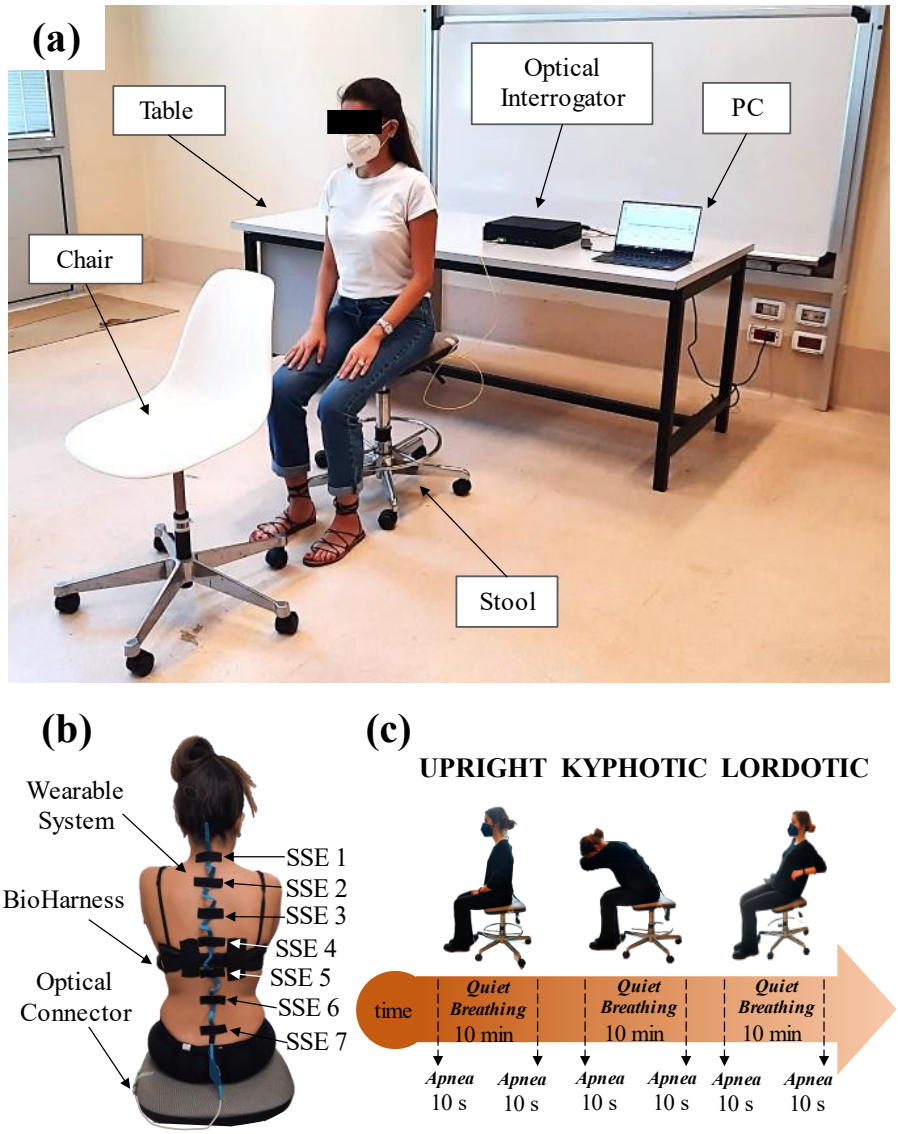

Figure 4.48. Representation of the experimental set-up (a) with an in-depth on the wearable system and reference device positioning (b), and illustration showing the experimental protocol (c).

B) Data analysis and results

The data were analyzed in MATLAB environment (MathWorks® Inc., USA) to discriminate the SPs and estimate the RR. The raw SSEs' signals collected for all the volunteers during the execution of the experiment were pre-processed by subtracting the mean of the first 10 λ_B values of each SSE in correspondence of the upright posture

(here considered as reference posture), so obtaining $\Delta\lambda_B$ signals. This step compensated for the variable pre-strain conditions to which the SSEs may have been subjected during application on different volunteers. In Figure 4.49, the $\Delta\lambda_B$ trend in time of one of the seven SSEs is reported as an example, together with the BH outputs, which are given as an angle variation in the sagittal plane for the torso position information (BH_P) and as a normalized voltage variation for the breathing waveform (BH_R).

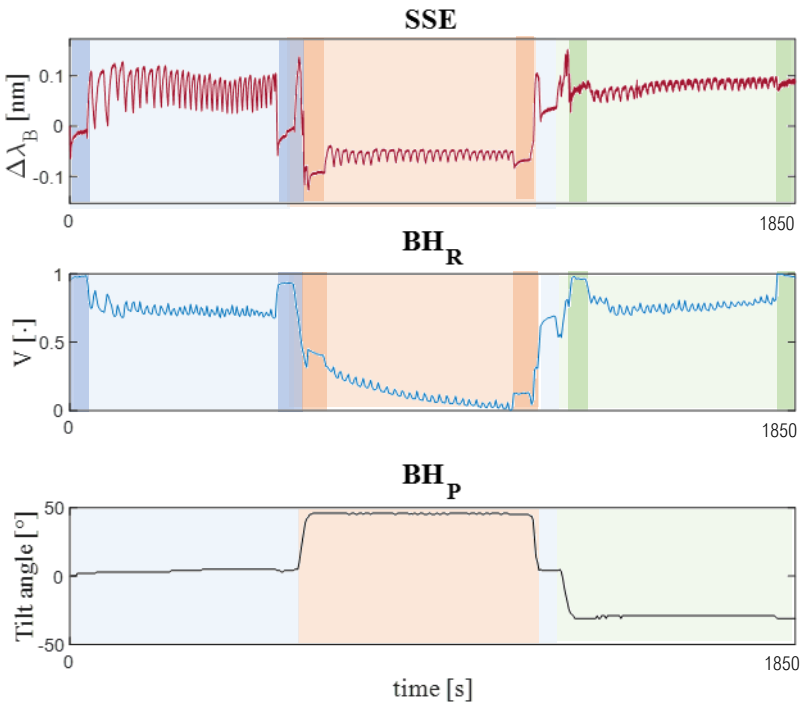

Figure 4.49. Example of the signals obtained for a volunteer by one of the seven SSEs ($\Delta\lambda_B$) and BH (BH_R showing the respiratory pattern and BH_P the inclination assumed by the torso in the three sitting postures). All signals were partitioned into the three postures by applying the following shaded coloring: light blue, orange and green for upright, kyphotic and lordotic postures, respectively. A more intense color grading was used to highlight the initial and final apneas (reported in SSE and BH_R signals) that enclose the respiratory signal in each of the three postures.

The seven SSEs' outputs (hereafter named $\Delta\lambda_B$ SSEs), the BH_P, and the BH_R signals obtained by each volunteer were then split into three traces related to the three performed SPs (i.e., upright, kyphotic, and lordotic) by cutting the signals comprised between the starting and final apneas. Then, for each posture, the seven $\Delta\lambda_B$ SSEs and BHR were synchronized by identifying the first minimum point after the initial apnea as the beginning point for each trace. BH_P was up-sampled at 25 Hz and synchronized with the respiratory signals consistently with the BH_R starting points. To summarize, for each volunteer, nine signals were retrieved for the upright, kyphotic, and lordotic SPs, respectively, subdivided into seven $\Delta\lambda_B$ SSEs trends, one BH_R, and one BH_P signals. The executed data analysis is reported below in different SP recognition and RR estimation subsections.

i) *Assessment of the wearable system in sitting posture recognition*

To assess the wearable system's ability to recognize the upright, kyphotic, and lordotic SPs assumed by the volunteers, a Naïve Bayes classifier [236] was implemented by exploiting the seven SSEs and BHP signals. It is a simple but efficient classification method that permits to categorize a cluster of data by attributing class labels. Naïve Bayesian classification assumes features to be independent, although good results have been obtained even for dataset in which such requirement was violated [237], [238]. This classifier has been largely used for posture and gesture recognition tasks [239]–[242] as allows easy algorithm development and rapid processing of large datasets.

The raw $\Delta\lambda_B$ SSEs values collected for all the volunteers in the three SPs manually labeled as upright, kyphotic, or lordotic, considering BHP as the reference for the posture identification: 0° for upright posture, positive angles for the kyphotic posture, and negative angles for lordotic posture (see Figure 4.49, bottom plot). The entire dataset consisted of a matrix 1760000x8 containing the $\Delta\lambda_B$ SSEs belonging to the 10 volunteers in columns ranging from 1 to 7, and the corresponding labels in column 8. Each volunteer presented an equal number of values for each of the three SP classes. The classifier was trained and validated on the data of seven subjects (i.e., 70% of the dataset) using a 7-fold cross validation method (i.e., leave-one-out approach [243]) which consisted, for each iteration, of training the algorithm on the data of six subjects and validating it on the excluded ones. The classifier obtained was then tested on the on the remaining three subjects' data (i.e., 30% dataset). The classification performances for training and testing were evaluated in terms of accuracy percentage (A%), which is defined as in Equation 4.18 for multi-class problems [244], [245]

$$A\% = \frac{\sum_{i=1}^{N} TP_i}{\sum_{i=1}^{N} C_i} \cdot 100 \qquad (4.17)$$

where N is the number of classes (i.e., 3), TP_i and C_i are the numbers of true predictions and the total number of observations made for the i-th class, respectively. Also, for each class and both in the training and testing phases, the true positive rate (TPR) and false negative rate (FNR) were evaluated as indexes of sensibility and specificity, respectively.

An average accuracy of 96.9% was obtained for the training phase, while a value of 97.6% was achieved for the test phase. Moreover, the values of TPR and FNR are reported in Table 4.11 for the upright, kyphotic, and lordotic SPs. In all the SPs, high percentages of TPR were obtained, ranging between 93.5% and 100%.

Table 4.11. TPR and FNR calculated for the three postures in the training and test phases.

Posture	Training		Test	
	TPR [%]	FNR [%]	TPR [%]	FNR [%]
U[a]	96.5	3.5	99.4	0.6
K[b]	100.0	0.0	100.0	0.0
L[c]	94.1	5.9	93.5	6.5

[a] Upright posture, [b] Kyphotic posture, [c] Lordotic Posture

ii) Assessment of the wearable system in respiratory rate estimation

To estimate RR in the three SPs, the seven $\Delta\lambda_{B\ SSEs}$ and BH_R signals related to each posture were analyzed. Signals were detrended, and a 1st order Butterworth pass-band filter (0.05 Hz and 1 Hz of cut-off frequencies) was implemented to minimize the frequency content not related to the respiratory activity.

The analysis in the frequency domain was performed to investigate the PSD of all the SSEs and BH signals. To preliminary assess which of the seven SSEs would be the most informative to retrieve RR, a first Welch's overlapped segment averaging estimator was applied on the 10 min $\Delta\lambda_{B\ SSEs}$ trends with a window length equal to the length of the analyzed signals. For each volunteer and posture, the SSE corresponding to the maximum value of the power spectrum was chosen among the seven as the best representative of respiratory pattern. Then, a second Welch's overlapped segment averaging estimator was applied to the chosen $\Delta\lambda_B$ SSE and the BH_R with a hamming window of 45 s length, 50% overlap value between windows, and update time of 5 s. The RR (expressed in breaths per minute - bpm) was calculated for each window as $RR_i = 60 \cdot f_{Ri}$ where f_{Ri} is the frequency (given in Hz) corresponding to the maximal value of the PSD spectrum of the i-th window, which embodies the signal's periodicity. An amount of 112 values of RR were computed both by the SSE and BH signals for each subject and SP. The RR mean (RR_{avr}^{SSE} and RR_{avr}^{BH}) and standard deviation (SD) values were retrieved.

To quantitatively assess the capability of the wearable system to estimate RR, a comparison with the reference system was carried out by calculating the mean absolute percentage error among all the volunteers and in the upright, kyphotic, and lordotic SPs. The MAPE was obtained as indicated in Equation 4.19:

$$\text{MAPE} = \frac{1}{n}\sum_{i=1}^{n} \frac{|RR_i^{SSE} - RR_i^{BH}|}{RR_i^{BH}} \cdot 100 \qquad (4.18)$$

where RR_i^{SSE} and RR_i^{BH} were the RR calculated in the i-th window from the SSE and the reference system signals, respectively, and n was the number of windows (i.e., 112). Moreover, the linear regression was executed to evaluate the correlation between the

RR_i^{SSE} and RR_i^{BH} of all the subjects in each posture. The R^2 coefficient and the linear regression slope β (obtained for y=α+βx when α=0) were evaluated. Also, the Bland-Altman analysis was performed to obtain the mean of differences (MOD) and the related limits of agreements (LOAs) values [210].

In Figure 4.50 (A), (B) and (C), the RR_i^{SSE} and RR_i^{BH} and SD values calculated for every volunteer in upright, kyphotic and lordotic postures, respectively, show good agreement between the wearable system and the reference instrument. A difference of 0.71 bpm was observed (i.e., volunteer 6 in lordotic posture), which is equivalent to the PSD plot resolution. Also, in Table 4.12, the average MAPE values on all the volunteers are reported for the three postures, showing the greater value in lordosis (i.e., 3.83%).

In Figure 4.50 (D), (E) and (F), the correlation plots are shown for the three postures and the R^2 and β values are reported in Table 4.12. β values range between 0.98 and 1 for the three postures. R^2 values are close to 1 in upright and kyphotic sitting showing good agreement with the linear fit, while the lordotic-related value is way lower (i.e., 0.66). Furthermore, in Table 4.12 the MOD and the LOAs obtained through the Bland-Altman analysis (see the plots in Figure 4.50 (G), (H), and (I) are presented for each posture. MODs are comparable along the three postures and close to zero. LOAs are < 1 in upright and kyphosis, while in lordosis are slightly higher (i.e., 0.98 bpm and 0.76 bpm vs. 3.63 bpm, respectively).

Table 4.12. MAPE, MOD, LOAS, R^2 and β calculated for the three postures.

Posture	MAPE [%]	R^2	β	MOD [bpm]	LOAs [bpm]
U[a]	1.03	0.98	0.99	–0.01	0.98
K[b]	0.74	0.98	1	0.01	0.76
L[c]	3.83	0.66	0.98	–0.20	3.63

[a] Upright posture, [b] Kyphotic posture, [c] Lordotic Posture

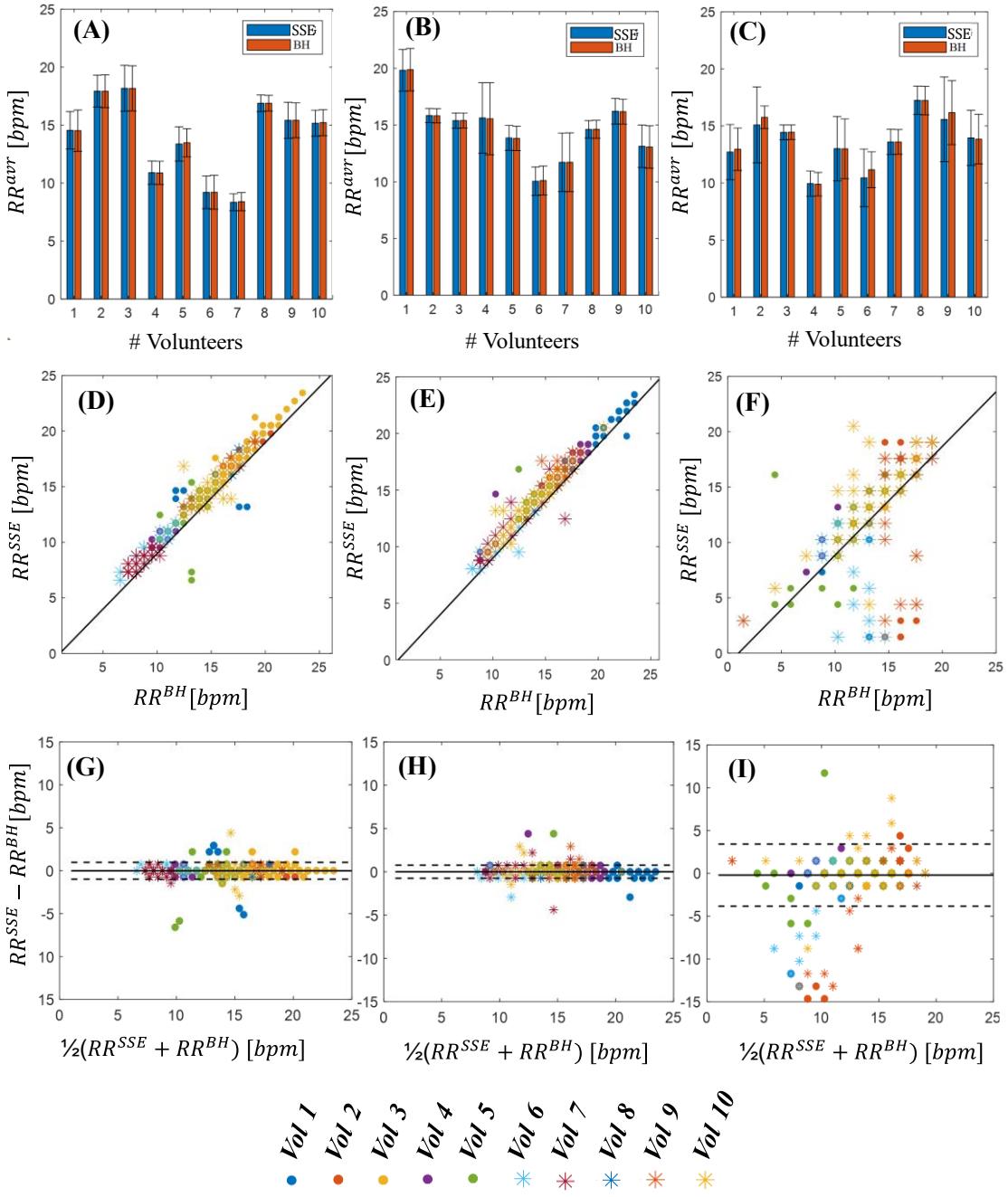

Figure 4.50. Analysis performed to compare the performance of the wearable system and the reference device in RR estimation. In (A), (B) and (C) barplots showing for each volunteer RR_{avr}^{SSE} and RR_{avr}^{BH} with the related SDs in upright, kyphotic and lordotic postures, respectively. The correlation plots displaying RR^{SSE} vs. RR^{BH} in upright (D), kyphotic (E) and lordotic (F) postures. Bland-Altman plots showing the bias between RR^{SSE} vs. RR^{BH} values expressed as MOD (black solid line) ± LOAs (black dotted lines) for upright (G), kyphosis (H) and lordosis (I).

iii) *Pilot test on additional subjects performing different depths and frequencies of breathing*

To test the ability of the implemented method to generalize, the algorithm was then applied to the data retrieved from three new subjects (all females, age 26.3±20.5 y.o., body mass 55.0±3.6 kg, and height 166.0±4.3 cm) wearing the wearable system (as detailed in Section 3.2.3, Subsection A, 100 Hz of sampling rate) and performing breathing tests assuming the three SPs under more challenging conditions. In particular, the experimental protocol was divided into two trials which were designed as follows: *i)* the subject was asked to breath at different frequencies by following the inspiratory and expiratory rhythm provided by a metronome. The trial consisted of 60 s of eupnea (i.e., set at 15 bpm [109]), 60 s of tachypnea (i.e., set at 30 bpm [109]) and 60 s of bradypnea breathing (i.e., set at 6 bpm [109]) interspersed with 5 s of apnea each. The exercise was repeated assuming each of the three SPs (i.e., upright, kyphotic and lordotic) (see Figure 4.51 (a)); *ii)* the subject was asked to perform 5 s of apnea, 60 s of deep breathing (i.e., at the maximal lung capacity) followed by 5 s of apnea and 60 s of shallow breathing (i.e., drawing a reduced amount of air in the lungs). No indications on the breathing rates were given at this stage. Respiratory data were collected at 10 Hz of sampling rate by a digital spirometer (MIR Spirolab III, MIR, Rome, Italy). The average tidal volumes were found to be 2.24 L, 1.49 L and 1.90 L in upright, kyphotic and lordotic posture, respectively, for the deep breathing, and 0.68 L, 0.68 L and 0.71 L for the shallow breathing. Once again, the test was repeated for each of the three SPs (see Figure 4.51 (b)).

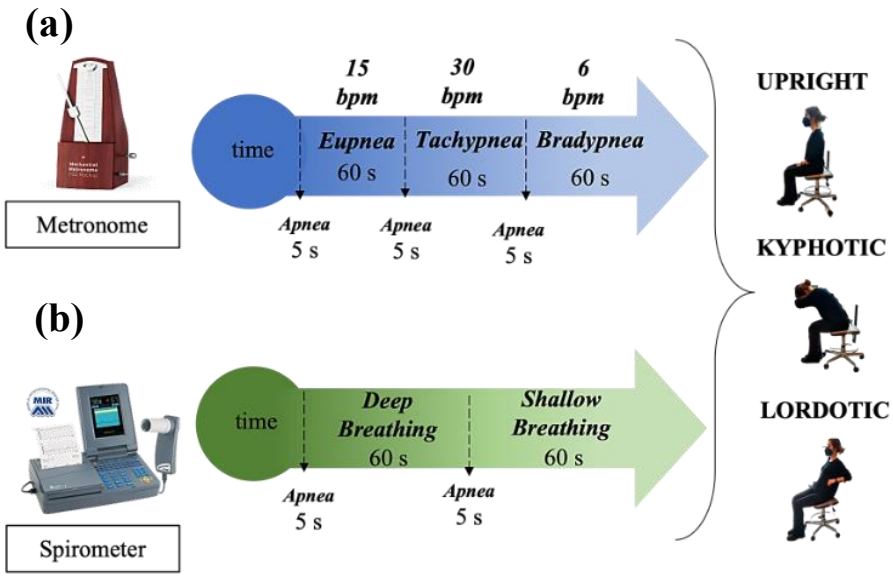

Figure 4.51. Representation of the experimental set-up and protocol carried out on three external subjects in different breathing conditions.

Raw data of each subject collected by the seven SSE were plot and the $\Delta\lambda_B$ value was achieved by subtracting the mean of the first 10 λ_B values in upright SP, as already detailed in Section 3.2.3, Subsection B. The model previously trained was tested on the dataset consisting of 270045 values for each SSEs (i.e., 90015 values for each volunteer), equally divided for the three class labels. An average accuracy of 97.5% was retrieved, while the TPR and FNR percentages are reported in Table 4.13.

$\Delta\lambda_B$ signals of each SSEs in the three SPs of trial *i)* were split into the three 60 s traces corresponding to eupnea, tachypnea and bradypnea by identifying the signals comprised between two following apneas. The $\Delta\lambda_B$ SSEs of trial *ii)* were synchronized by means of the first minimum after the first apnea with the correspondent spirometer signals. Then the traces corresponding to the deep and shallow breathing were identified for each SPs. The RR were calculated for the wearable system for each breathing condition (i.e., eupnea, tachypnea, bradypnea, deep and shallow breathing) and posture by applying the method detailed in Section 3.2.3, Subsection B. MAPE values were evaluated by comparing the RR values retrieved by the wearable system and the ones imposed by the metronome (i.e., for the eupnea, tachypnea and bradypnea breathing) and obtained by the spirometer (i.e., for deep and shallow breathing). In Table 4.13 MAPE values are reported, showing an overall error < than 3.6%.

Table 4.13. TPR, FNR and MAPE calculated for the three postures in eupnea, tachypnea, bradypnea, deep and shallow breathing.

Posture	TPR [%]	FNR [%]	MAPE [%]				
			E[d]	T[e]	B[f]	D[g]	S[h]
U[a]	92.6	7.4	2.36	2.34	2.30	3.11	3.56
K[b]	100.0	0.0	2.36	2.34	2.30	0.74	1.19
L[c]	99.9	0.1	2.36	1.56	2.30	0.91	2.88

[a] Upright posture, [b] Kyphotic posture, [c] Lordotic Posture
[d]Eupnea, [e]Tachypnea, [f]Bradypnea, [g]Deep Breathing, [h]Shallow Breathing

3.2.2. Discussions

In this section, the capability of a previously developed wearable system for rehabilitation monitoring purposes (refer to Paragraph 2, Section 2.3) to estimate sitting postures and assess RR was proven on 13 healthy volunteers performing breathing tasks assuming upright, kyphotic and lordotic sitting stances.

To assess the wearable system's ability to distinguish the upright, kyphotic and lordotic postures, a Naïve Bayes classifier was implemented, which, although basic, can prove very efficient. Satisfactory results have been obtained, as 96.9% and 97.6% of

accuracy was retrieved in the training and test phases conducted on seven and three subjects, respectively, while A= 97.5% was obtained by testing the developed model on three additional subjects performing different breathing tasks, so proving the model ability to adapt to new data. TPR percentages values were always > 92.5% in all the postures and 100% was always reported for the kyphotic class, due to the condition of greater strain of the SSEs during kyphosis which results in higher $\Delta\lambda_B$ dispersion and making this class more recognizable.

Concerning the RR estimation, the performance of the proposed system was evaluated by comparing the measurements obtained with those of the BH. Such reference system was, in this case, preferred to the more canonical MoCap for reasons of convenience and ease of use. However, it is believed that this choice did not substantially influence the evaluation. In fact, BH's performance may decrease for applications in dynamic scenarios (e.g., during sports activity), but the presented experiments were conducted under static conditions. In addition, RR_i^{BH} values were not obtained directly from the BH but were calculated by applying the same procedure explained in the subparagraph 3.2.1.B to the retrieved raw signals. The goodness of this process is also evidenced by the agreement between the wearable system and the reference one. In fact, no substantial differences were retrieved between RR_{avr}^{SSE} and RR_{avr}^{BH}. Moreover, the linear regression slope is > 0.98 for the three postures, while R^2 values are 0.98 in upright and kyphotic posture, while is 0.66 in lordotic one. Also, all MOD values are close to zero, with a maximum LOAs value of 3.63 bpm retrieved in lordosis. In the worst-case scenario, the MAPE was 3.83% (i.e., lordotic posture), while the kyphotic position obtained the lower value (i.e., 0.74 %). From a general point of view, the wearable system exhibits slightly better results in the kyphotic and upright positions, despite its performance remaining competitive even in lordosis. A potential explanation may be that the accentuated back arch experienced in lordosis causes the skin to wrinkle, resulting in a loss of adhesion of the SSEs. The good results achieved by applying the algorithm to the data retrieved by the three additional subjects proven the validity of the method in estimating RR, even in more challenging breathing conditions (maximum MAPE value < 3.6%).

As already underlined, no FBG-based wearables have already been proposed for the simultaneous monitoring of posture and RR.

Regarding posture assessment, several studies describing cushions and chairs embedding FBGs [180], [181] or, more in general, pressure or force sensors [246], [247] and exploiting different algorithms for sitting posture detection are reported. Nevertheless, the employment of cushions may affect the normal sitting physiology of the user, while the sensors' integration process into seats and backrests may result in substantial changes in the ergonomics of chairs, which could no longer conform to the characteristics required by the guidelines. Instead, the proposed wearable system represents a viable solution to these problems since it does not affect the sitting posture. Besides, this WD permits continuous monitoring, in contrast with smart

cushions and chairs whose performance is affected by loss of contact with the user. In contrast, wearables dedicated to RR monitoring are largely widespread, and mainly consist in chest straps [140], [144], smart T-shirts [133], [134] and corsets [137]. Compared to other wearables, the presented device showed some advantages. For example, it permits discrete application underneath ordinary clothes. This could represent a significant advantage as the use of given garments might not be pleasant to workers who need to adopt specific dress codes or, more in general, which would not limit their choice in dressing. Moreover, wearability-related issues are overcome thanks to the SSEs' modularity which makes the system adaptable to any body shape. Besides, smart textiles embedding sensing technologies could present concerns regarding the washing method to be adopted, while no sanitizing is required for our wearable system as the double-sided adhesive tape used to attach the SSEs is disposable.

Chapter 5 – Conclusion

1. Achievements of the thesis work

With the gradual increase in technological innovation that has led the occupational and healthcare sectors to a 4.0 level, wearable devices have played increasingly prominent roles in everyday life, as they allow continuous and non-intrusive monitoring of the individual's all-round health status [248].

In the past twenty years, there has been relevant exploitation of FBG sensors in the development of smart wearables [76], [249], [250]. These sensors' features (such as small dimensions, flexibility, high sensitivity to strain and immunity to electromagnetic radiations) have enabled the manufacture of smart systems (in the form of textiles, soft flexible devices and 3D printed elements) which are highly performant, lightweight, compliant with the human body shape, and compatible with the presence of electromagnetic fields. These characteristics make such devices suitable for occupational and clinical scenarios.

Building on this trend, this research work aimed to design and develop novel FBG-based wearable systems suitable for monitoring respiratory parameters and trunk motion activity in occupational and clinical environments, respectively.

This work lays its basis on the recognition of the different requirements that each device had to meet in terms of efficiency, wearability, usability, and acceptability.

The design study aims to answer to these requirements by proposing a system that is highly efficient in the required task, and, at the same time, that is resistant to daily usage. In addition, the user's characteristics, such as anthropometric features, daily habits or disabilities, must be taken into account to ensure the correct fit and to offer a solution that is easy to use and suitable for the environment in which the system is to be used.

At this juncture, starting from the literature, several strategies were identified that best allowed for the realization of a high-performing wearable which could overcome the limitations of the solutions that have been proposed in research up to that point.

On the respiratory side, the development of the wearables for RR detection which were presented in this work has proceeded along two separate paths, exploiting two different FBGs' configurations.

The first proposal consisted of two elastic bands to be worn around the torso and equipped with a total of four dumbbell-shaped soft flexible sensors dedicated to the detection of respiratory-related chest-wall movements. The strengths of this solution lie in the optimized shape of the sensors (conveying the strain on the central sensitive portion of the flexible sensors) and the adoption of a multi-sensor approach, which permits data to be collected at different sites of the torso instead of just one (as in the

canonical approaches). The redundancy of information has proved to be crucial because *i)* allows the detection of RR even in case that a sensor fails or in presence of artefacts (e.g., motion artefacts) and *ii)* enables the monitoring of respiratory patterns even in subjects affected by diseases in which the breathing activity is impaired.

The second solution came as an accessory whose sensitive part (i.e., an FBG functionalized in agar film) is intended to be placed under the nostrils to record the ΔRH of the inspiratory/expiratory airflows. The advantages brought by this system are *i)* open and non-invasive design (as opposed to masks or nasal cannulas) that avoids feelings of facial constriction and discomfort, and *ii)* small footprint, which also allows its usage in confined spaces such as MRI environments.

Turning instead to the trunk monitoring of movement and posture, unlike in the case of breathing, the literature lacked the presence of efficient wearable solutions based on FBG sensors. Therefore, the main difficulty encountered in this field was to answer the question of whether this technology (already widely used to detect small movements of various kinds) was indeed suitable for identifying large ranges of movement such as those related to the trunk. And, if so, which sensor configuration could have maximized the performance of the wearable without damaging the sensing parts.

Always bearing in mind that it was necessary to encapsulate the FBGs in soft, flexible silicone matrices to strengthen the fiber, several configurations have been explored. A first basic proof of concept was made by equipping a commercial T-shirt with flexible sensors placed on the back. This trial proven the feasibility of using FBG technology in monitoring back movements, but also emphasized the need to strengthen the sensitive elements. Thus, a wearable elastic structure with a single sensor element was fabricated, showing high wearability and ease-of-use. Lastly, a further step forward was made by producing a multi-sensor system for the entire back area monitoring. Moving from one solution to another makes the evolutionary trend of the shape of the sensing elements visible. In fact, ever smaller and thicker sensitive elements were fabricated to protect the embedded FBGs.

Also in this case, the adoption of a multi-sensor approach was of prominent relevance as it provided the opportunity to investigate a previously unexplored field, that is the simultaneously monitoring of both the respiratory path and trunk motion activity by means of FBG-based wearable systems. In particular, significant innovation has been brought by the use of the multi-sensor system which, together with RR monitoring, enabled the recognition of the three most common sitting postures via Naïve-Bayes classification.

In conclusion, in this thesis work, several wearable solutions were proposed for respiratory and trunk posture monitoring, overcoming some limitations of existing systems in respiratory field, and introducing brand new devices for the back motion monitoring.

The systems' development process always took into account the aim and the requirements that a wearable must meet but, most importantly, it helped to produce a tool tailored to the end user's needs. For this reason, different devices have been proposed for the same objective. In fact, although both effective, in different contexts one solution might be preferred over another. Therefore, it is possible to state that there is no perfect wearable system suitable for all applications but, given a defined goal and boundary conditions, a single wearable can be developed to be the optimal solution in relation to that context.

The results showed that all the solutions presented can provide useful support in representing an overall picture of the users' health status. More in particular, referring to the clinical context, such devices could support clinicians in the management of the hemiplegic patients in two main modalities:

i) Objective assessment of the patient's level of disability: to date, the assessment of the disability status is performed by the clinicians through the subjective evaluation of the patient's ability to perform specific tasks (i.e., assignment of the Fugl-Mejer index). The use of the described WDs could provide information on the respiratory and motor activity as a corollary, in order to execute conscious evaluations supported by objective data. In addition, a comparison of these data over time could provide interesting feedbacks on the evolution of the patient's health status and thus on the progress of the rehabilitation path;

ii) Objective evaluation of the correct execution of rehabilitation exercises: constant feedback while performing rehabilitation tasks could make the patient more aware and motivate him/her to perform the exercises correctly. WDs can also support the clinicians in assessing the correctness of the execution and defining personalized strategies to improve motor recovery.

Moreover, in the occupational scenario, the use of such systems could make the difference in two respects:

i) Awareness on the sitting position assumed: being aware of the acquired posture can help sedentary workers maintain proper sitting thus preventing musculoskeletal disorders, for the benefit of both the worker and the employer;

ii) Awareness on the state of psychological stress: altered RR values under conditions of physical rest are indicative of stress-related psychological diseases. Awareness on the condition of mental load can stimulate the worker and the employer to take steps for stress management.

2. Limitations

The main limitation in the use of such devices would be the encumbrance of the fiber optic interrogation unit. In fact, while in static contexts (such as in videoterminal working scenarios or during MRI examinations) this does not represent a major drawback, the size of fiber optic interrogators may limit the usability of the wearable devices in more active applicative contexts. However, constant technological advancement is leading to the production of portable interrogators of reduced sizes that do not need cable connection since they are powered by re-chargeable batteries and allow remote data transmission [251]–[253].

A second limit is represented by the high cost of the optical interrogation units. Prices depend on the device performance (mainly measured in terms of accuracy, resolution, sampling rate, number of channels and acquisition bandwidth). Of course, higher-performance devices will have higher prices, starting from a minimum of thousand euros, up to tens of thousands of euros. Such costs could be a major limitation for the use of FBG-based wearables. In fact, an expensive initial purchase of a large number of interrogators may not be sustainable, especially by small companies or small hospitals. However, constant technological innovation increases competition in the market, leading to a constant lowering of prices.

3. Recommendation for future works

Based on these conclusions, the aspect of the research that lends itself to greater investigation might be the use of the wearable systems in combination with classifiers. In fact, the large amount of high-quality data collected by FBG-based sensors can be used for database creation in the service of classifiers and machine learning. This approach could provide new insights into the classification of new sitting postures or can help recognizing conditions of abnormal breathing.

Starting from the basic classification algorithm applied in [235], practitioners may investigate new methodologies to enhance the quality of the classification (for example by applying the principal component analysis [254]–[256] or different normalization techniques [257], [258]).

Further efforts could be devoted to the development of a GUI that displays the user's posture and breathing activity in real time. This might be particularly useful as it would help identify the range of back curvature outside of which sitting posture is considered incorrect or detect compensatory movements performed during rehabilitation sessions. In addition, it could help in real-time recognition of respiratory stress situations that patients might experience due to overly intense rehabilitation sessions.

Reference List:

[1] E. G. Popkova, Y. V Ragulina, and A. V Bogoviz, *Industry 4.0: Industrial revolution of the 21st century*, vol. 169. Springer, 2019.

[2] K. Ejsmont, B. Gladysz, and A. Kluczek, "Impact of industry 4.0 on sustainability—bibliometric literature review," *Sustainability*, vol. 12, no. 14, p. 5650, 2020.

[3] S. Bag and J. H. C. Pretorius, "Relationships between industry 4.0, sustainable manufacturing and circular economy: proposal of a research framework," *Int. J. Organ. Anal.*, 2020.

[4] L. Monostori *et al.*, "Cyber-physical systems in manufacturing," *Cirp Ann.*, vol. 65, no. 2, pp. 621–641, 2016.

[5] R. Schmidt, M. Möhring, R.-C. Härting, C. Reichstein, P. Neumaier, and P. Jozinović, "Industry 4.0-potentials for creating smart products: empirical research results," in *International Conference on Business Information Systems*, 2015, pp. 16–27.

[6] G. Schuh, T. Gartzen, T. Rodenhauser, and A. Marks, "Promoting work-based learning through industry 4.0," *Procedia Cirp*, vol. 32, pp. 82–87, 2015.

[7] S. Paul *et al.*, "Industry 4.0 applications for medical/healthcare services," *J. Sens. Actuator Networks*, vol. 10, no. 3, p. 43, 2021.

[8] C. More, *Understanding the industrial revolution*. Routledge, 2002.

[9] H. Mohajan, "The first industrial revolution: Creation of a new global human era," 2019.

[10] H. Mohajan, "The second industrial revolution has brought modern social and economic developments," 2019.

[11] C. Cooper and R. Kaplinsky, *Technology and development in the third industrial revolution*. Routledge, 2005.

[12] K. Schwab, *The fourth industrial revolution*. Currency, 2017.

[13] S. S. Kamble, A. Gunasekaran, and S. A. Gawankar, "Sustainable Industry 4.0 framework: A systematic literature review identifying the current trends and future perspectives," *Process Saf. Environ. Prot.*, vol. 117, pp. 408–425, 2018.

[14] M. Hermann, T. Pentek, and B. Otto, "Design principles for industrie 4.0 scenarios," in *2016 49th Hawaii international conference on system sciences (HICSS)*, 2016, pp. 3928–3937.

[15] V. Roblek, M. Meško, and A. Krapež, "A complex view of industry 4.0," *Sage open*, vol. 6, no. 2, p. 2158244016653987, 2016.

[16] M. Brettel, N. Friederichsen, M. Keller, and M. Rosenberg, "How virtualization, decentralization and network building change the manufacturing landscape: An Industry 4.0 Perspective," *Int. J. Inf. Commun. Eng.*, vol. 8, no. 1, pp. 37–44, 2014.

[17] M. Mas-Machuca, J. Berbegal-Mirabent, and I. Alegre, "Work-life balance and its relationship with organizational pride and job satisfaction," *J. Manag. Psychol.*, 2016.

[18] A. Polak-Sopinska, Z. Wisniewski, A. Walaszczyk, A. Maczewska, and P. Sopinski, "Impact

of industry 4.0 on occupational health and safety," in *International Conference on Applied Human Factors and Ergonomics*, 2019, pp. 40–52.

[19] S. Bragança, E. Costa, I. Castellucci, and P. M. Arezes, "A brief overview of the use of collaborative robots in industry 4.0: human role and safety," *Occup. Environ. Saf. Heal.*, pp. 641–650, 2019.

[20] V. Leso, L. Fontana, and I. Iavicoli, "The occupational health and safety dimension of Industry 4.0," *Med. Lav.*, vol. 109, no. 5, p. 327, 2018.

[21] J. Lemos, P. D. Gaspar, and T. M. Lima, "Environmental Risk Assessment and Management in Industry 4.0: A Review of Technologies and Trends," *Machines*, vol. 10, no. 8, p. 702, 2022.

[22] A. Adem, E. Çakit, and M. Dağdeviren, "Occupational health and safety risk assessment in the domain of Industry 4.0," *SN Appl. Sci.*, vol. 2, no. 5, pp. 1–6, 2020.

[23] D. Podgorski, K. Majchrzycka, A. Dąbrowska, G. Gralewicz, and M. Okrasa, "Towards a conceptual framework of OSH risk management in smart working environments based on smart PPE, ambient intelligence and the Internet of Things technologies," *Int. J. Occup. Saf. Ergon.*, vol. 23, no. 1, pp. 1–20, 2017.

[24] J. R. Gisbert *et al.*, "Integrated system for control and monitoring industrial wireless networks for labor risk prevention," *J. Netw. Comput. Appl.*, vol. 39, pp. 233–252, 2014.

[25] R. Orji and K. Moffatt, "Persuasive technology for health and wellness: State-of-the-art and emerging trends," *Health Informatics J.*, vol. 24, no. 1, pp. 66–91, 2018.

[26] B. Lunenfeld, "An aging world–demographics and challenges," *Gynecological Endocrinology*, vol. 24, no. 1. Taylor & Francis, pp. 1–3, 2008.

[27] Department of Economic and Social Affairs of the United Nations, "World Population Prospects 2022: Summary of Results," 2022. https://www.un.org/development/desa/pd/sites/www.un.org.development.desa.pd/files/wpp2022_summary_of_results.pdf (accessed Nov. 09, 2022).

[28] C. L. Harrison-Felix, L. A. Hawley, A. W. Brown, and M. J. DeVivo, "Life expectancy and wellness," *Brain Inj. Med. Princ. Pract.*, pp. 319–333, 2013.

[29] J. S. Millar and C. Hull, "Measuring human wellness," *Soc. Indic. Res.*, vol. 40, no. 1, pp. 147–158, 1997.

[30] E. Jaul and J. Barron, "Age-related diseases and clinical and public health implications for the 85 years old and over population," *Front. public Heal.*, vol. 5, p. 335, 2017.

[31] E. Peters, R. Pritzkuleit, F. Beske, and A. Katalinic, "Demographic change and disease rates: a projection until 2050," *Bundesgesundheitsblatt. Gesundheitsforschung. Gesundheitsschutz*, vol. 53, no. 5, pp. 417–426, 2010.

[32] S. Tian, W. Yang, J. M. Le Grange, P. Wang, W. Huang, and Z. Ye, "Smart healthcare: making medical care more intelligent," *Glob. Heal. J.*, vol. 3, no. 3, pp. 62–65, 2019.

[33] D. Sharma, G. Singh Aujla, and R. Bajaj, "Evolution from ancient medication to human-centered Healthcare 4.0: A review on health care recommender systems," *Int. J. Commun. Syst.*, p. e4058, 2019.

[34] H. Zhu *et al.*, “Smart healthcare in the era of internet-of-things,” *IEEE Consum. Electron. Mag.*, vol. 8, no. 5, pp. 26–30, 2019.

[35] G. Aceto, V. Persico, and A. Pescapé, “Industry 4.0 and health: Internet of things, big data, and cloud computing for healthcare 4.0,” *J. Ind. Inf. Integr.*, vol. 18, p. 100129, 2020.

[36] J. Xu, E. Huang, L. Hsieh, L. H. Lee, Q.-S. Jia, and C.-H. Chen, “Simulation optimization in the era of Industrial 4.0 and the Industrial Internet,” *J. Simul.*, vol. 10, no. 4, pp. 310–320, 2016.

[37] H. Yin, A. O. Akmandor, A. Mosenia, and N. K. Jha, “Smart healthcare,” *Found. Trends® Electron. Des. Autom.*, vol. 12, no. 4, pp. 401–466, 2018.

[38] S. Majumder *et al.*, “Smart homes for elderly healthcare—Recent advances and research challenges,” *Sensors*, vol. 17, no. 11, p. 2496, 2017.

[39] J. Jasiewicz, W. D. Kearns, J. Craighead, J. L. Fozard, S. Scott, and J. McCarthy, “Smart rehabilitation for the 21st century: the Tampa Smart Home for veterans with traumatic brain injury,” *J. Rehabil. Res. Dev.*, p. vii, 2011.

[40] R. Mieronkoski, I. Azimi, L. Sequeira, and L.-M. Peltonen, “Smart home technology for geriatric rehabilitation and the Internet of Things,” in *Smart Home Technologies and Services for Geriatric Rehabilitation*, Elsevier, 2022, pp. 25–42.

[41] H.-J. Kim *et al.*, “Smart Decentralization of Personal Health Records with Physician Apps and Helper Agents on Blockchain: Platform Design and Implementation Study,” *JMIR Med. informatics*, vol. 9, no. 6, p. e26230, 2021.

[42] A. Holzinger, C. Röcker, and M. Ziefle, “From smart health to smart hospitals,” in *Smart health*, Springer, 2015, pp. 1–20.

[43] M. K. Hassan, A. I. El Desouky, S. M. Elghamrawy, and A. M. Sarhan, “Big data challenges and opportunities in healthcare informatics and smart hospitals,” *Secur. smart cities Model. Appl. challenges*, pp. 3–26, 2019.

[44] M. Dehghani, “An assessment towards adoption and diffusion of smart wearable technologies by consumers: the cases of smart watch and fitness wristband products.,” in *HT (Extended Proceedings)*, 2016, pp. 1–6.

[45] W. Schreurs, M. Hildebrandt, and E. Kindt, “Tehrani, K. and Michael, A.,‘Wearable Technology and Wearable Devices: Everything,” *Elgar Encycl. Law Data Sci.*, p. 240, 2022.

[46] S. F. Rasool, M. Wang, Y. Zhang, and M. Samma, “Sustainable work performance: the roles of workplace violence and occupational stress,” *Int. J. Environ. Res. Public Health*, vol. 17, no. 3, p. 912, 2020.

[47] S. Clarke and C. Cooper, *Managing the risk of workplace stress: Health and safety hazards*. Routledge, 2004.

[48] N. Chawla, “AI, IOT and wearable technology for smart healthcare? A review,” *Int J Green Energy*, vol. 7, no. 1, pp. 9–13, 2020.

[49] V. A. Goodyear, C. Kerner, and M. Quennerstedt, “Young people’s uses of wearable healthy lifestyle technologies; surveillance, self-surveillance and resistance,” *Sport. Educ. Soc.*, vol. 24, no. 3, pp. 212–225, 2019.

[50] T. Prioleau, E. Moore, and M. Ghovanloo, “Unobtrusive and wearable systems for automatic dietary monitoring,” *IEEE Trans. Biomed. Eng.*, vol. 64, no. 9, pp. 2075–2089, 2017.

[51] M. Zubair, K. Song, and C. Yoon, “Human activity recognition using wearable accelerometer sensors,” in *2016 IEEE International Conference on Consumer Electronics-Asia (ICCE-Asia)*, 2016, pp. 1–5.

[52] W. Lu *et al.*, “An arrhythmia classification algorithm using C-LSTM in physiological parameters monitoring system under internet of health things environment,” *J. Ambient Intell. Humaniz. Comput.*, pp. 1–11, 2021.

[53] M. Egger, M. Ley, and S. Hanke, “Emotion recognition from physiological signal analysis: A review,” *Electron. Notes Theor. Comput. Sci.*, vol. 343, pp. 35–55, 2019.

[54] F. Cavallo, F. Semeraro, G. Mancioppi, S. Betti, and L. Fiorini, “Mood classification through physiological parameters,” *J. Ambient Intell. Humaniz. Comput.*, vol. 12, no. 4, pp. 4471–4484, 2021.

[55] A. Nicolò, M. Girardi, and M. Sacchetti, “Control of the depth and rate of breathing: metabolic vs. non-metabolic inputs,” *J. Physiol.*, vol. 595, no. 19, p. 6363, 2017.

[56] M. J. Tipton, A. Harper, J. F. R. Paton, and J. T. Costello, “The human ventilatory response to stress: rate or depth?,” *J. Physiol.*, vol. 595, no. 17, pp. 5729–5752, 2017.

[57] M. A. Cretikos, R. Bellomo, K. Hillman, J. Chen, S. Finfer, and A. Flabouris, “Respiratory rate: the neglected vital sign,” *Med. J. Aust.*, vol. 188, no. 11, pp. 657–659, 2008.

[58] I. Smith, J. Mackay, N. Fahrid, and D. Krucheck, “Respiratory rate measurement: a comparison of methods,” *Br. J. Healthc. Assist.*, vol. 5, no. 1, pp. 18–23, 2011.

[59] S. Cook, M. Togni, M. C. Schaub, P. Wenaweser, and O. M. Hess, “High heart rate: a cardiovascular risk factor?,” *Eur. Heart J.*, vol. 27, no. 20, pp. 2387–2393, 2006.

[60] P. B. O’Sullivan, T. Mitchell, P. Bulich, R. Waller, and J. Holte, “The relationship beween posture and back muscle endurance in industrial workers with flexion-related low back pain,” *Man. Ther.*, vol. 11, no. 4, pp. 264–271, 2006.

[61] W. P. Neumann *et al.*, “A posture and load sampling approach to determining low-back pain risk in occupational settings,” *Int. J. Ind. Ergon.*, vol. 27, no. 2, pp. 65–77, 2001.

[62] J. Hartvigsen, C. Leboeuf-Yde, S. Lings, and E. H. Corder, “Is sitting-while-at-work associated with low back pain? A systematic, critical literature review,” *Scand. J. Public Health*, vol. 28, no. 3, pp. 230–239, 2000.

[63] C. Zeagler, “Where to wear it: functional, technical, and social considerations in on-body location for wearable technology 20 years of designing for wearability,” in *Proceedings of the 2017 ACM International Symposium on Wearable Computers*, 2017, pp. 150–157.

[64] V. G. Motti and K. Caine, “Human factors considerations in the design of wearable devices,” in *Proceedings of the human factors and ergonomics society annual meeting*, 2014, vol. 58, no. 1, pp. 1820–1824.

[65] G. Cho, *Smart clothing: technology and applications*. CRC press, 2009.

[66] W. J. Tharion, M. J. Buller, A. J. Karis, and S. P. Mullen, “Acceptability of a wearable vital

sign detection system," in *Proceedings of the human factors and ergonomics society annual meeting*, 2007, vol. 51, no. 17, pp. 1006–1010.

[67] R. Lin and J. G. Kreifeldt, "Ergonomics in wearable computer design," *Int. J. Ind. Ergon.*, vol. 27, no. 4, pp. 259–269, 2001.

[68] Y. Huang, Z. Tang, Z. Liu, J. Wei, H. Hu, and C. Zhi, "Toward enhancing wearability and fashion of wearable supercapacitor with modified polyurethane artificial leather electrolyte," *Nano-micro Lett.*, vol. 10, no. 3, pp. 1–8, 2018.

[69] S. Seneviratne *et al.*, "A survey of wearable devices and challenges," *IEEE Commun. Surv. Tutorials*, vol. 19, no. 4, pp. 2573–2620, 2017.

[70] A. Nag, S. C. Mukhopadhyay, and J. Kosel, "Wearable flexible sensors: A review," *IEEE Sens. J.*, vol. 17, no. 13, pp. 3949–3960, 2017.

[71] M. Amjadi, K. Kyung, I. Park, and M. Sitti, "Stretchable, skin-mountable, and wearable strain sensors and their potential applications: a review," *Adv. Funct. Mater.*, vol. 26, no. 11, pp. 1678–1698, 2016.

[72] N. Lu, C. Lu, S. Yang, and J. Rogers, "Highly sensitive skin-mountable strain gauges based entirely on elastomers," *Adv. Funct. Mater.*, vol. 22, no. 19, pp. 4044–4050, 2012.

[73] T. Yamada *et al.*, "A stretchable carbon nanotube strain sensor for human-motion detection," *Nat. Nanotechnol.*, vol. 6, no. 5, pp. 296–301, 2011.

[74] M. Amjadi, A. Pichitpajongkit, S. Lee, S. Ryu, and I. Park, "Highly stretchable and sensitive strain sensor based on silver nanowire–elastomer nanocomposite," *ACS Nano*, vol. 8, no. 5, pp. 5154–5163, 2014.

[75] J. Lee *et al.*, "A stretchable strain sensor based on a metal nanoparticle thin film for human motion detection," *Nanoscale*, vol. 6, no. 20, pp. 11932–11939, 2014.

[76] D. Lo Presti *et al.*, "Fiber bragg gratings for medical applications and future challenges: A review," *Ieee Access*, vol. 8, pp. 156863–156888, 2020.

[77] M. C., Z. M., L. P. D., N. A., T. D., and S. E, "Fiber Bragg Grating Sensors for Cardiorespiratory Monitoring: A Review," *IEEE Sens. J.*, pp. 1–1, 2020, doi: 10.1109/JSEN.2020.2988692.

[78] A. Leal-Junior *et al.*, "Polymer optical fiber Bragg gratings in CYTOP fibers for angle measurement with dynamic compensation," *Polymers (Basel).*, vol. 10, no. 6, p. 674, 2018.

[79] C. Massaroni, M. Zaltieri, D. Lo Presti, A. Nicolò, D. Tosi, and E. Schena, "Fiber Bragg grating sensors for cardiorespiratory monitoring: A review," *IEEE Sens. J.*, vol. 21, no. 13, pp. 14069–14080, 2020.

[80] A. D. Kersey *et al.*, "Fiber grating sensors," *J. Light. Technol.*, vol. 15, no. 8, pp. 1442–1463, 1997.

[81] T. Erdogan, "Fiber grating spectra," *J. Light. Technol.*, vol. 15, no. 8, pp. 1277–1294, 1997.

[82] A. Othonos, K. Kalli, and G. E. Kohnke, "Fiber Bragg gratings: Fundamentals and applications in telecommunications and sensing," *Phys. Today*, vol. 53, no. 5, p. 61, 2000.

[83] J. Skaar, L. Wang, and T. Erdogan, “On the synthesis of fiber Bragg gratings by layer peeling,” *IEEE J. Quantum Electron.*, vol. 37, no. 2, pp. 165–173, 2001.

[84] K. O. Hill, B. Malo, F. Bilodeau, D. C. Johnson, and J. Albert, “Bragg gratings fabricated in monomode photosensitive optical fiber by UV exposure through a phase mask,” *Appl. Phys. Lett.*, vol. 62, no. 10, pp. 1035–1037, 1993.

[85] A. Theodosiou *et al.*, “Modified fs-laser inscribed FBG array for rapid mode shape capture of free-free vibrating beams,” *IEEE Photonics Technol. Lett.*, vol. 28, no. 14, pp. 1509–1512, 2016.

[86] A. Lacraz, M. Polis, A. Theodosiou, C. Koutsides, and K. Kalli, “Femtosecond laser inscribed Bragg gratings in low loss CYTOP polymer optical fiber,” *IEEE Photonics Technol. Lett.*, vol. 27, no. 7, pp. 693–696, 2015.

[87] C. G. Askins, M. A. Putnam, G. M. Williams, and E. J. Friebele, “Stepped-wavelength optical-fiber Bragg grating arrays fabricated in line on a draw tower,” *Opt. Lett.*, vol. 19, no. 2, pp. 147–149, 1994.

[88] D. Tosi, E. Schena, C. Molardi, and S. Korganbayev, “Fiber optic sensors for sub-centimeter spatially resolved measurements: Review and biomedical applications,” *Opt. Fiber Technol.*, vol. 43, pp. 6–19, 2018.

[89] S. Korganbayev *et al.*, “Thermal profile detection through high-sensitivity fiber optic chirped Bragg grating on microstructured PMMA fiber,” *J. Light. Technol.*, vol. 36, no. 20, pp. 4723–4729, 2018.

[90] B.-J. Peng, Y. Zhao, J. Yang, and M. Zhao, “Pressure sensor based on a free elastic cylinder and birefringence effect on an FBG with temperature-compensation,” *Measurement*, vol. 38, no. 2, pp. 176–180, 2005.

[91] A. G. Leal-Junior, C. A. R. Díaz, A. Frizera, C. Marques, M. R. N. Ribeiro, and M. J. Pontes, “Simultaneous measurement of pressure and temperature with a single FBG embedded in a polymer diaphragm,” *Opt. Laser Technol.*, vol. 112, pp. 77–84, 2019.

[92] D. Tosi, “Review and analysis of peak tracking techniques for fiber Bragg grating sensors,” *Sensors*, vol. 17, no. 10, p. 2368, 2017.

[93] S. Poeggel *et al.*, “Differential in vivo urodynamic measurement in a single thin catheter based on two optical fiber pressure sensors,” *J. Biomed. Opt.*, vol. 20, no. 3, p. 37005, 2015.

[94] M. G. Xu, H. Geiger, and J. P. Dakin, “Modeling and performance analysis of a fiber Bragg grating interrogation system using an acousto-optic tunable filter,” *J. Light. Technol.*, vol. 14, no. 3, pp. 391–396, 1996.

[95] P. T. Macklem, “Respiratory mechanics,” *Annu. Rev. Physiol.*, vol. 40, no. 1, pp. 157–184, 1978.

[96] A. B. Otis, W. O. Fenn, and H. Rahn, “Mechanics of breathing in man,” *J. Appl. Physiol.*, vol. 2, no. 11, pp. 592–607, 1950.

[97] E. Mansour *et al.*, “Measurement of temperature and relative humidity in exhaled breath,” *Sensors Actuators B Chem.*, vol. 304, p. 127371, 2020.

[98] R. D. Branson and M. A. Gentile, “Is humidification always necessary during noninvasive

ventilation in the hospital?," *Respir. Care*, vol. 55, no. 2, pp. 209–216, 2010.

[99] A. De Groote, M. Wantier, G. Chéron, M. Estenne, and M. Paiva, "Chest wall motion during tidal breathing," *J. Appl. Physiol.*, vol. 83, no. 5, pp. 1531–1537, 1997.

[100] T. Kondo, T. Uhlig, P. Pemberton, and P. D. Sly, "Laser monitoring of chest wall displacement," *Eur. Respir. J.*, vol. 10, no. 8, pp. 1865–1869, 1997.

[101] L. Alwis, T. Sun, and K. T. V Grattan, "Optical fibre-based sensor technology for humidity and moisture measurement: Review of recent progress," *Measurement*, vol. 46, no. 10, pp. 4052–4074, 2013.

[102] J. Ascorbe, J. M. Corres, F. J. Arregui, and I. R. Matias, "Recent developments in fiber optics humidity sensors," *Sensors*, vol. 17, no. 4, p. 893, 2017.

[103] D. Lo Presti, C. Massaroni, and E. Schena, "Optical fiber gratings for humidity measurements: A review," *IEEE Sens. J.*, vol. 18, no. 22, pp. 9065–9074, 2018.

[104] Q. Chen and P. Lu, "Fiber Bragg gratings and their applications as temperature and humidity sensors," *At. Mol. Opt. Phys.*, pp. 235–260, 2008.

[105] S. Pant, S. Umesh, and S. Asokan, "Fiber Bragg grating respiratory measurement device," in *2018 IEEE International Symposium on Medical Measurements and Applications (MeMeA)*, 2018, pp. 1–5.

[106] P. K. Levangie and C. C. Norkin, *Joint structure and function: a comprehensive analysis*. FA Davis, 2011.

[107] C. C. Norkin and D. J. White, *Measurement of joint motion: a guide to goniometry*. FA Davis, 2016.

[108] G. L. Kinzel and L. J. Gutkowski, "Joint models, degrees of freedom, and anatomical motion measurement," 1983.

[109] C. Massaroni, A. Nicolò, D. Lo Presti, M. Sacchetti, S. Silvestri, and E. Schena, "Contact-based methods for measuring respiratory rate," *Sensors*, vol. 19, no. 4, p. 908, 2019.

[110] M. R. Miller *et al.*, "Standardisation of spirometry," *Eur. Respir. J.*, vol. 26, no. 2, pp. 319–338, 2005.

[111] E. Schena, C. Massaroni, P. Saccomandi, and S. Cecchini, "Flow measurement in mechanical ventilation: A review," *Med. Eng. Phys.*, vol. 37, no. 3, pp. 257–264, 2015.

[112] C. Massaroni, A. Nicolo, M. Sacchetti, and E. Schena, "Contactless methods for measuring respiratory rate: A review," *IEEE Sens. J.*, vol. 21, no. 11, pp. 12821–12839, 2020.

[113] L. Dziuda, J. Lewandowski, F. Skibniewski, and G. Nowicki, "Fibre-optic sensor for respiration and heart rate monitoring in the MRI environment," *Procedia Eng.*, vol. 47, pp. 1291–1294, 2012.

[114] L. Dziuda, F. W. Skibniewski, M. Krej, and P. M. Baran, "Fiber Bragg grating-based sensor for monitoring respiration and heart activity during magnetic resonance imaging examinations," *J. Biomed. Opt.*, vol. 18, no. 5, p. 57006, 2013.

[115] M. Fajkus, J. Nedoma, R. Martinek, and W. Walendziuk, "Comparison of the FBG sensor encapsulated into PDMS and FBG sensor glued on the plexiglass pad for respiratory and

heart rate monitoring," in *Photonics Applications in Astronomy, Communications, Industry, and High Energy Physics Experiments 2017*, 2017, vol. 10445, pp. 71–78.

[116] J. Hao, M. Jayachandran, P. L. Kng, S. F. Foo, P. W. Aung Aung, and Z. Cai, "FBG-based smart bed system for healthcare applications," *Front. Optoelectron. China*, vol. 3, no. 1, pp. 78–83, 2010.

[117] V. F. S. Fook *et al.*, "Non-intrusive respiratory monitoring system using Fiber Bragg Grating sensor," in *HealthCom 2008-10th International Conference on e-health Networking, Applications and Services*, 2008, pp. 160–164.

[118] L. Dziuda, F. Skibniewski, K. Rozanowski, M. Krej, and J. Lewandowski, "Fiber-optic sensor for monitoring respiration and cardiac activity," in *SENSORS, 2011 IEEE*, 2011, pp. 413–416.

[119] L. Dziuda, F. W. Skibniewski, M. Krej, and J. Lewandowski, "Monitoring respiration and cardiac activity using fiber Bragg grating-based sensor," *IEEE Trans. Biomed. Eng.*, vol. 59, no. 7, pp. 1934–1942, 2012.

[120] S. Schneegass and O. Amft, *Smart textiles*. Springer, 2017.

[121] V. Koncar, *Smart textiles and their applications*. Woodhead Publishing, 2016.

[122] X. Xiaoqiang, S. Ziqi, M. Yan, and D. Yang, "Research progress of fiber Bragg grating flexible sensor: A Review," in *2021 33rd Chinese Control and Decision Conference (CCDC)*, 2021, pp. 3150–3157.

[123] M. R. Khosravani and T. Reinicke, "Applications of additive manufacturing in fabrication of sensors—A review," *Sens. Actuators A Phys*, vol. 111916, 2020.

[124] K. Willis, E. Brockmeyer, S. Hudson, and I. Poupyrev, "Printed optics: 3D printing of embedded optical elements for interactive devices," in *Proceedings of the 25th annual ACM symposium on User interface software and technology*, 2012, pp. 589–598.

[125] J. Witt *et al.*, "Medical textiles with embedded fiber optic sensors for monitoring of respiratory movement," *IEEE Sens. J.*, vol. 12, no. 1, pp. 246–254, 2011.

[126] C. Massaroni *et al.*, "Smart textile for respiratory monitoring and thoraco-abdominal motion pattern evaluation," *J. Biophotonics*, vol. 11, no. 5, p. e201700263, 2018.

[127] D. Lo Presti *et al.*, "A Wearable System Composed of FBG-Based Soft Sensors for Trunk Compensatory Movements Detection in Post-Stroke Hemiplegic Patients," *Sensors*, vol. 22, no. 4, p. 1386, 2022.

[128] D. Lo Presti *et al.*, "The Effect of Infill Pattern and Density on the Response of 3-D-Printed Sensors Based on FBG Technology," *IEEE Sens. J.*, vol. 22, no. 20, pp. 19357–19365, 2022.

[129] A. Grillet *et al.*, "Optical fiber sensors embedded into medical textiles for healthcare monitoring," *IEEE Sens. J.*, vol. 8, no. 7, pp. 1215–1222, 2008.

[130] F. Narbonneau *et al.*, "FBG-based smart textiles for continuous monitoring of respiratory movements for healthcare applications," in *The 12th IEEE International Conference on e-Health Networking, Applications and Services*, 2010, pp. 277–282.

[131] M. Ciocchetti *et al.*, "Smart textile based on fiber bragg grating sensors for respiratory monitoring: Design and preliminary trials," *Biosensors*, vol. 5, no. 3, pp. 602–615, 2015.

[132] C. Massaroni *et al.*, "Design and feasibility assessment of a magnetic resonance-compatible smart textile based on fiber Bragg grating sensors for respiratory monitoring," *IEEE Sens. J.*, vol. 16, no. 22, pp. 8103–8110, 2016.

[133] D. Lo Presti *et al.*, "Respiratory and cardiac rates monitoring during MR examination by a sensorized smart textile," in *2017 IEEE International Instrumentation and Measurement Technology Conference (I2MTC)*, 2017, pp. 1–6.

[134] D. Lo Presti, C. Massaroni, P. S. E. Schena, D. Formica, M. A. Caponero, and G. Di Tomaso, "Smart textile based on FBG sensors for breath-by-breath respiratory monitoring: Tests on women," in *2018 IEEE International Symposium on Medical Measurements and Applications (MeMeA)*, 2018, pp. 1–6.

[135] K. Ogawa, S. Koyama, H. Ishizawa, S. Fujiwara, and K. Fujimoto, "Simultaneous measurement of heart sound, pulse wave and respiration with single fiber bragg grating sensor," in *2018 IEEE International Symposium on Medical Measurements and Applications (MeMeA)*, 2018, pp. 1–5.

[136] S. Koyama, A. Fujimoto, Y. Yasuda, and Y. Satou, "Verification of the propagation range of respiratory strain using signal waveform measured by FBG sensors," *Sensors*, vol. 20, no. 24, p. 7076, 2020.

[137] A. Issatayeva, A. Beisenova, D. Tosi, and C. Molardi, "Fiber-optic based smart textiles for real-time monitoring of breathing rate," *Sensors*, vol. 20, no. 12, p. 3408, 2020.

[138] D. Defrianto *et al.*, "External Perspective of Lung Airflow Model Through Diaphragm Breathing Sensor Using Fiber Optic Elastic Belt," *Indian J. Pure Appl. Phys.*, vol. 60, no. 7, pp. 561–566, 2022.

[139] A. F. da Silva, A. F. Goncalves, L. A. de Almeida Ferreira, F. M. M. Araujo, P. M. Mendes, and J. H. Correia, "PVC smart sensing foil for advanced strain measurements," *IEEE Sens. J.*, vol. 10, no. 6, pp. 1149–1155, 2010.

[140] A. F. Silva, J. P. Carmo, P. M. Mendes, and J. H. Correia, "Simultaneous cardiac and respiratory frequency measurement based on a single fiber Bragg grating sensor," *Meas. Sci. Technol.*, vol. 22, no. 7, p. 75801, 2011.

[141] J. P. Carmo, A. M. F. da Silva, R. P. Rocha, and J. H. Correia, "Application of fiber Bragg gratings to wearable garments," *IEEE Sens. J.*, vol. 12, no. 1, pp. 261–266, 2011.

[142] M. Fajkus, J. Nedoma, P. Siska, and V. Vasinek, "FBG sensor of breathing encapsulated into polydimethylsiloxane," in *Optical Materials and Biomaterials in Security and Defence Systems Technology XIII*, 2016, vol. 9994, pp. 31–35.

[143] J. Nedoma, M. Fajkus, P. Siska, R. Martinek, and V. Vasinek, "Non-invasive fiber optic probe encapsulated into PolyDiMethylSiloxane for measuring respiratory and heart rate of the human body," *Adv. Electr. Electron. Eng.*, vol. 15, no. 1, pp. 93–100, 2017.

[144] M. Fajkus, J. Nedoma, R. Martinek, V. Vasinek, H. Nazeran, and P. Siska, "A non-invasive multichannel hybrid fiber-optic sensor system for vital sign monitoring," *Sensors*, vol. 17, no. 1, p. 111, 2017.

[145] K. Chethana, A. S. Guru Prasad, S. N. Omkar, and S. Asokan, "Fiber bragg grating sensor based device for simultaneous measurement of respiratory and cardiac activities," *J. Biophotonics*, vol. 10, no. 2, pp. 278–285, 2017.

[146] D. Lo Presti *et al.*, "Wearable system based on flexible FBG for respiratory and cardiac monitoring," *IEEE Sens. J.*, vol. 19, no. 17, pp. 7391–7398, 2019.

[147] D. Lo Presti *et al.*, "Cardio-respiratory monitoring in archery using a smart textile based on flexible fiber Bragg grating sensors," *Sensors*, vol. 19, no. 16, p. 3581, 2019.

[148] D. Lo Presti, D. Bianchi, C. Massaroni, A. Gizzi, and E. Schena, "A Soft and Skin-Interfaced Smart Patch Based on Fiber Optics for Cardiorespiratory Monitoring," *Biosensors*, vol. 12, no. 6, p. 363, 2022.

[149] T. Li *et al.*, "A Skin-Like and Highly Stretchable Optical Fiber Sensor with the Hybrid Coding of Wavelength–Light Intensity," *Adv. Intell. Syst.*, vol. 4, no. 4, p. 2100193, 2022.

[150] C. Tavares *et al.*, "Respiratory and heart rate monitoring using an FBG 3D-printed wearable system," *Biomed. Opt. Express*, vol. 13, no. 4, pp. 2299–2311, 2022.

[151] C. Massaroni, M. A. Caponero, R. D'Amato, D. Lo Presti, and E. Schena, "Fiber Bragg grating measuring system for simultaneous monitoring of temperature and humidity in mechanical ventilation," *Sensors*, vol. 17, no. 4, p. 749, 2017.

[152] S. Iacoponi *et al.*, "Polymer-coated fiber optic probe for the monitoring of breathing pattern and respiratory rate," in *2018 40th Annual International Conference of the IEEE Engineering in Medicine and Biology Society (EMBC)*, 2018, pp. 1616–1619.

[153] C. Massaroni, D. Lo Presti, P. Saccomandi, M. A. Caponero, R. D'Amato, and E. Schena, "Fiber Bragg grating probe for relative humidity and respiratory frequency estimation: Assessment during mechanical ventilation," *IEEE Sens. J.*, vol. 18, no. 5, pp. 2125–2130, 2017.

[154] C. Massaroni *et al.*, "Multi-sensitive FBG-based needle for both relative humidity and breathing rate monitoring," in *2018 IEEE International Symposium on Medical Measurements and Applications (MeMeA)*, 2018, pp. 1–6.

[155] B. Jiang *et al.*, "Graphene oxide-deposited tilted fiber grating for ultrafast humidity sensing and human breath monitoring," *Sensors Actuators B Chem.*, vol. 293, pp. 336–341, 2019.

[156] Y. Liang, A. P. Mazzolini, and P. R. Stoddart, "Fibre Bragg grating sensor for respiratory monitoring," in *ACOFT/AOS 2006-Australian Conference on Optical Fibre Technology/Australian Optical Society*, 2006, pp. 75–77.

[157] J. Nedoma *et al.*, "Fiber-Optic Breathing Mask: An Alternative Solution for MRI Respiratory Triggering," *IEEE Trans. Instrum. Meas.*, vol. 71, pp. 1–13, 2022.

[158] M. Fajkus *et al.*, "MR fully compatible and safe FBG breathing sensor: A practical solution for respiratory triggering," *IEEE Access*, vol. 7, pp. 123013–123025, 2019.

[159] R. Sinha *et al.*, "Development and validation of a novel fibre-optic respiratory rate sensor (FiRRS) integrated in oxygen delivery devices," *J. Phys. D. Appl. Phys.*, vol. 54, no. 12, p. 124002, 2021.

[160] A. Gautam, K. Kinjalk, A. Kumar, and V. Priye, "FBG-based respiration rate sensing with arduino interface," *IEEE Sens. J.*, vol. 20, no. 16, pp. 9209–9217, 2020.

[161] A. Manujło and T. Osuch, "Temperature fiber Bragg grating based sensor for respiration monitoring," in *Photonics Applications in Astronomy, Communications, Industry, and*

High Energy Physics Experiments 2017, 2017, vol. 10445, pp. 362–367.

[162] F. U. Hernandez *et al.*, "Simultaneous temperature and humidity measurements in a mechanical ventilator using an optical fibre sensor," in *Sixth European Workshop on Optical Fibre Sensors*, 2016, vol. 9916, pp. 42–45.

[163] S. P. Morgan *et al.*, "Optical fiber sensors for monitoring in critical care," in *2019 41st Annual International Conference of the IEEE Engineering in Medicine and Biology Society (EMBC)*, 2019, pp. 1139–1143.

[164] R. W. Miller, "Introduction to the differential producer," *Flow Meas. Eng. Handb.*, vol. 1, 1996.

[165] S. Ambastha, S. Umesh, U. Maheshwari, and S. Asokan, "Pulmonary function test using fiber Bragg grating spirometer," *J. Light. Technol.*, vol. 34, no. 24, pp. 5682–5688, 2016.

[166] A. C. Nepomuceno, N. Alberto, P. André, P. F. da Costa Antunes, and M. de Fátima Domingues, "3D printed spirometer for pulmonary health assessment based on fiber Bragg gratings," *IEEE Sens. J.*, vol. 21, no. 4, pp. 4590–4598, 2020.

[167] A. Das, S. Ambastha, S. Sen, and S. Samanta, "Wearable system for Real-time Remote Monitoring of Respiratory Rate during Covid-19 using Fiber Bragg Grating," in *2020 IEEE 17th India Council International Conference (INDICON)*, 2020, pp. 1–4.

[168] S. Gao, A. P. Zhang, H.-Y. Tam, L. H. Cho, and C. Lu, "All-optical fiber anemometer based on laser heated fiber Bragg gratings," *Opt. Express*, vol. 19, no. 11, pp. 10124–10130, 2011.

[169] D. W. Lamb and A. Hooper, "Laser-optical fiber Bragg grating anemometer for measuring gas flows: application to measuring the electric wind," *Opt. Lett.*, vol. 31, no. 8, pp. 1035–1037, 2006.

[170] C. Jewart, B. McMillen, S. K. Cho, and K. P. Chen, "X-probe flow sensor using self-powered active fiber Bragg gratings," *Sensors Actuators A Phys.*, vol. 127, no. 1, pp. 63–68, 2006.

[171] R. Gao and D. Lu, "Temperature compensated fiber optic anemometer based on graphene-coated elliptical core micro-fiber Bragg grating," *Opt. Express*, vol. 27, no. 23, pp. 34011–34021, 2019.

[172] Y.-L. Park, "Soft wearable robotics technologies for body motion sensing," in *Human Modelling for Bio-Inspired Robotics*, Elsevier, 2017, pp. 161–184.

[173] E. Y. S. Chao, "Justification of triaxial goniometer for the measurement of joint rotation," *J. Biomech.*, vol. 13, no. 12, pp. 989–1006, 1980.

[174] M. P. Clapper and S. L. Wolf, "Comparison of the reliability of the Orthoranger and the standard goniometer for assessing active lower extremity range of motion," *Phys. Ther.*, vol. 68, no. 2, pp. 214–218, 1988.

[175] R. L. Gajdosik and R. W. Bohannon, "Clinical measurement of range of motion: review of goniometry emphasizing reliability and validity," *Phys. Ther.*, vol. 67, no. 12, pp. 1867–1872, 1987.

[176] M. Yahya, J. A. Shah, K. A. Kadir, Z. M. Yusof, S. Khan, and A. Warsi, "Motion capture sensing techniques used in human upper limb motion: A review," *Sens. Rev.*, 2019.

[177] E. Knippenberg, J. Verbrugghe, I. Lamers, S. Palmaers, A. Timmermans, and A. Spooren, “Markerless motion capture systems as training device in neurological rehabilitation: a systematic review of their use, application, target population and efficacy,” *J. Neuroeng. Rehabil.*, vol. 14, no. 1, pp. 1–11, 2017.

[178] M. Rahul, “Review on motion capture technology,” *Glob. J. Comput. Sci. Technol.*, 2018.

[179] Z. A. Abro *et al.*, “Development of FBG pressure sensors using FDM technique for monitoring sleeping postures,” *Sensors Actuators A Phys.*, vol. 331, p. 112921, 2021.

[180] V. F. S. Fook *et al.*, “Fiber bragg grating sensor system for monitoring and handling bedridden patients,” in *Smart Homes and Beyond, ICOST’2006 4th International Conference on Smart Homes and Health Telematics, Assistive Technology Research Series*, 2006, vol. 19, pp. 239–246.

[181] C. Tavares, M. F. Domingues, T. Paixão, N. Alberto, H. Silva, and P. Antunes, “Wheelchair pressure ulcer prevention using FBG based sensing devices,” *Sensors*, vol. 20, no. 1, p. 212, 2019.

[182] A. S. G. Prasad, S. N. Omkar, H. N. Vikranth, V. Anil, K. Chethana, and S. Asokan, “Design and development of Fiber Bragg Grating sensing plate for plantar strain measurement and postural stability analysis,” *Measurement*, vol. 47, pp. 789–793, 2014.

[183] A. F. Da Silva, A. F. Gonçalves, P. M. Mendes, and J. H. Correia, “FBG sensing glove for monitoring hand posture,” *IEEE Sens. J.*, vol. 11, no. 10, pp. 2442–2448, 2011.

[184] Q. Lin *et al.*, “Finger Bending Sensing Based on Series-Connected Fiber Bragg Gratings,” *Materials (Basel).*, vol. 15, no. 10, p. 3472, 2022.

[185] R. P. Rocha, A. F. Silva, J. P. Carmo, and J. H. Correia, “FBG in PVC foils for monitoring the knee joint movement during the rehabilitation process,” in *2011 Annual International Conference of the IEEE Engineering in Medicine and Biology Society*, 2011, pp. 458–461.

[186] M. F. Domingues *et al.*, “Energy-aware wearable e-Health architecture using optical FBG sensors for knee kinematic monitoring,” in *2018 IEEE Global Communications Conference (GLOBECOM)*, 2018, pp. 1–6.

[187] A. M. Butt, H. Alsaffar, M. Alshareef, and K. K. Qureshi, “AI Prediction of Brain Signals for Human Gait Using BCI Device and FBG Based Sensorial Platform for Plantar Pressure Measurements,” *Sensors*, vol. 22, no. 8, p. 3085, 2022.

[188] M. Jang, J. S. Kim, K. Kang, S. H. Um, S. Yang, and J. Kim, “Development of wearable motion capture system using fiber bragg grating sensors for measuring arm motion,” in *2019 IEEE Conference on Virtual Reality and 3D User Interfaces (VR)*, 2019, pp. 994–995.

[189] Z. A. Abro, C. Hong, N. Chen, Y. Zhang, R. A. Lakho, and S. Yasin, “A fiber Bragg grating-based smart wearable belt for monitoring knee joint postures,” *Text. Res. J.*, vol. 90, no. 3–4, pp. 386–394, 2020.

[190] Z. A. Abro, Y.-F. Zhang, C.-Y. Hong, R. A. Lakho, and N.-L. Chen, “Development of a smart garment for monitoring body postures based on FBG and flex sensing technologies,” *Sensors Actuators A Phys.*, vol. 272, pp. 153–160, 2018.

[191] P. Resta *et al.*, “A wearable system for knee flexion/extension monitoring: Design and assessment,” in *2020 IEEE International Workshop on Metrology for Industry 4.0 & IoT*,

2020, pp. 273–277.

[192] M. F. Domingues *et al.*, “Wearable eHealth system for physical rehabilitation: Ankle plantar-dorsi-flexion monitoring,” in *2019 IEEE Global Communications Conference (GLOBECOM)*, 2019, pp. 1–6.

[193] J. S. Kim *et al.*, “Wearable hand module and real-time tracking algorithms for measuring finger joint angles of different hand sizes with high accuracy using FBG strain sensor,” *Sensors*, vol. 20, no. 7, p. 1921, 2020.

[194] J. Guo *et al.*, “Wearable and skin-mountable fiber-optic strain sensors interrogated by a free-running, dual-comb fiber laser,” *Adv. Opt. Mater.*, vol. 7, no. 12, p. 1900086, 2019.

[195] H. Cheng-Yu, Z. Ahmed Abro, Z. Yi-Fan, and R. Ahmed Lakho, “An FBG-based smart wearable ring fabricated using FDM for monitoring body joint motion,” *J. Ind. Text.*, vol. 50, no. 10, pp. 1660–1673, 2021.

[196] J. Di Tocco *et al.*, “A wearable system based on flexible sensors for unobtrusive respiratory monitoring in occupational settings,” *IEEE Sens. J.*, vol. 21, no. 13, pp. 14369–14378, 2020.

[197] D. Lo Presti *et al.*, “Respiratory rate monitoring of video terminal operators based on fiber optic technology,” in *2021 IEEE International Workshop on Metrology for Industry 4.0 & IoT (MetroInd4. 0&IoT)*, 2021, pp. 439–443.

[198] M. Zaltieri *et al.*, “Preliminary assessment of a flexible multi-sensor wearable system based on fiber bragg gratings for respiratory monitoring of hemiplegic patients,” *Int. J. Environ. Res. Public Health*, vol. 19, no. 20, p. 13525, 2022.

[199] M. Drissi-Habti, V. Raman, A. Khadour, and S. Timorian, “Fiber optic sensor embedment study for multi-parameter strain sensing,” *Sensors*, vol. 17, no. 4, p. 667, 2017.

[200] “Rubber, Smooth-On, ‘Dragon Skin Series.’” https://www.smooth-on.com/product-line/dragon-skin/

[201] B. S. ISO, “37: 2011 Rubber, vulcanized or thermoplastic—Determination of tensile stress-strain properties,” *Br. Stand. Publ.*, 2011.

[202] A. R. Fugl-Meyer, H. Linderholm, and A. F. Wilson, “Restrictive ventilatory dysfunction in stroke: its relation to locomotor function.,” *Scand. J. Rehabil. Med. Suppl.*, vol. 9, pp. 118–124, 1983.

[203] B. Lanini *et al.*, “Chest wall kinematics in patients with hemiplegia,” *Am. J. Respir. Crit. Care Med.*, vol. 168, no. 1, pp. 109–113, 2003.

[204] D. C. Fluck, “Chest movements in hemiplegia,” *Clin Sci*, vol. 31, pp. 383–388, 1966.

[205] E. Cohen, A. Mier, P. Heywood, K. Murphy, J. Boultbee, and A. Guz, “Diaphragmatic movement in hemiplegic patients measured by ultrasonography.,” *Thorax*, vol. 49, no. 9, pp. 890–895, 1994.

[206] L. F. Teixeira-Salmela *et al.*, “Respiratory pressures and thoracoabdominal motion in community-dwelling chronic stroke survivors,” *Arch. Phys. Med. Rehabil.*, vol. 86, no. 10, pp. 1974–1978, 2005.

[207] M. FUGL, “The post-stroke hemiplegic patient. I. A method for evaluation of physical

performance," 1975.

[208] G. Ferrigno, P. Carnevali, A. Aliverti, F. Molteni, G. Beulcke, and A. Pedotti, "Three-dimensional optical analysis of chest wall motion," *J. Appl. Physiol.*, vol. 77, no. 3, pp. 1224–1231, 1994.

[209] C. Massaroni *et al.*, "Comparison of marker models for the analysis of the volume variation and thoracoabdominal motion pattern in untrained and trained participants," *J. Biomech.*, vol. 76, pp. 247–252, 2018.

[210] J. M. Bland and D. G. Altman, "Statistical methods for assessing agreement between two methods of clinical measurement," *Int. J. Nurs. Stud.*, vol. 47, no. 8, pp. 931–936, 2010.

[211] G. K. Prisk, J. Hammer, and C. J. L. Newth, "Techniques for measurement of thoracoabdominal asynchrony," *Pediatr. Pulmonol.*, vol. 34, no. 6, pp. 462–472, 2002.

[212] J. Hammer and C. J. L. Newth, "Assessment of thoraco-abdominal asynchrony," *Paediatr. Respir. Rev.*, vol. 10, no. 2, pp. 75–80, 2009.

[213] A. Aliverti, M. Quaranta, B. Chakrabarti, A. L. P. Albuquerque, and P. M. Calverley, "Paradoxical movement of the lower ribcage at rest and during exercise in COPD patients," *Eur. Respir. J.*, vol. 33, no. 1, pp. 49–60, 2009.

[214] D. Lo Presti *et al.*, "A Magnetic Resonance-compatible wearable device based on functionalized fiber optic sensor for respiratory monitoring," *IEEE Sens. J.*, pp. 1–13, 2020, doi: 10.1109/JSEN.2020.2980940.

[215] D. Lo Presti *et al.*, "Agar-coated fiber Bragg grating sensor for relative humidity measurements: Influence of coating thickness and polymer concentration," *IEEE Sens. J.*, vol. 19, no. 9, pp. 3335–3342, 2019.

[216] R. S. Figliola and D. E. Beasley, *Theory and design for mechanical measurements*. John Wiley & Sons, 2020.

[217] C. Massaroni, G. Senesi, E. Schena, and S. Silvestri, "Analysis of breathing via optoelectronic systems: comparison of four methods for computing breathing volumes and thoraco-abdominal motion pattern," *Comput. Methods Biomech. Biomed. Engin.*, vol. 20, no. 16, pp. 1678–1689, 2017.

[218] C. Massaroni *et al.*, "Respiratory monitoring during physical activities with a multi-sensor smart garment and related algorithms," *IEEE Sens. J.*, vol. 20, no. 4, pp. 2173–2180, 2019.

[219] M. Zaltieri *et al.*, "Feasibility assessment of an FBG-based wearable system for monitoring back dorsal flexion-extension in video terminal workers," in *2020 IEEE International Instrumentation and Measurement Technology Conference (I2MTC)*, 2020, pp. 1–5.

[220] L. E. Dunne, P. Walsh, B. Smyth, and B. Caulfield, "Design and evaluation of a wearable optical sensor for monitoring seated spinal posture," in *2006 10th IEEE International Symposium on Wearable Computers*, 2006, pp. 65–68.

[221] J. M. Williams, I. Haq, and R. Y. Lee, "Dynamic measurement of lumbar curvature using fibre-optic sensors," *Med. Eng. Phys.*, vol. 32, no. 9, pp. 1043–1049, 2010.

[222] B. A. Cloud, K. D. Zhao, R. Breighner, H. Giambini, and K.-N. An, "Agreement between fiber optic and optoelectronic systems for quantifying sagittal plane spinal curvature in sitting," *Gait Posture*, vol. 40, no. 3, pp. 369–374, 2014.

[223] M. Zaltieri *et al.*, "An FBG-based smart wearable device for monitoring seated posture in video terminal workers," in *2020 IEEE International Workshop on Metrology for Industry 4.0 & IoT*, 2020, pp. 713–717.

[224] M. Zaltieri *et al.*, "A wearable device based on a fiber bragg grating sensor for low back movements monitoring," *Sensors*, vol. 20, no. 14, p. 3825, 2020.

[225] N. Chockalingam, P. H. Dangerfield, G. Giakas, and T. Cochrane, "Study of marker placements in the back for opto-electronic motion analysis," in *Research into Spinal Deformities 3*, IOS Press, 2002, pp. 105–109.

[226] M. Suter, P. Eichelberger, J. Frangi, E. Simonet, H. Baur, and S. Schmid, "Measuring lumbar back motion during functional activities using a portable strain gauge sensor-based system: A comparative evaluation and reliability study," *J. Biomech.*, vol. 100, p. 109593, 2020.

[227] R. Bartalesi, F. Lorussi, D. De Rossi, M. Tesconi, and A. Tognetti, "Wearable monitoring of lumbar spine curvature by inertial and e-textile sensory fusion," in *2010 Annual International Conference of the IEEE Engineering in Medicine and Biology*, 2010, pp. 6373–6376.

[228] R. Ranganathan, R. Wang, B. Dong, and S. Biswas, "Identifying compensatory movement patterns in the upper extremity using a wearable sensor system," *Physiol. Meas.*, vol. 38, no. 12, p. 2222, 2017.

[229] S. J. Housman, K. M. Scott, and D. J. Reinkensmeyer, "A randomized controlled trial of gravity-supported, computer-enhanced arm exercise for individuals with severe hemiparesis," *Neurorehabil. Neural Repair*, vol. 23, no. 5, pp. 505–514, 2009.

[230] D. L. Presti *et al.*, "A multi-parametric wearable system to monitor neck movements and respiratory frequency of computer workers," *Sensors (Switzerland)*, vol. 20, no. 2, 2020, doi: 10.3390/s20020536.

[231] J.-I. Kang, D.-K. Jeong, and H. Choi, "Correlation between pulmonary functions and respiratory muscle activity in patients with forward head posture," *J. Phys. Ther. Sci.*, vol. 30, no. 1, pp. 132–135, 2018.

[232] C. Duc, P. Salvia, A. Lubansu, V. Feipel, and K. Aminian, "A wearable inertial system to assess the cervical spine mobility: Comparison with an optoelectronic-based motion capture evaluation," *Med. Eng. Phys.*, vol. 36, no. 1, pp. 49–56, 2014.

[233] Y. Wang *et al.*, "An intelligent wearable device for human's cervical vertebra posture monitoring," in *2018 40th Annual International Conference of the IEEE Engineering in Medicine and Biology Society (EMBC)*, 2018, pp. 3280–3283.

[234] M. Maselli, E. Mussi, F. Cecchi, M. Manti, P. Tropea, and C. Laschi, "A wearable sensing device for monitoring single planes neck movements: Assessment of its performance," *IEEE Sens. J.*, vol. 18, no. 15, pp. 6327–6336, 2018.

[235] M. Zaltieri *et al.*, "Assessment of a Multi-Sensor FBG-based Wearable System in Sitting Postures Recognition and Respiratory Rate Evaluation of Office Workers," *IEEE Trans. Biomed. Eng.*, 2022.

[236] M. A. Hall and E. Frank, "Combining naive bayes and decision tables.," in *FLAIRS conference*, 2008, vol. 2118, pp. 318–319.

[237] E. L. Eisenstein and F. Alemi, “An evaluation of factors influencing Bayesian learning systems,” *J. Am. Med. Informatics Assoc.*, vol. 1, no. 3, pp. 272–284, 1994.

[238] P. Domingos and M. Pazzani, “On the optimality of the simple Bayesian classifier under zero-one loss,” *Mach. Learn.*, vol. 29, no. 2, pp. 103–130, 1997.

[239] C. Mattmann, O. Amft, H. Harms, G. Troster, and F. Clemens, “Recognizing upper body postures using textile strain sensors,” in *2007 11th IEEE international symposium on wearable computers*, 2007, pp. 29–36.

[240] C.-C. Hsia, Y.-W. Hung, Y.-H. Chiu, and C.-H. Kang, “Bayesian classification for bed posture detection based on kurtosis and skewness estimation,” in *HealthCom 2008-10th International Conference on e-health Networking, Applications and Services*, 2008, pp. 165–168.

[241] J. Meyer, B. Arnrich, J. Schumm, and G. Troster, “Design and modeling of a textile pressure sensor for sitting posture classification,” *IEEE Sens. J.*, vol. 10, no. 8, pp. 1391–1398, 2010.

[242] C. Fang, T. Zhang, H. Zheng, J. Huang, and K. Cuan, “Pose estimation and behavior classification of broiler chickens based on deep neural networks,” *Comput. Electron. Agric.*, vol. 180, p. 105863, 2021.

[243] T. T. Wong, “Performance evaluation of classification algorithms by k-fold and leave-one-out cross validation,” *Pattern Recognit.*, vol. 48, no. 9, pp. 2839–2846, 2015, doi: 10.1016/j.patcog.2015.03.009.

[244] I. Markoulidakis, I. Rallis, I. Georgoulas, G. Kopsiaftis, A. Doulamis, and N. Doulamis, “Multiclass Confusion Matrix Reduction Method and Its Application on Net Promoter Score Classification Problem,” *Technologies*, vol. 9, no. 4, p. 81, 2021.

[245] A. Tharwat, “Classification assessment methods,” *Appl. Comput. Informatics*, 2020.

[246] C. Ma, W. Li, R. Gravina, and G. Fortino, “Posture detection based on smart cushion for wheelchair users,” *Sensors*, vol. 17, no. 4, p. 719, 2017.

[247] T. Fu and A. Macleod, “Intellichair: An approach for activity detection and prediction via posture analysis,” in *2014 International Conference on Intelligent Environments*, 2014, pp. 211–213.

[248] S. E. Delabrida Silva, R. A. Rabelo Oliveira, and A. A. F. Loureiro, *Examining developments and applications of wearable devices in modern society*. IGI Global, 2017.

[249] M. Mishra and P. K. Sahu, “Fiber Bragg Gratings in Healthcare Applications: A Review,” *IETE Tech. Rev.*, pp. 1–18, 2022.

[250] Z. Liu and H.-Y. Tam, “Industrial and medical applications of fiber Bragg gratings,” *Chinese Opt. Lett.*, vol. 14, no. 12, p. 120007, 2016.

[251] T. Xiaolin *et al.*, “A miniaturized, low-cost and portable fiber Bragg grating interrogation system for remote monitoring,” *Optik (Stuttg).*, vol. 248, p. 168054, 2021.

[252] K. Ogawa, S. Koyama, Y. Haseda, K. Fujita, H. Ishizawa, and K. Fujimoto, “Wireless, portable fiber Bragg grating interrogation system employing optical edge filter,” *Sensors*, vol. 19, no. 14, p. 3222, 2019.

[253] C. A. R. Diaz *et al.*, “Perrogator: A portable energy-efficient interrogator for dynamic monitoring of wavelength-based sensors in wearable applications,” *Sensors*, vol. 19, no. 13, p. 2962, 2019.

[254] A. Leal-Junior, L. Avellar, A. Frizera, and C. Marques, “Smart textiles for multimodal wearable sensing using highly stretchable multiplexed optical fiber system,” *Sci. Rep.*, vol. 10, no. 1, pp. 1–12, 2020.

[255] J. L. Rodríguez-Garciapiña, G. Beltrán-Pérez, J. Castillo-Mixcóatl, and S. Muñoz-Aguirre, “Application of the principal components analysis technique to optical fiber sensors for acetone detection,” *Opt. Laser Technol.*, vol. 143, p. 107314, 2021.

[256] Q. Song, G. Yan, G. Tang, and F. Ansari, “Robust principal component analysis and support vector machine for detection of microcracks with distributed optical fiber sensors,” *Mech. Syst. Signal Process.*, vol. 146, p. 107019, 2021.

[257] S.-B. Kim, K.-S. Han, H.-C. Rim, and S. H. Myaeng, “Some effective techniques for naive bayes text classification,” *IEEE Trans. Knowl. Data Eng.*, vol. 18, no. 11, pp. 1457–1466, 2006.

[258] Y. Dou, X. Guo, L. Yuan, D. R. Holding, and C. Zhang, “Differential expression analysis in RNA-Seq by a naive Bayes classifier with local normalization,” *Biomed Res. Int.*, vol. 2015, 2015.

[259] I. H. Lopez-Nava and A. Munoz-Melendez “Wearable inertial sensors for human motion analysis: A review.” *IEEE Sensors Journal*, 16(22), 7821-7834, 2016.

List of Publications:

Peer-reviewed journals:

1. Zaltieri, M., Presti, D. L., Bravi, M., Caponero, M. A., Sterzi, S., Schena, E., & Massaroni, C. (2022). Assessment of a Multi-Sensor FBG-based Wearable System in Sitting Postures Recognition and Respiratory Rate Evaluation of Office Workers. IEEE Transactions on Biomedical Engineering.

2. Zaltieri, M., Massaroni, C., Di Tocco, J., Bravi, M., Morrone, M., Sterzi, S., ... & Lo Presti, D. (2022). Preliminary Assessment of a Flexible Multi-Sensor Wearable System Based on Fiber Bragg Gratings for Respiratory Monitoring of Hemiplegic Patients. *International Journal of Environmental Research and Public Health*, 19(20), 13525.

3. Di Tocco, J., Lo Presti, D., Zaltieri, M., Bravi, M., Morrone, M., Sterzi, S., ... & Massaroni, C. (2022). Investigating Stroke Effects on Respiratory Parameters Using a Wearable Device: A Pilot Study on Hemiplegic Patients. *Sensors*, 22(17), 6708.

4. Barone, A., Grieco, D., Gizzi, A., Molinari, L., Zaltieri, M., Massaroni, C., ... & Filippi, S. (2022). A Simulation Study of the Effects of His Bundle Pacing in Left Bundle Branch Block. *Medical Engineering & Physics*, 107, 103847.

5. Zaltieri, M., Rossi, P., Bianchi, S., Polselli, M., Niscola, M., Fanti, V., ... & Cauti, F. M. (2022). Spatial temperature reconstructions in myocardial tissues undergoing radiofrequency ablations by performing high-resolved temperature measurements. *Journal of Interventional Cardiac Electrophysiology*, 1-10.

6. Lo Presti†, D., Zaltieri†, M., Bravi, M., Morrone, M., Caponero, M. A., Schena, E., ... & Massaroni, C. (2022). A Wearable System Composed of FBG-Based Soft Sensors for Trunk Compensatory Movements Detection in Post-Stroke Hemiplegic Patients. *Sensors,* 22(4), 1386.

7. Massari, L., Fransvea, G., D'Abbraccio, J., Filosa, M., Terruso, G., Aliperta, A., ... & Oddo, C. M. (2022). Functional mimicry of Ruffini receptors with fibre Bragg gratings and deep neural networks enables a bio-inspired large-area tactile-sensitive skin. *Nature Machine Intelligence*, 4(5), 425-435.

8. Filosa, M., Massari, L., Ferraro, D., D'Alesio, G., D'Abbraccio, J., Aliperta, A., ... & Oddo, C. M. (2022). A meta-learning algorithm for respiratory flow prediction from FBG-based wearables in unrestrained conditions. *Artificial Intelligence in Medicine*, 102328.

9. Molinari, L., Zaltieri, M., Massaroni, C., Filippi, S., Gizzi, A., & Schena, E. (2022). Multiscale and Multiphysics Modeling of Anisotropic Cardiac RFCA: Experimental-Based Model Calibration via Multi-Point Temperature Measurements. *Frontiers in physiology*, 13.

10. Zaltieri, M., Massaroni, C., Schena, E., & Cauti, F. M. (2021). Techniques for Temperature Monitoring of Myocardial Tissue Undergoing Radiofrequency Ablation Treatments: An Overview. *Sensors*, 21(4), 1453.

11. Zaltieri, M., Allegretti, G., Massaroni, C., Schena, E., & Cauti, F. M. (2020). Fiber Bragg Grating Sensors for Millimetric-Scale Temperature Monitoring of Cardiac Tissue Undergoing Radiofrequency Ablation: A Feasibility Assessment. *Sensors*, 20(22), 6490.

12. Zaltieri, M., Massaroni, C., Lo Presti, D., Bravi, M., Sabbadini, R., Miccinilli, S., ... & Schena, E. (2020). A Wearable Device Based on a Fiber Bragg Grating Sensor for Low Back Movements Monitoring. *Sensors*, 20(14), 3825.

13. De Vita, E.†, Zaltieri, M.†, De Tommasi, F. D., Massaroni, C., Faiella, E., Zobel, B. B., ... & Campopiano, S. (2020). Multipoint Temperature Monitoring of Microwave Thermal Ablation in Bones through Fiber Bragg Grating Sensor Arrays. *Sensors*, 20(11), 3200.

14. Di Tocco, J., Lo Presti, D., Zaltieri, M., D'Alesio, G., Filosa, M., Massari, L., ... & Schena, E. (2020). A wearable system based on flexible sensors for unobtrusive respiratory monitoring in occupational settings. *IEEE Sensors Journal*.

15. Massaroni, C., Zaltieri, M., Lo Presti, D., Nicolò, A., Tosi, D., & Schena, E. (2020). Fiber Bragg Grating Sensors for Cardiorespiratory Monitoring: A Review. *IEEE Sensors Journal*.

16. Lo Presti, D., Carnevale, A., D'Abbraccio, J., Massari, L., Massaroni, C., Sabbadini, R., Zaltieri M., & Schena, E. (2020). A Multi-Parametric Wearable System to Monitor Neck Movements and Respiratory Frequency of Computer Workers. *Sensors*, 20(2), 536.

17. Lo Presti, D., Massaroni, C., Zaltieri, M., Sabbadini, R., Carnevale, A., Di Tocco, J., ... & Formica, D. (2020). A Magnetic Resonance-compatible wearable device based on functionalized fiber optic sensor for respiratory monitoring. *IEEE Sensors Journal*.

Conference Proceedings:

1. Zaltieri, M., Massaroni, C., Bianchi, S., Cauti, F. M., & Schena, E. (2022, June). Analysis of the Spatio-Temporal Dynamics of Thermal Lesion Formation in Radiofrequency Cardiac Ablation. In 2022 *IEEE International Symposium on Medical Measurements and Applications*.

2. Lo Presti, D., Zaltieri, M., D'Amato, R., Caponero, M., Massaroni, C. & Schena, E. (2021, June). Feasibility assessment of an FBG-based soft sensor embedded into a single-use surgical mask for respiratory monitoring. In 2021 *IEEE International Workshop on Metrology for Industry 4.0 & IoT.*

3. Lo Presti, D., Zaltieri, M., Di Tocco, J., Massaroni, C., D'Alesio, G., D'Abbraccio, J., ... & Schena, E. (2021, June). Respiratory rate monitoring of video terminal operators based on fiber optic technology. In 2021 *IEEE International Workshop on Metrology for Industry 4.0 & IoT*.

4. Zaltieri, M., De Vita, E., De Tommasi, F., Massaroni, C., Faiella, E., Zobel, B. B., ... & Campopiano, S. (2020, October). Evaluation of the Thermal Response of Liver Tissue Undergoing Microwave Treatment by Means of Fiber Bragg Grating Sensors. In 2020 *IEEE Sensors*.

5. Zaltieri, M., Lo Presti, D., Massaroni, C., Schena, E., D'Abbraccio, J., Massari, L., ... & Sterzi, S. (2020, May). Feasibility assessment of an FBG-based wearable system for monitoring back dorsal

flexion-extension in video terminal workers. In 2020 *IEEE International Instrumentation and Measurement Technology Conference*.

6. Zaltieri, M., Di Tocco, J., Lo Presti, D., Massaroni, C., Formica, D., Schena, E., ... & Sarto, M. S. (2020, June). A Test Bench to Assess Systems for Respiratory Monitoring of Workers. In 2020 *IEEE International Workshop on Metrology for Industry 4.0 & IoT.*

7. Zaltieri, M., Lo Presti, D., Massaroni, C., Sabbadini, R., Schena, E., Bravi, M., ... & Formica, D. (2020, June). An FBG-based Smart Wearable Device for Monitoring Seated Posture in Video Terminal Workers. In 2020 *IEEE International Workshop on Metrology for Industry 4.0 & IoT.*

8. De Tommasi, F., Zaltieri, M., Schena, E., Massaroni, C., Faiella, E., Grasso, R. F., ... & Campopiano, S. (2020, June). Temperature Monitoring During Microwave Thermal Ablation of Ex Vivo Bovine Bone: a Pilot Test. In 2020 *IEEE International Workshop on Metrology for Industry 4.0 & IoT*.

9. Carnevale, A., Massaroni, C., Lo Presti, D., Di Tocco, J., Zaltieri, M., Formica, D., ... & Denaro, V. (2020, June). Conductive textile element embedded in a wearable device for joint motion monitoring. In 2020 *IEEE International Symposium on Medical Measurements and Applications.*

10. Korganbayev, S., Asadi, S., Wolf, A., Dostovalov, A., Zaltieri, M., Schena, E., ... & Saccomandi, P. (2020, April). Highly dense FBG arrays for millimeter-scale thermal monitoring during nanocomposite-enhanced laser ablation. In *Optical Sensing and Detection VI*.

11. D'Abbraccio, J., Aliperta, A., Oddo, C. M., Zaltieri, M., Palermo, E., Massari, L., ... & Schena, E. (2019, June). Design and Development of Large-Area FBG-Based Sensing Skin for Collaborative Robotics. In 2019 *II Workshop on Metrology for Industry 4.0 and IoT*.

12. Panicacci, S., Giuffrida, G., Baldanzi, L., Massari, L., Terruso, G., Zaltieri, M., ... & Fanucci, L. (2019, September). Empowering Deafblind Communication Capabilities by Means of AI-Based Body Parts Tracking and Remotely Controlled Robotic Arm for Sign Language Speakers. In *International Conference on Applications in Electronics Pervading Industry, Environment and Society.*

Book Chapter:

Czimmermann, T., Massari, L., D'Abbraccio, J., Terruso, G., Zaltieri, M., Fransvea, G., ... & Oddo, C. M. (2022). Physical Contact Localization with Artificial Intelligence and Large-Area Fiber Bragg Grating Tactile Sensors for Collaborative Biorobotics. In *Electronic Skin, River Publishers*.